KU LEUVEN

ARENBERG DOCTORAL SCHOOL
Faculty of Engineering Science

What is the role of activated sludge flocs in membrane fouling in membrane bioreactors (MBRs)?

Glenn Van De Staey

Supervisor:
Prof. dr. ir. I. Smets

Dissertation presented in partial fulfillment of the requirements for the degree of Doctor in Engineering Science: Chemical Engineering

November 2016

What is the role of activated sludge flocs in membrane fouling in membrane bioreactors (MBRs)?

Glenn VAN DE STAEY

Examination committee:
Prof. dr. ir. D. Vandermeulen, chair
Prof. dr. ir. I. Smets, supervisor
Prof. dr. ir. I. Vankelecom
Dr. ir. R. Van den Broeck
Prof. dr. M. L. Christensen
(Aalborg University, Denmark)
Dr. D. B. Mesquita
(University of Minho, Portugal)

Dissertation presented in partial fulfillment of the requirements for the degree of Doctor in Engineering Science: Chemical Engineering

November 2016

Preface

At the time of writing this preface, traditionally as the last piece of text before a manuscript is sent to the print shop, I believe a few words are in order when looking back on my PhD. It's been quite a ride, with ups and downs, and lefts and rights. But finally, the finish line is approaching, and it's approaching fast.

Looking back on the past four years I realise that I've learned much about, not only wastewater treatment, or membrane bioreactors, but also about research, about finding a goal and working towards it, about planning and project managing, about friendship, about love. I could literally write a PhD on everything I've learnt! Obviously, I'm not going to do that, but there are a few words of wisdom I would like to give to the reader:

- *Murphy's law is real!* Whenever a piece of tubing from a lab set-up can plug, it will plug...in the weekend.
- *Time is indeed relative* ...especially during lab experiments.
- The word *treat* is generally a PhD student's highest priority mailing subject.
- Writing a text in scientific English for the first time is hard. But nothing compared to writing a text in Dutch after writing several hundreds of pages in scientific English.
- Better a good colleague than a distant friend.
- If you think thesis deadlines are hard... *you ain't seen nothin' yet!*

To conclude, I would like to thank a few people. First and foremost, my promotor Ilse Smets, for providing the topic, the framework and the guidance to conclude this PhD. You've been a great and inspiring mentor and a good friend, not only regarding work, but far beyond.

For receiving the research grant, my sincerest gratitude to FWO.

Next, I would like to thank the people of my jury. For all the time and effort that you put in helping me succeed. For the remarks and points of healthy criticism and the collaboration.

I would like to thank every company and employee that helped me with acquiring the activated sludge samples, especially Aquafin. Without your help, this would not have been possible.

Also towards my colleages and fellow PhDers, I would like to show my gratitude. Jeroen, Kenneth, Iason, Liesel, The Anh, Hoang, Wouter, Leticia, Geert, Geert, Koen, Jan, Lynn and Lily, I will look back on our great office moments with a smile. Pieter, good luck with your PhD!

For the great work we accomplished together, I would like to thank my thesis students: Ine, Kelly, Caroline, Lenn, Anton, Jens and Laure. I learnt a lot from each of you.

To my girlfriend, Anneleen, you are amazing. No more words needed.

Finally, I would like to thank my friends and family, especially my grandparents. Without you, none of this would have been possible. For the continuous support and the warmth you offer me. *Dikke merci!*

Abstract

As an efficient technology for wastewater treatment, membrane bioreactors (MBRs) have gained a lot of popularity over the recent years. In an MBR, the secondary biological treatment step is combined with a pressure driven membrane filtration, which results in an effluent of consistently high quality, reliable operation and a reduced footprint in comparison with conventional activated sludge systems that rely on sedimentation. However, fouling, which is the undesired accumulation of retained material on the membrane, remains the main drawback of MBRs. Fouling results in a performance loss through the decline of flux in constant pressure systems, or an increase in required transmembrane pressure in constant flux systems.

In this work, the primary aim is to uncover the activated sludge characteristics that are responsible for the membrane fouling and to uncover the mechanisms behind this phenomenon. Three goals were put forward. The first goal was the creation of a framework for bioflocculation and filterability monitoring. Once this framework was set up, the secondary goal was the experimental determination of the relationship between bioflocculation and activated sludge separation. Finally, in the third goal, the specific role of cations for membrane fouling was studied to unravel insights that may validate or disprove existing theories.

The **first part** of this work tackles the first goal. The activated sludge image analysis program that was previously developed within the division, was modified to accomodate images from the new, more advanced, Olympus IX83 microscope. Improvements include: better segmentation and recognition routines, no more color-image requirements and the ability to analyse images of variable size. Twenty 3x3 images are deemed enough to provide statistically significant results. In the next chapter, the use of quantitative fluorescent image analysis for bioflocculation monitoring was explored. To this end, two image analysis routines were programmed as well. Alexa405-NHS ester was found to provide superior results over fluorescein isothiocyanate for labeling proteins and the results

correlate well with the protein content from the heat extracted extracellular polymeric substances (eEPS). The use of the concanavalin A-Alexa488 conjugate, which labels α-polysaccharides, did not yield any eEPS correlation, but showed distinct localisation. Nile Red staining was tested against the microbial adhesion to hydrocarbons measurement, but could only differentiate between inorganic and organic fractions in terms of hydrophobicity. Finally, a fluorescence based method for Gram staining was semi-quantitatively compared to the conventional method and yielded good similarities.

In the **second part** of this work, the focus was on finding correlations between activated sludge characteristics and sludge separation efficiencies. To this end, a measuring campaign was performed on sludge samples from sixteen different wastewater treatment systems. On the data, a multivariate statistical analysis, using partial least squares, was performed to unravel the most influential sludge characteristics for cross-flow and dead-end filtration and settling. In the next chapter, two longterm labscale experiments were performed in which synthetic glucose-based influent was differentiated in terms of cation composition. In accordance with the divalent cation bridging (DCB) theory, changing the monovalent-over-polyvalent (M/P) cation ratio to a high value (17) resulted in deflocculation, which significantly worsened filtration. Changing the ratio back to a low value (2.04) remediated the filterability issues and restored the floc structures over a few weeks. During these experiments, conventional systems were found to be more resilient and recovered faster from such disturbance than membrane systems.

The data from both experiments were analysed together with the data from the measuring campaign in the final chapter of the second part. From the results, it is concluded that colloidal and small particulate matter are the most detrimental constituents of activated sludge, together with the polysaccharide fraction of the soluble microbial products (SMP). The morphology of the sludge is found to be of influence as fractal dimension and fouling rates appeared to be correlated. A sludge with a high relative hydrophobicity and a low surface charge proves to be beneficial. For filtration, a reasonable number of filaments was shown to provide a protective barrier against fouling.

From the results it became clear that dead-end filtration tests cannot be used for MBR-filterability assessment. Moreover, dead-end filtration appeared to be more influenced by the deflocculation and disturbances in the sludge's properties since the total amount of formed cake was higher. An abundance of filaments appeared to be the main source for settling problems, but sludge density and surface roughness played a significant role as well. No significant effect was found for eEPS on neither separation performance indicator.

For the **third goal**, the effect of cations on bioflocculation and filtration performance was studied. The DCB theory could explain the long term phenomena. A unified theory, combining results from this and previous works was proposed on the basis of the DCB theory: a period of *shell shedding* preceeds the more profound deflocculation phase.

For the shortterm effects, the osmotic pressure effect was brought forward and experimentally tested. The osmotic pressure effect comes from the accumulation of charged groups in front of the membrane as a consequence of the total sludge retention. Functional groups on flocs and SMP require counterions to be present to preserve electro-neutrality, which leads to a locally increased ionic strength. This ionic strength difference across the membrane leads to a difference in osmotic pressure, which requires an extra driving force during filtration. Different ionic strengths and M/P ratios were tested but the osmotic pressure effect could not be validated or disproved. At high ionic strengths (I>350 mM), filterability worsened, regardless of the M/P ratio. For the high M/P this was attributed to the shortterm deflocculation effect, in accordance with the DCB theory. For the low M/P, precipitation or sweep flocculation, creating small (colloidal) particles, probably played a role.

Beknopte samenvatting

Membraanbioreactoren (MBRs) zijn de voorbije jaren sterk in populariteit toegenomen als een efficiënte technologie voor afvalwaterzuivering. In een MBR wordt de secundaire, biologische zuiveringsstap gecombineerd met een drukgedreven membraanfiltratie, wat resulteert in een effluent met een continu hoge kwaliteit en een betrouwbare, compacte bedrijfsvoering in vergelijking met conventionele actief-slibsystemen, die gebruik maken van bezinking. Membraanvervuiling, dat gedefinieerd is als de ongewenste opstapeling van weerhouden materiaal op het membraan, blijft het grootste nadeel van MBRs. Membraanvervuiling resulteert in een performantieverlies omdat bij drukgecontroleerde systemen de flux gradueel vermindert, of omdat bij fluxgecontroleerde systemen de benodigde transmembraandruk toeneemt.

Het hoofddoel van dit onderzoek bestaat erin om de actief-slibeigenschappen die verantwoordelijk zijn voor membraanvervuiling te achterhalen en de principes die het fenomeen bepalen, te verklaren. Hiertoe zijn drie doelen vooropgesteld. Het eerste doel is het creëren van een kader voor bioflocculatie- en filtreerbaarheidsmonitoring. Eens opgesteld, kan in het tweede doel, op experimentele wijze de relatie tussen bioflocculatie en actief-slibscheiding worden achterhaald. Ten slotte, in het derde doel, wordt de rol van kationen in het proces van membraanvervuiling onder de loep genomen om de verschillende theorieën die hieromtrent bestaan, te valideren of te weerleggen.

Het **eerste deel** van dit werk beschrijft de aanpassingen aan het actief-slib-beeldanalyseprogramma dat reeds vroeger in de divisie was ontwikkeld. Deze aanpassingen omvatten, onder andere, het verbeteren van de segmentatie- en herkenningsroutines, het incorporeren van de mogelijkheid om beelden met een variabele grootte te analyseren en ervoor te zorgen dat vanaf nu ook beelden met grijswaarden kunnen behandeld worden. Statistisch gezien blijken 20 grids van 3 bij 3 foto's genoeg om significante resultaten te verkrijgen.

In het volgende hoofdstuk werd de toepasbaarheid van kwantitatieve fluorescente beeldanalyse voor monitoring van bioflocculatie onderzocht. Hiertoe werden twee beeldanalyse routines geprogrammeerd. Voor de visualisatie van proteïnen werd vastgesteld dat Alexa405-NHS ester superieure resultaten opleverde, in vergelijking met fluorescein isothiocyanaat, en dat deze resultaten een goede correlatie vertoonden met de resultaten van de warmte-extractie methode voor gebonden extracellulaire polymere substanties (eEPS). Het gebruik van het concanavalin A-Alexa 488 conjugaat, dat specifiek bindt met α-polysachariden, gaf echter geen correlatie met de eEPS, maar toonde wel duidelijke localisatie aan van deze moleculen in de vlokmatrix. De conventionele MATH-methode voor het opmeten van de relatieve hydrofobiciteit werd vergeleken met Nile Red kleuring, maar het bleek enkel mogelijk om qua relatieve hydrofobiciteit een onderscheid te maken tussen anorganisch en organisch materiaal. Ten slotte werd ook een alternatieve methode voor Gram-kleuring getest. De methode werd op semi-kwantitatieve manier vergeleken met de traditionele methode en vertoonde gelijkaardige resultaten.

In het **tweede deel** van dit werk, lag de focus op het vinden van correlaties tussen de actief-slibeigenschappen en de slibscheidingsefficiënties. Hiertoe werden stalen van zestien verschillende waterzuiveringsinstallaties geanalyseerd. Op de data werd een multivariate statische analyse uitgevoerd met behulp van *partial least squares*. Hieruit werden de belangrijkste slibkarakteristieken voor *cross-flow* en *dead-end* filtratie en bezinking bepaald. In het hoofstuk daarop werden twee langetermijnexperimenten uitgevoerd. Het slib werd gevoed met een synthetische voeding die op glucose gebaseerd was, maar die verschilde in kationsamenstelling. In overeenkomst met de kationbrugtheorie (DCB) werd de monovalent-over-polyvalente kationratio verhoogt tot 17, wat resulteerde in een deflocculatie en een verslechterende filtratie teweegbracht. Wanneer de verhouding terug verlaagd werd naar 2.04, werd een deel van de filtratieproblemen onmiddellijk verholpen en herstelde de vlokstructuur zich na enkele weken. Tijdens deze experimenten bleek ook dat conventionele systemen minder gevoelig zijn voor zulke storingen en dat ze sneller herstellen dan membraansystemen.

De data van beide experimenten en de meetcampagne werden samen geanalyseerd in het laatste hoofdstuk van het tweede deel. Uit deze resultaten blijkt dat de colloïdale en kleine particulaire deeltjes de meest negatieve impact uitoefenen op de filtreerbaarheid, samen met de oplosbare microbiële producten (SMP). De morfologie van het slib blijkt ook belangrijk aangezien de fractale dimensie en de vervuilingssnelheid een correlatie vertonen. Bovendien blijkt dat slib met een hoge hydrofobiciteit en een lage oppervlaktelading goede scheidingskarakteristieken bezit. Ook een matig aantal filamenten is bevorderlijk voor filtratie door de vorming van een beschermende barrière.

Uit de resultaten werd duidelijk vastgesteld dat *dead-end* filtratietesten niet geschikt zijn om MBR-filtreerbaarheid te bepalen. Bovendien is de *dead-end* filtratiemethode veel gevoeliger voor deflocculaties en schommelingen in de slibeigenschappen, aangezien de hoeveelheid koeklaag die gevormd wordt, aanzienlijk hoger is. Wildgroei van draadvormende bacteriën blijkt het meest nefast voor bezinkbaarheid, maar ook de slibdensiteit en de oppervlakteruwheid spelen hierin een belangrijke rol. Voor geen van de scheidingsmethodes werd een significante invloed vastgesteld van de gebonden EPS.

In het **derde deel** van het werk, werd het effect van kationen op bioflocculatie en membraanvervuiling geanalyseerd. De DCB theorie kon de langetermijneffecten verklaren en een universele theorie gebaseerd op deze en eerdere resultaten werd vooropgesteld, op basis van de DCB theorie: complete deflocculatie wordt voorafgegaan door een periode van *shell shedding*.

Voor de kortetermijneffecten werd de validiteit van het osmotische drukeffect bestudeerd. Dit effect resulteert uit de accumulatie van geladen functionele groepen aan de retentaatzijde van het membraan. Omdat de ladingsneutraliteit behouden moet blijven, zullen kationen uit de bulk door deze groepen aangetrokken worden, waardoor de lokale ionische sterkte voor het membraan hoger is dan aan de permeaatzijde. Dit verschil in ionische sterkte leidt tot een verschil in osmotische druk, wat een extra drijvende kracht tegen filtratie veroorzaakt. Verschillende ionische sterktes en M/P-verhoudingen werden getest, maar het osmotische drukeffect kon niet gevalideerd of ontkracht worden. Hoge ionische sterktes (I>350 mM) bleken ten allen tijde nefast voor de filtreerbaarheid, ongeacht de M/P-verhouding. Voor de hoge M/P-verhouding werd dit effect gelinkt aan het kortetermijn deflocculerend effect volgens de DCB theorie, terwijl voor de lage M/P-verhouding de oorzaak vermoedelijk te vinden is bij neerslagvorming of *sweep-flocculation*, wat leidt tot de creatie van kleine (colloïdale) deeltjes.

List of abbreviations

A405-NHS	Alexa-Fluor405 NHS ester
AB	Hydrogen bonding interactions
AFR	Average fouling rate
BOD	Biochemical oxygen demand
BPC	Biopolymer clusters
BSA	Bovine serum albumin
CAS	Conventional activated sludge system
CCD	Charge-coupled device
CER	Cation exchange resin
CLSM	Confocal laser scanning microscopy
COD	Chemical oxygen demand
ConA-A488	Concanavalin A Alexa 488 conjugate
DCB	Divalent cation bridging
DLS	Dynamic light scattering
DLVO	Dejarguin-Landau-Verwey-Overbeek
DMSO	Dimethylsulfoxide
DNA	Deoxyribonucleic acid
DSM	Dynamic secondary membrane
DO	Dissolved oxygen
eEPS	Extractable extracellular polymeric substances
eEPS-H	Heat-extracted eEPS
eEPS-CER	Cation exchange resin-extracted eEPS
EL	Electrostatic interactions
EPS	Extracellular polymeric substances
ESS	Effluent suspended solids
Ex	Excitation wavelength
Em	Emission wavelength
FD	Fractal dimension
FISH	Fluorescent *in situ* hybridization
FITC	Fluorescein isothiocyanate
F/M ratio	Food-over-microorganisms ratio
FS	Flat sheet
GFP	Green fluorescent protein

GFR	Global fouling rate
HF	Hollow fiber
HI	Hexidium iodide
HRT	Hydraulic retention time
iMBR	immersed (or submerged) membrane bioreactor
LW	Van der Waals interactions
MBR	Membrane bioreactor
MF	Microfiltration
MFI	Modified fouling index
MIA	Multiple image acquisition
MLSS	Mixed liquor suspended solids
MLVSS	Mixed liquor volatile suspended solids
M/P	Monovalent-over-polyvalent cation ratio
MT	Multi-tubular
NF	Nanofiltration
OPE	Osmotic pressure effect
PCA	Principal component analysis
PE	Polyethylene
PES	Polyethersulphone
PHA	Polyhydroxyalkanoates
PI	Propidium iodide
PLS	Partial least squares
PN	Proteins
PP	Propylene
PRESS	Predictive sum of squares
PS	Polysaccharides
PVDF	Polyvinilidene difluoride
RH	Relative hydrophobicity
RNA	Ribonucleic acid
Rndns	Roundness
RO	Reverse osmosis
RSS	Residual sum of squares
SC	Surface charge
SE	Structuring element
SF	Sustainable flux
sMBR	Side-stream membrane bioreactor
SMP	Soluble microbial products
SRT	Sludge retention time
SS	Sum of squares
SVI	Sludge volume index
TOT	Time of transition
TMP	Transmembrane pressure
VIP	Variable influence of projection
UF	Ultrafiltration
XDLVO	Extended Dejarguin-Landau-Verwey-Overbeek

List of symbols

A	Absorbance
$A_{<13\mu m}$	Surface fraction of objects with Deq < 13 µm
α	Specific cake resistance
α_0	Specific cake resistance at zero pressure
β	Partial least squares regression coefficients
C_c	Concentration of charged species in cake
C_{feed}	Influent substrate concentration
C_i	Ion concentration
C_p	Concentration of charged species in permeate
$CI_{n,95}$	95% confidence interval for the n^{th} data point
D	Diffusion constant
D_t	Brownian diffusion coefficient
Deq	Equivalent floc diameter
Deq_w	Surface weighted equivalent diameter
d_p	Particle diameter
$d_{p,max}$	Maximal particle diameter
e	Electron charge
ϵ	Relative permittivity (Debye length)
ϵ	Cake layer porosity
ϵ_0	Vacuum permittivity
EC	Ellipse coverage
EC_{Crit}	Critical ellipse coverage
$f_{i,j}$	Pixel value at position (i,j)
G	Root mean square velocity gradient
I	Ionic strength
I	Intensity (Fluorescence)
J	Permeate flux
$J_{c,s}$	Strong form of critical flux
$J_{c,w}$	Weak form of critical flux
k_{kozeny}	Tuning parameter
K_m	Monod constant
k_s	Tuning parameter
K_{ss}	Shear-sensitivity

λ	Wavelength of laser light
λ_D	Debye length
$\mathrm{m}_{d,t}$	Dispersed mass concentration at time t
$\mathrm{m}_{d,0}$	Initial dispersed mass concentration
$\mathrm{m}_{d,\infty}$	Dispersed mass concentration at equilibrium
m_T	Total mass concentration of sample
μ	Specific growth rate (Monod kinetics)
μ_{max}	Maximum specific growth rate (Monod kinetics)
μ_{max}	Maximum friction coefficient (particle size theory)
η	Refractive index
η	Viscosity
η_p	Permeate viscosity
$\Delta\pi$	Osmotic pressure
ΔP_c	Pressure drop across the cake
P_a	Compressibility parameter
PixI	Pixel intensity
Q	Exponential rescaling parameter
Q_w	Daily volume of sludge wasted
Q_{feed}	Influent volumetric flow rate
Q^2Y	Goodness of prediction
R	Ideal gas constant
R_b	Biofilm formation resistance
R_c	Cake layer resistance
R_{cp}	Concentration polarization resistance
R_{mem}	Membrane resistance
R_p	Pore blocking resistance
R_{sc}	Scaling resistance
R_{tot}	Total resistance for flow through membrane
R_g	Radius of gyration
R^2Y	Goodness of fit
RR	Relative ratio
σ^2	Variance
σ_w^2	Intravariance
S	Substrate concentration
S	Conductivity (ionic strength measurement)
T	Temperature
TTF_{25}	Time to filter
V	Volume
V_{MBR}	MBR volume
WOF_{250}	Weight of filtrate
X	Biomass concentration
x_c	Molar fraction of charged species in cake layer
x_p	Molar fraction of charged species in permeate
w_b	Weighing factor
z_i	Ion valence

Contents

Chapter 1

Introduction

1.1 Why treat wastewater?

Will there be enough water to sustain the almost nine billion people that are expected to populate the earth by 2050? A question that is asked more and more frequently over the past decade, governed by the environmental threats posed by global warning, demographic growth, higher global living standards and industrial development. Freshwater withdrawals have increased globally by about one percent per year since the 1980s. In 2000, the world withdrew between 3500 and 4000 cubic kilometers of water for the purposes of food security, people's livelihoods, industrial growth and environmental protection. By 2050, this withdrawal is projected to increase by at least 50 percent [United Nations, 2016]. A review from Amarasinghe and Smakhtin [2014], summarizing 13 water demand projections, concluded that the current average per capita domestic water withdrawal already exceeds business as usual scenarios for 2025, developed in the early 2000s.

Launched on World Water Day, March 22, 2016, the UN World Water Development Report on Water and Jobs stated that three out of four jobs worldwide are water dependent and that water shortages or a lack of access may limit economic growth in the years to come. Moreover, several studies collected in this report proof that there exists a positive correlation between investments in the water sector and economic growth and that water plays a key role in the transition towards a green economy [United Nations, 2016].

1.2 Biological wastewater treatment

In biological wastewater treatment, the organic pollutants and nutrients present in the wastewater are consumed by a microbial community and hereby converted into additional biomass, gaseous components and other byproducts. This microbial community, also called activated sludge, serves three major functions:

- removal of dissolved organic components and nutrients,
- capturing and adhesion of suspended, non-settling colloidal matter,
- aggregation into dense flocs that can be easily separated from the surrounding treated liquor.

In general, a three step process is used. In the **primary treatment**, physico-chemical separation techniques are used to remove coarse material, such as dirt, sand and debris and to protect downstream equipment. These techniques include screens, grit chambers, sieves, flotation units and primary settlers.

During the **secondary treatment**, the actual biodegradation takes place and the organic components and nutrients present in the wastewater are broken down by the activated sludge, which is a heterogeneous mixture of predominantly bacteria, adsorbed inorganic and organic particles and protozoa, embedded in a matrix of extracellular polymeric substances (EPS). Typically, an aerated reactor is used for organic carbon removal and the sludge is kept in suspension by aeration and mixing. More advanced processes have multiple reactors, of which some have limited oxygen concentrations, to facilitate nutrient removal. When the organic pollutants are removed from the system, the bacteria need to be separated from the treated water. This solid-liquid separation can be accomplished in two major manners. In the first, *conventional activated sludge system (CAS)*, the sludge settles under influence of gravity and is thickened and recycled back to the biodegradation tanks. A second method, the *membrane bioreactor (MBR)* exploits micro- or ultrafiltration membranes to provide a solid-liquid barrier. In both systems, the amount of sludge increases over time. Thus, to provide steady conditions, part of this sludge needs to be removed and is usually de-watered, digested and incinerated or disposed.

Finally, to further purify the water to meet discharge or reuse standards, a **tertiary treatment** may be required. Tertiary treatment refers to a collection of methods that include, but is not limited to: (sand) filtration, ion-exchange, carbon adsorption, desinfection and (electro)dialysis.

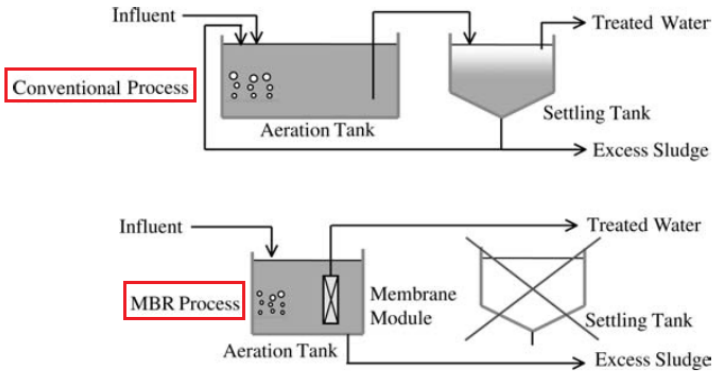

Figure 1.1: Schematic comparison between the conventional activated sludge process (**top**) and the MBR process (**bottom**) [http://www.airlimbah.com].

1.2.1 MBR compared to CAS

Figure 1.1 illustrates the main similarities and differences between the conventional activated sludge system and the membrane bioreactor configuration.

After the removal of the organic pollutants, the activated sludge needs to be separated from the treated water. In the **conventional system**, the density difference between the formed flocs and the surrounding water is exploited and the activated sludge is separated through sedimentation in settlers. The majority of the settled sludge is then returned to the mixed tank, while a fraction is wasted to maintain the desired activated sludge concentration and age and to prevent the accumulation of inorganics.

As mentioned before, in a **membrane bioreactor**, the activated sludge flocs are retained in the mixed tank by means of membrane modules. The use of membranes counters the challenges that are inherently coupled to the gravitational sedimentation, as the difference in density between the flocs and the treated water is often not high enough for adequate separation. Therefore, the use of MBRs enables a complete sludge retention and, given proper biodegradation, an effluent of consistently high quality and a lower need for subsequent disinfection. Moreover, the absolute barrier between the treated water and the mixed liquor, enables higher sludge concentrations and sludge ages, resulting in a wider biodiversity, a lower footprint and a more intensified process.

The most prevalent disadvantage of membrane bioreactors is the degradation of

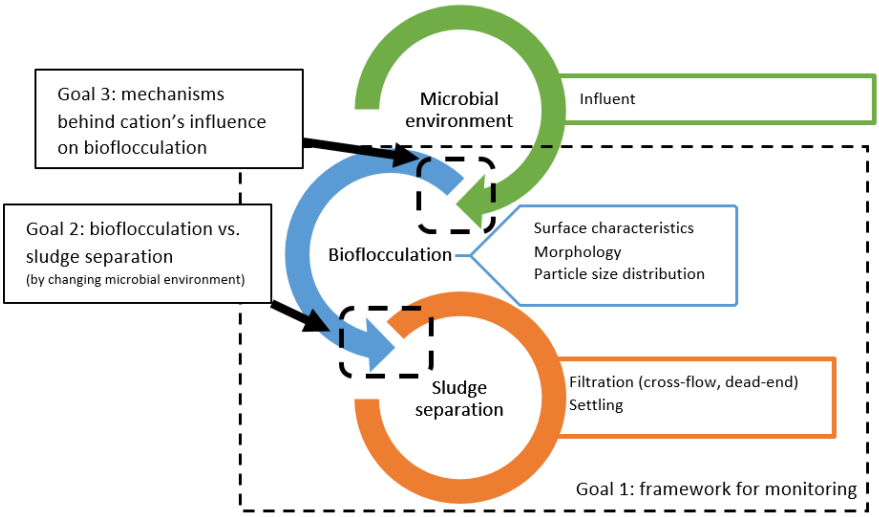

Figure 1.2: Schematic representation of this work's objectives.

filtration performance over time due to the accumulation of retained material in front of the membrane. When these accumulants attach to the membrane, resulting in a loss of permeability, one speaks of *membrane fouling*, which will be discussed in great detail in Section 2.2. Due to membrane fouling control strategies, MBRs have higher energy requirements (shear generation through mixing and aeration) and consume more chemicals (membrane cleaning) than conventional systems.

1.3 Objectives of this dissertation

Within our division, results have been published that exemplify the use of microscopy and image analysis as a monitoring tool for bioflocculation [Jenné et al., 2007]. These tools have been exploited to uncover the importance of sludge characteristics, such as hydrophobicity, particle sizes and morphology and extracellular polymeric substances (EPS) for MBR filtration [Van den Broeck, 2011] and settling [Van Dierdonck, 2013] and to integrate such information into a mechanistic filtration model [Cao, 2016]. It is within this context that this PhD started.

The primary aim of this work is to give a clear answer to *what sludge*

characteristics cause separation problems, what is the underlying cause and can it be avoided?. Separation problems is a general term, but in this work the focus will lie mostly on MBR-filtration.

To achieve the primary aim, the strategy of *divide and conquer* is applied. The primary aim is split up in three major goals. These goals are illustrated in Figure 1.2.

The **first goal** of this work, is to provide a monitoring framework for bioflocculation and MBR-filtration assessment. In order to study the role of activated sludge in fouling, both should be fully characterised. Therefore, the first goal involves the following tasks.

- Critically assess and improve existing monitoring tools for bioflocculation and cross-flow filtration monitoring (e.g., microscopic imaging, image analysis, EPS measurements, floc strength measurements, dead-end filtration tests).
- Develop new monitoring tools to fill existing gaps and explore new possibilities (e.g., quantitiative fluorescence measurements and the construction of a labscale filtration set-up with a minimal volume that still provides conditions close to real MBR hydrodynamics).

The **second goal** of this work is to unravel the sludge characteristics that are important for MBR operation, but also, in a broader sense, to sludge separation. To this end, several sludge samples of different origins are characterised and assessed for their separation performance. Next, using statistical techniques, the relevant parameters are identified. In this study, both sludge from municipal as industrial origin is tested.

One way to create a disturbance in bioflocculation is by changing the influent's ion concentration in terms of monovalent and polyvalent cations. This knowledge is used in two longterm experiments to create different bioflocculation states and observe their effect on sludge separation. During these studies, the impact of the reactor configuration (MBR versus CAS) is also assessed.

As such, an answer is to be provided on the following questions.

- What sludge characteristics are detrimental and beneficial for MBR-filtration?
- Can these characteristics be monitored and can they be influenced?
- What about other separation modes (dead-end filtration, settling)?

- Can dead-end filtration tests be used for MBR-assessment?
- What is the role of EPS in bioflocculation and activated sludge separation?

Obtaining this information would yield crucial insights in the phenomenon of membrane fouling and may lead to a more mechanistic approach of fouling prevention, mitigation and control.

The **third goal** focusses more on the mechanisms behind the salt's influence on bioflocculation. Whereas this influence is a known phenomenon, different, often conflicting, theories exist that describe this relationship. The data from the long term experiments is combined with several shortterm filtration/bioflocculation assessment studies to unravel principles in this matter.

1.4 Chapter-by-chapter overview

In **Chapter 2**, an extensive literature overview will be given regarding membrane bioreactors and membrane fouling. **Chapter 3** will tackle the process of bioflocculation, which is the formation of activated sludge flocs. In the second part of this chapter, different existing monitoring tools for bioflocculation will be discussed.

In **Chapter 4**, the different materials and methods that are *commonly* used throughout this work will be presented.

The results of this work are thematically structured along **three parts**.
In **Part I**, the development of bioflocculation monitoring tools will be addressed. First, in **Chapter 5**, the improvements that were made on the inhouse activated sludge image analysis program are presented. Next, **Chapter 6** presents an explorative study on the use of epifluorescence microscopy as a bioflocculation monitoring tool.

Part II will cover the influence of bioflocculation and sludge characteristics on activated sludge separation. In **Chapter 7**, a measuring campaign covering activated sludge samples from different municipal and industrial origins is presented. In this study, a multivariate statistical technique is used to link the activated sludge characteristics to filtration and separation performances. The results from this chapter have been presented at the Euromembrane2015 and Dycops-CAB2016 conferences and are published in Van De Staey et al. [2016].

The next chapter, **Chapter 8** will cover two longterm experiments in which bioflocculation was altered through the influence of changes in the influent's cation balance. These results are published in Van De Staey et al. [2015].

This second part concludes with **Chapter 9**, in which the results from Chapters 7 and 8 are bundled, compared with literature and discussed in a broader context.

The final part of this work, **Part III**, will cover the shortterm effects of cations on filtration. In **Chapter 10**, an attempt is made to verify the osmotic pressure effect, which will be introduced in Section 2.3.7.

Finally, conclusions are drawn in **Chapter 11** and an outlook is given on the future research potential.

Chapter 2

Membrane bioreactors (MBRs) and fouling

This chapter will provide the state of the art regarding membrane bioreactors. As this work focusses on one of their main disadvantages, namely membrane fouling. This fouling phenomenon will be extensively discussed in the second part of this chapter. In the third section, the link will be made with biomass characteristics, which is this thesis' main topic.

2.1 MBR fundamentals

In this section, an introduction is provided concerning membrane bioreactors. It starts with a general MBR description and a comparison with the conventional aerated system. Next, several technical MBR choices and features are discussed, including operation modes, membrane selection and configurations.

2.1.1 What is an MBR?

Membrane bioreactors are an alternative for the reactor/settler combination in the secondary step of a conventional wastewater treatment plant. In this secondary treatment step, the microorganisms that are aggregated into flocs and embedded in the EPS-matrix, reduce the wastewater's organic load by consuming it as substrate for energy production and replication. Typically,

complete nutrient removal requires a sequence of aerated, anoxic [1] and anaerobic conditions, but this study will focus only on the former.

The most important operational parameters for biodegradation control are the sludge retention time (SRT, Equation (2.1)), the hydraulic retention time (HRT, Equation (2.2)) and the feed-over-microorganisms loading ratio (F/M, Equation (2.3)). The SRT denotes the average time the activated sludge resides in the system and serves as a measure for the sludge age, while the HRT is the average residence time of the influent, as a measure of the purified water production rate per unit of reactor volume.

$$SRT = \frac{V_{MBR}}{Q_w} \tag{2.1}$$

$$HRT = \frac{V_{MBR}}{Q_{feed}} \tag{2.2}$$

$$F/M = \frac{C_{feed} \cdot Q_{feed}}{X} = \frac{C_{feed}}{HRT \cdot X} \tag{2.3}$$

in which:

V_{MBR}	=	MBR volume	[L]
Q_w	=	Daily volume of sludge wasted	[L/day]
Q_{feed}	=	Influent volumetric flow rate	[L/day]
C_{feed}	=	Influent substrate concentration	[gCOD/L]
X	=	Biomass concentration	[g/L]

In biological wastewater treatment, the microorganisms responsible for biodegradation are aggregated in activated sludge flocs. The reason behind this is the low F/M ratio employed in the process, which suppresses proliferation of individual bacteria, but promotes the formation of floc structures as a bacterial stress response to the starvation regime. Moreover, the *food-shortage* results in a partial suppression of growth, as most energy is used for microbial maintenance, thus limiting the sludge production. The floc structures are held together by interactions between the microorganisms themselves, but also by extracellular polymeric substances (EPS) in which they are embedded. Activated sludge is a very heterogeneous mixture, containing besides a multitude of different bacterial species and EPS, other constituents such as inorganics, fungi, archae and protozoa. More information on activated sludge, EPS and bioflocculation will be given further in this chapter and in Chapter 3.

[1] The absence of dissolved O_2 is indicated as *anoxic*, while the term *anaerobic* is used to indicate the absence of any common oxygen-containing electron acceptor such as nitrate, sulfate or dissolved O_2.

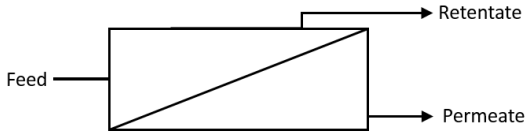

Figure 2.1: Schematic representation of a membrane process.

A membrane bioreactor (MBR) couples the biodegradation step with a pressure-driven membrane separation, by which the purified water is extracted from the mixed liquor.

A membrane, as applied to water and wastewater treatment is a perm-selective material, meaning it allows some physical or chemical components to pass more readily through it than others. The flow through the membrane is called the permeate, whereas the remainder is denoted as the retentate. A membrane process is schematically represented in Figure 2.1.

The degree of selectivity depends on the membrane pore size and surface properties. Typically, the coarsest membrane, which is used in microfiltration, can only reject particulate matter, whereas the most selective membrane, in reverse osmosis, is used to even reject monovalent ions, such as sodium Na^+ and chloride Cl^- (See also Section 2.1.3).

In membrane technology, the permeate flux (J, Equation (2.4)) describes the volumetric rate of permeate production (V/t) per unit of membrane surface (A):

$$J = \frac{V}{A\ t} \tag{2.4}$$

All membrane processes described in this work are pressure driven processes, which can be explained by Darcy's law:

$$J = \frac{TMP}{\eta_p\ R_{tot}} \tag{2.5}$$

with

J	=	permeate flux		[L/m^{2}h or m/s]
TMP	=	transmembrane pressure		[mbar or Pa]
η_p	=	permeate viscosity		[Pa s]
R_{tot}	=	total resistance for flow through membrane		[m^{-1}]

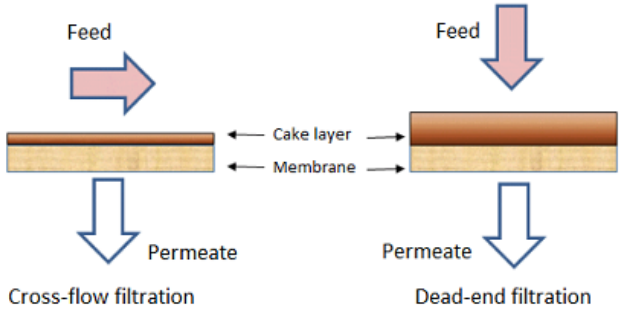

Figure 2.2: Schematic representation of cross-flow (**left**) and dead-end (**right**) filtration [http://www.onlinembr.info].

The total resistance R_{tot} comprises the membrane resistance R_{mem} and all the extra resistances that can be attributed to fouling phenomena, which will be explained in Section 2.2.

2.1.2 Cross-flow versus dead-end

In membrane filtration, two operation modes exist: cross-flow filtration and dead-end filtration, depending on the direction of the feed flow in relation with the membrane surface.

During **dead-end** filtration, the feed and permeate flow are parallel, both perpendicular to the membrane surface (Figure 2.2 (right)). All particles that can be screened by the filter will settle on its surface, resulting in the build-up of a cake layer over time. From time to time, backwashing is performed or the filter medium is replaced. Dead-end filtration, however, is only effective when the feed water carries a low level of foulants. It is used in surface water filtrations, some tertiary filtrations and in pretreatment methods for seawater reverse osmosis, but is not readily applied in MBR filtration.

In **cross-flow** filtration, the feed moves parallel to the membrane surface, as can be seen in Figure 2.2 (left). As such, the shear provided by the feed flow scours the membrane surface to control the cake layer thickness. Cross-flow filtration is used in systems where the feed water carries high levels of foulants such as suspended solids and macromolecules (as, e.g., in MBRs).

2.1.3 Membranes and configurations used in MBRs

Figure 2.3 depicts the pore sizes of membranes used in common membrane filtration operations. As can be seen from the image, membrane bioreactors typically operate using micro- or ultrafiltration membranes, which are able to retain bacteria, suspended solids and mostly viruses, giving MBRs a high sanitation power which greatly reduces the need for subsequent disinfection. When immersed systems are used (see Section 2.1.3), the pore size is usually limited to microfiltration or the higher end of ultrafiltration membranes due to vacuum pressure limitations. Side-stream configurations allow for selecting the pore size more freely.

A variety of materials is exploited to prepare membranes including ceramics and polymers. Metallic membrane filters exist as well, but have very specific applications that do not relate to MBR-technology. Generally a membrane is manufactured as a composite structure, consisting of a selective thin surface layer supported by a thicker porous layer which provides mechanical stability. Therefore, typical membranes are anisotropic and their orientation is highly flow dependent. The membrane material should comply to a few constraints, such as a high surface porosity and a narrow pore size distribution to provide adequate permselectivity and throughput. Moreover, the membrane material should be mechanically strong and have resistance against the thermal and chemical conditions of its targeted application. Ceramic membranes have superior chemical, thermal and hydraulic resistance, but are generally more expensive. Mostly used are the following polymeric membranes [Judd, 2011]:

- polyvinilidene difluoride (PVDF) (most used, 45% of all commercial MBR products [Judd, 2015]);
- polyethersulphone (PES);
- polyethylene (PE);
- polypropylene (PP).

Specific manufacturing techniques are used to craft the above polymers into membranes. However, these compounds are inherently hydrophobic, which relates to a low aqueous flux and a higher fouling susceptibility due to hydrophobic interactions with the biomass. The choice for these hydrophobic materials is made because they provide a good thermal and chemical stability, which makes them robust against cleaning agents used in MBR operation, whereas hydrophilic materials such as cellulose derivates or polyamides are less resilient against certain chemicals (mostly Cl). Therefore, surface modifications are used to improve the hydrophilicity of hydrophobic membranes, such as

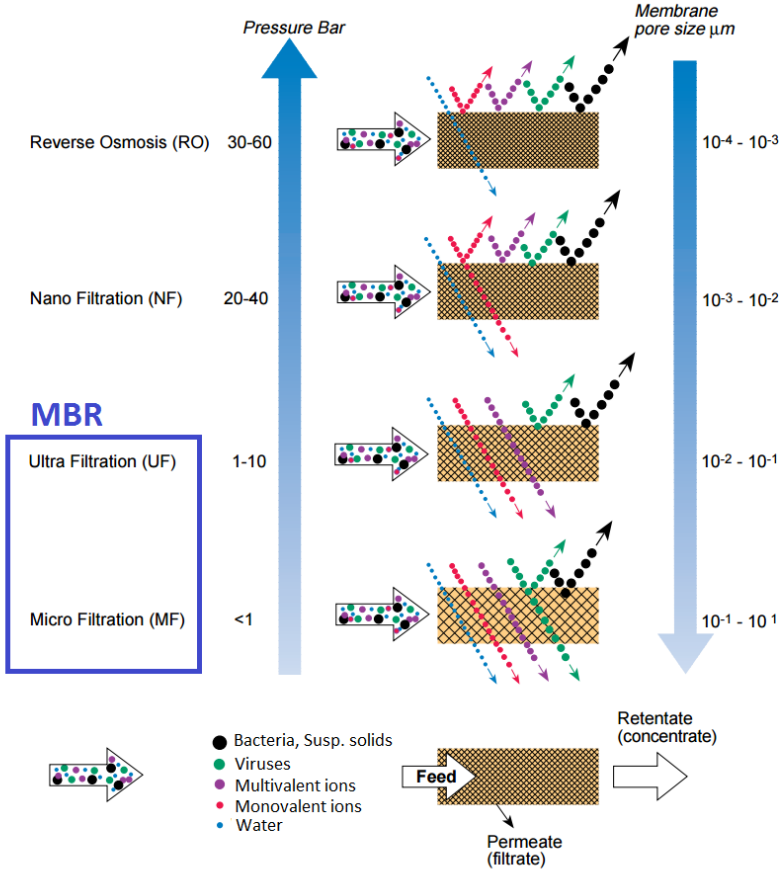

Figure 2.3: Pore sizes of membranes used in filtration operations [Bylund, 1995].

chemical oxidation or plasma treatment with CO_2 or NH_3, introducing polar groups. Another technique is the use of precoating with TiO_2 or ferric hydroxide (nano)particles [Le-Clech et al., 2006].

The membranes used in MBRs can be configured into different module designs, which defines how the membranes are arranged and determines the fluid management, energy demand, ability to handle suspended solids, ease of cleaning, replacement and packing density. In MBRs typically three module designs exist: flat sheets (FS), hollow fibers (HF) or (multi)tubular membranes (MT). These configurations are graphically illustrated in Figure 2.4. Other configurations, such as capillary tubes, spiral-wound membranes or filter cartridges are used in different membrane filtration processes, but will not be further discussed. Table 2.1 compares the three commonly used membrane module configurations in MBRs. Tubular membranes are solely used for side-stream MBRs, while hollow fibers and flat sheet modules are used for both immersed and side-stream configurations.

Table 2.1: Typical membrane module configurations in MBRs.

	FS	HF	MT
Packing density	Moderate	High	Low
Energy	Low	Low	High
Solids handling	Good	Moderate	Good
Cleaning	Moderate	Poor	Good
Backflushable	No	Yes	No
Replacement	Sheet	Bundle	Tube
Relative cost	High	Very low	Very high

FS = flat sheet, HF = hollow fibers, MT = multi-tubular

Typically, two module locations are used in MBR processes. If the membrane module is situated inside the aerated tank, one speaks of an **immersed** (or submerged) MBR. In the alternative **side-stream** MBR, the membrane module is located on the outside of the aeration tank. Figure 2.5 schematically depicts these concepts.

Immersed MBR (iMBR) systems are generally used to treat influents that are easily degradable. The membrane can either be submerged inside the bioreactor itself, or have a separate membrane-tank, but in both scenarios the membranes are placed directly into the mixed liquor and air scouring is performed to mitigate membrane fouling. Generally, the specific energy required per permeate volume is much less in iMBRs as compared to the side-stream variants. However, since the permeate is obtained using vacuum suction, the

Figure 2.4: Membrane modules used in MBR processes. **Top:** flat sheet membranes (Kubota), **Middle**: tubular membranes (PCI membranes), **Bottom**: hollow fibers membranes (Zeeweed).

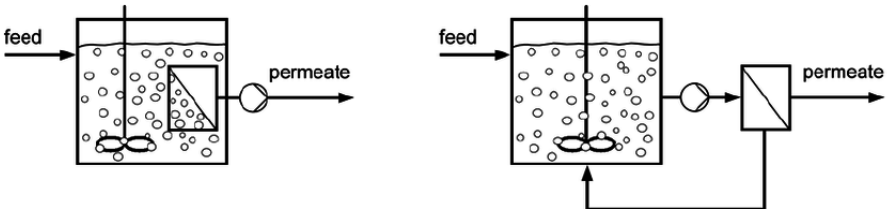

Figure 2.5: Schematic representation of an immersed MBR (**left**) and a side-stream MBR (**right**) [Drews and Kraume, 2005].

maximum attainable transmembrane pressures (TMP) are relatively modest. Whereas the theoretically maximal obtainable limit is 1 atm, maximum TMPs of 50-300 mbar are used in practice, leading to fluxes between typically 10-50 L/m^{2}h [Yoon, 2016].

In side-stream MBR (sMBR) systems, high pressure (3-6 bar) is used to primarily maintain high cross-flow velocities on the membrane surface and to provide shear. However, this shear often leads to break-up of sludge flocs, inducing small particles and very dense cake layers, which have low permeability. As a result, the average flux of sMBRs is between 50-100 L/m^{2}h, albeit with a high attainable TMP. The combination of high capital costs, high energy costs and a larger footprint, make sMBRs a far less attractive alternative than iMBR for most municipal wastewater treatment applications [Yoon, 2016]. However, since sMBR systems provide a more direct hydrodynamic control of membrane fouling and an easier membrane replacement, several industrial applications exist, such as wastewaters from food processing, pulp and paper, oily and petrochemical industry [Lin et al., 2012]

2.1.4 Constant flux or constant TMP mode of operation

Membrane filtration can be performed in two modes of operandi. During **constant flux** operation, the TMP increases as permeate is produced, while a **constant TMP** process results in a declined permeate flux as the membrane fouls. Nearly all MBR applications operate at constant flux. The reasoning behind this choice is that often severe fouling is observed at the start of a constant TMP run, which occurs because of the high initial flux (i.e., low virgin membrane mass transfer resistance) that provides a large foulant drag force. Operation at constant flux overcomes this problem.

Miller et al. [2014] compared constant flux to constant TMP experiments by analysis of the total resistance R_{tot} at times when both methods had produced equal amounts of permeate. Using ultrafiltration membranes and emulsified oil solutions, they came to the conclusion that the results obtained from both methods were in good agreement for low/medium fluxes below the threshold flux (in their study 62 L/m^{2}h, see below for a description of the threshold flux), but that constant flux operation resulted in a higher resistance for higher fluxes.

2.2 Membrane fouling

This section will focus on membrane fouling, its causes and its characterisation.

2.2.1 What is membrane fouling?

Fouling is defined as the coverage of the membrane surface (internal and external) by deposits which absorb, adsorb and accumulate during operation [Drews, 2010], leading to several phenomena that cause a loss in membrane permeability. To overcome this permeability loss, larger membrane surfaces, higher applied pressures or cross-flow velocities, both leading to increased energy costs, or frequent membrane cleanings are required. In the end it is clear that membrane fouling still remains a very high cost factor.

The high cost of fouling is affirmed by a recent (February 2015) stakeholders-survey conducted via The MBR Site that points out that membrane fouling is still among the priority issues to be solved regarding MBR-operation, together with membrane screening, channel clogging and overloading [Judd, 2015].

Time scale of different types of fouling

Figure 2.6, adopted from Drews [2010], depicts the traditional classification of fouling according to its respective time scale. Generally, reversible fouling refers to fouling that can be removed without chemical cleaning, but solely through physical operations such as backflushing or relaxation under cross-flow conditions. In earlier times, irreversible fouling was often referred to as the fouling that can only be removed by thorough chemically enhanced cleaning methods. However, in full-scale MBR systems, minimal maintenance cleanings are often performed on a weekly or two-weekly basis to suppress irreversible fouling. The fouling that is removed by these maintenance cleans is denoted as residual fouling, while the fouling that remains until a more thorough cleaning

is performed is then denoted as irreversible fouling. Finally, some fouling will always remain that cannot be removed by any cleaning. This irrecoverable fouling will ultimately determine the membrane's life span.

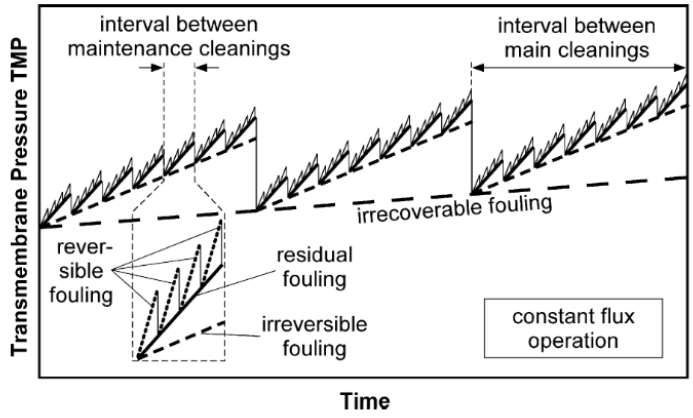

Category	Fouling rate in mbar/min	Time frame
Reversible fouling (cake filtration)	0.1–1	10 min
Residual fouling	0.01–0.1	1–2 weeks
Irreversible fouling	0.001–0.01	6–12 months
Irrecoverable fouling	0.0001–0.001	Years

Figure 2.6: Schematic representation of temporal fouling distribution during long-term operation of full-scale MBRs [Drews, 2010].

Resistance-in-series model

In fouling modeling, the total resistance R_{tot} from Equation (2.5) is often described as a sum of individual contributions, each with their physical relevance. An extended version of this so-called *resistance-in-series* model is given by Busch et al. [2007] and is summarized by Equation (2.6).

$$R_{tot} = R_{mem} + R_c + R_p + R_b + R_{cp} + R_{sc} \tag{2.6}$$

with:

R_{mem}	=	membrane resistance
R_c	=	cake layer formation
R_p	=	pore blocking
R_b	=	biofilm formation
R_{cp}	=	concentration polarization
R_{sc}	=	scaling

In many applications, the last three resistances from Equation (2.6) are neglected [Diez et al., 2014; Li and Wang, 2006]. This way, Equation (2.6) simplifies to:

$$R_{tot} = R_{mem} + R_c + R_p \tag{2.7}$$

In the next paragraphs, the different components from Equation (2.6) will be explained briefly.

The **membrane resistance** (R_{mem}) denotes the resistance of the membranes themselves and the module (tubing etc.) and is considered constant throughout the filtration.

Cake layer formation (R_c) is often denoted as the most important resistance for filtration [Cho and Fane, 2002; Li and Wang, 2006; Lin et al., 2009]. Therefore, although present, other fouling phenomena will only be briefly touched in this work. Cake formation describes the build-up of the fouling layer that gradually increases in size and consolidates as the filtration progresses. In this study, therefore, the focus will be on the effect of the sludge characteristics on the cake layer formation.

To model the cake layer resistance, Broeckmann et al. [2006] designed a model based on the forces that act on a single particle, balancing permeation drag-force with back-transport cross-flow velocity. For such a particle, the existence of a critical diameter was derived, above which the particle would have no resulting force towards the membrane, thus, no fouling propensity. More information on this model will be given in Section 2.3.3.

Pore blocking (R_p) is de deposition of fouling constituents inside the membrane's pores and essentially results in a decrease of the membrane's porosity. Pore blocking is caused by bulk phase particles that are small enough to enter the membrane's pores. Hence, in MBR-filtration pore blocking is a phenomenon that is entirely caused by colloidal matter that is slightly smaller than the membrane's pore size (see Section 2.1.3). An extensive model for pore blocking is given by Broeckmann et al. [2006] but although relevant for some MBR operations, pore blocking will not be specifically studied in this work.

Biofilm formation (R_b) in aqueous environments is a long known phenomenon,

caused by the attachment of microorganisms to a surface. As the concentrations of microorganisms and extracellular polymeric substances are both high in MBRs, biofilm formation is always present. Biofilms are constructed by microorganisms through secretion of a polymer-EPS matrix and consist for more than 90% of water. Biofilm formation is assumed to be a four-stage phenomenon including:

- reversible attachment of microorganisms and EPS;
- transition to irreversible attachment;
- EPS production and growth of microorganisms;
- detachment.

As it is known that the presence of EPS and other natural organic matter strongly influences MBR-filtration behaviour, biofouling is an increasingly active area of research [Lee et al., 2004]. Detailed models for biofilm formation have been presented by Flemming [1999]; Nagaoka et al. [1998] and Laspidou and Rittmann [2001]. Although important, biofilm formation will not be further explained since it is no part of this study's scope.

Concentration polarization (R_{cp}, see Figure 2.7) is inherent to all membrane filtration processes and describes the tendency of solutes to accumulate at the membrane/solution interface within a concentration boundary layer, or liquid film, during cross-flow operation [Judd, 2011]. The boundary layer is a near-stagnant liquid layer, since hydrodynamics dictate that at the membrane's surface the fluid velocity must be zero. Within the boundary layer, the only mode of transport is diffusion. However, it has been shown by Romero and Davis [1991] that the transport away from the membrane is not only determined by Brownian diffusion but also partly by the amount of shear present at the boundary layer. This effect was denoted *shear-induced diffusion.* A comprehensive review concerning concentration polarization in pressure-driven membrane processes is given by Shirazi et al. [2010].

Nevertheless, rejected materials will accumulate adjacent to the membrane and their concentration will increase in comparison to the bulk's concentration at a rate that increases roughly exponentially with increasing flux. The thickness of the concentration polarization boundary layer is entirely determined by the system's hydrodynamics. The boundary layer decreases when turbulence is promoted [Judd, 2011]. Although the process of concentration polarization itself is entirely reversible, it does promote the formation of less-reversible cake layers and other fouling mechanisms such as scaling, adsorption and pore blocking and biofilm formation. Especially for colloidal particles, macromolecules and particles with a size smaller than 1 µm, concentration polarization is relevant,

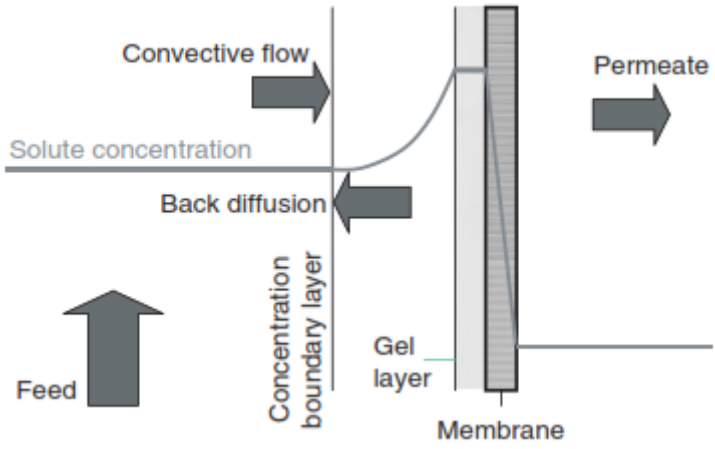

Figure 2.7: Concentration polarization [Judd, 2011].

since, according to Melin and Rauntenback [2004], diffusion forces start to dominate hydrodynamic effects in the submicron size range.

Scaling (R_{sc}), which is the deposition of inorganic pollutants on the membrane surface, is often negligible for aerobically treated wastewater, as rarely situations occur in which concentrations of inorganic substances are close to their solubility. In some industrial cases, dealing with high salt contents, scaling might, however, be significant.

2.2.2 Critical, sustainable and threshold fluxes for fouling

Critical flux

The critical flux was originally introduced by Field et al. [1995] as a flux, below which a decline of flux with time does not occur and above which fouling is observed. Two definitions were introduced based on the steady state flux-TMP profile, defining the critical flux as the flux for which this profile deviates from linearity. In the **strong form** ($J_{c,s}$) definition, the slope for subcritical conditions was deemed equal to the slope found in the clean water profile, whereas in the **weak form** ($J_{c,w}$), a higher resistance was allowed due to an initial resistance increase caused by adsorption (R_{ads}), which even takes place at very low fluxes [Field et al., 1995]. The strong and weak form of the critical

flux are illustrated in Figure 2.8 (left). For the strong form, Equation (2.5) translates into:

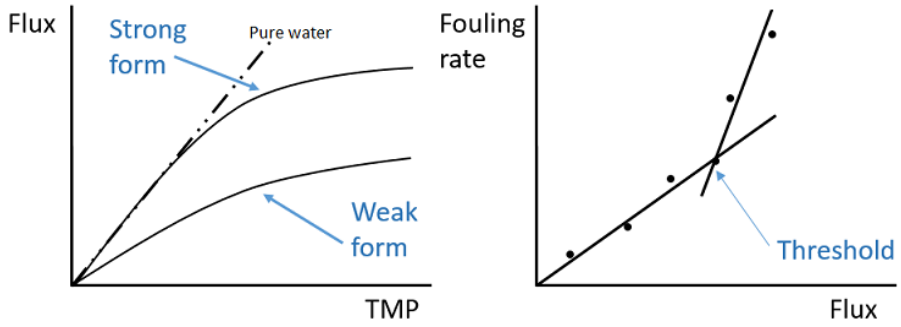

Figure 2.8: **Left:** Strong and weak form of critical flux. **Right:** Threshold flux.

$$J < J_{c,s} : J = \frac{TMP}{\eta_p \; R_{mem}} \tag{2.8}$$

$$J > J_{c,s} : J = \frac{TMP}{\eta_p \; (R_{mem} + R_{rev} + R_{irrev}(+R_{irrecov}))}$$

For the weak form, Equation (2.5) becomes:

$$J < J_{c,w} : J = \frac{TMP}{\eta_p \; (R_{mem} + R_{ads})} \tag{2.9}$$

$$J > J_{c,w} : J = \frac{TMP}{\eta_p \; (R_{mem} + R_{ads} + R_{rev} + R_{irrev}(+R_{irrecov}))}$$

It was pointed out by Bacchin et al. [2006] that the strong and weak form of the critical flux must be evaluated via the overall resistance. Indeed, it may be so that the TMP remains invariant during the new flux-step, but this does not guarantee that the resistance remained unaltered. A small amount of fouling may occur rapidly when making a step change, after which no subsequent increase in TMP is observed [Field and Pearce, 2011].

A more practical definition of the critical flux was used by Fan et al. [2006], who defined the critical flux as the first flux at which the TMP no longer linearly increases with the flux.

However, the concept of critical flux does not provide a lot of guidance for the MBR plant designer or operator. Therefore, two other concepts have been recently introduced, namely the *threshold flux* and the *sustainable flux*.

Threshold flux

From a mathematical point of view, the **threshold flux** is the flux for which the flux - fouling rate profile deviates from linearity (see Figure 2.8 (right)). In practice, the threshold flux for a particular operation, is the flux below which a low and near constant rate of fouling occurs, but above which the fouling rate increases significantly. In contrast with the critical flux, the fouling rate plays an important role for the threshold flux, especially for multi-component applications in industry where typically operation occurs at an acceptable fouling rate between different cleanings. In this regard, the goal is to successfully design a system where a sufficiently high flux is achieved, while fouling rates are kept at an acceptable level. If there is a break-point in the rate of fouling versus flux curve, this threshold flux can be determined to make a distinction between low and high fouling rates, even in many applications where there might not even be a critical flux, since a zero rate of TMP-increase may never be obtained [Field and Pearce, 2011].

Sustainable flux

Including economic aspects, the **sustainable flux** was introduced as the *net flux that can be maintained using mechanical and chemical enhancing means to meet an operation cost objective over the project life of the membrane*. Thus, the sustainable flux is a pragmatic concept that is used for commercial operations where controlled fouling is allowed, to provide an optimal balance between moderate operating costs (opex) and moderate capital costs (capex). The net flux in the prior definition denotes the total permeate flux minus permeate consumption during possible backwash [Field and Pearce, 2011].

In a research context, the sustainable flux can be used as a flux that relates to filtration within reasonable boundaries of fouling, without the need for too frequent membrane cleaning or surpassing the instruments' measuring capacity. An example of this methodology is given by Guglielmi et al. [2008], who define the transition to unsustainability at the flux that leads to a permeability loss of more than 90% in comparison with the permeability from the first filtration step. Alternatively, van der Marel et al. [2009] assigned the sustainable flux value to the lowest flux for which the average increase in fouling rate is higher than 0.1 mbar/min.

2.3 Relating biomass properties to sMBR fouling

As can be seen in Figure 2.9, adopted from Le-Clech et al. [2006], the different factors that affect fouling in sMBRs can be classified into four categories:

- membrane and module characteristics;
- operation conditions;
- feed characteristics;
- biomass characteristics.

While all of the aforementioned factors are important, this thesis focusses on the interactions between the biomass, and to some extent the feed characteristics. Therefore, the membrane and module characteristics will only be briefly discussed in Section 2.3.1. Afterwards, the biomass and mixed liquor characteristics in relation with fouling will be more extensively explained in Section 2.3.2. Finally, although important for MBR operation, the many operational parameters such as aeration, SRT and HRT will not be discussed since they are not within the scope of this research.

2.3.1 Membrane and module characteristics

Pore size

It is expected that smaller pore sizes would reject a higher variety of materials, as shown in Figure 2.3, which would result in the creation of a fouling layer with a higher resistance. However, the fouling layer formed during filtration with such membranes, is often more reversible and more easily removed, as membrane systems with larger pores are far more prone to internal pore clogging and blocking [Chang et al., 2001; Le-Clech et al., 2006]. In large microfiltration applications, pore sizes usually range between 0.1 - 0.4 µm [Judd, 2011].

Therefore, although higher fluxes can be reached in the short term, increasing the pore size may decrease membrane surface fouling but at the expense of internal adsorption, which eventually leads to a tremendous increase in resistance [Le-Clech et al., 2003a; Ognier et al., 2002].

The transition between pore closure, at low levels of fouling, and cake layer formation, at higher levels of fouling, is critical in fouling progression. As the effective pore size is reduced, the local flux increases during constant flux

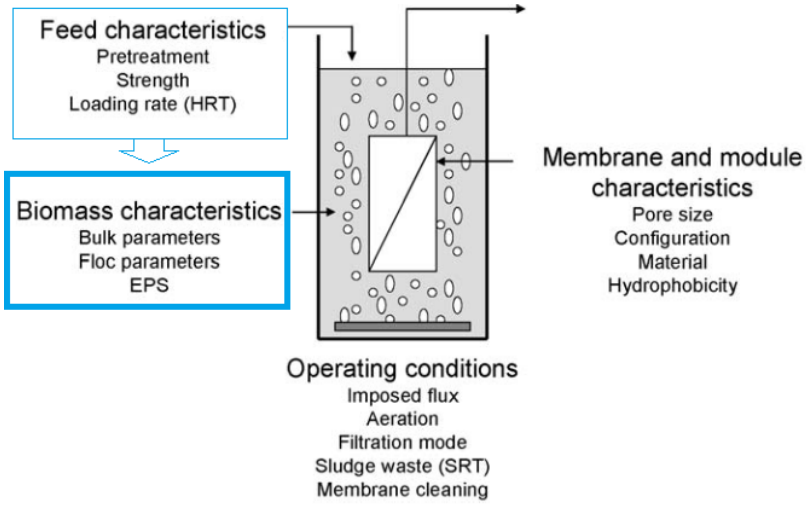

Figure 2.9: Factors affecting fouling in submerged MBRs [Le-Clech et al., 2006]. This thesis focusses on the relationship between the biomass characteristics and fouling.

operation, yielding higher convective forces towards the membrane, and hereby attracting larger foulants [Zhang et al., 2006].

Hydrophobicity

As mentioned in Section 2.1.3, mostly hydrophobic membrane materials (albeit functionalized to become more hydrophilic), such as PVDF are being used due to their high chemical stability. Unfortunately, because of the hydrophobic interactions that occur between solutes, microbial cells and the membrane material, membrane fouling is expected to be more severe with hydrophobic than with hydrophilic membranes [Le-Clech et al., 2006]. Historically, in studies involving the ultrafiltration of proteins and macromolecules, indeed lower levels of fouling were attributed to smooth hydrophilic membranes [Fane and Fell, 1987; Marschall et al., 1993; Matthiasson, 1983; Nilsson, 1990].

However, as stated by Le-Clech et al. [2006], in mixed species feeds, the surface chemistry of the membrane may be masked by adsorption of the multitudes

of macromolecular species and the benefits of hydrophilicity may be obscured during long-term operation.

Membrane material

Although possessing superior chemical, thermal and hydraulic resistances, ceramic membranes have a high cost impeding their potential application in most wastewater treatment applications. However, for the treatment of specific high-strength industrial wastewaters or anaerobic biodegradations, ceramic modules have been succesfuly implemented. Ceramic membranes are generally used in side-stream configurations, requiring a higher pressure and turbulence, which comes with an increased energy cost. Therefore, in most MBR configurations, polymeric membranes are used. In their study, Yamato et al. [2006] concluded that polyethylene membranes suffer more from irreversible fouling than PVDF membranes. However, the authors clearly mentioned that the composition of irreversible fouling is dependent on the membrane material and that specific biomass fractions may present a higher affinity for certain polymeric materials.

Configurations

For submerged membrane bioreactors, typically vertical flat sheet modules or hollow fibers bundles are used as membrane configurations (see Section 2.1.3). Hollow fiber modules have many attractive features. They are generally cheaper to manufacture, can be configured in a high membrane density and can tolerate backwashing. However, due to their typical configuration, hollow fibers may be more prone to fouling and require more frequent washing and cleaning. In their study on hollow fiber versus flat sheet modules, Gunder and Krauth [1998] affirmed this observation by demonstrating the better hydraulic performance of flat plate systems. Moreover, the backwashing requirement (up to 25% of the permeate volume [Judd, 2002]) of the hollow fiber systems removes the upper cake layer and gives irreversible foulants a new opportunity to reach the membrane and necessitates a higher flux than during continuous operation to reach the same permeate production [Drews, 2010]. Another important design factor for hollow fibers systems is the packing density. The distance between adjacent membranes directly impacts the mass transfer and thereby the shear and aeration demands. Increasing the packing density can lead to severe clogging by gross foulants and may cause aeration inefficiencies since bubble rise velocities may be diminished. Yeo and Fane [2005] carried out experiments with hollow fiber bundles and concluded that the inner fibers are far less productive than the outer fibers. At high feed concentrations, the inner fibers became blocked and eventually provided only negligible throughput. The

authors adviced that packing density should be lowered below 30% for fiber bundles to operate similarly to single fibers.

2.3.2 Mixed liquor and biomass (bulk) characteristics

Biomass concentration

In literature, controversial findings about the effect of the biomass concentration are reported, including negative correlations with performance [Chang and Kim, 2005; Cicek et al., 1999], positive relationships [Brookes et al., 2006; Defrance and Jaffrin, 1999] and insignificant impacts [Hong et al., 2002; Le-Clech et al., 2003b; Lesjean et al., 2005]. A more detailed study was performed by Rosenberger et al. [2005], who reported decreasing fouling with an increase in mixed liquor suspended solids (MLSS) for low concentrations (MLSS < 6 g/L) but an increase when MLSS levels rose above 15 g/L. The first trend can be explained by the creation of a dynamic secondary cake layer, consisting of suspended solids that form a barrier for colloidal and soluble materials to prevent pore blocking. It was concluded that MLSS concentration alone is a poor indicator of biomass fouling propensity [Le-Clech et al., 2006].

Extracellular polymeric substances

The name extracellular polymeric substances (EPS) is a collective term for different classes of macromolecules, such as polysaccharides, proteins, nucleic acids, (phospho)lipids and other polymeric compounds that are found at the outside of the cell and that aid in the construction of microbial aggregates such as biofilms and activated sludge flocs.

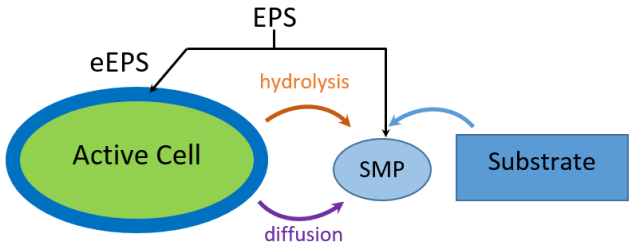

Figure 2.10: Simplified representation of extractable (eEPS) and soluble (SMP) extracellular polymeric substances (based on Le-Clech et al. [2006]).

EPS can typically be divided into two categories. The bound or extractable EPS (eEPS) are located at the cell wall and are attached to the active cell, whereas the soluble EPS or soluble microbial products (SMP) are dissolved in the liquid phase of the bulk mixture (see Figure 2.10). For a long time, due to many conflicting results, EPS have been the origin of much discussion concerning the relationships between membrane fouling, separation problems and bioflocculation. One possible reason for these discrepancies is the availability of a multitude of extraction methods. Separating SMP from the mixed liquor is often performed by filtration, centrifugation, sedimentation or a combination of the above. A general applicable protocol has been suggested by Van Dierdonck et al. [2012b]. Extraction of eEPS can be performed using an even wider multitude of methods, such as heat treatment, the use of cation exchange resins or centrifugation with formaldehyde [Zhu et al., 2015]. Therefore, it is important to keep in mind that the exact definitions of eEPS and SMP are directly dependent on the methods used to obtain and chemically characterise these solutions [Le-Clech et al., 2006]. Moreover, the EPS-terminology itself can be confusing at times as well. A clear summary on the definitions used throughout the literature was given by Wang et al. [2013].

In this work, SMP and eEPS are quantified by their relative protein and carbohydrate content, using the methods of [Lowry et al., 1951] and [Dubois et al., 1956], respectively.

Soluble microbial products (SMP)

Although their contribution to the mixture's total mass is small, SMP have been shown to have a high filtration resistance [Ng et al., 2005; Shen et al., 2015]. SMP are defined as soluble cellular components that are lost during synthesis or cell lysis or that can diffuse through the cell membrane. During filtration, these components can adsorb on the membrane surface, block pores or form a compressible gel structure on the membrane surface that may provide a nutrient source for biofilms or binding site for subsequent floc deposition [Jørgensen et al., 2014; Le-Clech et al., 2006; Poorasgari et al., 2015].

In MBRs, SMP levels were shown to be higher than in CAS plants, presumably due to the retention by the membrane [Teychene et al., 2008]. As this was the only difference between both mixed liquors, the observed higher fouling rate for the MBR sludge was attributed to the higher SMP concentrations. De Temmerman et al. [2015] and Menniti et al. [2009] measured increasing SMP levels at higher aeration shear rates, resulting from the breaking up of sludge flocs. In their studies, SMP, together with colloidal matter through blinding, caused significant fouling as well.

Several studies indicated that the carbohydrate content in the SMP might be the major foulant [Le-Clech et al., 2005; Lesjean et al., 2005; Menniti et al., 2009; Rosenberger et al., 2005]. In their study using confocal laser scanning microscopy (CLSM), Hwang et al. [2012] measured increased SMP levels in the cake layer as compared to the bulk mixture. Moreover, the relative polysaccharide content was higher in the cake as well. However, other studies confirm the significance of the protein fraction as well [Drews et al., 2005; Evenblij and van der Graaf, 2004].

Bound extracellular polymeric substances (eEPS)

Bound EPS are an important component for bioflocculation as they determine the floc surface characteristics and are involved in the process of bioflocculation (see also Chapter 3). The protein fraction of EPS generally has a higher hydrophobic tendency, while the carbohydrates are more hydrophilic of nature [Liu and Fang, 2003]. The exact role of EPS on membrane fouling is not clear, although some studies have already identified its importance [Chang and Lee, 1998; Cho and Fane, 2002; Rosenberger and Kraume, 2002].

Since EPS play a key role in hydrophobic and electrostatic interactions involved in bioflocculation, too low EPS levels may cause floc deterioration [Jang et al., 2005]. However, a positive correlation between fouling and EPS levels has also been observed [Fawehinmi et al., 2004]. Therefore, it is assumed that an optimum EPS level exists, for which the floc structure is maintained without causing too high fouling [Le-Clech et al., 2006].

Viscosity

Viscosity and biomass concentration are closely linked to each other. A critical MLSS concentration has been reported below which the viscosity remains low and only increases slowly with the MLSS. Above the critical value, the suspension viscosity tends to increase exponentially [Brookes et al., 2003; Itonaga et al., 2004]. The critical concentration was estimated between 10 and 17 g/L, depending on different operating conditions.

The importance of viscosity lies in the fact that it affects bubble sizes and hydrodynamics and that the movement of hollow fibres in submerged bundles is dampened by an increase in viscosity, resulting in a greater fouling rate [Brookes et al., 2003]. Moreover, an increased viscosity affects the efficiency of oxygen transfer and may reduce dissolved oxygen concentrations.

Temperature

Temperature influences membrane filtration through its influence on the permeate viscosity [Mulder, 2000]. Therefore, hydraulic performances are normalized with temperature (e.g., at 293 K) to enable a fair comparison. Fan et al. [2006] propose a non-linear regression between the critical flux and temperature:

$$J_c(T) = J_c(293\ K) \cdot 1.025^{T-293\ K} \tag{2.10}$$

However, even after normalization, higher fouling propensities were observed at low temperature [Jiang et al., 2005], which could be related to (*i*) an increase in viscosity at low temperature, (*ii*) deflocculation, which caused a reduction in floc size and released EPS into the solution, (*iii*) lower particle back transport velocities (e.g., Brownian diffusion velocities increase with temperature) and (*iv*) reduced biodegradation of COD, resulting in higher concentrations of solute and particular COD in the reactor. The last observation was affirmed by Fawehinmi et al. [2004], who observed higher SMP levels in an anaerobic MBR operated at 20°C rather than at 30°C.

Dissolved oxygen

The dissolved oxygen concentration (DO) in submerged MBRs is controlled by the aeration which also serves to limit fouling formation at the membrane surface. Generally, a higher DO leads to better filterability and a lower fouling rate, as with an increase of dissolved oxygen, a larger average floc size and a greater porosity are observed [Ji and Zhou, 2006; Kim et al., 2006]. A too low dissolved oxygen concentration leads to anoxic and anaerobic sludges, which have been shown to cause floc deterioration [Jang et al., 2004]. In anoxic conditions, oxygen limitation was paired with a decrease in cell surface hydrophobicity.

Endogeneous decay, which occurs in microbial sites that suffer from oxygen deficiency, was simulated and revealed increased levels of carbohydrate contents in the EPS, leading to inferior filtration performances.

Ionic Strength

The ionic strength (I), see Equation (2.11), is a measure of the total ion concentration present in the bulk mixture and is calculated as half of the sum

of all ion concentrations (C_i) multiplied by their respective valence (z_i) to the second power.

$$I = \frac{1}{2} \sum z_i^2 C_i \tag{2.11}$$

As will be further explained in Section 2.3.3 and Chapter 3, activated sludge flocs posses negatively charged surfaces. It is known that charged surfaces in solution surround themselves by a double layer of counterions (see Figure 2.11). The *stern layer* is a layer of ions which is directly adsorbed to the surface and which is immobile, while the *diffuse layer*, or Gouy-Chapman layer consists of mobile ions which concentration is determined by a balance between the electrostatic interaction with a charged surface and diffusion [Butt et al., 2008].

As can be seen from the figure, the electrostatic potential decreases exponentially with an increased distance from the particle's surface. The decay length is given by $\lambda_D = \kappa^{-1}$ and is called the *debye length* and can be calculated using Equation (2.12). When increasing the ionic strength from 1 mM to 500 mM, the debye length decreases from 20 nm to 0.2 nm [Hermansson, 1999].

$$\kappa = \lambda_D^{-1} = \sqrt{\frac{e^2}{\epsilon \epsilon_0 k_B T} \sum z_i^2 C_i} \tag{2.12}$$

in which:

λ_D	=	Debye length	[µm]
e	=	charge of an electron	[C]
ϵ	=	relative permittivity	[-]
ϵ_0	=	vacuum permittivity	[F/m]
k_B	=	Boltzmann constant	[J/K]
T	=	temperature	[K]
z_i	=	valence of ion	[-]
C_i	=	concentration of ion	[M]

The potential at the point where the bound Stern layer ends and the mobile diffuse layer begins is denoted the zeta (ζ) potential. When two charged objects come in proximity, the electrostatic repulsions caused by the overlap of their diffuse layers will hinder their contact. As can be seen from Equation (2.12), an increase in the ionic strength reduces the radius of the diffuse layer. As activated sludge cake layers consist of charged particles, an increase in ionic strength will result in the creation of a more dense cake layer [Butt et al., 2008; Faibish et al., 1998].

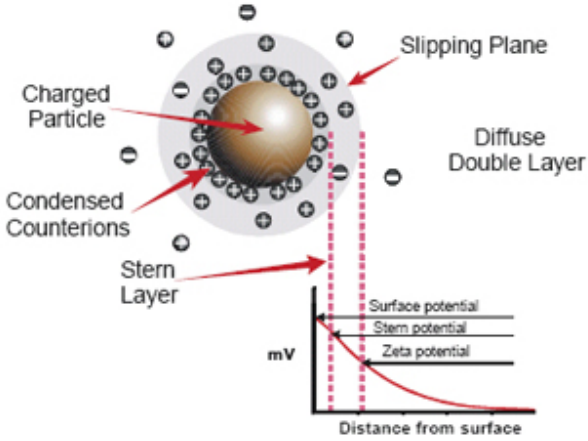

Figure 2.11: Schematic showing the distribution of ions around a charged particle [bcf.assic.sinica.edu.tw/images/zeta.jpg].

In their study on the effect of ionic strength on membrane fouling, Wang et al. [2014] state that, although hydrodynamics are responsible for bringing the particles in proximity of the membrane, thermodynamic forces are responsible for the actual binding of the particle to the membrane. They used the extended Dejarguin-Landau-Verwey-Overbeek (XDLVO)-theory to describe the balance between the attractive acid/base (AB), the attractive Van Der Waals (LW) and the repulsive electrostatic double layer (EL) forces. Combining these interactions yields Figure 2.12.

In the figure, the free interaction energy (dotted line) is given as a function of the distance between the membrane and a sludge particle. As can be seen from the figure, two minima in interaction energy are separated by an energy barrier, which is entirely caused by the electrostatic repulsions, as described above. The authors demonstrate that a critical ionic strength exists above which the energy barrier disappears and the resulting interaction between both entities becomes positive. In their study, this critical value was calculated to be around 34 mM, which is in line with the moderate variation of ionic strength in MBRs treating real wastewater [Lin et al., 2012].

However, when Wang et al. [2014] assessed the influence of the ionic strength on filtration resistance using dead-end filtration experiments in which the supernatant was replaced by a solution with a known ionic strength, no influence of the ionic strength on the cake layer resistance was observed. It was concluded

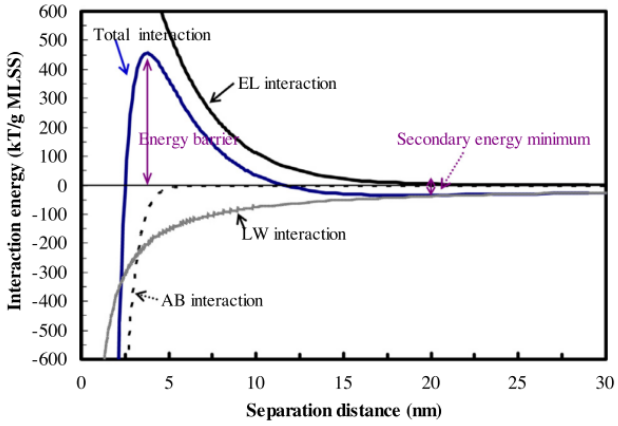

Figure 2.12: Profiles of interaction free energies for membrane-sludge flocs combination as a function of the separation distance [Wang et al., 2014]. The repulsive electrostatic interactions (EL) work on a longer separation distance than the attractive van der Waals (LW) and hydrogen-bonding (AB) forces. Balancing the forces creates an energy barrier between the primary and secondary energy minimum that has to be overcome for permanently binding between membrane and sludge-floc.

that, although the increase of ionic strength above the critical value removed the energy barrier, the cake resistance was not strongly affected by the increase in ions. What the authors did notice was that the removal of SMP from the solution yielded a significant increase in filterability. This effect was attributed to the osmotic pressure effect and will be explained in Section 2.3.7.

A remark that can be made from the study of Wang et al. [2014] is that the energy barrier was only significant for interactions between the membrane and the first line of particles that deposited. In their study, it was calculated that the electrostatic forces upon interaction between two similar sludge particles were negligible in comparison with the other forces present. Therefore, it can be concluded that the effect of the ionic strength for fouling and cake layer formation according to the XDLVO theory was only limited.

pH

pH affects membrane fouling through two effects: alterations of the electrostatic surface potential and biological stress responses.

The first effect is coupled to the XDLVO-theory and the surface charge. As the pH increases, a multitude of functional groups present on the activated sludge surface and the EPS matrix become charged due to their weak acid-like character. This increase in surface charge leads to a higher electrostatic energy barrier as described above. As the energy barrier is increased, reduced fouling is expected, while an increase in fouling at low pH conditions has been reported by Brink et al. [2000]. In contrast, Sweity et al. [2011] reported that reducing the pH led to less severe fouling. At lower pH, the functional groups present on the EPS would carry fewer negative charges (repression of weak acid dissociation in a strong acid environment), leading to a reduced electrostatic repulsion between neighboring functional groups and smaller macromolecular configurations, while at high pH values, EPS have a larger conformation and a stronger stickiness, resulting in faster pore blockage. Alternatively, Zhang et al. [2013] explains the reduced fouling at lower pH using the osmotic pressure effect as will be explained in Section 2.3.7.

2.3.3 Floc characteristics

Particle size distribution

The occurrence of small particulate or colloidal matter in the activated sludge mixture has been related to significant fouling [De Temmerman et al., 2014; Faust et al., 2014; Gao et al., 2013; Ivanovic et al., 2008]. In general, it is known that small constituents can create a more dense and less permeable cake layer, or, when they are small enough, penetrate the membrane's pores to affect the internal structure of the membrane.

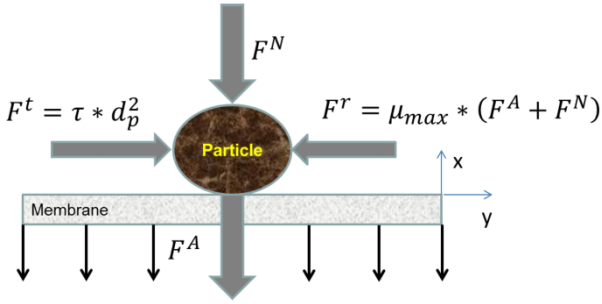

Figure 2.13: Force balance on a sludge floc near the membrane surface [Broeckmann et al., 2006].

Moreover, in their MBR-fouling model, Broeckmann et al. [2006] used a mechanistic approach to determine which sludge particles can, from a hydrodynamical point of view, actively contribute to cake layer fouling in cross-flow filtration. Using a force balance (see Figure 2.13), it was determined that a maximal floc diameter ($d_{p,max}$) exists. For particles with diameters above this $d_{p,max}$, the balance between the permeate suction and back-transport shear forces would favor the latter, resulting in the inability of large particles to remain on the membrane's surface. Small particles, however, are less sensitive to shear. Therefore, it is postulated that only the smaller constituents from the activated sludge's particle size distribution can actively contribute to membrane fouling in MBRs. The value of $d_{p,max}$ depends on different factors. In their model, [Broeckmann et al., 2006] neglected adhesion forces between particles themselves or with the membrane, and used the Kozeny-Carman equation for cake permeability to solve for $d_{p,max}$, resulting in Equation (2.13):

$$d_p \leq \frac{\mu_{max}\ k_s\ \eta_p\ J}{\tau}\ (360\ k_{kozeny}\ \frac{(1-\epsilon)^2}{\epsilon^3})^{0.4} = d_{p,max} \tag{2.13}$$

in which:

μ_{max}	=	maximum friction coefficient	[-]
k_s	=	tuning parameter	[-]
η_p	=	permeate viscosity	[Pa s]
J	=	permeate flux	[L/m^{2}h]
k_{kozeny}	=	tuning parameter	[-]
ϵ	=	cake porosity	[-]

The equation describes those particle sizes that are able to adhere to the membrane surface. From the relationship follows that $d_{p,max}$, and, equivalently, the fraction of the particle size distribution that can contribute to membrane fouling, increases when

- the flux (J) increases;
- the shear stress (τ) decreases;
- the viscosity (η) increases;
- the cake porosity (ϵ) decreases.

The latter is an effect of the local flux distribution. When the flux through a certain porous surface remains the same, but the free pore surface decreases, then the local flux through the open pores increases, resulting in a locally higher suction force [Zhang et al., 2006]. Therefore, cake layers that have a well formed,

open structure are expected to be more permeable than irregularly packed cakes.

The addition of small, submicron, particles is detrimental for filtration. Not only do they form very dense cake layers, but often they cause a significant decrease in cake permeability through *blinding*, which is the filling up by voids, resulting in decreased cake porosity [Poorasgari et al., 2015].

Using the XDLVO that was described before, Shen et al. [2015] used a thermodynamic approach to asses the specific interaction energy between the membrane surface and sludge particles as a function of their size and concluded that although the specific energy barrier decreases slightly with an increase in particle size, smaller particles, who can hydrodynamically reach the membrane more easily, have a much higher binding affinity, expressed by the specific interaction energy with the membrane.

Hydrophobicity and surface charge

Hydrophobic flocs are known to have a low interaction with the generally hydrophilic membrane. The direct impact of activated sludge hydrophobicity on membrane fouling is often difficult to assess. However, the largest impact of hydrophobic floc-surfaces are their tendency to promote bioflocculation, which will be discussed in Section 3.1.2 [Le-Clech et al., 2006].

Hydrophobicity and surface charge are usually inversely correlated. Activated sludge flocs are negatively charged due to the ionization of anionic functional groups on their surfaces and bound EPS.

The occurence of charge within the activated sludge matrix provides possible bridging effects with cations (see also Section 3.1.3) [Sobeck and Higgins, 2002; Van den Broeck et al., 2010]. Moreover, as discussed in Section 2.3.2, the increase of surface charge increases the extent of the double layers surrounding the charged particles, resulting in a more permeable cake layer [Faibish et al., 1998].

However, as will be discussed in Section 2.3.7, electro-neutrality within the cake layer is maintained. As such, the retention of more counterions due to a higher surface potential might provide an additional osmotic filtration resistance [Shen et al., 2015].

Fractal dimension

The fractal dimension characterizes the complexity of an object's perimeter and is expressed by the ratio of change in detail when the scale is reduced. Although different definitions of the fractal dimension exist, they all have increasing values when the roughness or irregularity of the object's border increases. In one definition, i.e., the box counting algorithm, an object is covered by grids of decreasing size (see Figure 2.14). For every grid, the number of boxes that is required to cover the whole perimeter is counted. Suppose N(d) is the number of boxes of size e required to cover the object perimeter, then the box-counting fractal dimension F_D is defined as:

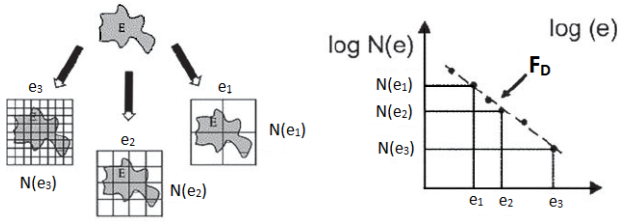

Figure 2.14: Schematic representation of box counting algorithm for fractal dimension.

$$F_D = \lim_{d \to 0} \frac{log\ N(d)}{log(1/d)} \tag{2.14}$$

The permeability of single aggregates has been shown to be decreasing with an increased fractal dimension [Li and Logan, 2001; Veerapaneni and Wiesner, 1996], which hampers settling and filtration. Guan et al. [2001] and Lee et al. [2005] studied the impact of floc size and fractal dimension on the permeability of biosolids filter cakes and found that for cakes consisting of small flocs, the permeability of cake layer is more strongly affected by the fractal dimension since the intra-aggregate porosity plays a higher role. Both authors concluded that an increase in fractal dimension leads to a reduction of permeability.

Combining both intra and inter-aggregate porosity, Park and Lee [2006] constructed a theoretical model. In this model, the specific cake resistance was found to be decreasing upon increasing the aggregate size and decreasing the fractal dimensions. The model was verified using polystyrene latex beads and results agreed reasonably well with theoretical expectations.

Using centrifugation to fractionate activated sludge into large and small flocs, Lin et al. [2011] measured a higher fractal dimension for the small flocs and significant differences in microbial communities between the two classes. Moreover, the specific filtration resistance of the smaller fraction was higher.

2.3.4 Compressibility

Activated sludge flocs are compressible entities. In MBR systems that are operated in constant flux mode, maintaining the set flux results in a gradual TMP increase, which results in compaction of the fouling layer. This compaction reduces the cake permeability and increase operation costs. Cake compression can be expressed using Equation (2.15) [Poorasgari et al., 2015].

$$\alpha = \alpha_0 \left(1 + \frac{\Delta P_c}{P_a}\right) \tag{2.15}$$

in which:

α	=	specific cake resistance	[m/kg]
α_0	=	specific cake resistance at zero pressure	[m/kg]
ΔP_c	=	pressure drop across the cake	[Pa]
P_a	=	compressibility parameter	[Pa]

P_a can be interpreted as the pressure drop that is required to double the specific cake resistance [Jørgensen et al., 2014]. It follows that highly compressible cakes have low P_a values, while for incompressible materials, $P_a = \infty$. For highly compressible materials, volumetric flux and pressure drop are independent, which for constant flux operation may result in very high specific cake resistances [Sveegaard et al., 2012].

Cake layers are known to exhibit compression [Sveegaard et al., 2012]. Poorasgari et al. [2015] also observed compression for the gel layer consisting of SMP, but noted these effects only above a yield stress between 49-78 mbar. Cake and SMP gel layer compression were determined to be partially reversible [Jørgensen et al., 2014; Poorasgari et al., 2015; Sveegaard et al., 2012].

2.3.5 Filaments

As will be discussed in Section 3.1.1, the balance between filamentous and floc forming bacteria is crucial in the creation of well settling and filterable activated sludge flocs. However, for MBR filtration, the role of filaments is more ambiguous. In their work, Meng et al. [2006] measured increasing fouling rates during the proliferation of bulking sludge. The exessive growth of filaments

was paired with an increase of SMP, which led to an increased stickiness of the membrane onto which suspended material could more easily deposit. The same observations were obtained by Pan et al. [2010], who also noticed an increasing fouling rate that could be attributed to SMP released during a bulking event. On the other hand, the absence or shortage of filaments leads to poor bioflocculation, resulting in small flocs and increased amounts of colloidal and particulate matter, which in turn leads to increased fouling [Bugge et al., 2013]. Therefore, it may be assumed that there is a balance in the amount of filaments that is beneficial for MBR operation (which in turn will also depend on the type of dominant filament). In Section 2.3.6, the dynamic membrane theory will be explained. In this sense, filaments are expected to play a role as well.

2.3.6 Dynamic secondary membrane hypothesis

An important hypothesis that is put forward in this thesis is the dynamic secondary membrane (DSM) hypothesis. The DSM-hypothesis was first mentioned by Holdich and Boston [1990] and is schematically illustrated in Figure 2.15 [Wang and Wu, 2009]. The idea is that the formation of a well structured and reversible cake layer could serve as a secondary dynamic membrane to filter SMP and colloids. This way, the dynamic membrane could prevent small particles from adsorbing on the membrane surface or inside the membrane pores. Filamentous bacteria could entrap flocs in the formation of a secondary net, which can be removed during backwash or relaxation. An alternative version of the DSM-theory is proposed by Geilvoet [2010] who relates the beneficial effects of well-formed bioflocs to their adsorption capacity for small colloidal and dissolved particles in the bulk mixture rather than at the membrane's surface.

A few researches have already proposed operational strategies that involve the DSM hypothesis. As the formed loosely bound cake layer is effectively backwashed or removed during relaxation, the novel method proposed by Wu et al. [2008] involves the usage of a high instantaneous flux (60 L/m^2h) at the beginning of each filtration cycle, attracting larger particles to the membrane and creating the secondary cake layer that serves to protect the primary membrane by the adsorption of SMP and smaller sludge particles. A, to some extent, similar strategy was adopted by Diez et al. [2014], who used a higher, so-called precompression flux (1.75 times the normal flux) to limit pore blocking and irreversible fouling.

Giraldo and Le Chavellier [2007] tested an aeration control strategy in which the aeration rate is matched to the permeate flux in assisting the creation of a

thick cake with relatively low filtration resistance, but that still could serve as a secondary barrier.

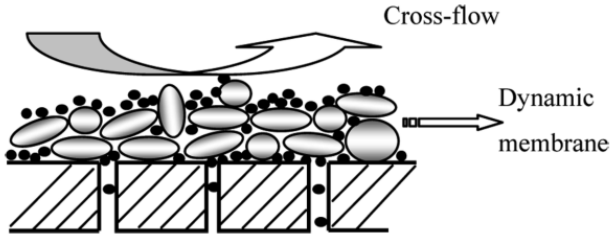

Figure 2.15: Schematic of the secondary dynamic membrane formed on primary membrane surfaces [Wang and Wu, 2009].

A more extented application of the dynamic secondary membrane theory is the application of self-forming dynamic membranes [Jeison et al., 2008; Zhou et al., 2008]. In these filtration systems, a coarse mesh or cloth-like material is used instead of micro- and ultrafiltration membranes to separate the solids and liquids in the bioreactor. Although this technique is highly dependent on the bioflocculation propensity and the formation of a well structured cake layer, it avoids membrane replacement costs and allows for higher operational fluxes.

2.3.7 Osmotic pressure effect

In their work, Shen et al. [2015] studied the effect on the specific filtration resistance when the activated sludge's supernatant was replaced with a 5 mM NaCl solution. The result was an eightfold reduction of the resistance, when the supernatant containing soluble microbial products (SMP) and biopolymer clusters (BPC) was omitted, although these bioproducts only accounted for less than 0.3% of the total biomass.

It was apparent that the Carman-Kozeny equation, which is often used for cake filtration (see Section 2.3), could not explain the phenomenon, as it is structure-dependent but not material-dependent. Shen et al. [2015] attributed the observed phenomenon to the **osmotic pressure effect** (OPE), which is illustrated in Figure 2.16.

As can be seen in the figure, the biopolymer matters, including eEPS, SMP and BPC contain negatively charged functional groups. When the sludge suspension is filtered, a cake layer is formed with a high concentration of these functional groups. Since the macroscopic electro-neutrality cannot be lost, counterions

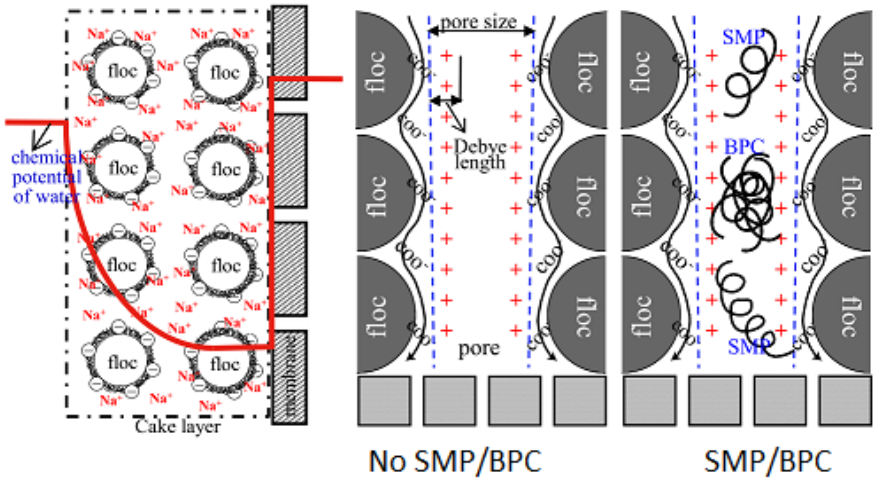

Figure 2.16: Schematic representation of the osmotic pressure effect [Shen et al., 2015].

remain present in the biopolymer matrix. As a result, the chemical potential, which is a function of the ionic strength, in the cake layer is higher than that of the permeate. Since filtration is a process of transporting water from a low to a high chemical potential, this higher chemical potential results in an osmotic pressure-induced resistance.

The difference between the situation with and without the supernatant is explained by the Debye length, which can also be interpreted as a measure for the distance in which electrostatic forces retain the counterions in the biopolymer matrix. The authors calculated this Debye length as 4.5 nm, whereas the cake's pore size is estimated around 0.05-0.5 µm. Therefore, the functional groups on the bound EPS and the sludge flocs alone are not significant.

However, when the biopolymer matter is present in the pores, the charge density increases, as these polymers can provide a lot of binding sites for counterions, giving rise to a high osmotic pressure induced resistance.

The osmotic pressure effect can be modeled by an effective reduction of the transmembrane driving pressure force. In this case, an osmotic pressure ($\Delta\pi$) is substracted from the TMP, by which Equation (2.5) changes into:

$$J = \frac{TMP - \Delta\pi}{\eta_p \; R_{tot}} \tag{2.16}$$

with $\Delta\pi$ = the osmotic pressure [Pa]

Assuming the molar fractions of the dissolved ions and charge-containing groups is much lower than the molar fraction of water, the osmotic pressure can be related to the molar concentration difference of charged species directly across the membrane:

$$\Delta\pi \approx \frac{RT}{V}(x_c - x_p) = C_c RT - C_p RT \tag{2.17}$$

	x_p	=	the molar fraction of charged species in permeate	[mol]
	x_c	=	the molar fraction of charged species in cake layer	[mol]
	V	=	volume	[L]
wherein:	R	=	gas constant	[J/molK]
	T	=	temperature	[K]
	C_p	=	the molar concentration of charged species in permeate	[mol/m^3]
	C_c	=	the molar concentration of charged species in cake layer	[mol/m^3]

In their study, Zhang et al. [2013] proposed a methodology to link the osmotic pressure to the presence of charged functional groups within the EPS matrix of the cake layer in front of the membrane. Assuming only monovalent cations are trapped in the cake layer, the concentration of trapped ions in the cake layer approximates the molar concentration of effectively dissociated functional groups. Using this approximation, the following expression is proposed:

$$C_c = \frac{n_c}{V_w} = \frac{\sigma\rho V_t(1-\epsilon)}{V_t\epsilon} = \sigma\rho\frac{1-\epsilon}{\epsilon} \tag{2.18}$$

	n_c	=	the molar number of charged EPS groups in cake	[mol]
	V_w	=	the water volume in cake layer	[L]
with:	V_t	=	the total volume of cake layer	[L]
	σ	=	the molar density of charged groups in cake	[mol/kg]
	ρ	=	the density of cake layer	[kg/L]
	ϵ	=	the porosity of cake layer	[-]

The next assumption made by Zhang et al. [2013] assumes that proteins are mainly responsible for providing the negatively charged functional groups in the EPS matrix and that the contribution of charge can be attributed to four amino acids, being glutamic acid, aspartic acid, cysteine acid and tyrosine acid with side chain pK_as of, respectively, 4.25, 3.86, 8.33 and 10.07. As the dissociation of these groups and thus their contribution to the surface charge, is dependent on the pH, a dissociation number δ is used that indicates the fraction of effectively dissociated functional groups as a function of pH.

$$\delta = \sum_{i=1}^{4} \frac{K_{ai}}{K_{ai} + 10^{-pH}} x_i \tag{2.19}$$

Using the above mentioned information, a function for the osmotic pressure is derived:

$$\Delta\pi = \frac{\sigma_t \rho RT(1-\epsilon)}{\epsilon} \sum_{i=1}^{4} \frac{K_{ai}}{K_{ai} + 10^{-pH}} x_i - C_p RT \tag{2.20}$$

To allow for modeling the effects of compression (TMP) and ionic strength related effects, an alternative form is proposed:

$$\Delta\pi = [f_1(TMP) \wedge f_2(C_p)] \cdot \sigma_t \rho RT \sum_{i=1}^{4} \frac{K_{ai}}{K_{ai} + 10^{-pH}} x_i - C_p RT \tag{2.21}$$

In this expression, σ_t equals σ/δ and $f_1(TMP)$ and $f_2(C_p)$ are functions that allow, respectively, the inclusion of compression (TMP) and ionic strength. In their study, both effects are assumed to be inversely proportional to the porosity of the cake layer, for which the functions translate into:

$$f_1(TMP) = \frac{TMP}{f_{TMP} + b_{TMP} TMP} - 1 \tag{2.22}$$

for TMP, and

$$f_2(C_p) = \frac{C_p}{f_{C_p} + b_{C_p}} - 1 \tag{2.23}$$

for ionic strength, which is equal to the permeate ion concentration if only monovalent salts are used. In both cases the f and b variables are constants used for empirical fitting.

In their study, Zhang et al. [2013] used experimental data to verify the two primary conclusions from the theoretical model, namely that (*i*) osmotic pressure during cake layer filtration accounts for the major fraction of operational TMP and (*ii*) osmotic pressure is significantly controlled by pH, applied pressure and ionic strength.

Modeling $\Delta\pi$ with a permeate ion-concentration of 5 mM, a cake layer porosity of 0.6 and a solid cake density of 1.220 kg/L, the osmotic pressure was calculated

around 450 mbar at neutral pH, which is in line with the relatively high TMPs that occur in typical MBR operation. Moreover, the typical effect of pH in the model via the dissociation of the different functional groups was also observed when measuring specific cake resistance (see Figure 2.17). Experimental verification showed indeed increasing trends for specific cake resistances when higher TMPs and ionic strengths were applied (data not shown), although these effects may as well be caused by other influences (see sections above), plus the physical meaning regarding the above made assumptions for $f_1(TMP)$ and $f_2(C_p)$ is unclear.

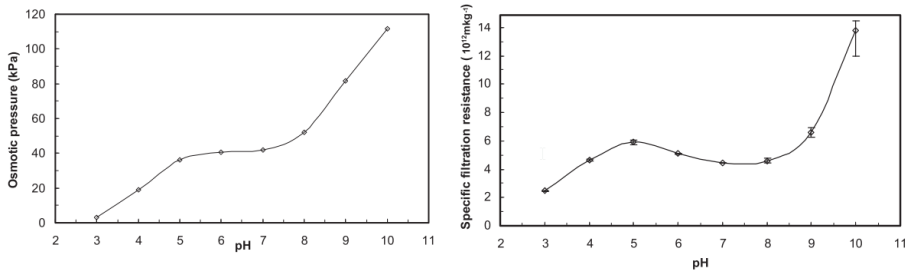

Figure 2.17: Effect of pH on osmotic pressure effect. **Left:** simulation, **Right:** experimental verification [Zhang et al., 2013].

However, when comparing influent versus effluent conductivity as a measure for the total ion concentration, the authors pointed out that there is sort of a constant gap between both measurements, as depicted in Figure 2.18. This gap is attributed to the entrapment or interception of the counterions by the dissociated functional groups in the cake layer and may well represent the ions responsible for the osmotic pressure effect.

The previous sections have shown the basics regarding MBRs and fouling. In the next chapter, the principles behind bioflocculation will be addressed.

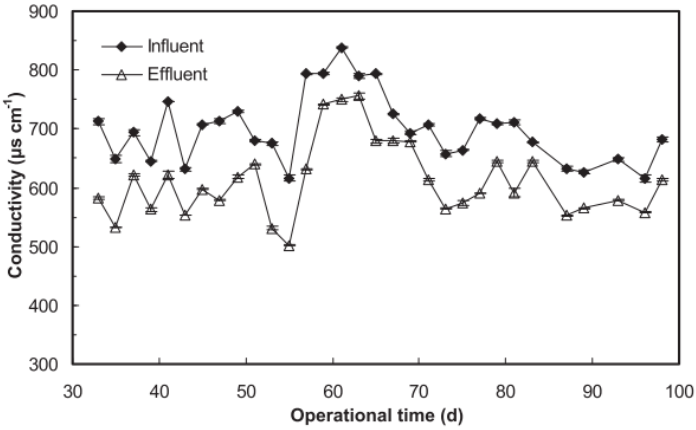

Figure 2.18: Variation of the conductivity of the influent and effluent during the operation of an immersed MBR [Zhang et al., 2013].

Chapter 3

Bioflocculation

In this chapter, an overview will be given regarding the formation of activated sludge flocs, in other words: bioflocculation. In Section 3.1, the fundamentals about bioflocculation will be discussed. In Section 3.2.1, different monitoring tools for bioflocculation are illustrated, including microscopy and image analysis (Section 3.2.1), laser-based particle sizes (Section 3.2.2) and floc strength analysis techniques (Section 3.2.3). Lastly, statistical techniques that deal with multivariate data, called chemometrics, are discussed in Section 3.2.4.

3.1 Bioflocculation fundamentals

3.1.1 Structure of activated sludge flocs

Activated sludge flocs are the result from bioflocculation of individual bacteria as a response to the low feed-over-microorganisms ratio exploited in activated sludge plants (see Section 2.1.1). The process of bioflocculation is highly dynamic, depending on the microbial community structure, environmental and operating conditions [Liao et al., 2006]. Several theories provide insight in the process, which will be presented in the next paragraphs.

In the *filamentous backbone theory*, a two-level structure is proposed. Floc-forming bacteria create small microflocs that combine with filamentous bacteria, which serve as a filamentous backbone, into macroflocs. In this regard, a good balance between the floc and filament forming bacteria is essential for the creation of a well settling and filtering activated sludge.

A good balance between flocs and filaments is closely related to the feeding regime. According to the kinetic selection theory, as developed by Chuboda et al. [1973], the growth of both filamentous and floc forming bacteria can be described using Monod kinetics, as is shown in Equation (3.1):

$$\mu = \mu_{max} \cdot \frac{S}{S + K_m} \tag{3.1}$$

with

μ	=	specific growth rate	$[h^{-1}]$
μ_{max}	=	maximum specific growth rate	$[h^{-1}]$
S	=	substrate concentration	[g/L]
K_m	=	Monod constant or half saturation concentration	[g/L]

According to the theory, due to their higher surface per volume, filamentous bacteria have a higher affinity (K_m value) for substrate when this does not reach saturation levels. However, generally their maximum growth rate is lower at high substrate concentrations. Substrate can be interpreted as organic substrate, but also as oxygen or nutrients. Therefore, when substrate limitation occurs, filamentous bacteria will thrive. It is for this reason that feast-famine cycles are often preferred over continuous feeding regimes [Chiesa et al., 1985].

An alternative structural model is given by Jorand et al. [1995]. In their model, the smallest constituents, called primary particles, are between 0.5 - 5 µm and are composed of single bacteria or small colonies. The second level, called microcolonies, are primary particles that are embedded in EPS that holds the structure together. These microcolonies can further aggregate into a third level, having an average size of about 125 µm. As the detrimental effect of small sludge constituents on filtration has already been discussed in Section 2.3.3, the primary particles are of prime interest in this study.

As said before, bioflocculation is a dynamic process and is in fact the balance between aggregation and floc growth versus deflocculation and floc decay. Deflocculation can typically occur in two different manners: erosion and fragmentation. During erosion, primary particles are released from the edges of the floc structures, resulting in a slightly smaller floc size and a higher number of free primary particles. During fragmentation, floc structures split up, resulting in more and smaller flocs, but only slightly elevated levels of primary particles.

Bioflocculation can be affected by a large number of process parameters. A longer SRT is known to produce larger, well flocculated sludge. Hydrophobic interactions have been shown to be improving bioflocculation, while an excessive amount of shear causes sludge flocs to break up. In this study, it was chosen to focus in depth on the effect of cations on bioflocculation and subsequently,

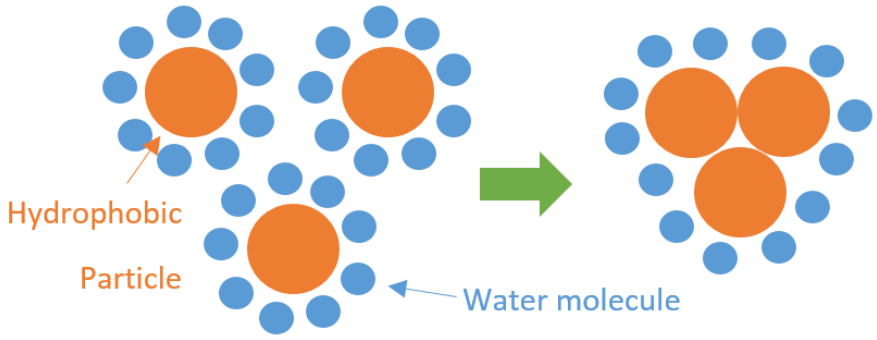

Figure 3.1: Schematic illustration of hydrophobic interactions. Aggregation reduces the hydrophobic surface that is exposed to the watery phase, resulting in a reduction of Gibbs free energy.

on activated sludge separation. The reason is twofold. Firstly, to verify the observed effect of cations on flocculation and secondly, to actually create sludges of different bioflocculation states that can be used to study the relationship between bioflocculation and activated sludge separation.

In the following sections, hydrophobic interactions will be discussed (Section 3.1.2) and different interactions between cations and bioflocculation will be explained (Section 3.1.3).

3.1.2 Hydrophobic interactions

Activated sludge flocs are known to have hydrophobic regions trapped within their structure [Urbain et al., 1993]. As stated before, most hydrophobicity is expected to be caused by the production of hydrophobic macromolecules such as proteins or lipids and EPS are assumed to play a crucial role herein [Liu and Fang, 2003; Raszka et al., 2006]. Moreover, hydrophobicity is strongly affected by the community balance that makes up the activated sludge flocs [Jorand et al., 1994]. The principle of hydrophobic aggregation can be explained as a reduction of Gibbs free energy. When hydrophobic particles aggregate, a reduced hydrophobic surface is exposed to the watery phase. This principle is illustrated in Figure 3.1.

3.1.3 Interactions between cations and bioflocculation

Three theories for mechanisms of cation-induced bioflocculation have been proposed by Sobeck and Higgins [2002], namely the DLVO-theory, which is later expanded into the XDLVO-theory as described before, the divalent cation bridging (DCB) theory and the alginate theory. In the following sections, these theories will be briefly presented.

XDLVO-theory

The XDLVO-theory has already been explained in Section 2.3.2. In this theory, the electrostatic repulsions between two similarly charged particles is countered by the adhesion forces of the van der Waals and hydrogen-bonding interactions. Typically, increasing the ionic strength of the medium reduces the Debye length (Equation (2.12)), which is a measure of the distance at which electrostatic effects persist. In this regard, the charge of the cation is only relevant through the increase in ionic strength (Equation (2.11)). The possibility of this effect was measured by Hamoda and Al-Attar [1995], who, in contrast to other researchers (see below), observed aggregation and sedimentation improvement when high sodium chloride concentrations were dosed to activated sludge.

Divalent cation bridging

Figure 3.2 describes the divalent cation bridging (DCB) theory. Divalent or multivalent cations can bridge between the negatively charged functional groups that are present on the surface of activated sludge flocs or within the EPS-matrix. This way, microcolonies (see Section 3.1.1) can bond to create macroflocs and filaments can be incorporated in floc structures. As monovalent cations would compete for these binding sites and do not possess enough charge to provide this binding effect, a high concentration of these ions can cause disruptions in the floc matrix. Novak et al. [1998] studied the effects of different ion concentrations on activated sludge flocculation and concluded that a critical monovalent-over-polyvalent cation ratio[1] (M/P) of 2 exists above which deflocculation occurs. The DCB theory has been verified a few times in literature [Van den Broeck et al., 2010; Van Dierdonck et al., 2013a] and is often regarded as the most valid explanation for cationic effects on bioflocculation.

[1] The cation ratio is expressed in terms of equivalents, with an equivalent being equal to the number of moles of the ion multiplied by its valence.

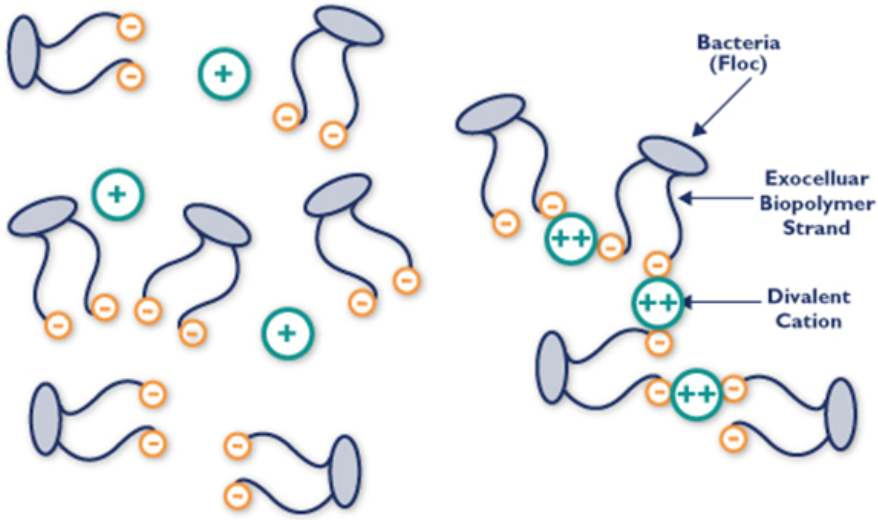

Figure 3.2: Schematic illustration of divalent cation bridging (DCB) theory. **Left:** divalent cations compete with monovalent cations for binding sites on negatively charged functional groups. **Right:** only divalent (or multivalent) cations can bridge negatively charged functional groups in the activated sludge matrix [http://thioguard.com].

Alginate

A third theory described by Sobeck and Higgins [2002] is the alginate theory. Alginate is a polysaccharide that is the result of the combination of two monomers (mannuronic and guluronic acid). Different bacteria that are often present in the activated sludge matrix are known to produce alginate, such as *Azotobacter* and *Pseudomonas aeruginosa* [Wingender et al., 2001]. Alginate can be regarded as a specific subset of the DCB theory since in combination with Ca^{2+} it forms a typical structure, typically referred to as an *eggbox* (see Figure 3.3), while this affinity is much lower for other divalent cations.

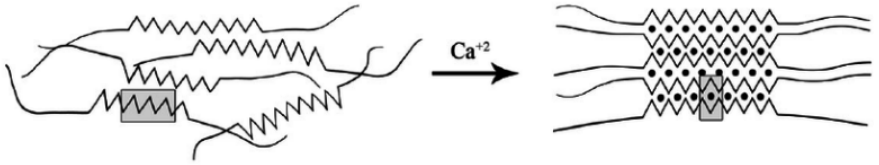

Figure 3.3: Principle of egg-box formation by addtion of Ca^{2+} to alginate matrix [E. Kirti, 2014.]

3.2 Monitoring bioflocculation

3.2.1 Microscopic imaging and image analysis

Microscopic imaging is a widely used tool to assess sample morphologies and to reveal fine details. A microscope accomplishes three tasks: a magnified image of the specimen is created (magnification), details are separated in the image (resolution) and the details are rendered visible to the eye or camera (contrast). A wide range of microscopic techniques are being used in activated sludge research. The microscopic techniques used in this work will be further explained.

Brightfield transmission microscopy

Brightfield transmission microscopy is the most commonly used. Two basic configurations can be found: upright and inverted microscopes. In an upright microscope, light from a lamp passes through a sub-stage condenser and subsequently through a transparent sample that is placed over an opening in the stage. The condenser serves to gather the light from the light source and concentrate it in a set of parallel beams such that the sample is illuminated uniformly. Light is then gathered by the objective, which focuses the image of the specimen at the level of the eyepiece or camera CCD. Inverted microscopes have a fixed stage (in the vertical direction), with the objectives underneath the stage. Above the stage, there is a moveable condenser and light source. Apart from having a different geometry, their functionality is essentially the same as for upright microscopes [Abramowitz, 2003]. Figure 3.4 illustrates both geometries.

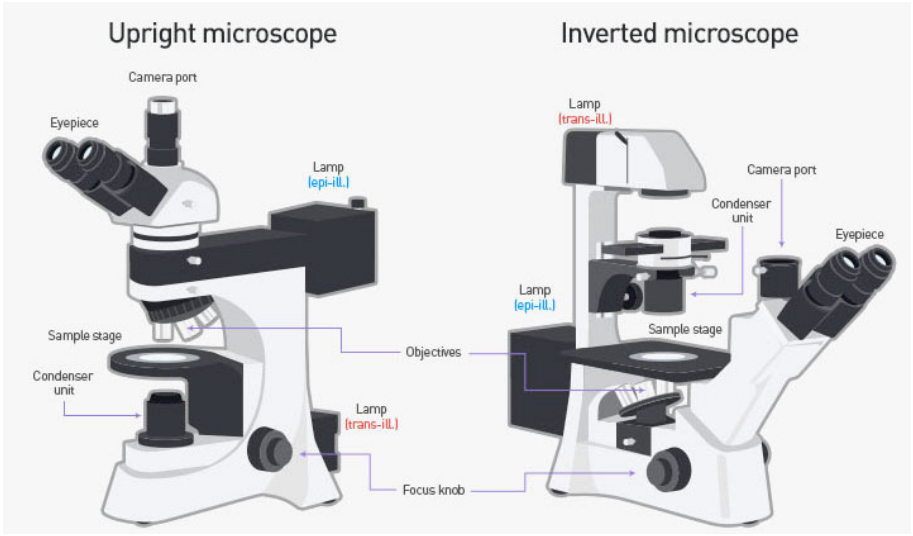

Figure 3.4: Graphical illustration of the geometry of upright and inverted brightfield and epi-fluorescence microscopes (www.thermofisher.com).

Phase contrast transmission microscopy

The foundations for phase contrast microscopy were laid in the early 1930s by the Dutch physicist Zernike [1942]. Unstained samples that show limited light absorbance, like some bacteria, including most filamentous types, are nearly invisible using classical brightfield illumination. However, they slightly alter the phase of the diffracted light by differences in the sample's thickness or refractive index. Usually this phase change is a $1/4^{th}$ wavelength retardation of the light, causing it to lag slightly behind. Phase differences are, unfortunately, invisible to both the human eye and camera.

The method developed by Zernike [1942] aims at converting this phase difference into a measurable amplitude difference by speeding up the direct light by another $1/4^{th}$ wavelength, causing the direct and diffracted light to interfere destructively and thereby increasing contrast. To speed up the direct light, a phase plate is installed inside the objective, at the rear focal plane, with a ring shaped phase shifter, which is optically thinner than the rest of the plate. Undeviated focussed light consequently travels a shorter distance through the objective, causing it to be $1/2^{th}$ of a wavelength ahead of the diffracted light, resulting in destructive interference [Davidson and Abramowitz, 1999]. The concept of phase contrast microscopy is illustrated in Figure 3.5.

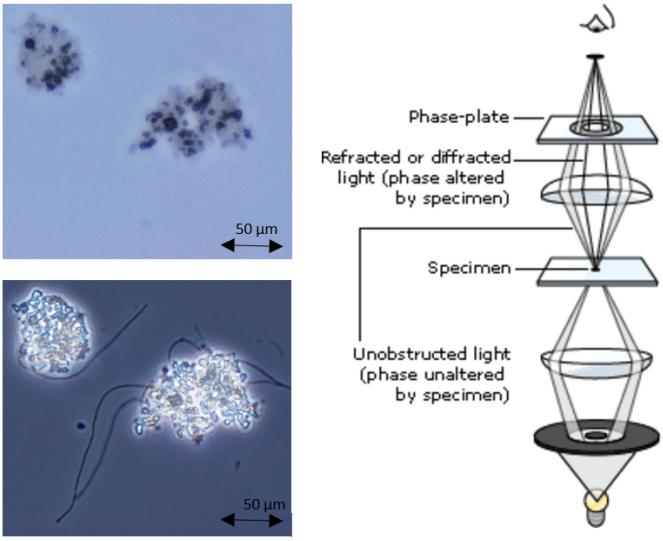

Figure 3.5: Left: Difference between brightfield (top) and phase contrast (bottom) vizualization. Whereas the filaments are nearly invisible in the brightfield image, they are clearly shown using the phase contrast technique. The typical halos surrounding the phase contrast flocs are also shown.
Right: Conceptual illustration of phase contrast microscopy (www.nobelprize.org).

Epifluorescence microscopy

Fluorescence is the emission of light by a molecule after absorption of light or electromagnetic radiation and occurs when an orbital electron relaxes from an excited to a ground state. Consequently, in nearly all cases, the emitted light has a longer wavelength, and thus a lower energy level than the absorbed radiation. This phenomenon is called the Stokes shift and forms the basis of fluorescence microscopy.

In fluorescence microscopic imaging, the sample contains one or several fluorescent molecules. Those polyatomic molecules have excitation and emission spectra, rather than discrete electronic transitions. The principle is explained in Figure 3.6. From a light source, usually a xenon arc or mercury vapor lamp, part of the spectrum is selected by an excitation filter and sent *through*[2] the

[2]The term *epi*-fluorescence comes from the Greek meaning *the same* and refers to the objective, that serves as a conduit for both exciting and emitted light.

objective to illuminate the sample. In the sample, the fluorescent molecules become excited and emit fluorescent light upon returning to the ground state. In accordance with the Stokes shift, this emitted light is of longer wavelength than the excitation spectrum and is collected again by the objective. Next, a dichroic beamsplitter or mirror is used to differentiate the incoming emitted wavelengths from the outgoing excited ones, illustrating the importance of the Stokes shift. Finally, in most cases, the emitted light passing through the dichroic mirror is filtered again before being sent to the camera or eyepieces; this time, the filter is called the emission filter. Figure 3.4 also depicts the location of the fluorescent light source in both upright and inverted microscope configurations. The combination of dichroic mirror, excitation and emission filters is usually provided as a filter cube that can easily be selected in the microscope. One microscope may hold several of such filter cubes to allow the vizualization of multiple fluorescent species, each with their respective excitation/emission characteristics.

Often in research, a confocal laser scanning microscope (CLSM) is used instead of a traditional epifluorescence microscope. The basic principles of fluorescence are the same in both methods, but a CLSM provides a higher resolution. This increase in resolution comes from the use of lasers rather than excitation filters for sample illumination, narrowing the excitation range to a few nanometers, which is a tenfold decrease from the range of wavelengths selected using excitation filters. Moreover, the use of a pinhole, that permits light from only a very narrow section of the sample, provides a means for optical sectioning. This way, only light from a certain depth in the sample is allowed to pass through to the detector, out-of-focus light is removed and the measurement of 3D-structures is made possible. However, the depth of penetration remains limited to only a few tens of micrometers, the measurement is much more time consuming, the equipment much more expensive and specialized training is required to operate such a microscope.

Two major sources of fluorescence exist in biological research. **Autofluorescent** molecules are naturally present in the system or stem from genetically modifying the microorganisms to produce them autonomously. In anaerobic sludge research, the autofluorescent coenzyme F420, which is naturally present in methanogenic bacteria, has become a signature molecule for identifying them. This low molecular weight coenzyme that fluoresces with a strong absorption at 420 nm under oxidized conditions, serves as a chemical equivalent to NAD in its biological redox activity and is assumed to be the major electron transfer currency in hydrogenothrophic bacteria [Cheeseman et al., 1972; Reynolds and Colleran, 1987].

Since the discovery of green fluorescent protein (GFP) in 1961 and its first isolation in 1992, GFP has been used in many research applications where

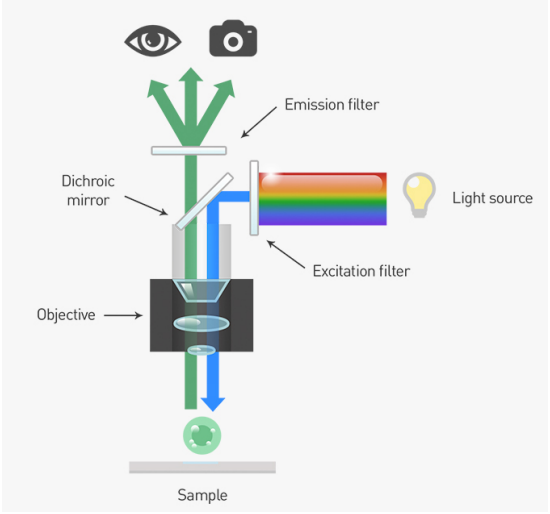

Figure 3.6: Working principle of an epi-fluorescence microscope (www.thermofisher.com).

autofluorescence is introduced to a (micro)organism to study its growth, responses to stress and behaviour [Chalfie and Kain, 2006; Errampalli et al., 1999].

Most used are **fluorescent markers and dyes**. These compounds typically consist of a reactive part, that binds to a specific target (e.g., DNA, reactive functional groups) and a fluorescent part that provides the illumination upon excitation. Figure 3.7 depicts the fluorescent marker fluorescein isothiocyanate (FITC), that is used to label proteins. It consists of the original fluorescein molecule, functionalized with an isothiocyanate reactive group, that binds with amine and sulfhydryl groups on proteins. Since the introduction of fluorescence microscopy, many fluorescent markers and dyes have been developed. Selecting the appropriate dye for an application strongly depends on the following factors [Johnson and Spence, 2010].

Target. The target is determined by the objective of the study and can be a general or specific DNA sequence (e.g., in Fluorescent In Situ Hybridization (FISH)), or a specific molecule or reactive functional group, or surface characteristics, like hydrophobicity.

Selectivity. When staining a specific target in a bacterial agglomeration like activated sludge, interference from non-target molecules should be avoided as much as possible.

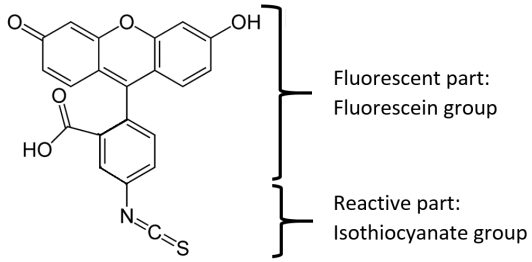

Figure 3.7: Fluorescein isothiocyanate (FITC) as an example of a fluorescent marker.

Reactivity. Ideally, a fluorescent marker binds covalently to its target. Diffusion, cell wall penetration and reaction kinetics all determine the time required for binding.

Fluorescence excitation spectrum. This is the spectrum of wavelengths that can excite a sample. The optimal instrument set-up is the one that delivers excitation light as closely to the peak of the excitation spectrum as possible.

Fluorescence emission spectrum. This is the spectrum of emitted wavelengths upon excitation. In multicolor labeling experiments, it is vital that either the excitation or emission bandwidths of the different fluorophores do not coincide.

Extinction coefficient. This is the capacity of a fluorophore to absorb light at a specific wavelength and should be as high as possible.

Quantum yield. This is the number of fluorescence photons emitted per photon absorbed. The product of the quantum yield and the extinction coefficient determines the fluorescence output.

Background fluorescence. Some fluorescent markers change in extinction coefficient or quantum yield upon binding to their target, making them emit significantly more fluorescence when bound. These, unfortunately more expensive dyes are of interest since they relief the need for washing the stained substance after dye incubation. Background fluorescence can occur through the fluorescence of unwashed dye or through the excitation of autofluorescent species present in the sample.

Quenching. This is the loss of fluorescence signal due to short-range interactions between the fluorophore and the surrounding molecules. Quenching should be avoided as much as possible.

Photobleaching. The process of fluorescence is cyclical. A fluorophore can be repeadedly excited and detected. However, a fraction of fluorophores is lost in the process. This effect, called photobleaching, depends on the duration and the intensity of light exposure, but is also dependent on the photostability of the dye and in some cases on the fluorophore's environment.

Other factors. These may include: solvent polarity, pH of the medium and proximity and concentrations of quenching species.

The use of fluorescent markers in activated sludge research counts numerous examples. In their research, Mesquita et al. [2011a] used the BacLight Bacterial Gram and Viability kit (Molecular Probes, Eugene, Oregon, USA) to classify activated sludge bacteria in dead, alive Gram-positive and alive Gram-negative species, using the fluorescent dyes SYTO9, prodium iodide and hexidium iodide, that differ in spectral characteristics and in their ability to penetrate bacterial cells. The same authors successfully predicted intracellular storage polymers in polyphosphate accumulating organisms using fluorescent techniques [Mesquita et al., 2013b]. In their work, Szilveszter et al. [2012] used several fluorescent dyes to visualize the spatial distribution of different biopolymers and extracellular enzymes in activated sludge flocs. The staining of EPS has been performed by other authors as well [Chen et al., 2006; Hwang et al., 2012; Lin et al., 2009; Neu et al., 2001].

Fluorescence *in situ* hybridization (FISH) is a molecular technique that comes down to hybridizing a fluorescently labelled oligonucleotide probe to its complementary sequence present in a microorganism's DNA or RNA, obeying the Watson-Crick hydrogen-bonding rules [Cerqueira et al., 2008; Volpi and Bridge, 2008]. FISH is widely used in the field of microbiology for identifcation, quantification and characterization of phylogenetically defined bacterial populations in complex environments like activated sludge [Rocha et al., 2016]. E.g., Wilén et al. [2008] and Morgan-Sagastume et al. [2008] used FISH to relate broad bacterial groups to shear-dependent deflocculation. In other studies, FISH was used to identify filamentous bacteria responsible for sludge bulking problems [Mielczarek et al., 2012; Nielsen et al., 2009], to relate filtration problems to specific microbial communities [Bugge et al., 2013] and to identify population dynamics involved in phosphorus and nitrogen removal [Mielczarek et al., 2013; Saunders et al., 2013].

Quantitative image analysis

Quantitative image analysis is the extraction of quantifiable data from microscopic images. These images can be obtained using a variety of visualization techniques, among which those that have been discussed in the previous sections. These images are usually obtained through the use of digital cameras. The signal produced by such cameras consists of a matrix of picture elements (pixels) of which the value is proportional to the light intensity it has received. Typically, for grayscale images, these pixels can contain 256 discrete grayscale levels, corresponding to an 8-bit depth. Color images are typically digitalized as 24-bit, containing the red, green and blue channels as if they were 8-bit gray channels.

Basically, image analysis holds two major steps after the image acquisition: image preparation and data extraction. During image preparation, the images are prepared for processing. This preprocessing usually starts with background correction and image enhancing operations, followed by segmentation to separate the objects from the background using one or several thresholding strategies. In the second step, the segmented image is processed and the different objects on the segmented image are analysed. This step usually yields parameters relating to the size or the shape of the objects that are present on the image. In the case of fluorescent image analysis, also intensity-related parameters can be obtained.

In their recent review, Mesquita et al. [2013a] provided an exhaustive list of applications of quantitative image analysis in activated sludge research. Some of the earlier examples of image analysis in activated sludge monitoring were the study from Grijspeerdt and Verstraete [1997], that successfully linked the sludge's form factor to the diluted SVI, and the studies from Li and Ganczarcyk [1987, 1991] on the porosity and size distribution of activated sludge flocs. The relevance of the fractal dimension concept in the description of activated sludge flocs was introduced by Snidaro et al. [1997] and Thill et al. [1998] and has been readily used in the study of activated sludge flocs [Jin et al., 2003; Perez et al., 2006; Schmid et al., 2003] and membrane fouling in MBRs [Lin et al., 2011; Meng et al., 2005].

Mesquita et al. [2010] compared the brightfield and phase contrast visualization techniques using two tailor made image analysis programs and came to the conclusion that both techniques yield similar results, but that for well-balanced activated sludge systems, with a good distribution of flocs and filaments, the brightfield method was superior. This conclusion was drawn from the fact that the phase contrast observation technique was less robust and systematically overestimated the size of flocs, while underestimating the length of filaments, which was the direct result from the characteristic phase contrast halos. Furthermore, in the same study, it was clearly mentioned that difficulties

may be encountered when sludge samples containing lengthy filaments are to be analysed using brightfield. This observation was already illustrated in Figure 3.5.

Nevertheless, both observation methods are widely used in combination with image analysis in activated sludge research. The brightfield method has been employed by Droppo et al. [1996] and Perez et al. [2006]. Amaral and Ferreira [2005] used both methods according to their aforementioned best suited target, i.e., phase contrast for filaments and brightfield for flocs. Phase contrast quantitative microscopy was proposed by Cenens et al. [2002] and has been used at KU Leuven since the development of ACTIAS, a fully automated activated sludge image analysis system, by Jenné et al. [2002]. ACTIAS has previously been used for dynamic modeling of filamentous bulking in lab-scale activated sludge systems [Smets et al., 2006], assessing the stability of activated sludge [Van den Broeck et al., 2009; Van Den Kerkhof et al., 2013], studying influent compositions and loading rates on activated sludge development [Van den Broeck et al., 2010, 2011; Van Dierdonck et al., 2012a, 2013b] and unraveling correlations between MBR-sludge characteristics and fouling [Van den Broeck et al., 2012].

3.2.2 Laser-based particle size detection methods

In this section, laser-based particle size detection methods will be explained and compared.

Laser diffraction

Their capacity for a rapid and accurate polydispersity measurement makes the use of laser diffraction particle sizers, such as the Malvern Mastersizer, popular in activated sludge research [Arabi and Nakhla, 2009; Gao et al., 2013; Jin et al., 2003; Shen et al., 2015]. A laser diffractor's working principle is based on the Rayleigh scattering of light by particles, which differs according to the particles' sizes. An instrument like the Mastersizer consists of at least one source of high intensity monochromatic light, a sample chamber and an array of photodiodes to detect the scattered light [Horiba Instruments, 2014].

Next, an algorithm is used to translate the measured scattered intensities into particle sizes by the use of an optical model. The oldest optical model is the *Fraunhofer approximation*, which provides reasonable results for particles of moderate sizes. To simplify the calculation (hence approximation), a few assumptions are made, i.e., the particles are assumed to be spherical, opaque

and to scatter equivalently at wide and narrow angles, while interacting in a different manner with the light than the medium does. Unfortunately, these restrictions render the Fraunhofer approximation inaccurate below particle sizes of 20 µm.

Therefore, another optical model was developed by Gustav Mie based on Maxwell's electromagnetic equations for scattering from spheres. This model, however, requires knowledge of the refractive indices of the particles and the dispersing medium. Like Fraunhofers approximation, the *Mie scattering theory* assumes spherical particles. Moreover, particles are also assumed to be homogeneous.

From the above observations it is clear that, although its high popularity, laser diffraction is not a very suitable particle size measuring technique for activated sludge. More specifically, when a prime interest lies in monitoring the abundance of small sludge particles, Fraunhovers approximation cannot be used, while even Mie's theory faces difficulties since activated sludge flocs are generally heterogeneous and non-spherical. Moreover, their refractive indices are not easily measured and can vary strongly among different sample origins.

Dynamic light scattering

An alternative for the measurement of (sub)-micron particles is the use of dynamic light scattering (DLS). DLS determines the particles sizes by measuring the random changes in scattered light from a suspension that stem from the Brownian motion. This random motion is particle size dependent and is used in the measurement principle. Light from the laser source illuminates the sample and is scattered. The scattered light is then collected with several detectors and processed using an autocorrelation function to yield the Brownian diffusion coefficient D_t. Next, the wavelength of the laser light (λ) and the refractive index of the liquid (η) is inserted with the diffusion coefficient into the Stokes-Einstein Equation (3.2) to yield the particle diameter d_p [Horiba Instruments, 2014].

$$d_p = \frac{k_b \cdot T}{3\pi\eta D_t} \tag{3.2}$$

The use of dynamic light scattering for the study of activated sludge (sub-)micron particles has been demonstrated by De Temmerman et al. [2014, 2015]. However, prior to their analysis, the small particles needed separation (centrifugation followed by filtration) from the larger activated sludge flocs. In this process, their concentration and distribution might have been altered. Therefore, the

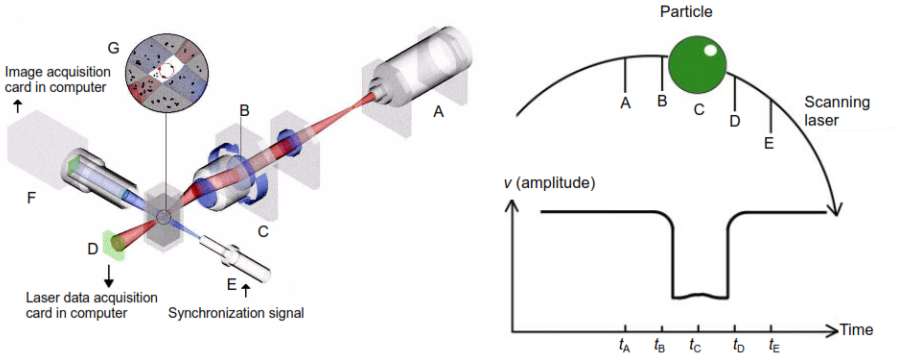

Figure 3.8: Left: CIS-100 measuring system. A: laser source, B: focussing prism, C: scanner, D: photodiode detector, E: strobing light source, F: CCD video microscope, G: focal volume of measurement. Right: principle of time of transition [van der Schoot, 2004].

authors were uncertain whether the measured concentration was representative for the real distribution of (sub-)micron particles. The measurement was deemed only accurate for the relative comparison of the different samples tested.

Time of transition

In their study for the determination of activated floc size distribution by different techniques, Govoreanu et al. [2004] compared laser diffraction with image analysis. Moreover, they included a third technology, namely the CIS-100, which combines size analysis based on the time of transition (TOT) principle with a dynamic size and shape characterization method based on image analysis using an online camera. The working principle of the analyser and the time of transition technology is shown in Figure 3.8 [van der Schoot, 2004]. As the name points out, the time it takes for a particle to move through the laser beam is recorded. From this information, the average particle diameter is calculated.

The TOT-method, however, has a few disadvantages as well. In their comparison, Govoreanu et al. [2004] concluded that the method often fails at separating multiple objects. Indeed, two very close opaque particles were seen as a bigger transparent one, yielding a bimodal distribution, which was not in agreement with the results of the other technologies tested.

In general, it can be concluded that image analysis remains the most versatile measurement method for determining the particle size distribution. Moreover,

the other techniques all assume spherical particles, while the only technique that can describe particle size using multiple values is automated image analysis [Horiba Instruments, 2014].

3.2.3 Floc strength

To assess floc strength, activated sludge is often subjected to shear, which leads to a breakup of the floc structure and a reduction of the floc sizes. Sludge breakup can occur by two mechanisms of different nature. *Fragmentation* of flocs results in a shift towards smaller flocs by breaking up bigger flocs in several smaller ones, while the number of very small (primary) particles remains constant. *Erosion* of primary particles from floc surfaces causes an increase in the number of particles, while the average floc size only decreases marginally [Parker et al., 1970].

Mikkelsen and Keiding [2002a] proposed a shear-sensitivity assessment protocol as a possilibity for a standardised floc strength test. The method analyzes the trend of activated sludge supernatant turbidity after application of shear via mixing with a single bladed paddle. The supernatant was obtained through centrifugation (2 minutes, 3000 rpm). The authors suggest operating with a shear rate determined by a root-mean-square velocity gradient[3] (G) of 800 s^{-1}. The supernatant turbidity was measured spectrophotometrically at 650 nm and converted to formazine turbidity units using a calibration curve. These results were then fitted on the erosion-kinetics formula, defined in their earlier work [Mikkelsen and Keiding, 1999], as is shown in Equation (3.3).

$$m_{d,t} = m_{d,\infty} + (m_{d,0} - m_{d,\infty})\frac{6}{\pi}\sum_{N=1}^{9}\frac{1}{N^2}e^{-N^2 Dt} \tag{3.3}$$

where $m_{d,t}$ is the dispersed mass concentration at time t, $m_{d,0}$ and $m_{d,\infty}$ are the dispersed mass concentrations initially and at equilibrium, respectively, N is an integer and D is the effective diffusion constant.

The shear-sensitivity (K_{ss}) can then be calculated as follows: $K_{ss} = \frac{m_{d,\infty}}{m_T}$ with $m_{d,\infty}$ found through fitting Equation (3.3) and m_T, the total mass concentration of the sample (usually standardized to 4 g/L).

The method proposed by Mikkelsen and Keiding [2002a] has been extensively tested during the duration of this work, but was discarded since no reliable results

[3] $G = \sqrt{\frac{P}{\eta V}}$ where P is the power input, η is the fluid viscosity and V is the suspension volume.

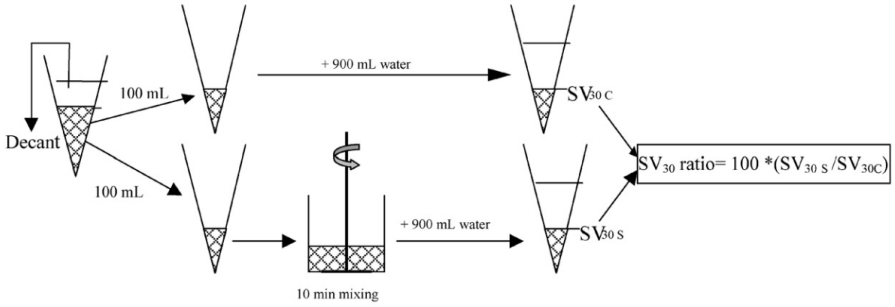

Figure 3.9: Schematic representation of the shear-SV test procedure [Seka and Verstraete, 2003].

could be obtained. Moreover, since the aforementioned method is cumbersome and the necessary centrifugation setup prior to turbidity measurement is not representative for separation through sedimentation, Seka and Verstraete [2003] developed an easy-to-use shear-SV test procedure, which is shown in Figure 3.9. The shear is expressed by the ratio (%) obtained by dividing the sludge volume after 30 min settling (SV_{30}) of sheared sub-sample by another non-sheared sub-sample (control).

3.2.4 Chemometrics: principal component analysis and partial least squares

Chemometric techniques are multivariate statistical methods that are fit to tackle issues often found in datasets with numerous variables, such as rendundancy and intercorrelation between variables. Therefore, they can be useful in unraveling underlying trends, discovering outliers or just reducing the data numbers. Two multivariate techniques and their relation to bioflocculation monitoring will be discussed: principal component analysis (PCA) and partial least squares (PLS).

Principal component analysis

In principal component analysis (PCA), the data is compressed and projected from a high dimensional space into a lower one in order to find the key variables of the system. The new, latent variables are linear combinations of the old ones chosen in a way such that most of the variance from the old dimensions is retained. This way, the majority of the information content will be kept when the number of variables is strongly reduced. PCA can be employed to find

relationships between measured parameters, for monitoring trends and for the detection of abnormalities in processes [Eriksson et al., 2013].

Van Den Kerkhof et al. [2013] used PCA to assess the stabilization time for activated sludge in laboratory conditions. In another work, PCA succesfully reduced the number of variables from 12 to 3 for a statistical process control study on an activated sludge system with the IWA activated sludge model ASM1. The variables were clustered in three groups, respectively relating to the microorganisms and particulate matter, the substrate and flow rate and the pH [Tomita et al., 2002]. Mesquita et al. [2011b] used PCA for clustering of image analysis data, allowing the identification of process disturbances such as filamentous bulking, pinpoint flocs and zoogleal bulking, as well as normal conditions. In a study on the effect of metal toxicity in municipal wastewater activated sludge, PCA unravelled a higher sensitivity of the nitrifiers compared to the heterothrophs to the heavy metals copper, zinc and nickel [Principi et al., 2006].

Partial least squares

Partial least squares (PLS) is a linear regression technique that holds many similarities to PCA. In both cases, a projection is made on latent structures, in order to reduce the number of variables. In PLS, however, two sets of variables are projected: the input variables X and the output responses Y. PLS aims at projecting both X and Y onto two new sets of lower dimensions, but with the underlying goal of seeking the best correlation between both sets. In essence, the data in X that best describes most of the variance in Y is captured and used for the creation of a multi-linear regression model [Eriksson et al., 2013].

PLS has been used in a number of studies in activated sludge research. One use is the case of multivariate calibration. This calibration method tries to link a number of readily obtainable measurements (e.g., data from image analysis or spectrophotometric wavelengths) to data from another, usually more time-consuming method (e.g., chromatography). If successful, the time-consuming method can then be omitted in further experiments. This technique has been used by Sarraguça et al. [2009] to measure COD, nitrate and total suspended solids online using UV-visible and near-infrared spectroscopy and by Mesquita et al. [2013b] to replace the elaborate chromatographic measurements of glycogen and polyhydroxyalkanoates (PHAs) in anaerobic systems by fluorescent image analysis. In another study, Mesquita et al. [2015] used PLS to compare two staining methods for PHAs.

The use of PLS to use quantitative image analysis techniques in the prediction of activated sludge concentration (MLSS) and settleability (SVI) has been

demonstrated twice by Amaral and Ferreira [2005] and Amaral et al. [2013]. In the modeling of activated sludge plants, PLS has been exploited in a few case studies, linking the plant's operational and influent conditions to its performance [Lee et al., 2006; Teppola et al., 1997]. A final demonstration of PLS has been given by Van den Broeck et al. [2011] in their study relating activated sludge characteristics to MBR-filterability in municipal and industrial MBRs. In this study, PLS was used to propose a filterability classification factor based on the number of sludge fragments, inferred from image analysis, and the sludge's hydrophobicity.

With this chapter, the literature study concludes. In the next chapter, several materials and methods will be presented that are used throughout this work. Afterwards, the three goals, as described in Section 1.3, will be tackled.

Chapter 4

Materials and methods

In this chapter, the experimental methods and data analysis techniques that are *commonly* employed throughout the rest of the work, will be discussed. The first section describes the activated sludge characterisation methods. Microscopic imaging and image analysis will be tackled in a second section. In a final section, the separation performance indicators are explained.

4.1 Activated sludge characteristics

4.1.1 Sludge and effluent solids concentration

MLSS. The mixed liquor suspended solids (MLSS) denote the total suspended solids concentration in the mixed liquor. A fixed sample volume (10 mL) is filtered (Machery Nagel GF-3) and dried during two hours (105°C). After cooling in a dessicator, the accumulated mass is weighed. The MLSS denotes the respective mass-over-volume ratio (g/L).

MLVSS. To measure the mixed liquor volatile suspended solids (MLVSS), the dried filter from the MLSS measurement is heated up to 550°C for one hour. At this temperature, organic material combusts and evaporates as CO_2 and H_2O. After cooling, the resulting mass is substracted from the initial mass. The ratio of this mass difference over the initial suspension volume yields the MLVSS (g/L).

ESS. The effluent suspended solids (ESS) are measured in a similar manner as the MLSS. However, as their concentration is relatively low, a higher sample

volume is used, usually 100 mL. ESS can be expressed in g/L or as a percentage of the reactor's MLSS.

4.1.2 Chemical oxygen demand (COD)

The chemical oxygen demand (COD) is the amount of oxygen required to completely oxidize the organic material present, and is used as a measure of the organics concentration and effluent quality. To measure the COD, test kits are used (Hach Lange, LCK series). After adding a specified sample volume to the testing tube, the sample is heated (2 hours, 150°C). Subsequently, the concentration is measured using a spectrophotometer (Hach Lange DR 5000).

4.1.3 Relative hydrophobicity

The microbial adhesion to hydrocarbons (MATH) assay was used to analyse the relative hydrophobicity of the activated sludge. After mixing with hexane, hydrophobic sludge consituents are retained in the apolar hexane phase and separated from the watery phase through decantation. Hence, sludge of a hydrophobic nature will result in a less turbulent watery phase [Rosenberg et al., 1980].

50 mL diluted activated sludge (1 g/L using filtered supernatant) was centrifuged ($5000g$, 2 min, 4°C). The supernatant was replaced with MilliQ (Sartorius 611DI) and the sludge pellet was re-suspended by shaking. The procedure was repeated twice and resulted in dispersed sludge.

From this sludge, four 10 mL samples were taken, with addition of 10 mL hexane to three of the four samples. The fourth sample served as a control. The samples and control were gently shaken for 15 minutes at 40 rpm, followed by settling. From the heavier watery phase, 7 mL was decanted after 5 minutes. The absorbance (A) was measured in threefold at 650 nm using a spectrophotometer (VWR UV-1600PC), with brief vortexing before each measurement. From this measurement, the relative hydrophobicity (RH) can be calculated using Equation (4.1).

$$RH = (1 - \frac{A_{HEXANE-TREATED}}{A_{CONTROL}}) \cdot 100\% \tag{4.1}$$

4.1.4 Surface charge

The surface charge of sludge (SC) was determined by colloid titration, using polybrene and polyvinyl sulphate potassium salt (PVSK) as the cationic and anionic standards [Morgan et al., 1990].

5 mL of diluted sludge (1 g/L) is further diluted to 100 mL using MilliQ (Sartorius 611DI). To this mixture, 0.5 mL toluidine blue indicator solution (0.1 %) and 5 mL polybrene solution (0.001 N) is added. Polybrene is added in excess and titrated back using a 0.001 N PVSK solution. At the equivalence point, the toluidine blue mixture changes color from blue to pink. This procedure is repeated 5 times on sludge and MilliQ (blank). The surface charge can then be calculated using Equation (4.2),

$$SC = \frac{(V_{BLANK} - V_{SLUDGE}) \cdot C_{PVSK}}{m_{SAMPLE}} \tag{4.2}$$

where C_{PVSK} denotes the charge concentration of PVSK, which equals -0.001 eq/mL and m_{SAMPLE} denotes the weight of the biomass of the 5 mL sludge sample, which should equal 0.005 g.

4.1.5 Extracellular polymeric substances

In Section 2.3.2, it was explained that EPS can be divided in soluble microbial products (SMP) and bound or extractable EPS (eEPS). This fractionation is performed experimentally, after which the composition of each fraction is determined. Extraction and analysis are both performed in triplicate.

Extraction and fractionation

Soluble microbial products (SMP) were extracted from the sludge using the method proposed by Van Dierdonck et al. [2012b]. A sludge sample (100 mL) is centrifuged (5000g, 10 min, 4°C, Eppendorf 5810R using rotor F34-6-38). Next, the supernatant is filtered through a pre-rinsed Whatman Grade 1 filter, which yields the **SMP** as permeate.

The pellet is resuspended using milliQ. This suspension can be used to extract the eEPS, which can be performed using the heat treatment or cation exchange resin (CER) method. In the first method, the suspension is heated for 10 minutes at 80°C using the thermoblock (Merk TR620). Afterwards, the suspension is

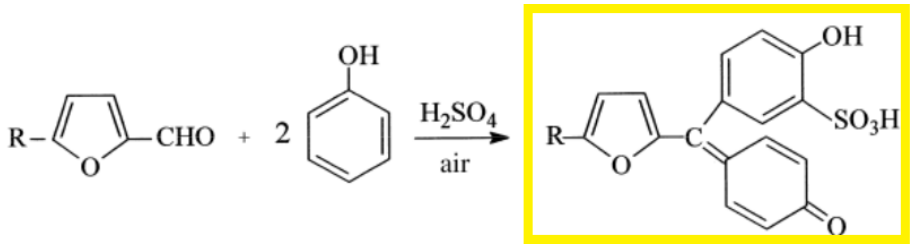

Figure 4.1: General reaction scheme of the phenol-sulphuric acid or Dubois method illustrating the reaction of a reactive furfural intermediate with phenol in a sulphuric acid medium. The yellow reaction product can be detected colorimetrically at 490 nm.

cooled down, and the same method as for SMP-extraction is repeated to yield the **heat-treated-eEPS** (eEPS-H) in the permeate.

In the CER-method, 70 g dried and pre-washed cation exchange resin (Dowex Marathon C, Sigma-Aldrich) is added per gram of MLVSS in the resuspended sludge. CER is pre-washed in PBS-buffer to reduce its acidity, which would hamper efficient eEPS-extraction. The sludge-CER mixture is stirred during one hour at 600 rpm, which is in accordance with the mild extraction method as described by Frølund et al. [1996]. After stirring, the SMP-extraction method is repeated to yield the **CER-treated-eEPS** (eEPS-CER) in the permeate.

Composition

EPS fractions were measured as the sum of proteins and polysaccharides, since they are the most prevalent constituents.

Polysaccharides were determined using the phenol-sulfuric acid method, as described by Dubois et al. [1956]. To a 1 mL sample containing polysaccharides, a strong acid (2.5 mL of 98% sulphuric acid) is added, which causes the polysaccharides to be hydrolyzed into their constituent monosaccharides. Next, the resulting monosaccharides are dehydrated to reactive species (e.g., furfural). Adding phenol (0.5 mL of a 5 % phenol solution) causes these intermediates to react (30 min incubation time) into yellow products, that can be measured colorimetrically at 490 nm (see Figure 4.1). Finally, the absorbance value is converted into an equivalent glucose concentration by the use of a calibration curve, obtained with standard glucose solutions.

Proteins were initially measured in accordance with Lowry et al. [1951]. The

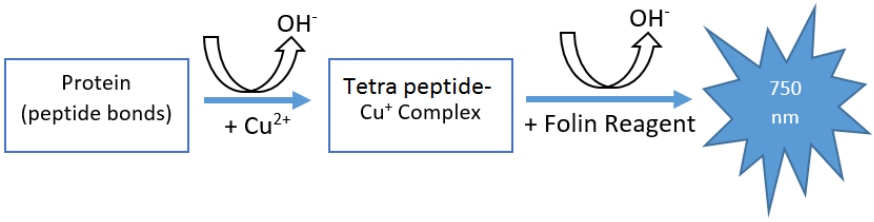

Figure 4.2: General reaction scheme of the Lowry method for protein quantification.

Lowry method is based on the reduction of the Folin-Ciocalteau agent (see Figure 4.2). An alkaline solution of Cu^{2+} is made, using the reagents described in Table 4.1. From this solution, 2 mL is added to the sample (0.8 mL). The added alkaline solution is allowed to react during 10 min in which the copper ions are reduced and form a complex product with the nitrogen atoms in the peptide bonds. Subsequently, 200 μL of the Folin-Ciocalteau reagent (sodium tungstate, sodium molybdate, phosphoric acid and HCl, Sigma) is added to the solution, which reacts with the Cu^{+}-peptide complex. This reaction, which is still poorly understood, results in the formation of the unstable phosphomolybdotungstate intermediate, which is reduced to heteropolymolybdenum blue by the copper-catalyzed oxidation of aromatic amino acids. The reactions result in a strong blue color, which depends partly on the tyrosine and tryptophan content. Next, the absorbance is measured colorimetrically at 720 or 750 nm. A calibration curve with standard protein solutions of bovine serum albumin (BSA) is used to convert this absorbance value into an equivalent protein concentration (mg BSA/L).

Table 4.1: Composition of reagents used for protein quantification according to Lowry et al. [1951].

Ratio	Components	
100	143 mM NaOH	270 mM Na_2CO_3
1	57 mM $CuSO_4$	
1	124 mM Na_2-tartrate	

However, Lowry's method is known to experience interference from humic acids. To this end, protein contents from municipal or industrial samples were

measured using the modified Lowry method [Frølund et al., 1995].

Frølund et al. [1995] state that without $CuSO_4$ addition, the colour developed by bovine serum albumin decreases to 20 % but that no decrease is observed for humic acids. Using this observation, the following series of equations is used to calculate the protein content:

$$A_{total} = A_{protein} + A_{humic} \tag{4.3}$$

$$A_{blind} = 0.2\ A_{protein} + A_{humic} \tag{4.4}$$

$$A_{protein} = 1.25\ (A_{total} - A_{blind}) \tag{4.5}$$

where A_{total} is the total absorbance with $CuSO_4$, A_{blind} is the total absorbance without $CuSO_4$ and $A_{protein}$ and A_{humic} are the absorbances of proteins and humic acids, respectively.

Since humic acids are only produced by biodegradation of organic plant matter, their presence in experiments that run with synthetic influents, is assumed to be negligible [Raszka et al., 2006; Tan, 2014], thus for these measurements, the modifications presented by Frolund et. al. could be omitted.

4.1.6 Microscopy

Olympus IX83

Images were taken using the Olympus IX83 inverted microscope (see Figure 4.3). The fully motorized microscope is operated through CellSens (Olympus Corporation, Tokyo, Japan) and is equipped to visualize samples using three major observation methods: brightfield, phase contrast and epi-fluorescence (see Section 3.2.1). Magnifications from 4x to 100x are possible, although the 10x objective is the most used objective in this study. The installed fluorescence filter cubes are shown in Table 4.2 and the excitation light is provided by a 120W Mercury Vapor Short Arc lamp (Lumen dynamics type X-cite series 120 Q). The other important microscope features for this study will be briefly discussed.

Autofocus. The microscope is able to automatically focus on a sample which allows sequentially taking images on multiple locations, without the operator having to focus each time.

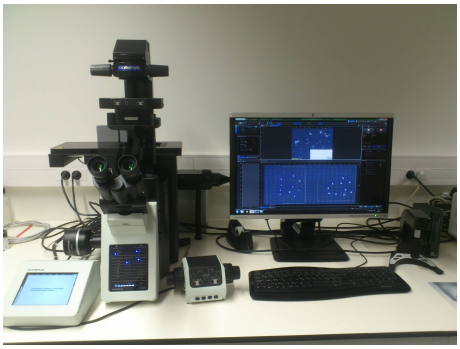

Figure 4.3: Olympus IX83 fully motorized inverted microscope.

Table 4.2: IX83 fluorescent filter cubes.

Filter Cube	Excitation Filter	Dichroic Mirror	Emission Filter
BFP (Near UV-Blue)	390-420 nm	425 nm	435-490 nm
U_FBWA (Blue)	460-495 nm	505 nm	510-550 nm
U_FGWA (Green)	530-550 nm	570 nm	575-625 nm
U_FYW (Yellow)	640-485 nm	595 nm	>600 nm

Multichannel image acquisition. Using this feature, the microscope can automatically change between different observation methods or fluorescence cubes, hence taking images with multiple channels without operator interference.

Stage navigator. The stage navigator is used to quickly scan an overview of the microscope slide, which simplifies selection of the locations of interest.

Multiple image acquisition (MIA) and stitching. This is probably the most important feature, which allows multiple fields of view to be stitched together into one larger image. As such, large sludge flocs can be visualized as a whole or, when using a higher magnification, greater detail can be depicted without compromising the shown area.

Shading correction. With this function, background shading from uneven illumination is corrected for. Shading correction is very important when stitched images need to be further processed using an image analysis tool. When the shading correction is omitted or not correctly applied, the

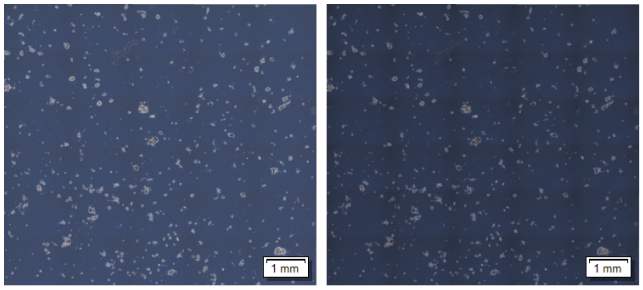

Figure 4.4: Effect of shading correction. Left: including shading correction. Right: not including shading correction. The image clearly displays the stitching grid.

stitched images clearly show a stitching grid (see Figure 4.4), which is detrimental for further image processing.

Z-stacking. A Z-stack is a collection of layers on the same X-Y position, but with different focus heights (Z). Z-stacks are mostly used in conjunction with the extended depth of focus method (see below).

Extended depth of focus. The extended depth of focus routine can be applied to a Z-stack. This routine merges the different layers into one layer, which bundles all the objects in focus from the different planes. Although some 3D-information is lost in the process, this functionality provides a good alternative for large flocs or flocs with long protruding filaments that would otherwise yield blurry images since it is nearly impossible to have the whole object in focus.

Sample preparation

Nearly all samples were analysed in suspension. A sample glass (Menzel-Gläzer) was cleaned using ethanol and wiped dry using dust-free wipes (Kimtech). Two 10 µL droplets were pipetted onto the sample glass and covered with a cover glass (Menzel-Gläzer), which was fixated using nail polish. Samples were diluted to a MLSS of 1 g/L prior to analysis using filtered supernatant, unless otherwise specified, in order to avoid osmotic shocks that could lead to floc rupture or distort the sludge's morphology.

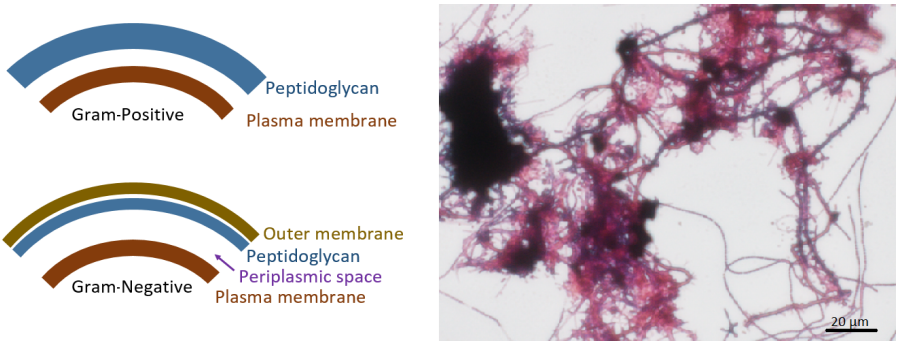

Figure 4.5: Left: Difference between Gram-positive and Gram-negative bacterial cell walls. Right: Example of Gram-stained activated sludge. Gram-negative bacteria appear red, Gram-positive bacteria appear dark violet.

Classical gram staining

Gram staining

Principle. Gram staining is a bacteriological staining technique used in conjunction with brightfield microscopy, that allows to differentiate bacterial species into two large groups: Gram-positive and Gram-negative, based on the physical properties of their cell walls. In Gram-negative bacteria, the thin peptidoglycan layer of their cell wall is surrounded by a secondary outer membrane. Gram-positive bacteria, that do not possess this outer membrane, have a thicker peptidoglycan wall instead (see Figure 4.5, left). The procedure of gram staining utilizes this difference in thickness. In both cases, the peptidoglycan layer is first colored purple by application of the crystal violet dye. Subsequently, the cells are washed with an alcohol solution. This solution dissolves the outer membrane in Gram-negative cells, and decolorizes the then exposed coloured peptidoglycan layer. In Gram-positive bacteria, part of the thicker peptidoglycan layer is also decolorized, but, when executed properly, part of it remains purple. Finally, a counterstain (safranin or fuchsine) is added, which recolorizes the bacteria red or pink. The counterstain may also be absorbed by the Gram-positive bacteria, but the darker, more pronounced violet stain predominates visually. Gram-negative bacteria will appear pink/red and Gram-postive bacteria will appear violet/dark on the final brightfield image (see Figure 4.5, right).

Method. The following solutions are used in this staining method.

The **Crystal Violet solution** is prepared as follows: 2 g Crystal Violet is added to 20 mL ethanol (95 vol%). This solution is added to 80 mL distilled water, containing 0.8 g ammonium oxalate. The mixture is stored for 24 h and filtered (Machery Nagel GF-3) prior to use.

The **Mordant Gram's Iodine solution** is prepared by grinding the iodine (1.0 g) and potassium iodide (2.0 g) in a mortar and slowly adding 300 mL of distilled water.

The **Safranin counterstain stock solution** is obtained by dissolving 2.5 g Safranin O in 100 mL ethanol (95 vol%). This stock solution is diluted 10x using distilled water to obtain the working solution.

Next, the staining procedure is discussed. On a heat-fixed smear of activated sludge a few drops of Crystal Violet are added. The Crystal Violet dissociates and penetrates through the cell wall and membrane of both Gram-positive and negative cells. After 60 seconds, the object glass containing the sludge is rinsed using tap water. Next, a few drops of Iodine solution are added. During this period, the iodide interacts with the Crystal Violet ions to create large purple complexes, trapping the colorants inside the peptidoglycan layers of both cells. After 60 seconds, rinsing is repeated. The following step is the decolorization using ethanol. With the addition of ethanol, the Gram-negative cells lose their outer lipopolysaccharide mebrane, exposing the inner peptidoglycan layer. In both cases, the purple coloured peptidoglycan layer is removed, but only partly in the case of the Gram-positive bacteria when timed correctly (20 seconds), since for these bacteria, this layer is much thicker. The timing of the decolorzation step is crucial. When the ethanol is left too long on the sample, the peptidoglycan layers of the Gram-positive bacteria are also removed, which would render the discrimination impossible. After decolorization, the Gram-positve cells remain purple, and Gram-negative cells lose their color. Finally, a Safranin solution (120 seconds, a few drops) is used as a counterstain to give the decolorized Gram-negative bacteria a pink color. The sample is rinsed again using tap water and is then ready for visualization.

4.2 Separation performance indicators

4.2.1 Sludge volume index (SVI)

The sludge volume index (SVI) is defined as the volume (in mL) occupied by 1 g of activated sludge after 30 min settling in a 1 L measuring cylinder and

is the default measurement used to assess settleability [1] [Mohlman, 1934]. A 1 L graduated cylinder is filled with sludge sample and allowed to settle for 30 minutes, after which the occupied volume by the sludge is read (SV_{30} in mL/L). Next, the SVI is calculated from the SV_{30} value by dividing this value by the sludge concentration (Equation (4.6)).

$$SVI = \frac{SV_{30}}{MLSS} \tag{4.6}$$

4.2.2 Dead-end filtration characteristics

Dead-end filtration tests, as a measure of sludge dewaterability, were carried out in the vacuum filtration set-up that is also used in the MLSS measurement, using glass fiber Macherey-Nagel GF-3 filters (0.6 μm pore size).

The measured parameters include time to filter (TTF_{25}) and weight of filtrate (WOF_{250}) measurements. Both tests were conducted in threefold, on diluted activated sludge (1 g/L, using filtered supernatant) to minimize the effect of MLSS variations on filterability.

Time to filter (TTF_{25})

The time to filter (TTF_{25}) measures the time to yield 25 mL permeate from a 50 mL starting suspension.

Weight of filtrate (WOF_{250})

Because the time to filter test causes a large uncertainty for suspensions with a bad filterability, the weight of filtrate test (WOF_{250}) was also conducted. In this test, the weight of filtrate collected after a fixed filtration duration (2 minutes) of 250 mL suspension, is measured.

4.2.3 Small-scale cross-flow filterability assessment

In order to assess the filterability of activated sludge of different origins, a small scale filtration reactor was designed and built. In comparison with common filterability assessment techniques such as the time to filter, the small filtration

[1] In retrospect, for samples with a high MLSS, the use of the diluted sludge volume index (DSVI) may have been a more appropriate measuring technique for settling assessment.

reactor performs a filtration test in a submerged cross-flow manner, as opposed to the dead-end manner of the time to filter test. This creates a testing environment which is practically more representative for the real MBR process and thus provides much more industrially relevant information. In the set-up, the flux is controlled by peristaltic pumping and the transmembrane pressure (TMP) is measured.

The original set-up consisted of a 1.6 L PMMA reactor with a small 161 cm^2 submerged membrane connected to a high accuracy pressure transducer (Omega Engineering PX409 Series) and a peristaltic pump with variable pump drive (Masterflex L/S Series). The equipment was controlled via a LABVIEW program (National Instruments) and a data acquisition interface (National Instruments USB-6008). Aeration was provided by an air diffuser glued at the bottom of the reactor. The membrane was manufactured in the lab by cutting and glueing existing standard A4 Kubota membranes) and was tested for leaks prior to usage. To accomodate standard A4 Kubota membranes and in order to limit membrane variability, a second 2 L reactor was built, omitting the need for membrane remanufacturing. In the final stage of the PhD, the addition of a second permeate line was concluded, allowing two vessels to be subjected to the same flux-step profile, while monitoring the TMP separately (see Figure 4.6 left). Alternatively, to conduct long-term filtration experiments, the existing setup could also be modified to hold a standard A4 Kubota membrane inside a 20 L reactor vessel (see Figure 4.6 right).

The software, created using the LABVIEW program, is flexible in a way that it allows the user to specify the membrane surface, the tubing used and the desired flux step profile the activated sludge sample will be subjected to. Furthermore, it is programmed as a series of *state machines*, making future program enhancements relatively easy.

4.3 Partial least squares (PLS)

In this section, the multivariate technique of partial least squares (PLS) is explained. PLS aims at reducing the dimensions of two datasets by projecting them both onto two new coordinate systems. The projections are chosen in such a manner that the resulting coordinate systems from both sets of variables have maximum correlation with each other. As such, PLS is often denoted as a multivariate regression technique.

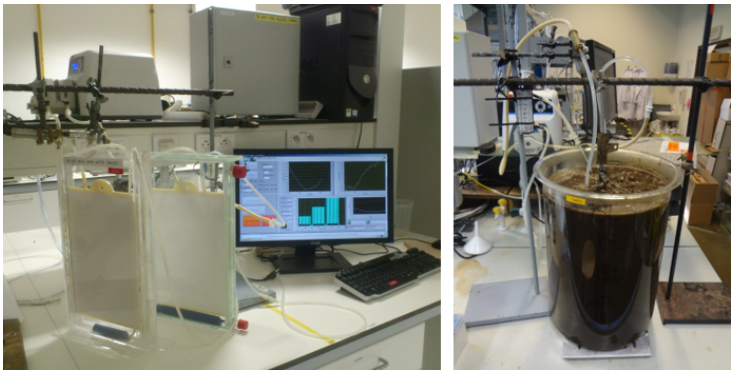

Figure 4.6: Left: small scale filtration set-up fit for cross-flow filtration using two 2 L PMMA vessels holding a standard A4 Kubota membranes. Right: a modification holding a A4 Kubota membrane inside a 20 L reactor vessel.

4.3.1 Definitions and principles

The principle and applications of PLS in activated sludge research have already been illustrated in Section 3.2.4. In this section, the theory behind the statistical technique will be clarified.

PLS is a multivariate technique, that attempts to perform two functions:

- overcome redundancy and intra-correlation in two datasets ($\mathbf{X}$ and $\mathbf{Y}$) by means of a reduction of the number of variables. This is done by projecting the variables from both datasets onto new variables (*scores*). The vectors that determine this projection are called the *loadings*.
- find the relationship between $\mathbf{X}$ and $\mathbf{Y}$. The X-variables are assumed to be independent variables, while the Y-variables are assumed dependent variables. Thus, the second aim of PLS is to extract the information in $\mathbf{X}$ that can explain the important trends in $\mathbf{Y}$. To do this, the directions of the loading-vectors are chosen in such a manner that the covariance between the new $\mathbf{X}$-scores and $\mathbf{Y}$-scores is maximized.

Figure 4.7 depicts a schematic representation of partial least squares. It is assumed that $\mathbf{X}$ is a matrix of n observations and k variables, while Y has n observations of m variables. Because the variables in $\mathbf{X}$ and $\mathbf{Y}$ probably have

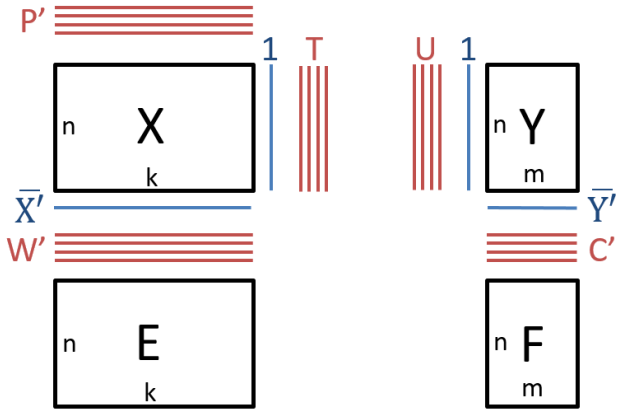

Figure 4.7: Schematic representation of partial least squares.

different ranges, both matrices are first mean-centered using z-scores[2]. The averages of both matrices are shown in $\bar{X}$ and $\bar{Y}$. The matrix **T** contains the X-scores, determined by the loadings **P**, while matrix **U** holds the Y-scores that are constructed using the loadings **C**. The **W**-matrix holds the weights for the P-vectors to maximise the covariance between **T** and **U** . Combining **W** and **P** yields the **W**$*$ matrix: $\mathbf{W}* = \mathbf{W}(\mathbf{P}'\mathbf{W})^{-1}$, which reflects how the original **X**-variables combine to give **T**. In the schematic, four PLS-components (number of dimensions in the scores) are chosen. Since a dimension-reduction inevitably leads to a loss of data, errors are introduced by projecting the matrices **X** and **Y** onto their scores **T** and **U**. These errors are denoted by **E** and **F**, respectively. The exact calculation of the scores and loadings is performed using specific algorithms such as the NIPALS algorithm. Their rationale, however, is left to the user [Abdi, 2010].

4.3.2 Loading-plots and predicted/observed plots

Figure 4.8 depicts a PLS-example adopted from Eriksson et al. [2013] and will be used to explain the interpretation of loading plots and predicted/observed plots. The example concerns the production of a polymer that is used in the plastic covering of mobile phones. The desired profile of the polymer has low

[2] z-score $= \dfrac{X - \bar{X}}{\sigma}$ with $\bar{X}$ and σ being the vectors containing the averages and standard deviations of the variables, respectively.

warp[3] and high strength. Four constituents (glas, crtp, mica and amtp) are mixed in the polymer formulation. 17 mixtures were tested and every mixture was subjected to 14 determinations of the warp and strength. The objective was to uncover which combination of the four ingredients yielded the best results.

In the figure on the left, the loadings (vectors that determine the projection of the old variables onto the new coordinate system) are shown. The X-loadings, $\mathbf{W}*$, which are the 4 components, are shown against the Y-loadings, $\mathbf{C}$, depicted by the 6 strength and 8 warp responses. When loadings are closely plotted together, they are directly correlated and when they are on opposing sides of the origin, they are inversely correlated. If an angle of 90 degrees is between two loadings, they are not related. The further a loading is situated from the origin, the higher its significance in constituting the scores from the original variables. The following observations can be visually made from the plot.

- The eight warp responses are situated together, which indicates that they are strongly correlated, while the six stress responses are less well correlated.
- The glas factor is situated on the same side of the graph as most strength and all warp responses. This indicates that increasing the glas content, also increases both warp and strength. Hence, changing the glas content will not help to achieve the desired goal.
- Lowering the amount of crtp does not influence warp to a large extent, meanwhile the strength increases strongly while doing so.
- To decrease warp, the amount of mica should be increased and the amount of amtp decreased.

A popular validation of a PLS model's performance is the use of predicted vs. observed charts (see Figure 4.8 on the right). Part of the X-Y observations is omitted in constructing the PLS model and is later used to *predict* the Y-values using the PLS model and the X-values. This prediction is plotted against the actual observation. More information on this topic is given in the next paragraphs.

4.3.3 β PLS regression coefficients

In the end, the goal of PLS is to find the relationship between the independent X-variables and the dependent Y-responses. This relationship can be expressed using the linear regression coefficients β, yielding Equation (4.7):

[3]Warp denotes the deformation of a polymer after molding.

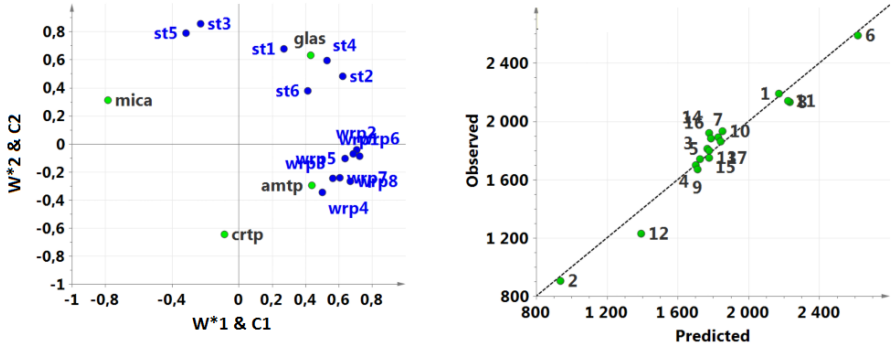

Figure 4.8: PLS-example adopted from Eriksson et al. [2013]. Polymers for mobile phones are manufactured using 4 components (k=4 X-variables): mica, crtp, glas and amtp. Each polymer is tested on performance using 8 warp (wrp) and 6 strength (st) responses (m=14 Y-variables). 17 formulations of the 4 components are tested (n=17 observations). **Left**: Loading plot of the first two principal X-loadings ($\mathbf{W}*$) versus their Y-counterpart ($\mathbf{C}$). **Right**: predicted versus observed value for the third strength respons (st3). A good agreement is found between the predicted value, by using the PLS model and the formulation as input, and the observed measurement response.

$$\mathbf{Y} = \bar{Y} + \mathbf{X} \cdot \beta + \mathbf{E} \tag{4.7}$$

From the previous definitions, β can be calculated using Equation (4.8):

$$\beta = \mathbf{W}(\mathbf{P}'\mathbf{W})^{-1} \cdot \mathbf{C}' = \mathbf{W} * \cdot \mathbf{C}' \tag{4.8}$$

These β-coefficients can be positive or negative. For each Y-variable, there exists one corresponding β-vector that depicts the regression coefficients corresponding to each X-variable, thus explaining for each X-variable its influence on the Y-variable.

4.3.4 Variable influence of projection (VIP)

In the values of the β-coefficients, the effect of each X-variable on the different Y-variables is captured. However, it can be so that although for a variable a

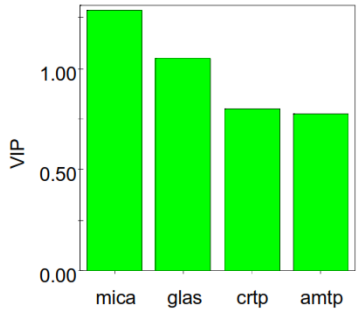

Figure 4.9: Variable influence on projection values for the 4 different polymer components [Eriksson et al., 2013]

low β-coefficient is measured, it still is of major significance to the overall fit. The variable influence of projection (VIP) is a parameter that summarizes the importance of the X-variables throughout the whole PLS-regression. Therefore, the importance is summarized in one VIP-vector for all the X-variables, which is defined as the weighted sum of squares of $\mathbf{W}*$ taking into account for each PLS-component (dimension) the importance of that dimension. More information on the calculation of the VIP is found in Wold et al. [1993].

Since the calculation involves a squared function of the X-variable PLS loadings $\mathbf{W}*$, the VIP yields a positive value for every component. VIP values higher than one denote X-variables that are important in the PLS-regression model. Figure 4.9 depicts the VIP-vector for the aforementioned example [Eriksson et al., 2013]. As can be seen in the figure, the importance of mica is the highest, while the amounts crtp and amtp do not influence the model as much. Note that each variable's VIP relates to its respective distance to the origin in Figure 4.8. Although glas is deemed the second most important variable in building the model, the variation of crtp or amtp would be of importance in the real life situation as well, since the variation of glas, although it affects two parameters, will invoke a compromise between high strength or low warp.

4.3.5 Selecting the number of PLS-components

There is no universal guideline in the selection of the number of PLS components. In general, adding more components will result in a better fit, but might not always provide an improvement in prediction due to overfitting. This effect is shown schematically in Figure 4.10. An optimal balance is found between the

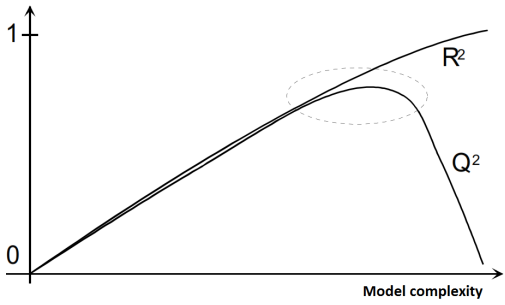

[b]

Figure 4.10: Schematical representation of the trade-off between the goodness of fit, R^2Y and the goodness of prediction, Q^2Y. The vertical axis denotes the amount of explained or predicted variation, while the horizontal axis depicts the model complexity (as a function of the number of PLS-components).

goodness of fit R^2Y and the goodness of prediction Q^2Y, which are defined using Equations (4.9) and (4.10) [Eriksson et al., 2013].

The goodness of fit (R^2Y), also called the explained variance in $\mathbf{Y}$ is expressed as follows:

$$R^2Y = 1 - \frac{RSS}{SS_Y} \tag{4.9}$$

with RSS the residual sum of squares (sum of squares of the residuals matrix $\mathbf{E}$ from Equation (4.7)) and SS_Y the total variance in $\mathbf{Y}$ after mean centering.

The goodness of prediction (Q^2Y), also called the predicted variance in $\mathbf{Y}$ is calculated as follows:

$$Q^2Y = 1 - \frac{PRESS}{SS_Y} \tag{4.10}$$

with $PRESS$ the predictive residual sum of squares.

In this study, the $PRESS$ value is calculated using **crossvalidation**. In crossvalidation, a fraction of the data, called the validation data, (in our case, 10% of the data) is left out. The PLS model is constructed using the other data. Next, the validation data is used to predict the values for $\mathbf{Y}$, giving $\hat{\mathbf{Y}}$. The procedure is repeated by moving the validation-window, until every Y-value has been predicted once. Next, the overall procedure is repeated several times (in our case 1000x), with randomized sequences of the data. Now that every Y-value has been predicted several times, the predictions are averaged, giving

$\hat{\hat{\mathbf{Y}}}$. The $PRESS$ can then be calculated as: $PRESS = \sum_{i=1}^{n} (Y_i - \hat{\hat{Y}}_i)^2$. In large datasets, separate training and validation sets are preferred over crossvalidation.

From the $PRESS$-value, the number of PLS-components can be selected directly. Generally, when a PLS-fit is possible, the $PRESS$-curve will decrease first and increase after several components due to the overfitting. Selecting a number of PLS-components for which this initial decrease is significant and for which adding an additional component does not provide much more improvement usually results in a good number of PLS-components [Abdi, 2010].

Part I

Monitoring bioflocculation through microscopy and image analysis

Chapter 5

Improvements on the activated sludge image analysis program (ASIAP)

In this chapter, adaptations and improvements to the phase contrast image analysis program for monitoring activated sludge morphology are discussed.

5.1 Introduction

From Chapter 3, it is clear that microscopic monitoring of bioflocculation in activated sludge has become an indispensible tool for problem identification in sludge separation systems, like sedimentation in conventional activated sludge systems and membrane filtration in membrane bioreactors.

Within the former Bio- and Chemical Process Technology and Control division of the Chemical Engineering Department at the KU Leuven, an objective and time efficient automated image analysis procedure was developed several years ago. This so-called ACTIAS (ACTivated sludge Image Analysis System) performed well after a major revision by The Anh Cao in 2011-2013 [Cao, 2016]. This revision included several improvements on the segmentation and classification routines, dealing with images that contained a lot of small fragments, images with dark floc regions or with bright filaments and significantly reduced the complexity of the recognition routine and computation time.

However, with the acquisition of a new, fully motorized Olympus IX83 inverted microscope in 2013, the existing image analysis software required a complete overhaul to deal with the challenges of a new file format, images of variable and larger size, higher resolutions and multi-layered pictures. Since this overhaul changed more than half of the former program's code, it was baptised with a new name. The Activated Sludge Image Analysis Program (ASIAP) was born.

5.2 A brief introduction to the former ACTIAS program

In this section, an short introduction will be provided on the operating mechanisms of the former image analysis program ACTIAS. As mentioned before, the images analysed by ACTIAS were obtained using a different microscope set-up as the ones from most of this study. Activated sludge images were obtained using a light microscope (Olympus BX51) with phase contrast illumination at the maginifcation of 10x10 times. The microscope was equipped with a 3CCD color video camera (Sony DXC-950P), connected to a computer. Activated sludge images were saved in JPG format (768x576 pixels) using Zeiss KS100.3 acquisiution software.

ACTIAS, which is embedded in the MATLAB *Image Processing Toolbox 4.2* (The Mathworks Inc., Natick, MA) uses a consecutive segmentation and recognition algorithm and classifies activated sludge objects into three classes: flocs, filaments and fragments. For each class, a set of morphological properties is calculated, such as the mean floc size and diameter, roundness, length of filament and fragment area.

5.2.1 Segmentation in ACTIAS

Segmentation is the first step of the ACTIAS image analysis routine. The original image is converted into a black and white image, in which the objects (flocs, filaments and fragments) are separated from the background. Figure 5.1 depicts an image and the corresponding histogram of a typical activated sludge sample. A histogram is a graph in which the intensities of the image's pixels (0-255) are plotted against their number of occurrences. As can be seen from the image, the filaments are typically darker than the background, while the flocs are brighter. In the following sections, it is explained how this image is converted into a black and white segmented image. This is performed using a top-hat transformation, after which flocs and filaments are put in the same intensity-range, followed by a contrast-enhancing exponential transformation

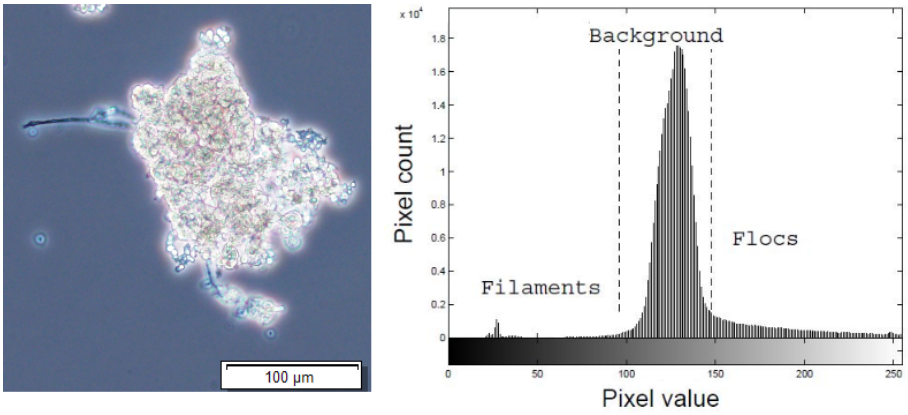

Figure 5.1: A typical activated sludge floc (left) and histogram (right) of an activated sludge sample visualized using phase contrast microscopy. Filaments are typically darker than the background, while flocs are brighter.

and eventually a single-thresholding, separating objects from the background. This procedure is repeated on both the red and blue constituent of the color images taken by the Olympus BX51 microscope. Before delving into these topics, a few important morphological operations are explained.

Important morphological operations

In taking the **complement** of an image, every pixel's value is replaced by 255 minus its original value. Black, therefore, becomes white and vice versa.

Figure 5.2 is used to explain four basic binary morphological operations: dilation, erosion, opening and closing.

A **structuring element** (SE) (Figure 5.2 (a)) is defined. This structuring element can be interpreted as a small moving window of interest. The structuring element's origin (white dot in the figure) determines its position in the original image (Figure 5.2 (b)), while the other pixels of the structuring element define its range. The larger the structuring element, the more impactfull the discussed morphological operations are on the final image will be. Structuring elements of one pixel do not yield any difference. For simplicity in calculation, square structuring elements are usually used, but other shapes, like circular or rectangular structuring elements exist.

Binary **dilation** (Figure 5.2 (c)) is a morphological operation which increases

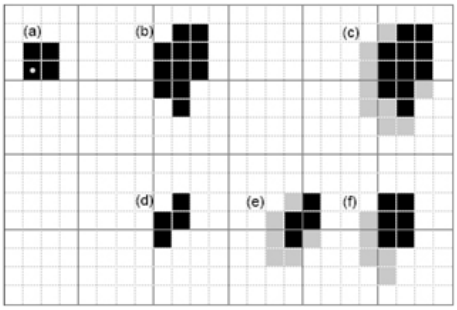

Figure 5.2: Morphological operations. **(a)** Structuring element with origin in the bottom left corner; **(b)** Original image; **(c)** Dilation of object b by structuring element a; **(d)** Erosion of object b by structuring element a; **(e)** Opening of object b by structuring element a; **(f)** Closing of object b by structuring element a.

objects in size. The structuring element's origin is placed in all pixels of the source image. If any of the pixel locations of the structuring element correspond to an object (black) pixel, the origin pixel will be black in the resulting dilated image. In grayscale dilation, the pixel value of the origin in the structuring element is replaced by the highest value in the structuring element's range.

Binary **erosion** (Figure 5.2 (d)) is similar to dilation, and is in fact a dilation of the complement set. Erosion decreases objects in size. The structuring element's origin is again placed in all pixels of the source image. Only when all pixels of the structuring element are object (black) pixels, the origin pixels will remain black. Otherwise, it is transformed in a background pixel (white) instead. In grayscale erosion, the pixel value of the origin in the structuring element is replaced by the lowest value in the structuring element's range.

Opening (binary or grayscale) is a combination of erosion followed by dilation. The result is shown in Figure 5.2 (e). Dilating Figure 5.2 (d) therefore, yields the same result.

Closing (binary or grayscale) is a combination of dilation followed by erosion. The result is shown in Figure 5.2 (f). Eroding Figure 5.2 (c) therefore, yields the same result.

Top-hat transformation

As mentioned before, using phase contrast illumination, flocs and filaments are visualised in different intensity regions of the histogram, being separated by

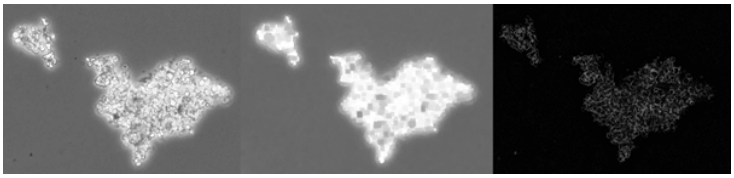

Figure 5.3: Top-hat transformation: Left: original image; Middle: closed version (SE = 9x9 pixels); Right: absolute difference between the left and middle picture.

the large background peak. The first segmentation step involves the use of a top-hat transformation, which is suited to convert the original image in such a manner that both flocs and filaments are found in the same intensity region [Glasbey and Horgan, 1995]. A top-hat transformation consists of subtracting the closed grayscale image from the original image, emphasizing narrow dark features.

Figure 5.3 depicts an overview of all steps involved during the top-hat transformation. As described above, the grayscale closing enlarges and intensifies white zones. Flocs, as a mixture of pixels with bright or regular intensities will be significantly brightened, whereas the background, that is much more uniform, will be affected in a limited way. It is thus necessary for a floc to consist of black and white scatters, since the eventual result in the top-hat transformed image is caused by this difference. If a floc contains a very dark zone, in which there are very few white pixels present, this black zone is quasi unaffected by the closing procedure and will yield similar intensity values as the background. Therefore, these zones require special attention.

Narrow black objects, such as filaments, are removed by the closing procedure because of the typical phase contrast glow around them. When subtracting the closed image from the original one, only negative values are obtained, since a closing operation can only increase pixel values. For objects that are significantly altered, such as bright flocs or dark filaments, this difference is large, whereas for the background, which is not significantly changed by to the closing, this difference is very small. This is illustrated on the right in Figure 5.3, where the absolute value of this difference is plotted.

Exponential rescaling

To convert the negative values from the top-hat transformation and to the enhance contrast between objects (flocs and filaments) and the background, an exponential rescaling is used. The transformation function is displayed in Equation (5.1). The parameter Q that is introduced here, determines the curvature that yields the contrast enhancement. Figure 5.4 illustrates the exponential rescaling.

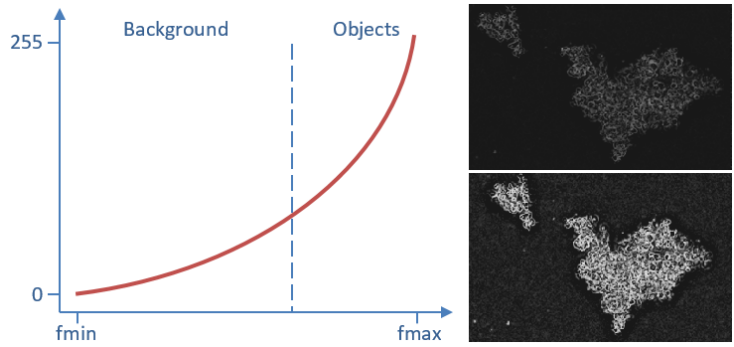

Figure 5.4: Graphical representation of exponential transformation curve (left) and its contrast-enhancing effect (right).

$$f_{ij,r} = \frac{255}{exp(Q(f_{max,s} - f_{min,s})) - 1}[exp(Q(f_{ij,s} - f_{min,s})) - 1] \qquad (5.1)$$

$f_{ij,r}$: the pixel value at position (i,j) in the re-scaled image,

$f_{ij,s}$: the pixel value at position (i,j) in the subtracted image,

$f_{max,s}$: the highest pixel value in the subtracted image,

$f_{min,s}$: the lowest pixel value in the subtracted image.

Thresholding using the intermeans algorithm

Now that the contrast between flocs and filaments on the one hand, and the background on the other hand has been increased, a single threshold can separate the objects from the background. To this end, the intermeans algorithm has been shown to be the most suitable for thresholding grayscale activated sludge images [Jenné et al., 2002].

The intermeans algorithm uses the histogram of the exponentially transformed images to iteratively find an appropriate threshold t. The histogram is represented as a number of pixels h_0, h_1, ..., h_N where h_k denotes the number of pixels with the intensity value k and N is the maximum pixel value (usually 255). As a first guess for the threshold, half of the median of all pixel values is used. This value divides the histogram into two parts, from which the mean pixel value (μ) in each part is calculated. For the left and right hand side of the threshold value this translates into Equation (5.2) and (5.3), respectively.

$$\mu_1 = \frac{\sum_{k=0}^{t} k h_k}{\sum_{k=0}^{t} h_k} \tag{5.2}$$

$$\mu_2 = \frac{\sum_{k=t+1}^{N} k h_k}{\sum_{k=t+1}^{N} h_k} \tag{5.3}$$

Next, a new threshold is calculated that lies in the middle of the two mean values μ_1 and μ_2, hence the name *intermeans*, using Equation (5.4). This new threshold redefines both parts of the histogram, such that both mean values will need to be recalculated. This iterative procedure is repeated until the threshold value t ceases to change. The threshold is calculated as a normalized value (between 0 and 1). Multiplying this threshold with the maximum intensity (255) yields the actually used threshold.

$$t_{new} = \frac{\mu_1 + \mu_2}{2} \tag{5.4}$$

As described before, when the intensity of the floc parts is too uniform, as is the case when flocs contain very dark regions, problems with the top-hat transformation occur. The effect of these problems is that part of the flocs will reside in the background peak of the final intensity histogram, which will cause the creation of artificial holes in the segmented image. To overcome this problem, a solution was designed that consists of two parts: the addition of the halos to the segmented image, and the classification of holes in flocs into *real* or *artificial* holes.

First, the average intensity of the holes in the original image is tested against the background peak. If this average intensity is situated in the background peak in the intensity histogram, the hole is classified as a *real hole*. In the other case, when the average intensity of the hole is lower than the background peak (see Figure 5.5), the hole is considered as an *artificial hole* and is filled up and added to the objects. However, sometimes, artificial holes can occur on the sides of flocs. E.g., when a dark region encompasses part of the floc perimeter,

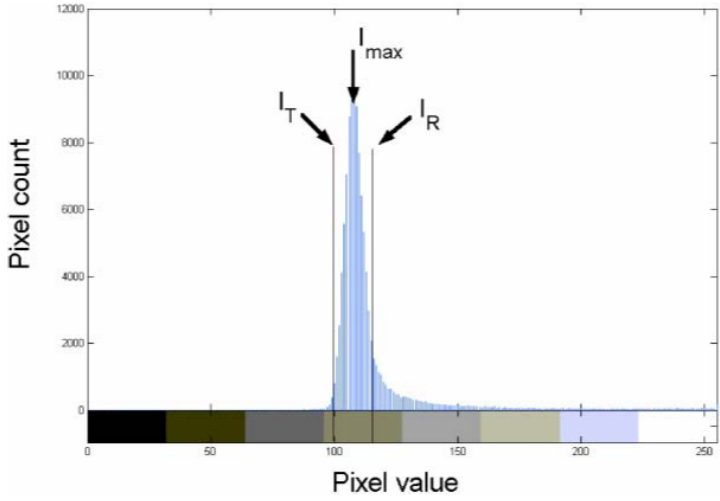

Figure 5.5: Background peak in original phase contrast histogram. The background peak is determined by all pixels in (I_T, I_R). I_T is determined as the pixel value left of the maximum for which the number of pixels drops below an arbitrary value T (in this dissertation, a value of T = 2978 is used). I_R is the pixel value right of the maximum I_{max} for which the number of pixels drops below $0.15 \cdot I_{max}$

.

this procedure would not work. To overcome this problem, the halos around the sludge flocs, which are characteristic for phase-contrast microscopy, are added to the objects in the segmented image. These halos are all pixels with an intensity higher than 240. The downside of this is that all objects are slightly enlarged. However, adding the halos ensures all holes are situated within the floc borders. A final note: to correct for the occurrence of halos on the edges of the holes, a correction factor is used on the average intensity of the holes. Experimentally, this correction factor was optimized to be 0.93.

After segmentation, the image is converted into a binary image, in which the objects are black (intensity 0) on a white background (intensity 1). In the next section, the segmented objects are divided into three classes: flocs, filaments and fragments.

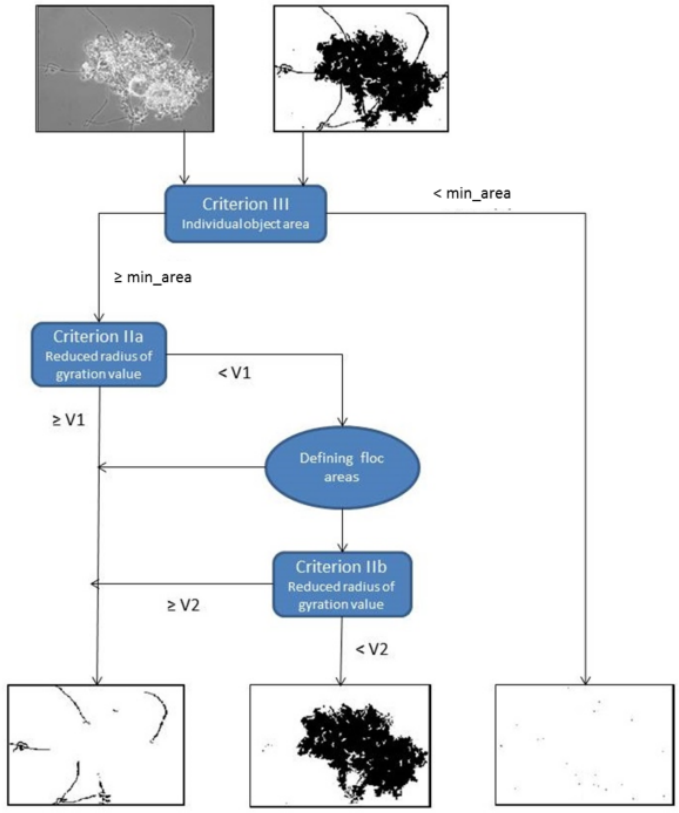

Figure 5.6: Recognition procedure used in ACTIAS.

5.2.2 Recognition in ACTIAS

After the conversion of the grayscale images into a binary file containing all relevant objects, a distinction is made between flocs, filaments and fragments. Figure 5.6 depicts this recognition procedure.

First, small objects and debris are separated from the larger flocs and filaments. These small constituents, denoted *fragments*, comply with the size criterion from Equation (5.5). In this study, fragments are classified as objects with an equivalent diameter smaller than 5 µm, which corresponds[1] to a *PixelArea* smaller than 8. Since the images from the BX51 microscope have a resolution of

[1]Using the Olympus BX51 microscope with a magnification of 10x10 the side of one pixel corresponds to 1.645 µm.

768x576 pixels, the value of OPP is calibrated to be 55300. This value may of course be adjusted in accordance with the definition of a *fragment* and depends on the microscope configuration used.

$$PixelArea < \frac{I_x \cdot I_y}{OPP} \tag{5.5}$$

$PixelArea$**:** the number of pixels from an object,

I_x**:** the size of the image in the x-direction in pixels,

I_y**:** the size of the image in the y-direction in pixels,

OPP**:** size parameter (user defined).

Next, the reduced radios of gyration R_g, which is a measure of the elongation of objects, is used to discriminate between filaments and flocs. It is defined as the division of the average distance between the object pixels and its centroid, by half of the equivalent diameter (D_{eq}, Equation (5.6a, right)). The radius of gyration R_g is calculated using Equation (5.6a, left). In the definition of this equation, (x_i, y_i) represents the position of a pixel i of an object of N pixels.

$$R_g = \sqrt{\frac{M_2x + M_2y}{D_{eq}/2}} \qquad D_{eq} = 2\sqrt{\frac{area}{\pi}} \tag{5.6a}$$

$$M_2x = \frac{\sum(x_i - x_g)^2}{N} \qquad M_2y = \frac{\sum(y_i - y_g)^2}{N} \tag{5.6b}$$

$$x_g = \frac{\sum(x_i)}{N} \qquad y_g = \frac{\sum(y_i)}{N} \tag{5.6c}$$

A circle has an R_g of $\sqrt{2}/2$ while a more elongated object has a larger value, which makes that $\sqrt{2}/2 \leq R_g \leq \infty$. Therefore, filaments tend to have longer radii of gyration than flocs. To this end, a critical value, *V1*, is defined as a first classification between flocs and filaments (see Figure 5.6). However, this criterion would only detect free filaments. Most filaments, however, are bound to sludge flocs. To separate these filaments, the morphological operation of *opening* (see Section 5.2.1) is used. Opening removes pixels from the borders of objects, and therefore,when they are slim enough, removes the filaments. The difference before and after opening yields the attached filaments, which are classified using the same criterion, but with a different critical value (*V2* in Figure 5.6).

5.2.3 Data extraction in ACTIAS

The final step in the image analysis procedure is the quantification of morphological characteristics of the activated sludge by means of data extraction from the distinguished flocs, filaments and fragments obtained during recognition. This data can be divided in a part that reflects the distribution of the different classes among the activated sludge, and a part that morphologically describes the different classes. Both parts are presented in Tables 5.1 and 5.2, respectively.

Table 5.1: Extracted information by ACTIAS: distribution parameters.

Surface	Number
Total floc surface	Number of flocs per image
Total filament length	Number of filaments per image
Total fragment surface	Number of fragments per image
Surface proportion filaments to flocs	Number proportion filaments to flocs
Surface proportion fragments to flocs	Number proportion fragments to flocs
Global openness of floc structure	

Table 5.2: Extracted information by ACTIAS: morphology parameters per object class.

Flocs		
Length	Width	Surface
Perimeter	Equivalent diameter	Roundness
Form factor	Convexity	Solidity
Compactness	Aspect ratio	
Reduced radius of gyration		
Fractal dimension (box counting algorithm)		
Filaments		
Length	Width	Surface
Perimeter		
Fragments		
Length	Width	Surface
Perimeter	Equivalent diameter	

5.3 Improvements and adaptations to ASIAP

Because the acquisition of the new fully automated Olympus IX83 entailed several new functionalities, the existing image analysis software required some adaptation. In this section, these adaptations will be discussed.

5.3.1 Format compatibility

The software from the Olympus IX83, CellSens, uses the *.vsi* format as the default file format for image storage. This versatile file format has the advantage of retaining all relevant image properties and storing the image without any data loss. However, the Olympus file format was not yet recognized by MATLAB. Therefore, the *BioFormats* plugin, developed by The Open Microscopy Environment (www.openmicroscopy.org) was used to overcome this problem. After implementation and some minor code adjustments, several hundreds of images of different activated sludge origins, stored as .vsi were converted into .tif files, which already could be analysed using ACTIAS, and both sets of images were analysed using the new version of ASIAP. Both results did not yield any difference in results. Therefore, it was concluded that with the implementation of the plugin, the .vsi format could be successfully used.

The main advantages of adopting the .vsi file format are the following.

- There is no need to convert the images into another file format, which saves time.
- All microscope information is stored, regarding the used objective, exposure time, pixel size, ... The files can be used to copy their settings for the next acquisition.
- The flexible .vsi format allows the storage of multiple acquisition layers (e.g., a phase contrast and a fluorescence layer) in one single image.

5.3.2 Grayscale imaging

Early versions of ACTIAS based their recognition routines to distinguish flocs and filaments not only on shape criteria, but also on differences in brightness in both the red and blue color consitituents [Jenné et al., 2002]. However, these procedures have been proven to give rise to misrecognitions and have been removed by The Anh Cao in his complete review of the program. In the first version of ASIAP used in this study, both the red and blue channels

were still analysed during segmentation, but the followed procedure was nearly identical for both colors. Moreover, as will be described in Section 6.2.1, the use of phase contrast in combination with epi-fluorescence requires the phase contrast images to be taken in grayscale. Two extra benefits from the use of grayscale images are the reduction of computation time and file storage space. Therefore, the existing ASIAP software was modified such that both grayscale and color images could be analysed and were treated in a similar manner. Color images are first converted to their grayscale equivalents and then analysed using the same procedure. This modification was also tested by several hundreds of images, and did not yield significant differences.

5.3.3 Improvements on segmentation

Segmentation problem caused by erroneous thresholding

With the conversion of ACTIAS to ASIAP to adapt the image analysis to the new microscope equipment, software and file format, a severe problem in the segmentation was discovered. The problem is illustrated in Figure 5.7. The left figure shows the original activated sludge image, while the middle figure illustrates the segmentation problem. Clearly, this is not a normal outcome where fragments, flocs and filaments can be distinguised easily. Moreover, there is a clear grid visible, which gave rise to the question whether the erroneous segmentation could be attributed to the multiple image acquisition (MIA) and stitching routine (see Section 4.1.6). Moreover, the problem never occurred in single-field-of-view images, but only manifested when MIA and stitching was used.

The manifestation of the segmentation problem originates from the intermeans thresholding algorithm, that calculates a too high threshold. When the threshold is too high, parts of the background peak (that lies at the bright end of the histogram after exponential rescaling) are segmented as very small objects. This theory was tested by manually imposing a lower threshold, which is shown and affirmed in Figure 5.7 on the right, where the numerous falsely identified objects have disappeared after manually reducing the normalized threshold to 0.6. Figure 5.8 depicts the calculated thresholds of 32 analyzed images, half of which were incorrectly segmented. From the graph, it is clear that the correctly segmented images all have a normalized threshold around 0.62, while the wrongly segmented images have a much higher value. In the next paragraphs, an explanation and solution is sought for this problem.

It was already mentioned before that the segmentation problem only occurred when MIA and stitching were used. Therefore, the combined effects of the

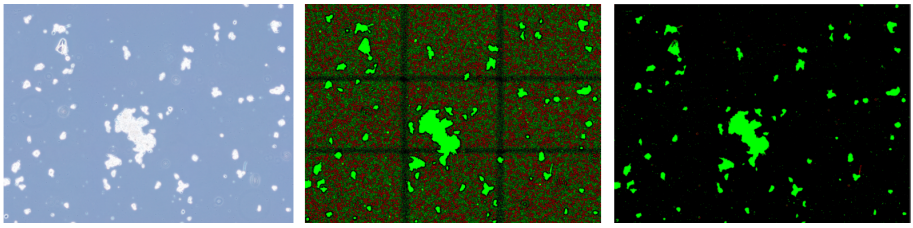

Figure 5.7: Segmentation problems in ASIAP caused by a too high threshold. Left: original image. Middle: wrongly segmented image. The grid that is shown in this image originates from the stitching of multiple fields of view. Right: correctly segmented image using a manually normalized threshold of 0.6.

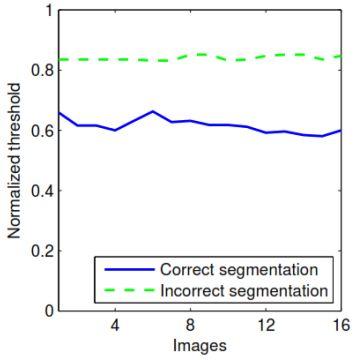

Figure 5.8: Comparison of normalized thresholds for 16 correctly segmented and 16 incorrectly segmented images. The results clearly show that the incorrect segmentation is caused by a too high normalized threshold.

stitching and the subsequent segmentation were studied. When stitching images, a partial overlap between different fields of view is used to combine them into one larger image. This principle is shown in Figure 5.9. The larger this overlap, the easier the stitching but of course the more fields of view it requires to capture a whole image. Now, importantly, in the overlap region, the pixel values from both images, are averaged, which results in a relatively higher uniformity in intensity of background pixels in those regions.

In the first part of the segmentation routine, a top-hat transformation is used to separate the background from the flocs and filaments (see Section 5.2.1). This top-hat transformation is mostly based on differences in **intensity-variation** between objects (bright/dark zones in flocs, narrow dark filaments surrounded by a bright halo) and background (not much variation). As mentioned in the

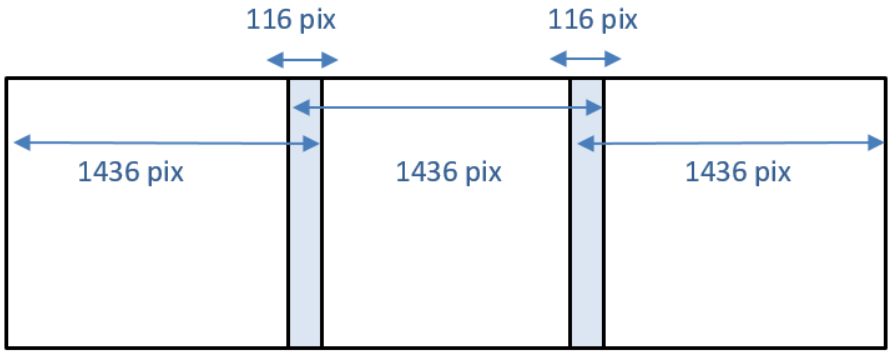

Figure 5.9: Schematic representation of multiple image acquisition (MIA) and stitching, combining three fields of view into one larger image.

previous paragraph, the background of the overlap regions, in which the pixel values are much more uniform, contains less variation than the background from the rest of the image and will, according to this hypothesis, be segmented more properly. The verification of this hypothesis can be seen in the wrongly segmented image in the middle of Figure 5.7, where clearly, the occurrence of wrongly segmented small objects is much lower in the grid stemming from the stitching. The overall result from the stitching is the average increase of the background peak's intensity in the image histogram after top-hat transformation and exponential rescaling.

In the previous image analysis program, ACTIAS, the background was less uniformly distributed. Both versions use the intermeans algorithm to define a threshold that separates the background from the objects after top-hat transformation and exponential rescaling (see Section 5.2.1). However, since on average the background peak in the new images has been even further emphasized due to reasons mentioned in the previous paragraphs, this intermeans algorithm calculates a too high threshold for the segmentation of the new images.

Improved thresholding

To overcome the thresholding problem, two solutions are provided. Whereas the top-hat transformation emphasizes the background, the first solution aims at **enhancing the objects**. The second solution provides two **alternatives for intermeans**, by means of Otsu's thresholding algorithm or by manually choosing the threshold.

To enhance the objects, their contrast with the background needs to be increased. Potentially, changes could be made to the size of the structuring element of the top-hat transformation or the Q-value of the exponential transformation. However, these adaptations did not yield the desired improvements, thus a new approach was sought. To this end, after the exponential rescaling, the image was subjected to another set of morphological operations to improve the contrast between the objects and their surroundings. The first step was the division of all pixels into two sets of pixels, by using half of the original threshold as the separating value. All pixels on the left of this lowered threshold in the histogram are now definitely objects, while the right half contains the background and some part of the objects, which will be referred to as the *background half* for brevity. The objects are put on black background, while the background half is put on a white background, as depicted in Figure 5.10.

Next, the left half, containing the objects, is closed, while the background half is opened. As discussed earlier, closing increases and intensifies white zones while opening intensifies black zones. Objects on both halves are, therefore, increased in contrast. Subsequently, both halves are merged by resubstituting the zeros from the floc matrix (left), with their respective values in the background matrix (right).

After increasing the contrast between the objects and background, the image needs to be thresholded. In most cases, the intermeans algorithm will now provide a proper result. However, to anticipate on future cases where intermeans-thresholding might fail, two additional thresholding options are added to the code and can optionally be selected by the user as a replacement.

The first alternative is the use of **Otsu's method** for thresholding. Otsu's method, like intermeans, is a histogram-based method, which determines the threshold such that the intravariance of both groups in the histogram, determined by this threshold, is minimized [Lin and Yu, 2011]. Otsu's method has already proven its use in other applications for activated sludge image analysis ([Amaral and Ferreira, 2005; Mesquita et al., 2010]).

The intravariance (σ_w^2) of two groups is defined by Equation (5.7).

$$\sigma_w^2 = w_b\sigma_b^2 + w_o\sigma_o^2 \tag{5.7}$$

The weights w_b and w_o are the relative surfaces of the background and objects in the histogram, respectively, and their variances are σ_b^2 and σ_o^2.

The second alternative is the use of **manual thresholding**. In this case, no algorithm will be used, but rather a value of the normalized threshold provided by the user. This method is mostly suited for using during longterm experiments, when the sludge's brightness and intensity distribution remain

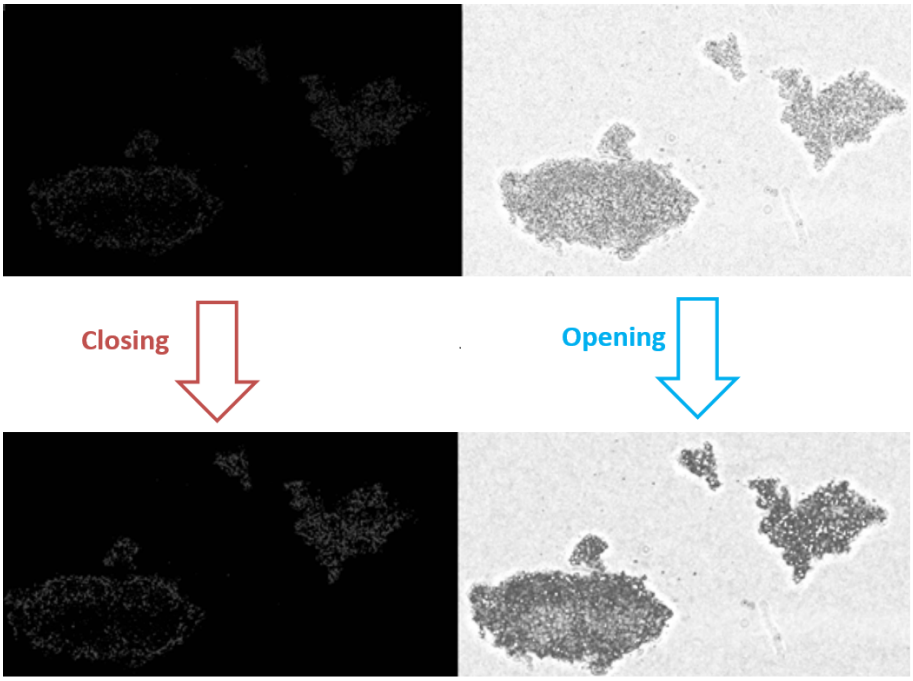

Figure 5.10: Enhancement of objects during segmentation. Left: objects on black background are closed (enhancement of white pixels). Right: background and parts of flocs on a white background are opened (enhancement of black pixels).

unchanged and when the same microscope settings can be guaranteed. When the chosen threshold is too high, the problem that has been discussed will occur. When it is too low, parts of the flocs are not recognized, resulting in artificial holes (see Figure 5.11).

5.3.4 Improvements on the recognition of filaments

In this section, two improvements to the recognition of filaments are discussed. First, a new recognition criterion is presented, which replaces the first round of filament-floc classification based on the reduced radius of gyration. Then, an issue in which filaments are broken up when they are not completely in focus, is solved.

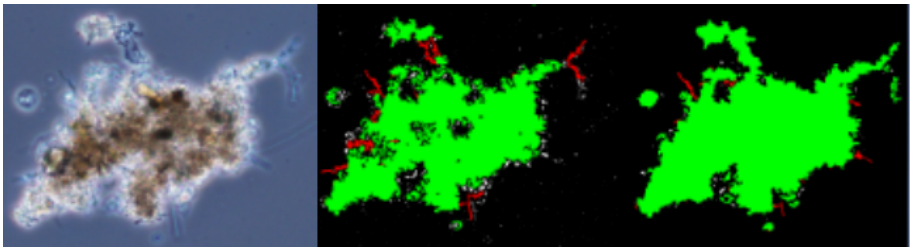

Figure 5.11: Left: original image. Middle: too low manual threshold causing artificial holes. Right: improved thresholding.

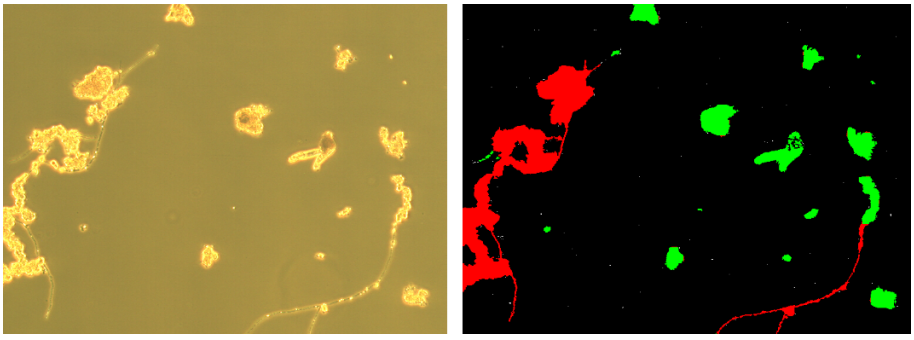

Figure 5.12: Left: an image taken using the BX51 microscope, showing two structures that are made of both filaments and flocs. Right: the ACTIAS output.

Ellipse-coverage criterion

In ACTIAS, the recognition between flocs and filaments is initiated by a primary classification based on the reduced radius of gyration (see Section 5.2.1), which is a measure for the elongation of objects. However, processing mistakes occur when a structure consists of multiple filaments and flocs, as shown in Figure 5.12.

To improve the first classification, a solution is found by replacing the reduced radius of gyration criterion by a new criterion relying on the ellipse-coverage. It is important in this classification that objects containing flocs are not classified as filaments, since in the recognition scheme, once an object is classified as a filament, it will remain a filament (see Section 5.2.2 and Figure 5.6). However, there is a second round of classification after the opening of flocs. In this round, the filaments that are attached to the flocs (as is the case in the misclassified objects that this modification tries to resolve), are detached and the classification

between flocs and filaments is repeated.

From each object, using the *regionprops* functionality in MATLAB, the area, minor axis length (MiAL) and major axis length (MaAL) are measured. Using the axis lengths, an ellipse is computed which can be superimposed on the original object. The area of this ellipse is found by using Equation (5.8). The ellipse coverage (EC) then defines the ratio between the area of the object and the area of the superimposed ellipse, as shown in Equation (5.9).

$$Area_{ellipse} = \frac{1}{2} \cdot \pi \cdot \frac{MaAL}{2} \cdot \frac{MiAL}{2} \tag{5.8}$$

$$EC_{object} = 100 \cdot \frac{Area_{object}}{Area_{ellipse}} \tag{5.9}$$

Implementing a single value threshold for EC_{crit} (calibrated at a value of 21) already significantly improves the primary classification. However, for some large elongated objects, it still suffers from some misrecognition. Therefore, a variable threshold is adopted, which decreases when the area of an object is larger than a certain size limit. Testing for a multitude of previously wrongly classified objects yielded that 10,000 pixels is a sufficiently high number for the critical area and that the EC for the large elongated objects yields good results for an EC threshold of 15. The criterion is summarized in Equation (5.10).

$$EC_{crit} = \begin{cases} 15, & Area_{object} > 10^4 \\ 21, & Area_{object} \leq 10^4 \end{cases} \quad EC_{object} < EC_{crit} \rightarrow Filament \tag{5.10}$$

Figure 5.13 illustrates the improved primary classification based on the ellipse-criterion. The use of this criterion led to the decrease of faulty classified filaments by 80% without significantly increasing the computation time.

Reconnecting broken filaments

During the image acquisition only a limited layer of depth can be visualized in focus. The thickness of this layer is strongly affected by the used objective and magnification, with thinner layers when the used magnification is increased. Activated sludge flocs, however, are three-dimensional structures, which makes it difficult to visualize their complete morphology in focus. In the subsequent image analysis, especially the filaments suffer from these shortcomings. When

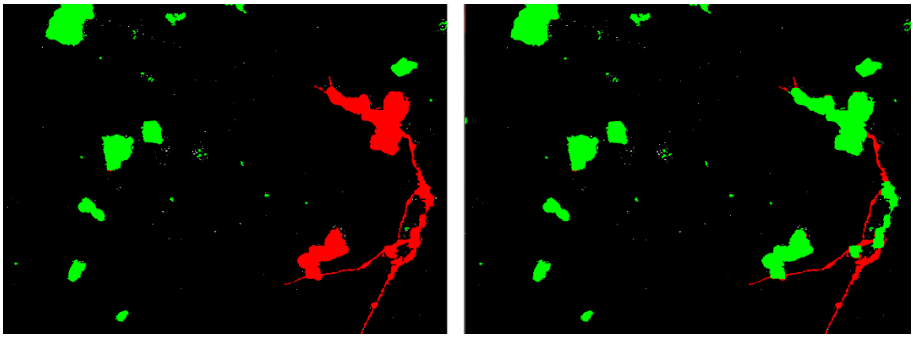

Figure 5.13: Improved floc/filament classification based on the ellipse-criterion. Left: single ellipse threshold, Right: variable ellipse threshold.

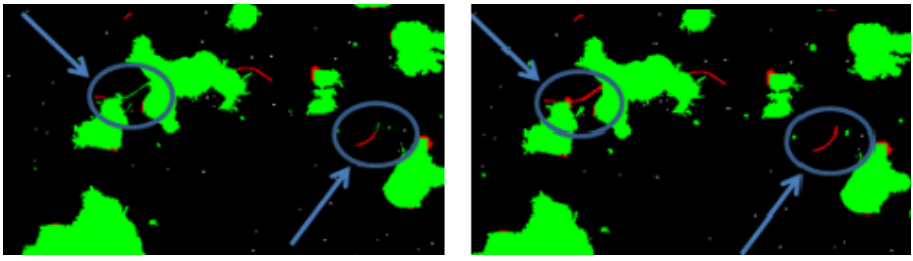

Figure 5.14: Left: Example of broken filaments after segmentation of which parts are wrongly recognized. Right: Results after reconnection.

part of a filament is not in focus on the image, it happens that during the segmentation this part dissolves in the background, effectively breaking up the filament. An example of this problem is depicted in Figure 5.14 on the left. The broken filament parts subsequently are processed through the fragment and filament filters (Figure 5.6) and may not even be recognized properly.

To overcome this problem, dilation can be used. In Section 5.2.1, it was already explained that dilation increases objects in size by systematically adding pixels to the object around its border. As such, filament pieces that are separated by only a few pixels, can be made whole again. However, the addition of pixels around flocs also results in a loss of detail and increases the size of every object. To avoid having to make this compromise, it was opted to implement selective dilation.

Selective dilation is the dilation of only a portion of the objects. In this case, only the smallest objects will be dilated. All objects are first separated according to their size. Subsequently, objects with a number of pixels smaller than a given

dilation limit F, will be processed. For the dilation, several structuring elements were tested. For all activated sludge samples tested, a structuring element of 4x4 yielded good results.

Next, the size of the dilation limit F is determined. Ideally, this limit remains low, such that the surface roughness and size of most objects would remain unaltered. The size of F is determined as a factor of the fragment[2] threshold *MinOpp* (see Section 5.3.5), in order to allow for future changes in magnification without having to change the threshold. Several dilation limits are tested: 3xMinOpp, 2.5xMinOpp, 2xMinOpp and 1.75xMinOpp. After analysing the results, it was concluded that a dilation limit of 2xMinOpp was sufficient. Lowering the value further would leave some filaments fragmented, whereas increasing it more resulted in a loss of detail in surface roughness. Figure 5.14 on the right, shows the results of the reconnecting feature.

Moreover, the dilation operation increases the size of the objects. The effect of this increase is shown in Table 5.3. Since the fragments are all increased in size, as they fall below the dilation limit, their classification criterion needs to be adjusted as well. This can be achieved by the use of a correction factor ($CF_{dilation}$). E.g., using the old BX51 microscope, fragments had a maximum number of pixels of 8, which, after dilation doubles to 16 (see Table 5.3). Therefore, the correction factor for classification of fragments should be 2. For the new IX83 microscope, the resolution increases, which leads to a smaller pixel size, and thus a higher number of 101 pixels for a fragment of 5 µm. After dilation, this fragment's number of pixels increases to 130, which leads to a correction factor of 1.29. More on this subject will be explained in the next section, that deals with improvements on the recognition of fragments.

5.3.5 Improvements on the recognition of fragments: absolute size criterion

During this study, the term *fragments* is used to define small activated sludge particles, debris and microcolonies that are visible using light microscopy and that have a maximum equivalent diameter of 5 µm.

In ACTIAS, fragments were classified according to a criterion based on the OPP-parameter that linked their size to the image size, which was always the same (768x576 pixels). However, with the acquisition of the new Olympus IX83 microscope and the stitching utility, images of varying sizes that are stitched

[2]In this study, the fragment threshold is chosen to be 5 µm, which corresponds to 8 pixels for images taken using the BX51 microscope, or 101 pixels for the IX83 microscope, both using the 10x objective, but with a different resolution of 1 pixel = 1.645 µm and 1 pixel = 0.440 µm, respectively.

Table 5.3: The effect of the dilation operation on the size of an object. It is clear that the relative size increase is higher for small objects. In general the correction factor decreases as the area before dilation increases. Differences from this trend are due to the variations in object shapes.

Area before dilation (pixels)	Area after dilation (pixels)	Correction Factor (-)
1	4	4.00
2	6	3.00
3	8	2.67
4	9	2.25
6	12	2
8	16	2
12	23	1.92
31	53	1.71
81	102	1.26
101	130	1.29
124	152	1.23

together from multiple fields of view can be obtained. These varying image sizes render the previous relative size criterion unusable. To solve this problem, a more intuitive approach is taken in the adoption of an absolute size criterion.

First, using a calibration glass, the actual size of one pixel ($PixelLength$) is measured. For the BX51 microscope, using the 10x objective, one pixel corresponds to 1.645 µm, while for the IX83 microscope that has a higher resolution, a pixel, using the 10x objective, has a size of 0.440 µm. Next, using this calibration, the number of pixels corresponding to a fragment with an equivalent diameter D_{frag} is calculated using Equation (5.11). In this study, where fragments are maximally 5 µm in diameter, this yields a critical value, denoted *MinOpp*, of 7 pixels for the BX51 microscope and 101 pixels for the IX83 microscope. These values are now used as a new size-exclusion criterion for the recognition of fragments from the object-pool, as shown in Equation (5.12)

$$OPP_{frag} = \pi \cdot \left[\frac{D_{frag}/2}{PixelLength}\right]^2 \tag{5.11}$$

$$MinOpp = \begin{cases} 7, & \text{Olympus BX51} \\ 101, & \text{Olympus IX83} \end{cases} \qquad OPP_{obj} < CF_{dilation} \cdot MinOpp \rightarrow Fragment \tag{5.12}$$

The correction factor ($CF_{dilation}$) from Equation (5.12) stems from the dilation used to reconnect broken filaments, as mentioned in Section 5.3.4. Herein, all objects smaller than 2xMinOpp are dilated, hence including all fragments. Values for this correction factor can be found in Table 5.3.

5.3.6 Improvements on data extraction

Lastly, two improvements on data extraction are discussed. First, some parameters that were previously defined per image (e.g., flocs per image) need a new definition. Secondly, several new parameters are introduced.

Redefining parameters per image

As shown in Table 5.1, several variables in ACTIAS were defined as the number of occurrences of a class, like flocs, filaments or fragments per image. However, as previously discussed, the image size of the IX83-images may vary, depending on the number of fields of view stitched together by the user. Therefore, the previously used definitions needed reshaping. Therefore, new relative criteria are defined, not based on the number of images, but on their size as well, expressed by their number of pixels. Table 5.4 depicts the new class-distribution variables and their descriptions.

Number and surface distributions

Next to the new variables per megapixel of image, a few other parameters are introduced. First, the concept between a number- and surface-distribution is explained. Consider Figure 5.15, where 11 different flocs are shown of which the 10 blue ones have a size of, lets assume, 10 pixels, and the larger red one has a size of 1000 pixels. Now, the average size of an object would be calculated as: $(10 \cdot 10 + 1 \cdot 1000)/11 = 100$ pixels. This is 100% correct, and will be denoted as the *number average*. However, there are two remarks to this approach. Firstly, the image has a limited field of view and can only contain one large floc. Secondly, although it is only one floc, it does cover 10 times the surface of all the smaller flocs combined. In this regard, it will also take

Table 5.4: New extracted information from ASIAP: distribution parameters.

Variable	Description
RelFlocNum	Number of flocs per megapixel of image
RelFilNum	Number of filaments per megapixel of image
RelFragNum	Number of fragments per megapixel of image
RelObjNum	Number of objects (flocs, filaments and fragments) per megapixel of image
RelFlocSurf	Number of floc-pixels per megapixel of image
RelFilSurf	Number of filament-pixels per megapixel of image
RelFragSurf	Number of fragment-pixels per megapixel of image
RelObjSurf	Number of object-pixels per megapixel of image
FiltoFlocNum	Number of filaments per floc
FiltoFlocSurf	Number of filament-pixels per floc-pixel
FragtoFlocNum	Number of fragments per floc
FragtoFlocSurf	Number of fragment-pixels per floc-pixel

up much more space in the activated sludge mixed liquor. If these remarks are taken into account, another possible way of calculating the average can be adopted, which will be denoted as the *surface average*, i.e., the weighted average of an object's property in which the weighing factor is its surface.

This would yield: $$\frac{10 \cdot (10 \text{ pix} \cdot 10 \text{ pix}) + 1 \cdot (1000 \text{ pix} \cdot 1000 \text{ pix})}{10 \cdot 10 \text{ pix} + 1 \cdot 1000 \text{ pix}} = 910 \text{ pixels}.$$

Both approaches are usable, but when considering an average or a particle size distribution, it should always be clearly stated how this parameter is calculated. In the improved version of ASIAP, the data variables for flocs in Table 5.2 are now averaged using both the number- and the surface-approach, where the latter will be denoted with the $_W$-subscript (weighted).

Finally, using both approaches, the particle size distributions (PSD) are calculated. In these distributions, only the flocs and the fragments are taken into account. The PSDs are initially calculated with bands of 1 µm ranging from 0 until 1000 µm, but these limits can be fine-tuned by the user. After initial calculation, these bands are combined into 8 ranges: <1 µm, 1-5 µm, 5-13 µm, 13-25 µm, 25-50 µm, 50-100 µm, 100-500 µm and >500 µm (example shown in Figure 5.16). The first two ranges denote the fragments. The ranges 5-13 µm and 13-25 µm denote the microcolonies and very small flocs. The ranges 25-50 µm and 50-100 µm denote the mesoflocs, while the flocs larger than 100 µm are considered large macroflocs. In the particle size distributions, the

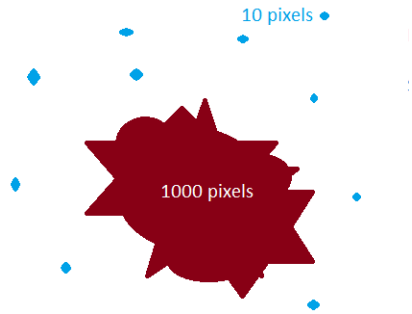

Figure 5.15: A schematic representation of the difference between surface and number averages. The 10 blue flocs have 10 pixels, while the big red floc has 1000 pixels. The number average is, therefore, 100 pixels, while the surface average is 910 pixels.

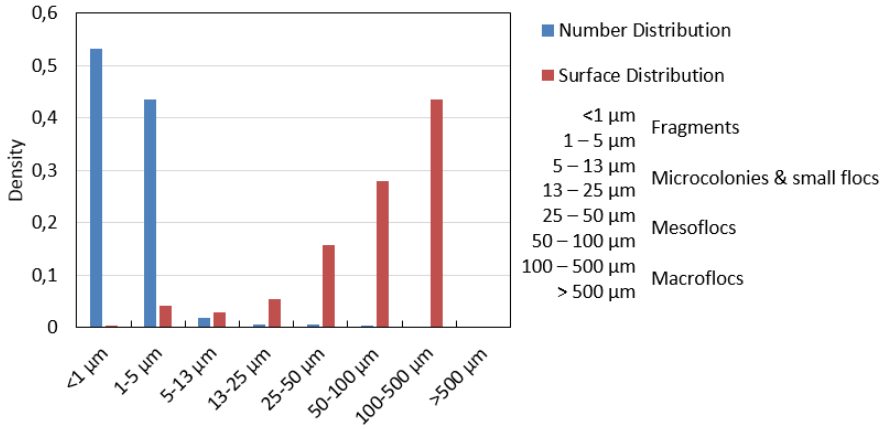

Figure 5.16: An example particle size distribution of activated sludge. Clearly, the small fragments are abundant in numbers, but do not make up for a large surface fraction of the image. The reverse is true for the larger flocs.

results are normalized into particle densities. The sum of all particle densities over the whole range of sizes equals one.

5.4 Statistical analysis to determine the required number of images

As a final section of this chapter, the number of images required to obtain statistically significant results is defined. In the previous ACTIAS program, using the BX51 microscope, this number was estimated to be 50 [Jenné et al., 2002]. However, with the higher resolution of the new microscope and the use of MIA and stitching, this number may no longer be accurate. Therefore, the method used by Contreras et al. [2004], that was originally proposed by Drouin et al. [1997] is applied.

During this study, the 10x objective is used to acquire images that consist of 3x3 stitched fields of view. These 3x3 stitches will from now on be referred to as *grids*. It was chosen to use 3x3 grids since a further increase in tile numbers leads to a substantial increase in computation time (82s for a 3x3, while 145s for a 4x4). Moreover, the larger the grid, the higher the chance that anomalies like dust or air bubbles are present on the image, rendering it useless. Using a grid larger than 20 fields of view, MATLAB occasionally crashes, while grids exceeding 60 tiles can not even be analysed due to memory issues. Grids smaller than 3x3 pose no problem regarding analysis, but may not be able to completely cover the largest sludge flocs.

From a typical communal activated sludge sample, a total of 60 grids is vizualized. These grids are each independently analysed using the improved ASIAP image analysis routine. Next, four image analysis parameters (mean floc area, mean floc equivalent mean, average filament length and mean fractal dimension of flocs) are selected for performing the statistical analysis, that follows the proposed method by Drouin et al. [1997].

From the 60 captured grids, a random array is defined, one for each parameter. Using this array, a new data series is constructed. In this data series, each data point ($\bar{x}_n$) is equal to the average of all parameter values in the array up to the index of the data point element. E.g., for the fractal dimension: the first data point will simply be the fractal dimension of the first grid in the random array. The second data point will be the average between the first and the second fractal dimension. For the third data point, the average of the first three array-elements are taken, and so on.

For each data point, the 95% confidence interval is calculated. The 95% confidence interval $CI_{n,95}$ for the n^{th} data point in the averages-series ($\bar{x}_n$) is given by Equation (5.13) with x_i the i^{th} value of the first array. $t_{n-1,0.025}$ is the t-statistic with n-1 degrees of freedom for the 95% confidence interval.

$$CI_{n,95} = \bar{x}_n \pm \frac{\sqrt{\frac{\sum_{i=1}^{n}(x_i - \bar{x}_n)^2}{n-1}}}{\sqrt{n}} \cdot t_{n-1,0.025} \tag{5.13}$$

The confidence intervals are depicted in Figure 5.17 on the left. It consists of three curves: the values for $\bar{x}_n$, surrounded by its confidence limits. The x-axis denotes the amount of grids that are taken into account. As can be seen in the graph, the mean value, and limits converge to constant values. As can be seen in the figure, the consolidation starts when 15 grids are taken into account. A similar analysis was made for an industrial sludge sample, which showed more variation (see Figure 5.18), and yielded a consolidation starting from 20 grids. Therefore, 20 grids were selected as a validation number for the subsequent step in the procedure.

In the validation step, the number of 20 grids is tested on its ability to obtain statistically significant results. The approach is as follows: from the 60 initially captured grids, 50 sets of 20 randomly selected grids are chosen. Each of the 50 sets is analysed using ASIAP and plotted against the global mean from the total of 60 grids. The results are shown in Figures 5.17 and 5.18 on the right. In the plots, the horizontal lines denote the global mean ± 15%. The amount of grids chosen is deemed sufficient if not too many of their average points fall out of the bounds set by these lines. As can be seen in the image, this occurs only for the mean floc area, where only 10% of the sets yielded slightly altered results. For the other parameters tested, the average values of the sets stayed well between the limits set by the global mean ± 15%. It can be concluded that 20 3x3 grids, taken with the Olympus IX83 objective, are sufficient for the calculation of statistically significant image analysis data.

5.5 Conclusion

The following improvements have been made to the phase contrast image analysis program.

- The image format *.vsi*, which is native to the new IX83 Olympus microscope, is incorporated into the MATLAB program.
- It is no longer required to take color images for the software to work correctly.

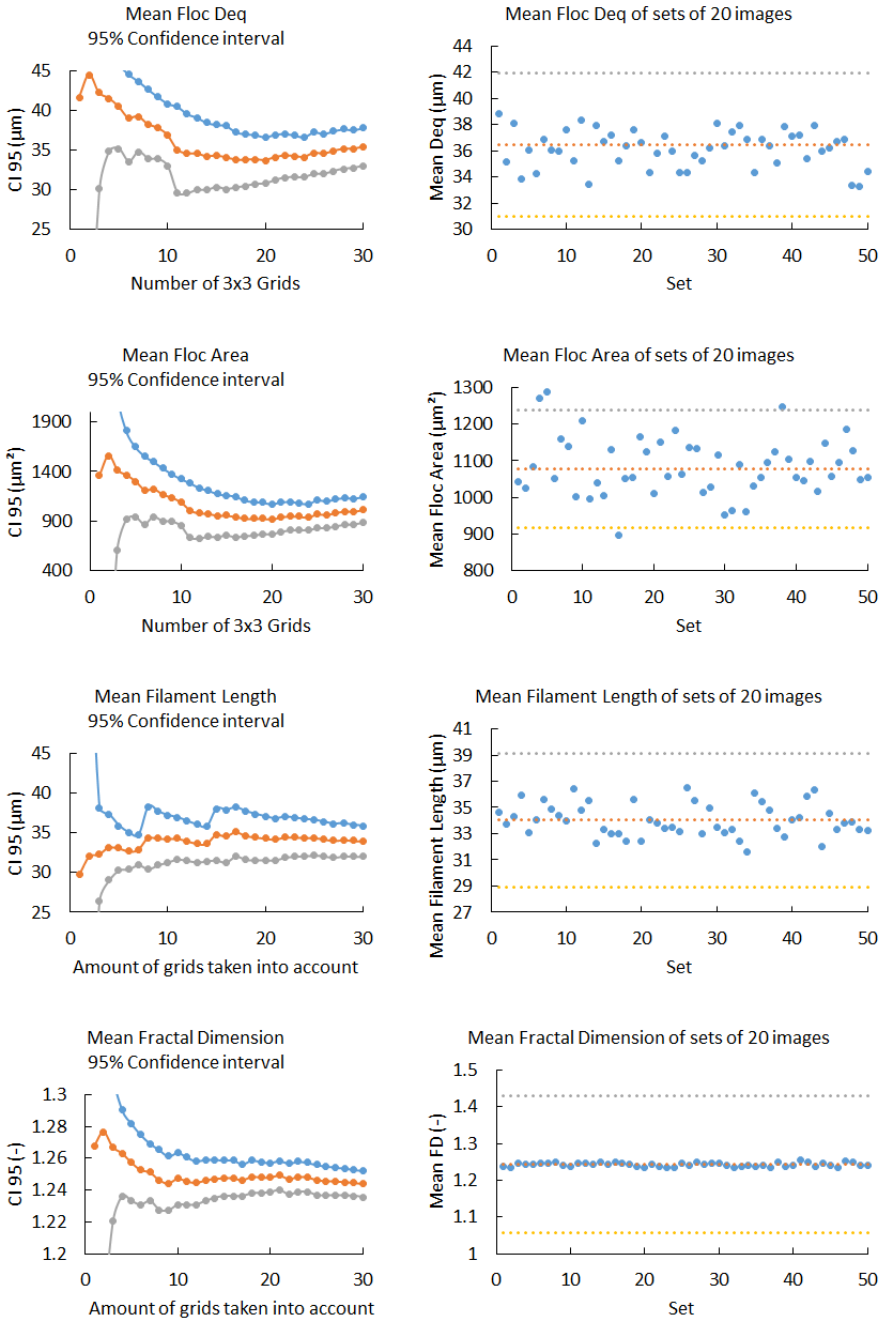

Figure 5.17: Statistical analysis on communal sludge for 4 distinct image analysis parameters (mean floc equivalent diameter, mean floc area, mean filament length and mean fractal dimension of flocs) to determine the required number of 3x3 grids to obtain statistically significant results. **Left**: evolution of 95% confidence intervals for the 4 parameters as a function of the number of analysed grids. **Right**: mean variables of 50 sets of 20 randomly chosen grids plotted against the global mean over the 50 sets (middle line) ± 15% deviation (top and bottom lines).

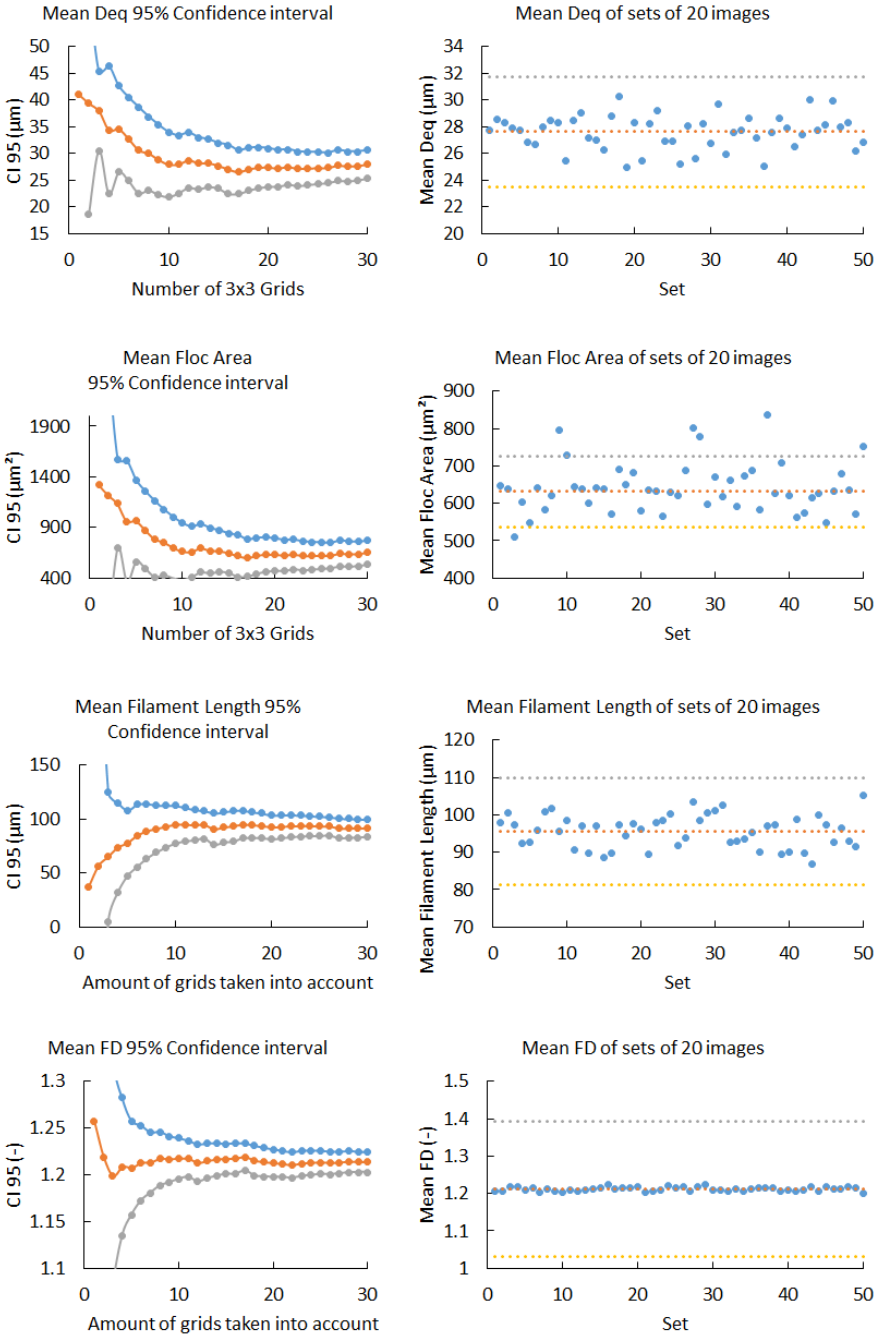

Figure 5.18: Statistical analysis on 4 distinct image analysis parameters for industrial sludge. **Left**: evolution of 95% confidence intervals for the 4 parameters as a function of the number of analysed grids. **Right**: mean variables of 50 sets of 20 randomly chosen grids plotted against the global mean over the 50 sets (middle line) ± 15% deviation (top and bottom lines).

- The segmentation routines have been improved through better thresholding methods. Manual thresholding has been implemented for images that are difficult to analyse.
- Recognition of filaments has been improved through the ellipse criterion. Broken filaments are also reconnected in a better fashion.
- The classification of fragments is done in an absolute manner rather than relative to the image size.
- The results are redefined as parameters per number of pixels rather than per image, since the images may vary in size themselves.
- Number and surface particle size distributions have been implemented.
- The number of images required for statistically significant results has been determined. Twenty 3x3 fields of view suffice.

Chapter 6

Explorative study on the use of epifluorescence microscopy for bioflocculation monitoring

In this chapter, the use of the fluorescence feature of the IX83 microscope for the study of bioflocculation is explored. The first section describes the selected fluorescent dyes and staining procedures. Next, two developed image analysis routines for the analysis of fluorescent images are discussed. Thirdly, the fluorescent measuring techniques are tested against their chemo-colorimetric counterparts. Lastly, the novel method for Gram-staining, proposed by Mesquita et al. [2011b], is compared with the traditional method.

6.1 Selected dyes and staining procedures

6.1.1 Dye description

In Section 3.2.1, several fluorescent dye selection criteria have already been described. In this section, the selected fluorescents that were chosen, will be discussed. Fluorescent markers are expensive, light and temperature sensitive speciality chemicals. Their stock solutions are stored in non-transparent vials in the freezer (-20 °C). Table 6.1 depicts these stock solutions.

From the stock solutions, working solutions for day to day staining are prepared.

These working solutions have a limited shelf life (usually a couple of weeks) and can be stored in the fridge in a non-transparent container. Their volume should be prepared according to the expected usage as defrosting the stock solutions should be avoided as much as possible. The working concentrations are prepared in accordance with the suppliers guidelines. Table 6.2 depicts the working solutions.

Table 6.1: Stock solutions and targets of the fluorescent markers used in this study. Stock solutions are stored in the freezer (-20°C); DMSO = dimethylsulfoxide. Ex/Em = excitation wavelength/emission wavelength.

Fluorescent marker	**Target**	**Ex/Em** (nm)	**Stock solution**
SYTO®40	All DNA	420/441	5 mM in DMSO
SYTO®9	All DNA	483/503	3.34 mM in DMSO
Hexidium iodide	Gram positive bacteria	518/600	4.67 mM in DMSO
Nile Red	Hydrophobic sites	552/635	31.4 mM in acetone
Fluorescein isothiocyanate (FITC)	Proteins: -NH_2 termini	495/519	1% solution in DMSO
Alexa Fluor 405 NHS-ester	Proteins: -NH_2 termini	404/428	972 µM in DMSO
Concanavalin A - Alexa 488 Conjugate	Polysaccharides: α-D-mannosyl and α-D-glucosyl residus	490/525	1.25 g/L in carbonate buffer (pH 8.3)

In the next sections, the working mechanisms and the rationale behind the different dyes will be explained. Most information from this chapter is taken from The Molecular Probes® Handbook [Johnson and Spence, 2010].

All DNA: SYTO®40 and SYTO®9

The SYTO® nucleic acid stains for DNA and RNA are cell-permeant cyanine dyes. A large number of SYTO® dyes exist, all differing in excitation and emission spectra. However, they share a number of important characteristics:

- permeability to virtually all (bacterial) cell membranes, regardless of Gram status;
- strong molar absorptivity with very high extinction coefficients;

Table 6.2: Working solutions of the fluorescent markers used in this study. Working solutions are used for day to day use and can be stored for a few weeks in the fridge; DMSO = dimethylsulfoxide.

Fluorescent marker	**Volume**	**Preparation**
SYTO®40	50 µL of 500 µM	5 µL stock + 45 µL DMSO
Nile Red	121 µL of 1 mM	4 µL stock + 121 µL acetone
Gram Mix: SYTO®9	5 mL	3 µL of each dye in 5 mL 0.85% NaCl
Gram Mix: Hexidium iodide		
Fluorescein isothiocyanate (FITC)	Use stock solution	
Alexa Fluor 405 NHS-ester	200 µL of 200 µM	41 µL stock + 159 µL DMSO
Concanavalin A - Alexa 488 Conjugate	50 µL of 250 µg/mL	10 µL stock + 40 µL carbonate buffer (pH 8.3)

- extremely low intrinsic fluorescence, with quantum yields below 0.01 when not bound to their target (DNA, RNA);
- quantum yields that increase to more than 0.4 when bound to nucleic acids. This feature omits the need for a washing step.

SYTO®9 is often used in combination with propidium iodide for Live/Dead staining or with hexidium iodide as a fluorescent alternative for traditional Gram staining. In this work, SYTO®40 is also tested, since its excitation and emission spectra are located in the blue fluorescence region and show minimal spectral overlap with other dyes tested.

Extracellular DNA and dead cells: propidium iodide
Gram positive bacteria: hexidium iodide

Hexidium iodide (HI) is a moderately lipophilic phenanthridinium dye (see Figure 6.1 left) that selectively stains DNA from Gram-positive bacteria. In combination with SYTO®9, it can be used to differentiate between bacterial Gram status.

Propidium iodide (PI) is structurally comparable to hexidium iodide (see Figure 6.1 right), but is generally not able to penetrate the cell wall of viable cells. As mentioned above, it is used as marker for dead cells, or as indicator for extracellular DNA, which is often denoted as an EPS constituent.

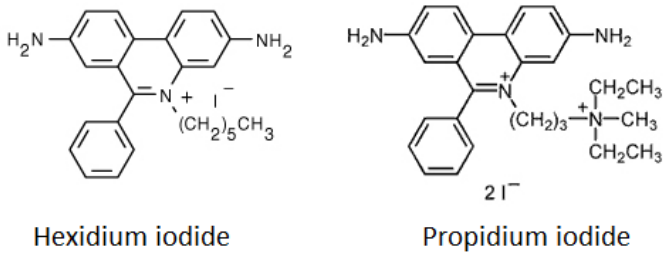

Figure 6.1: Structural formula of the lipophilic phenanthridinium dyes hexidium iodide (left) and propidium iodide (right) (Invitrogen).

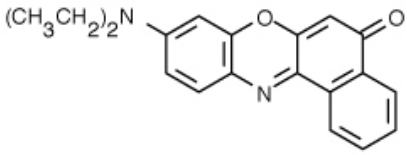

Figure 6.2: Structural formula of the phenoxazine dye Nile Red (Invitrogen).

Both HI and PI intercalate to DNA with no sequence preference, with one molecule of dye per four to five base pairs. When bound to DNA their fluorescence is enhanced nearly tenfold, omitting the need for washing. However, in comparison with SYTO® dyes, their molar absorptivities (extinction coefficients) are relatively low. Moreover, since SYTO® markers bind all DNA, when used in combination with SYTO®9 or 40, it is important that HI or PI are added in excess. Since their excitation and emission spectra practically overlap, hexidium and propidium iodide cannot be applied on the same sample.

Hydrophobic sites: Nile Red

The phenoxazine dye Nile Red (see Figure 6.2) is almost nonfluorescent in water and polar solvents, but undergoes strong fluorescence enhancement in nonpolar environments. In this study, an attempt is made to employ this environmental sensitivity for the visualization of hydrophobic regions in sludge flocs.

Proteins: Fluorescein isothiocyanate (FITC) and Alexa-Fluor405 NHS ester (A405-NHS)

For a long time, the amine-reactive fluorescein derivates have been the most prevalently used fluorescent derivatization reagents. Fluorescein isothiocyanate (see Figure 3.7) is a prime example. It consits of the fluorescent molecule fluorescein, functionalized with an isothiocyanate reactive group.

Fluorescein has a relatively high molar absorptivity, excellent fluorescence quantum yield and a good water solubility. However, its conjugates suffer from a few significant drawbacks, such as a relatively high rate of photobleaching, pH-sensitive fluorescence that is signifcantly reduced below pH 7, self-quenching tendencies and a relatively broad fluorescence emission spectrum, making it more difficult to use in multicolor applications.

Alexa Fluor® dyes are the state of the art fluorophores, producing exceptionally bright and photostable conjugates and having several other interesting attributes, among which:

- strong absorption at wavelengths of maximum output of common excitation sources;
- good water solubility;
- insensitivity to pH over a broad range;
- high quantum yields and long fluorescence lifespans;
- well-differentiated spectra, simplifying their use in multicolor experiments.

Isothiocyanates form thioureas upon reaction with amines, which is the basis of protein-labeling by FITC (see Figure 6.3 top). However, their long term stability is not always guaranteed. Therefore, succinimidyl (NHS) esters are more reliable alternatives. Their structure and reaction scheme is shown in Figure 6.3 bottom.

Alpha-polysaccharides: Concanavalin A - Alexa 488 Conjugate (ConA-A488)

Lectins are carbohydrate-binding proteins that bind to specific sugar molecules. Concanavalin A (Con A) selectively attaches to α-mannopyranosyl and α-glucopyranosyl residues. In moderately acidic environments (pH 4.5-5.6), the lectin exists as a dimer with a molecular weight of approximately 52,000 Da.

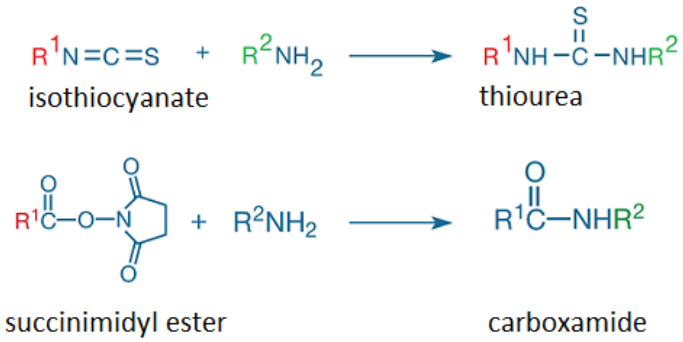

Figure 6.3: General reaction schemes of isothiocyanates (top) and succinimidyl (NHS)-esters (bottom).

Above pH 7, it transforms into a tetramer. ConA, as a metalloprotein, requires a calcium or manganese ion per subunit for carbohydrate binding. When Con A is succinylated with succinic anhydride, which is the case in the Alexa Fluor ® 488 conjugate, it is irreversibly converted into a dimer. However, the native sugar-binding specificity from its parent lectin is retained.

6.1.2 Staining and visualization procedures

Incubation and washing

Fluorescently stained samples should always be exposed to light as little as possible and be gently mixed for **dye-incubation**. To this end, the sludge samples were prepared using minimal light, using darkly colored Epps. After preparation, they were wrapped in aluminium foil and gently rotated head-over-end. An incubation time of 30 minutes was sufficient for all dyes tested. Longer incubation times did not yield better results. In Table 6.3, the staining procedures are depicted for the dyes used in this study. Different dye/sludge ratios have been tried. The table depicts the ratios that provided good results for the samples tested.

Fluorescent markers that do not show quantum yield increase on binding, exhibit a strong fluorescent signal even when unbound to their target. The relatively simple dye FITC is a prime example of this. In order to correctly vizualize samples stained with FITC, the unbound excess dye needs to be removed after incubation. This is performed using a centrifugal **washing** step. The fluorescently stained activated sludge flocs are separated from the supernatant

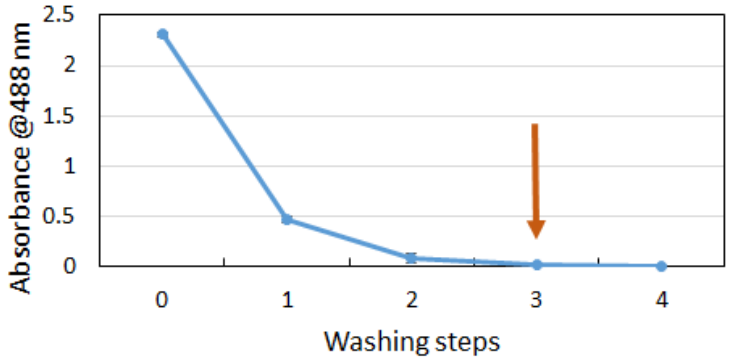

Figure 6.4: Supernatant absorbance at 488 nm of mixed liquor stained with FITC as a function of washing steps (10 minutes centrifugation, 500g, 4 °C. After three washing steps, supernatant absorbance (as a measure of background absorbance) decreases to 0.69% of its original value.

that contains the excess of dye. Afterwards the sludge flocs are resuspended in fresh, uncolored supernatant. This procedure is repeated a few times until nearly all excess dye has been removed and background fluorescence becomes negligible. To distort the sludge's morphology as little as possible, mild centrifugation speeds (e.g., 500g) are used. A centrifugation time of ten minutes is usually long enough. Figure 6.4 depicts the effect of the number of washing steps on the residual supernatant absorbance. Three washing steps is deemed optimal.

6.2 Quantitative fluorescent image analysis

To analyse the images originating from fluorescent microscopic imaging, a fluorescence image analysis program is required. In this work, two versions of such quantitative image analysis system are made. The first version, ASIAP-Fluo, is a fluorescence add-on for the existing ASIAP program. The second version, FLASIAP, is a standalone version that no longer requires ASIAP for its use. Both versions will be explained briefly.

6.2.1 ASIAP-Fluo: a fluorescence add-on for ASIAP

The first quantitative fluorescence image analysis program is designed as an add-on for the existing phase contrast program, ASIAP (see Chapter 5). Since the software of the IX83 microscope allows for readily switching between different

Table 6.3: Staining procedures for different fluorescent markers.

Fluorescent marker	**Staining concentrations**	**Washing?**
SYTO®40	10 µL working solution in 500 µL diluted[1] sludge sample	No
Nile Red	50 µL working solution in 500 µL diluted sludge sample	No
Gram Mix: SYTO®9 Gram Mix: Hexidium iodide	50 µL working solution added to 100 µL undiluted sludge sample	No
FITC	25 µL stock solution + 50 µL carbonate buffer (pH 10.0) in 500 µL diluted sludge sample	Yes
Alexa Fluor 405 NHS-ester	100 µL working solution in 500 µL diluted sludge sample	Yes
Concanavalin A - Alexa 488 Conjugate	20 µL working solution + 250 µL carbonate buffer (pH 8.3) in 500 µL diluted sludge sample	Yes

[1]When using diluted sludge samples, filtered supernatant is always used as a dilutant to reduce the **final** sample concentration (including the volume addition from the dyes and/or buffers) to an MLSS of 1 g/L.

observation methods and capturing these different observation methods in the same image, a phase contrast layer can easily be obtained along with the desired fluorescence layer.

The fluorescence image analysis then holds two steps. In the first step, the previously explained ASIAP routine is used to determine the positions of the flocs, filaments and fragments in the image. In the second step, the pixel values (intensities) of the fluorescence layers at those positions are extracted and several parameters are calculated:

Average Intensity (I). The average intensity of flocs, filaments and fragments. Each object has equal weight in the average, regardless of its size.

Average Pixel Intensity (PixI). The average intensity of a pixel belonging to a floc, filament or fragment. The calculation is as follows: all flocs are combined into one large floc. Of this floc, the average intensity is calculated. The PixI is in fact equal to the area-weighted average intensity.

Relative Ratio (RR). A measure of the fluorescence per area spread in the flocs, filaments and fragments. This parameter can be used to formulate expressions like *flocs are on average brighter than fragments or filaments.*

Fraction > 0.1 MAX. For each floc or filament, the fraction of pixels that has a higher or equal intensity than 10 percent of the maximum[1] intensity within that floc or filament is calculated. These fractions are averaged.

Fraction > 0.5 MAX. Similar description as above with the intensity limit being 50 percent.

The advantage of ASIAP-Fluo is that since the existing phase contrast routine is also ran on the images, the morphology can effectively be linked to the composition (e.g., organic fraction, EPS) or the surface properties (hydrophobicity) on the same flocs, rather than having to acquire different sets of images. Fluorescence can be expressed as a quantitative value per floc, filament or fragment surface, and its distribution over the objects themselves or over the different classes can be calculated. Another advantage is that the user does not need to worry about thresholding in the fluorescence-layer, since it is not necessary.

However, the use of the software combination ASIAP-Fluo has a few disadvantages. Firstly, in samples where the user is only interested in the fluorescence channel, the acquisition of the phase contrast layer and its subsequent analysis using ASIAP needs to be performed before the actual fluorescence analysis can be done. This is both time consuming and entails a doubling in required hard drive storage space. Secondly, the acquisition of the phase contrast layer results in a higher illumination of the sample, which can be very detrimental for light sensitive fluorescent molecules or markers. However, when the autofocus functionality is used, the exposure time required for focussing is much lower in the phase contrast channel than in the fluorescence channel. Therefore, it is advised, when acquiring images based on the fluorescence measurement alone, to focus on a neighbouring object and switching to the desired object's location (which is only to be a field of view away) before the actual image acquisition.

[1]It should be noted that this maximum can be high or low. When the maximum is low, it can be so that the fraction is large, while the whole floc shows a rather low fluorescence intensity. Therefore, this value should always be put in respect to the average floc intensity.

6.2.2 FLASIAP: a standalone fluorescent image analysis program

To overcome the need for phase contrast acquisition, a standalone fluorescent image analysis program (FLASIAP) was developed. In this image analysis routine, the use of the phase contrast layer is omitted and instead the whole analysis is performed on the fluorescent layers.

First, the acquired fluorescent images are thresholded using Otsu's method (see Equation (5.7) in Section 5.3.3). Since all objects are now situated in the bright part of the histogram, the use of a top-hat or exponential transformation is no longer required. However, also in FLASIAP, the option is left to the user to perform manual thresholding instead of using Otsu's method. When the thresholding has been performed, all fluorescent values lower than the threshold are nullified, since they are deemed to occur from residual background fluorescence (due to improper washing) or from light scattering.

After the thresholding, the images are processed. All objects smaller than a given size can be removed via an optional noise filter. The use of this noise filter is of interest in the study of objects that are expected to have at least a given size, e.g., in the study of bacteria expressing the green fluorescent protein.

Finally, in the last step, the objects that have been defined through the thresholding are analysed. As in ASIAP, two sets of parameters are defined. The first parameters are the global averages. These averages are calculated as if all images were combined into one large image and define the number of objects, the number of fluorescent pixels (i.e., the total area of objects), and the total fluorescence intensity per megapixel of picture.

The second set of parameters are individual criteria. For each object, its area, equivalent diameter, minimum, maximum and average intensity is calculated. These parameters are then statistically represented (average, standard deviation, median, ...) and denoted using three number distributions: equivalent diameter, area and intensity. All above calculations are also performed for every image individually, which provides a means to detect faulty images.

Tailored versions of FLASIAP are currently being used by other researchers for the study of Cofactor F420 content in anaerobic sludge samples, Live/Dead staining and have been used for the quantification of green fluorescent bacteria in water-oil emulsions [De Wael, 2016].

6.3 A partial least squares regression analysis between quantitative fluorescence methods and volumetric measurements

In this section, several fluorescent markers are compared with their classical measuring methods. If positively evaluated, quantitative fluorescence methods can provide an alternative that is easier to measure, require a smaller sample size and provide information that goes beyond an average value for the whole volume, but may relate composition characteristics to morphology and particle sizes of flocs.

The samples from this chapter are the same sludge samples from Chapter 7, where their origin, morphology and other sludge characteristics will be extensively explained.

6.3.1 Selected methods

The conventional measuring methods used in this section are described in Chapter 4. Fluorescent staining is performed using the procedure that was explained in Section 6.1. Images were analysed with the ASIAP-Fluo MATLAB routine as described in Section 6.2.1.

6.3.2 General fluorescence observations

Table 6.4 depicts average quantitative fluorescent variables for all samples tested. It is clear that Nile Red, which fluoresces in hydrophobic regions yields the brightest staining, as shown by the high average intensity and pixel intensity. The average hydrophobic character of activated sludge is thus affirmed.

In Figure 6.5, an activated sludge sample of industrial origin that contains a high number of inorganic material is depicted. This sludge has been stained with Nile Red (left) and with SYTO® 40 (right). As can be seen in the Nile Red figure, only part of the floc structure is colored orange, while the other part does not show any fluorescence. This means that the colored parts exhibit a far greater hydrophobicity than the non-colored parts. In the figure on the right, DNA is colored using SYTO® 40 as a measure for the bacteria present in the sludge flocs. Both morphologies are compared and it is remarkable that the morphology of the material colored by SYTO® 40 is exactly the same as the morphology of the parts depicted using Nile Red. Thus, it can be concluded

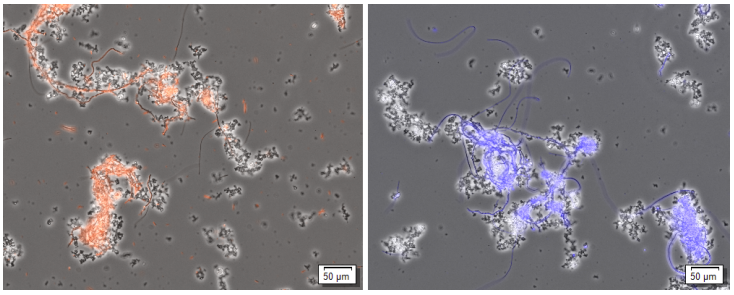

Figure 6.5: Industrial activated sludge sample containing a high number of inorganics. Left: staining of hydrophobic sites with Nile Red. Right: staining of all DNA as a measure of bacteria using SYTO® 40.

that the bacterial material is more hydrophobic than the inorganic constituents of the activated sludge.

Both protein labels (A405-NHS and FITC) show comparable intensity values. However, Alexa405-NHS ester has the advantage of showing much lower background fluorescence over FITC and being less sensitive to bleaching.

The average intensity values of ConA-A488 are the lowest from the fluorescent markers tested, which may nourish the idea that proteins are more abundant EPS consitituent than polysaccharides. However, care should be taken to draw such conclusions prematurely, since the dyes' intrinsic binding affinities and fluorescence yields (as the product of quantum yield and exctinction coefficient, see Section 3.2.1) should be taken into account, and they may differ between the markers tested. A better comparison is made when looking at the fluorescent surface fraction of flocs, since the presence of fluorescence itself is independent of the dyes' brightness. Interestingly, in nearly all samples tested, the low quantification value of ConA-Alexa 488 conjugate suggests a distinct localised colorization for polysaccharides (see Figure 6.6). This effect will be discussed further in the next section.

When looking at the relative ratio's, it can be concluded that no single dye showed significant differences in fluorescence when binding with the three sludge consituents: flocs, filaments and fragments.

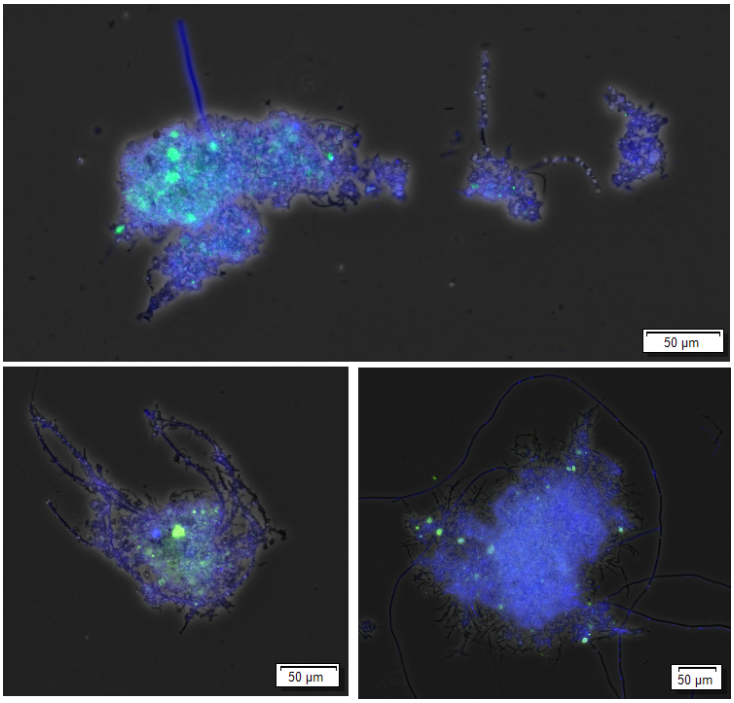

Figure 6.6: Fluorescent staining of eEPS proteins (blue, using Alexa405-NHS ester) and α-polysaccharides (green, using ConA-A488 conjugate) from three different activated sludge samples. The images show a relatively uniform spread of proteins, while the fluorescence originating from the polysaccharides is much more localized.

6.3.3 Comparing quantitative fluorescence measurements with chemo-colorimetric techniques

Polysaccharides

Polysaccharides present in the eEPS were extracted using the CER and heat treatment methods and subsequently determined using the phenol-sulfuric acid colorimetric method, as described in Section 4.1.5. First, these results were subjected to a 1-versus-1 correlation analysis against the average floc intensity, floc pixel intensity and floc fraction$_{<0.1Max}$ of ConA-Alexa 488 conjugate. The results from this analysis are shown in Table 6.5. From the table, the following observations can be made.

Table 6.4: Average quantitative fluorescence variables per fluorescent marker for all samples tested.

Target	ConA-A488 Polysaccharides		A405-NHS Proteins		FITC Proteins		Nile Red Hydrophobicity	
Floc PixI	4.1	± 3.9	15.4	± 11.8	19.4	± 9.5	63.4	± 23.9
Floc I	3.0	± 1.6	6.0	± 4.9	7.6	± 2.6	30.0	± 11.8
Floc Frac.$_{>0.1Max}$	36	± 8	58	± 20	54	± 12	80	± 9
Floc Frac.$_{>0.5Max}$	3	± 1	9	± 6	5	± 3	20	± 12
Rel. Ratio$_{Floc}$	0.28	± 0.11	0.29	± 0.08	0.33	± 0.16	0.28	± 0.07
Rel. Ratio$_{Filament}$	0.31	± 0.12	0.35	± 0.05	0.34	± 0.07	0.34	± 0.09
Rel. Ratio$_{Fragment}$	0.40	± 0.21	0.36	± 0.11	0.33	± 0.22	0.39	± 0.13

The 80% correlation between both eEPS methods shows that both procedures extract reasonably similar amounts of polysaccharides. However, no significant correlation is found between both extraction methods and the fluorescent imaging parameters. This observation is reinforced when an attempt is made to link each eEPS method to the fluorescence data using a PLS regression model[2]. In both cases, the prediction sum of squared errors (PRESS) increases with the number of applied PLS components, which indicates the impossibility of proper regression.

The reason for this discrepancy might be the difference in selectivity between the fluorescent method and the phenol-sulphuric acid method. Concanavalin A, which is a sugar-binding lectin, selectively attaches to α-mannopyranosyl and α-glucopyranosyl residues, which are often denoted as some of the major polysaccharides present in activated sludge EPS. However, they may not be the only polysaccharides present. Sulphuric acid, however, hydrolizes all present polysaccharides into their monovalent constituents, which are subsequently colorimetrically detected after reaction with phenol (see Section 4.1.5).

The selectivity of ConA can also explain the reason why in all but a few cases, the fluorescently detected polysaccharides were found to be strongly clustered (see Figure 6.6). Since it is probably that only specific populations of bacteria produce these specific cell surface polymers, if their colonies are not uniformly spread among the sludge flocs, neither will their respective carbohydrate fluorescence be.

[2]See Section 4.3 for a brief introduction to PLS regression.

Table 6.5: Pearson correlations coefficients between both eEPS extraction methods for polysaccharides and selected quantitative fluorescence parameters.

	eEPS-H-PS	eEPS-CER-PS
eEPS-CER-PS	0.80	
ConA-Flocs-PixI	-0.55	-0.14
ConA-Flocs-I	0.05	0.49
ConA-Floc Frac.$_{>0.1Max}$	-0.81	-0.75

Proteins

Proteins in the bound extracellular polymeric substances were determined using the modified Lowry method after extraction using the CER or heat treatment method (see Section 4.1.5). First, similarly to the previous section, a 1-versus-1 correlation is made between the chemo-colorimetrically determined eEPS and the fluorescently quantified protein present in activated sludge flocs, using Alexa Fluor 405 NHS ester as a fluorescent marker. The results from this study are shown in Table 6.6. The same procedure was applied using fluorescein isothiocyanate as an alternative marker for proteins. However, this experiment did not yield satisfactory results and will be omitted in this study.

Table 6.6: Pearson correlations coefficients between both eEPS extraction methods for proteins and selected quantitative fluorescence parameters.

	eEPS-H-PN	eEPS-CER-PN
eEPS-CER-PN	-0.35	
A405NHS-Flocs-PixI	0.55	-0.26
A405NHS-Flocs-I	0.37	-0.02
A405NHS-Floc Frac.$_{>0.1Max}$	0.33	-0.20

Table 6.6 clearly shows that both extraction methods yield different results and presumably extract different proteins, which was already observed by several authors [Sun et al., 2015; Zhu et al., 2015]. Furthermore, all fluorescence parameters seem to be positively correlated with the data obtained using the heat extraction method, while they are negatively or negligably correlated with the CER extraction results. This observation affirms the consensus that heat treatment is a more universal EPS-extraction method while the CER method selectively extracts cation-bound proteins.

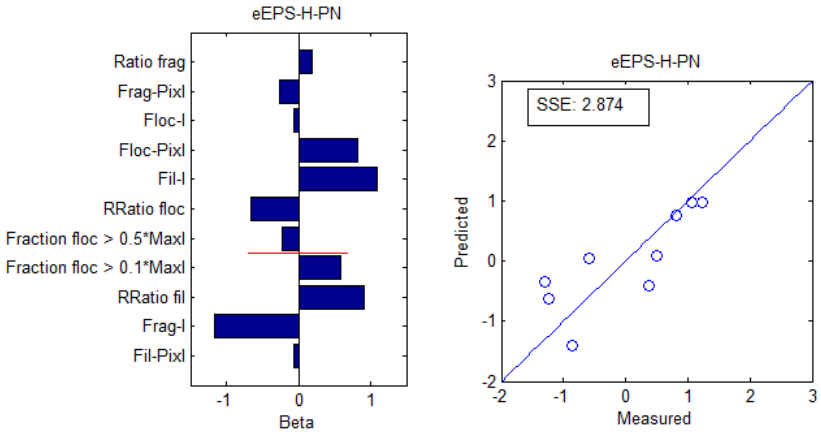

Figure 6.7: PLS regression of Alexa Fluor 405 NHS ester bound protein versus heat treatment extracted EPS. Left: PLS regression coefficients linking the quantitative fluorescence information to the eEPS measurements. Right: predicted versus measured values using crossvalidation (leave one out)

For both methods, a PLS regression model is built. As expected, the CER-method did not yield satisfactory results and will not be adressed further. The heat treatment's β-regression coefficients and the predicted versus measured data are shown in Figure 6.7. For the model, five PLS components are used, which is the first number for which the PRESS significantly decreases [Abdi, 2010].

From these results, several observations can be made. The presence of fluorescence on fragments is negatively correlated with the eEPS, which is reasonable, since fragments are washed out during SMP-separation, that happens prior to the actual eEPS-extraction (see Section 4.1.5). The presence of fluorescence on filaments and the spread of fluorescence over flocs is positively correlated. The positive effect of floc pixel intensity is confirmed as well. It can be concluded that a high spread of Alexa 405 NHS-ester over flocs and filaments correlates with a high measured value of heat-extractable EPS-proteins.

Relative Hydrophobicity

Nile Red has been shown to fluoresce in the presence of hydrophobic sludge flocs (see Figure 6.5). Table 6.7 depicts the 1-versus-1 correlations between the relative hydrophobicity (RH) and absolute surface charge (|SC|) (see Sections

4.1.3 and 4.1.4) against the quantitative fluorescence parameters using Nile Red (see Section 6.1).

From Table 6.7, it is clear that among the samples tested, the relative hydrophobicity was only slightly inversely correlated with the flocs surface charge. Moreover, neither did the relative hydrophobicity show much correlation with the different fluorescence parameters. It can be concluded that Nile Red may not provide sufficient predictive capabilities for activated sludge's hydrophobicity among the samples tested. Unsurprisingly, it was not possible to make a feasible PLS-regression between the fluorescence parameters and the relative hydrophobicity.

A reasonable explanation for this discrepancy is the fact that Nile Red, nearly in all cases, uniformly stained the biomass and that subtle differences in hydrophobicity were not detected. It is possible that, using much lower concentrations of dye, these differences might become more visible. This assumption, however, was not tested.

Although Nile Red did not correlate with the relative hydrophobicity, it does seem to be correlating more with the absolute value of the surface charge, as shown in the third column of Table 6.7. When the surface charge becomes more extreme, the fluorescence of Nile Red decreases, which is in accordance with its property of reducing fluorescence in polar media. Unfortunately, the PLS-regression did not yield satisfactory results, as the PRESS kept on increasing with the number of PLS components used.

Table 6.7: Correlations between the microbial adhesion on hydrocarbons (MATH) assay for relative hydrophobicity (RH), the absolute surface charge |SC| and selected quantitative fluorescence parameters using Nile Red.

	RH	|SC|
|SC|	-0.16	
Nile Red-Flocs-PixI	-0.10	-0.57
Nile Red-I	-0.23	-0.38
Nile Red Frac.$_{>0.1Max}$	0.18	-0.75

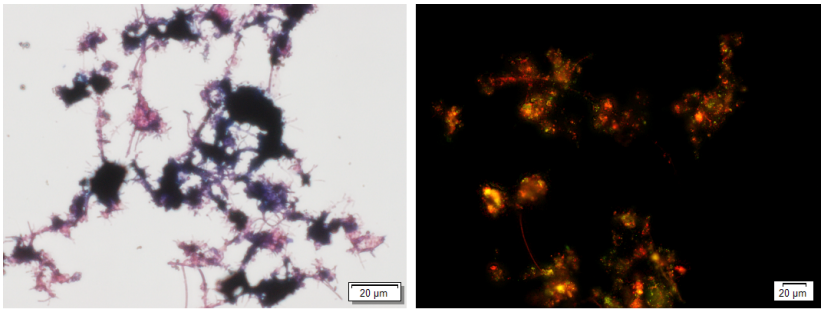

Figure 6.8: Example of both Gram-staining methods. Left: classical method using Violet-Blue/ethanol/Safranin. Gram-positive bacteria are dark purple, while Gram-negative bacteria are pink. Right: novel fluorescence method using SYTO® 9 and hexidium iodide. Gram-positive bacteria are red, Gram-negative bacteria are green.

6.4 A novel method for Gram staining: evaluation and semi-quantitative comparison

In this section, a comparison is made between the classical Gram staining method (see Section 4.1.6) and a novel, fluorescence based method using SYTO® 9 and hexidium iodide (see Section 6.1). Figure 6.8 depicts an example of both staining methods.

Since quantitative comparison between both Gram staining methods would require the development of a dedicated image analysis program for the traditional method, only a semi-quantitative comparison was made between both staining methods. To this end, a set of predefined characteristics was used to determine whether the results of the new method approximate those from the traditional method. An illustration of these characteristics is given in Figure 6.9. For each of the characteristics, a semi-quantitative score was given between 0 and 5.

Flocs are Gram-positive. A measure for the fraction of sludge flocs consisting of Gram-positive bacteria.

Flocs are Gram-negative. A measure for the fraction of sludge flocs consisting of Gram-negative bacteria.

Filaments are Gram-positive. A measure for the fraction of sludge filaments consisting of Gram-positive bacteria.

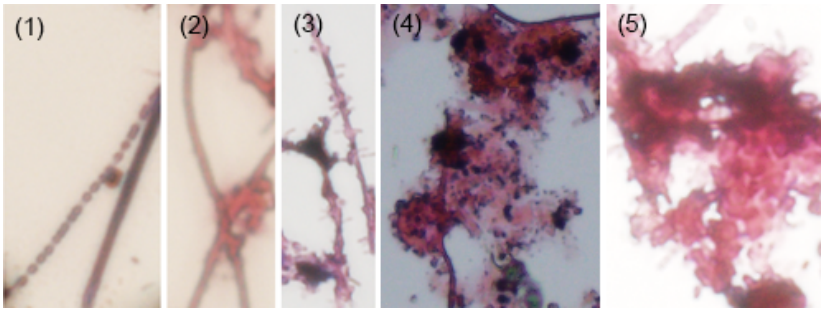

Figure 6.9: Examples of evaluation criteria on images obtained through the classical Gram staining. Red zones are Gram-negative and purple/black zones are Gram-positive. (1) Filament consisting of alternate zones with and without staining. (2) Difference between core and border of filament. (3) Appendages on filaments. (4) Intense zones of Gram-positive staining. (5) Staining is much more uniform.

Filaments are Gram-negative. A measure for the fraction of sludge filaments consisting of Gram-negative bacteria.

Staining of whole filament. This criterion captures the fact that some filaments consist of alternate zones with and without staining.

Gram-positive staining is localized. In some cases, the staining is limited to a few very intense zones, while in other cases, the staining is much more uniform.

Gram-negative staining is localized. Same criterion as above, but for the Gram-negative stain.

Differences between core and border of filament. In some cases, there is a difference in color between the middle and the edge of the filaments.

Filaments have appendages. Appendages, which probably consist of attached microbial colonies, are frequently present around filamentous bacteria. This effect is captured by this characteristic.

The procedure is performed on six distinct sludge samples. After rating all samples, with a few days in between rating the classical method and the novel method, the results are summarized, their differences are tested statistically using the *t-test* and shown in Table 6.8.

The second column in the table depicts the p-values of the paired differences *t-test* for each characteristic between both methods. The averages and deviations

of the paired differences are shown in the last column. The average values of the characteristics and their deviations for both methods are shown in the two middle columns.

When the p-value for a parameter is higher than 0.05 (5 %), a difference in this parameter between both methods could not be statistically proven. In contrast, a low p-value indicates a very slight chance that differences between both measured methods occur due to measurement noise and inaccuracies. As can be seen from Table 6.8, only for the fraction of flocs that are Gram-positive, such low p-value can be obtained. This might indicate that there are some differences in Gram-classification between both methods. However, in the fourth column, depicting the average differences between both methods, it can be seen that the difference is not very high (only 1.08 point on average).

Moreover, the data show that on average over all activated sludge flocs tested, Gram-positive bacteria are more predominantly present and more uniformly spread, as opposed to Gram-negative bacteria that show a more localised tendency. Filaments occur to be of both natures, with similar characteristics regarding Gram-sign, complete staining and appendage-characteristics. However, the classical method showed more differences between the core and the border of the filaments. This might be a result of the sensitivity towards the decolorization-step of the classical method.

Table 6.8: Results from semi-quantitative criteria for evaluating Gram-staining methods. p-values are obtained using the two side *t-test* with 5% confidence limit.

	p-value ($\alpha = 5\%$)	Classical method	Fluorescence method	Paired difference
Flocs are Gram-positive	0.010	2.91 ± 0.66	4.00 ± 0.00	1.08 ± 0.66
Flocs are Gram-negative	0.203	2.30 ± 0.67	2.00 ± 0.71	0.25 ± 0.42
Filaments are Gram-positive	0.797	2.70 ± 1.10	3.20 ± 0.84	0.17 ± 1.50
Filaments are Gram-negative	0.897	2.70 ± 0.83	2.20 ± 1.30	0.08 ± 1.50
Staining of whole filaments	0.673	4.10 ± 1.24	3.90 ± 0.55	0.25 ± 1.37
Gram-positive staining is localised	1.000	1.70 ± 0.97	1.80 ± 0.84	0.00 ± 0.71
Gram-negative staining is localised	0.867	3.00 ± 1.06	3.30 ± 0.45	0.08 ± 1.16
Difference between core and border of filament	0.052	3.10 ± 1.75	1.60 ± 1.56	1.58 ± 1.53
Filaments have appendages	1.000	2.20 ± 1.79	2.20 ± 2.36	0.00 ± 0.71

Although only a few different activated sludge samples have been tested, their origins were highly diverse. Hence, the range and number of flocs tested should provide a decent sample size. The results are promising with only minor qualitative differences between both methods. The use of the fluorescent method is preferred since the sensitivity for the decolorization of the classical method is overcome. Moreover, images from the fluorescent method probably are more easily quantified using a tailor made image-analysis program since both Gram-signs can be acquired in different observation methods and thus stored in different image layers.

6.5 Conclusion

In this chapter, the use of quantitative fluorescent imaging for the study of bioflocculation was assessed. Two image analysis programs were designed. ASIAP-Fluo serves as a fluorescence add-on for the phase contrast program (Chapter 5), while FLASIAP can extract information from images with only fluorescence layers.

To assess relative hydrophobicity, the use of Nile Red was proposed. Although the floc's biomass was clearly more hydrophobic than the inorganic precipitates, it was unfortunately not possible to distinguish between hydrophobic regions in the organic parts themselves. Possibly, the amounts of dye used were too high. Future research regarding the use of Nile Red is, therefore, advised.

Polysaccharides were determined using Concanavalin A-Alexa 488 conjugate, which binds to to α-mannopyranosyl and α-glucopyranosyl residues. Results indicated spots of high concentrations of these residues within the sludge flocs. Neither conventional EPS-PS extraction methods correlated with the results from the quantitative image analysis. A reasonable explanation is that the fluorescently visualized α-sugars were not the only carbohydrates present in the flocs. Still, both EPS-extraction methods (heat treatment and CER treatment) yielded similar carbohydrate concentrations and were correlated.

The conventional EPS-extraction methods did not correlate well for the extraction of proteins, confirming a clear difference in specificity between both methods. Therefore, comparing results from different studies may not be straightforward. A good correlation was found between the quantitative image analysis data from proteins that were fluorescently visualized with Alexa 405 NHS-ester and the results from the conventional heat treatment method. No correlations were found for the CER-method. Fluorescein isothiocyanate (FITC) was tried as a less expensive alternative for A405-NHS, but did not yield good results.

Finally, a quantitative fluorescent analysis method was proposed as an alternative for traditional Gram staining. Semi-quantitative comparison between both methods resulted in good agreement, from which it can be concluded that the fluorescent method is viable.

Part II

Bioflocculation versus activated sludge separation

Chapter 7

A partial least squares study unravelling the relationship between bioflocculation and activated sludge separation

In this chapter, the partial least squares technique is used to answer the question: *Which sludge characteristics are important for membrane fouling and settling?*. Sixteen activated sludge samples from different origins were subjected to an extensive characterisation and tested for their fouling propensity and settling properties. Next, PLS is used to infer the relationship between those two sets of variables.

The results of this chapter have been published in Van De Staey, G., Gins, G., Smets, I. (2016). Biofocculation and Activated Sludge Separation: A PLS Case Study. 11th IFAC Symposium on Dynamics and Control of Process Systems, including Biosystems: Vol. 11. NTNU Trondheim, Norway, 6-8 June 2016 (pp. 1151-1156).

7.1 Materials and methods

7.1.1 Sample origins

A total of sixteen samples of different origin were analysed. Samples included activated sludge from four municipal wastewater, from four longterm lab-scale experiments and from eight different industrial processes. The industrial samples include two breweries, two food-manufacturing industries, three chemical companies and one hospital.

7.1.2 Sludge characterisation

The sludge characterisation methods have been discussed in Section 4.1 from Chapter 4. The following methods have been used.

- Mixed liquor (volatile) suspended solids (ML(V)SS) - Section 4.1.1.
- Relative hydrophobicity (RH) - Section 4.1.3.
- Surface charge (SC) - Section 4.1.4.
- SMP extraction: proteins (mod. Lowry) and polysaccharides - Section 4.1.5.
- eEPS heat extraction: proteins (mod. Lowry) and polysaccharides - Section 4.1.5.
- Phase contrast microscopy and image analysis (ASIAP) - Section 4.1.6 and Chapter 5.

7.1.3 Performance indicators

To assess the activated sludge separation performance, three performance indicators were used. **Settleability** was measured via the sludge volume index (Section 4.2.1).

Filtration will be assessed using two newly introduced parameters: the average fouling rate, for the measurement of **reversible fouling** and the global fouling rate, for the measurement of **irreversible fouling**. Both concepts will be further explained with the use of Figure 7.1.

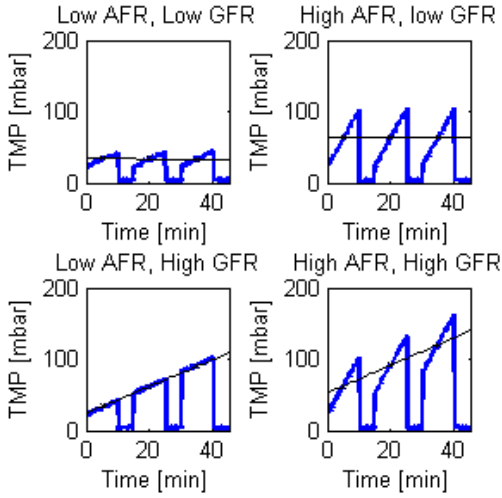

Figure 7.1: Illustration of average fouling rate (AFR) and global fouling rate (GFR).

The filtration tests were perfomed using the submerged 20 L lab-scale set-up (see Figure 4.6 right in Section 4.2.3). Filtration was flux-driven using a standard A4 Kubota flat sheet membrane with an effective filtration surface of 0.11 m^2. The transmembrane pressure (TMP) was measured during 9 steps of 15 minutes filtration at constant flux and 5 minutes relaxation. This procedure was repeated for fluxes of 10, 20 and 30 L/m^2h. However, most of the samples were unable to complete the filtration profile since the maximum TMP of 200 mbar was surpassed. Therefore, the subsequent analysis is only performed on the two lowest fluxes. The average fouling rate (AFR) for a flux is measured as the average of the 9 slopes of the TMP-versus-time fitted curve during the filtration steps. The global fouling rate (GFR) for a given flux is measured as the slope of the fitted curve throughout the whole series of filtrations/relaxations.

7.1.4 Data analysis

Prior to the partial least squares-regression, from the different sludge characterizing variables, a selection was made to use in the PLS-regression. From the large list of image analysis parameters, a selection was made from those that describe similar properties (e.g., roundness, convexity, form factor). Otherwise, the spread of variance over the PLS-dataset would be uneven and

weighted too much towards this cluster of variables. Table 7.1 depicts the image analysis parameters that were chosen to be included in the PLS-study.

Table 7.1: Image analysis parameters.

Abbreviation	**Description**	**Units**
RelFlocNum	Number of sludge flocs per megapixel of image	Megapixel^{-1}
RelFilNum	Number of sludge filaments per megapixel of image	Megapixel^{-1}
RelFragNum	Number of sludge fragments (diameter < 5 μm) per megapixel of image	Megapixel^{-1}
RelFragSurf	Pixel area of sludge fragments per megapixel of image	(-)
Deq	Mean equivalent floc diameter	μm
Deq_W	Mean equivalent floc diameter, weighted with floc size	μm
FilLength	Mean filament length	μm
FD	Mean fractal dimension of flocs (box counting algorithm)	(-)
FD_W	Mean fractal dimension of flocs, weighted with floc size	(-)
Rndns	Mean roundness of flocs	(-)
Rndns_W	Mean roundness of flocs, weighted with floc size	(-)

Next, a PLS analysis (see Section 4.3) was performed to unravel the relationships between the sludge characteristics on one hand, and the reversible fouling (AFR), the irreversible fouling (GFR) and the settleability (SVI) on the other hand. Since the dataset was limited (16 samples, see Section 7.1.1), it was decided to use crossvalidation as an assessment tool for predictive power. More information on crossvalidation can be found in Section 4.3.5.

7.2 Results and discussion

This section will cover the results obtained in this study. A detailed comparison with other studies and experiments will be provided in Chapter 9.

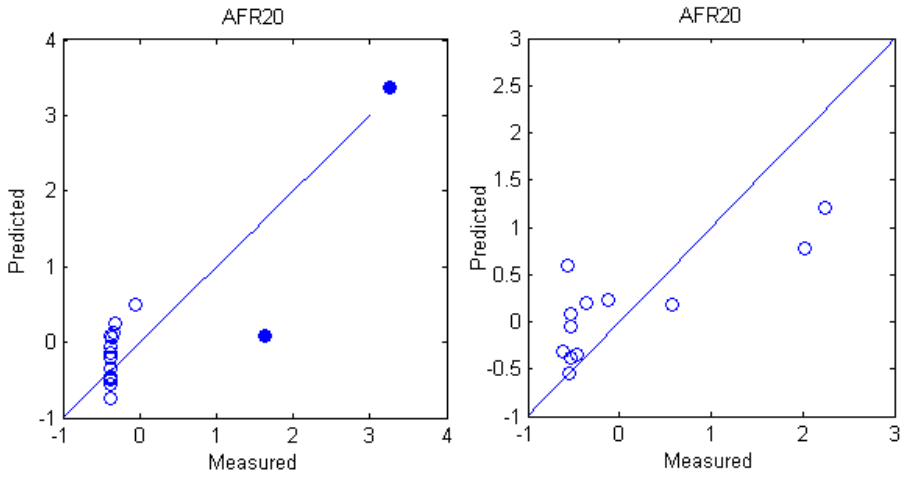

Figure 7.2: Z-scores of measured vs. predicted AFR_{20}. Left: first run, all data. Outliers are denoted with filled markers and are left out in the second run. Right: second run, no outliers.

7.2.1 Reversible fouling - Average fouling rate

Reversible fouling is measured by the average fouling rate (AFR) and is characterised as membrane fouling that can be removed by relaxation or backwashing. In the next paragraphs, a PLS model is introduced that attempts to link the activated sludge characteristics to reversible fouling.

First Run: all data

Figure 7.2 (left) depicts the measured versus predicted normalized values of AFR_{20}, when all data is taken into account. The graph shows that, while most sludge samples exhibit a moderate filterability, two samples have far larger values. These values have filled markers in the graph. As the PLS technique is strongly influenced by such outliers, the predictability of the other observations is undermined. Therefore, it was decided to remove the two outliers from the dataset for the second run.

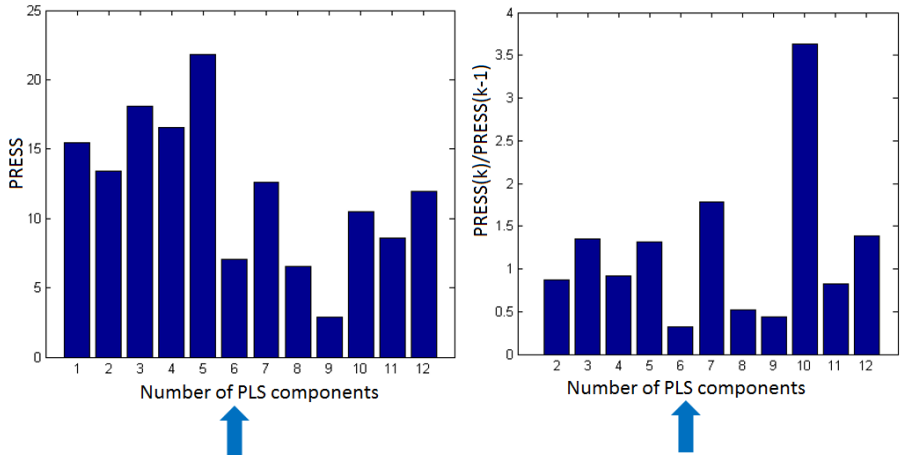

Figure 7.3: Number of selected PLS components. Left: Predictive residual sum of squares (PRESS). Right: PRESS (k)/ PRESS (k/1) as an indication of the reduction of PRESS by adding that extra component.

Second Run: no outliers

Figure 7.2 (right) shows the measured versus predicted normalised values of AFR_{20} after removal of the outliers. As can be seen in the figure, the data is spread more uniformly. For this study, 6 PLS components were chosen, as depicted in Figure 7.3.

As discussed in Section 4.3.2, loading plots can be used as a visual representation of the projection of the old variables onto the new latent structures. These loading plots, which show the location of the old variables in the new coordinate system, can give a clear indication about the relations between the different measured traits. Figure 7.4 depicts the position of the loadings (variables) and scores (samples) in the first two dimensions of the latent PLS space. The positions of the average fouling rates ($AFR_{10,20}$) are indicated with big (green) dots. As can be seen on the graph, the fouling rates for both fluxes are closely located to each other. Moreover, the SMP-PS and the relative fragment surface are in close proximity to the AFR variables, which points to direct correlation. In contrast, the relative hydrophobicity can be seen on the opposite side of the origin, thus probably inversely related with the average fouling rates. Since, e.g., MLSS and MLVSS are closely situated to the origin, these variables are not very influential for the PLS model.

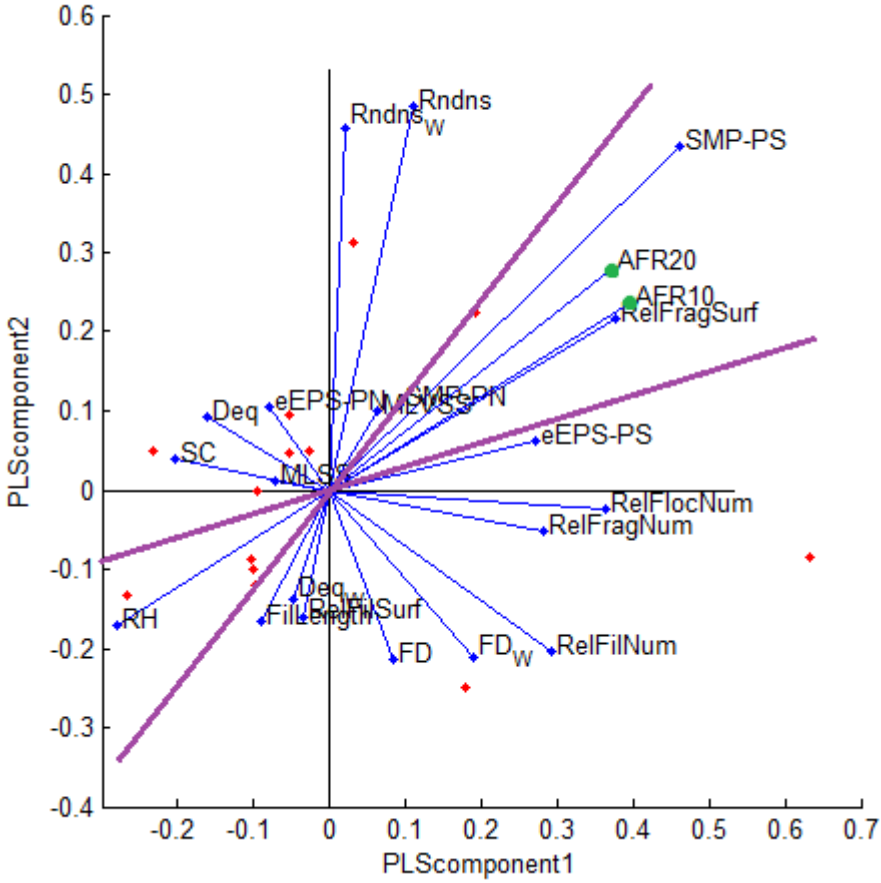

Figure 7.4: Biplot of AFR PLS regression. Weights are denoted by the blue lines, scores are denoted by the small (red) dots.

Although Figure 7.4 depicts a good illustration of the relationships between the different variables, it only depicts the first two PLS dimensions. Different sets of principal components may show different relationships. Therefore, three-dimensional plots can be constructed to include a third PLS-component, or multiple two-dimensional plots can be graphed. Ultimately, all PLS-components can be combined into the β-coefficients, which characterise the regression between the sludge characteristics ($\mathbf{X}$) and the average fouling rates: $\mathbf{AFR} = \beta \cdot \mathbf{X}$. Figure 7.5 depicts the β-regression coefficients between the normalised sludge characteristics and the normalised average fouling rates for a flux of 10 L/m^{2}h (left) and 20 L/m^{2}h (right).

Variables are vertically listed in order of ascending variable influence of projection (VIP) value, with the red line denoting the critical value of VIP >1. Variables under the red line are thus, statistically, deemed relevant. As can be seen on the graph, the SMP-polysaccharide content is, together with the surface of fragments the most influential for the average fouling rate among the samples tested, both deteriorating filtration as their concentrations increase. The eEPS-polysaccharide content is correlated with AFR as well and could be directly attributing to fouling, or be in equilibrium with the SMP. Having hydrophobic flocs is deemed beneficial for filtration.

When the flux increases from 10 to 20 L/m^{2}h, the influence of the hydrophobicity decreases, while the detrimental effect of fragments and SMP-polysaccharides even further increases. Moreover, a slight positive effect of filaments is noted. Presumably, having filaments present might create a secondary network of flocs/filaments that can easily be removed during flux relief and that can capture small particles as they are being sucked towards the membrane. This idea is supported by the negative β value for FilLength and RelFilSurf that increases (absolutely) as the flux increases. However, these values do not have a high VIP-value.

It is clear from the data that the model illustrates the detrimental effect of small particulate (fragments) and colloidal (SMP) on filtration. Moreover, having large (Deq_w) and hydrophobic flocs can improve the filtration properties through the formation of a well structured cake layer.

7.2.2 Irreversible fouling - Global fouling rate

The irreversible fouling is denoted by the global fouling rate (GFR) as explained in Figure 7.1. Using the same dataset and number of PLS-components as the on the AFR, without the outliers, another PLS model was made. The normalised GFR predictions versus measurements are shown in Figure 7.6.

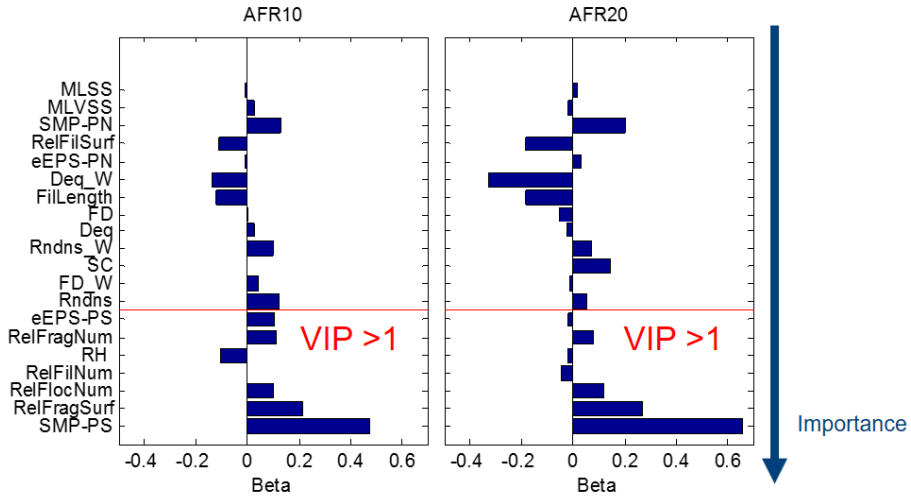

Figure 7.5: Regression coefficients β between normalised sludge characteristics and normalised average fouling rates @10 L/m^{2}h (left) and 20 L/m^{2}h (right).

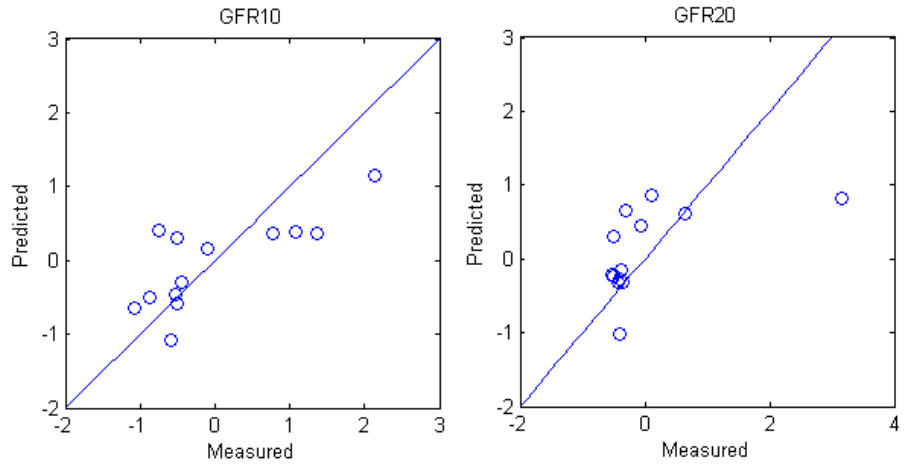

Figure 7.6: Z-scores of measured vs. predicted GFR @ 10 L/m^{2}h (left) and 20 L/m^{2}h (right).

Figure 7.7 depicts the regression coefficients β between the normalised global fouling rates at 10 and 20 L/m^{2}h and the activated sludge characteristics. As can be seen in the figures, both the SMP polysaccharide content and the relative fragment surface remain important for the global fouling rate at both fluxes.

As the suction force decreases when lowering the flux from 20 to 10 L/m^{2}h, the surface characteristics of the flocs become more important than their sizes, probably explaining why the influence of the relative hydrophobicity is more pronounced at the lower flux.

With a higher flux, larger particles are attracted towards the membrane, which explains the increased positive influence of the weighted mean equivalent diameter (Deq_W) on filterability (although this parameter has a VIP slightly lower than 1). The seemingly contradictory behaviour of the roundness (Rndns) variable can be explained in a similar manner. The roundness exhibits a detrimental effect in the case of a low flux, but becomes beneficial for higher fluxes, which might be because small flocs generally are round of shape, due to their limited number of pixels, but when larger flocs are attracted, having flocs of a regularly round shape may attribute to an easier removal by relaxation or backwash.

As mentioned before, having filaments present might create a secondary network of flocs and filaments which protects the membrane from internal fouling, explaining why the relative filament number has a positive impact on reducing the irreversible fouling rate.

7.2.3 Settleability - Sludge volume index

Aside from filterability, the potential use of PLS models was also tested on the settleablity indicator, captured by the sludge volume index (SVI).

Figure 7.8 (left) illustrates the biplot of the first two PLS components, showing variable weights and score values[1]. As can be seen in the figure, the relative filament surface and the mean filament length are he most important variables (largest distance from the origin). Both parameters, together with the surface weighted mean equivalent floc diameter (Deq_W) seem to be closest related to the sludge volume index (depicted with the big (green) dot), while the relative hydrophobicity is situated at the other side of the origin.

[1]The MLSS and MLVSS measurements are left out of the model, since the SVI formula is directly dependent on the MLSS measurement (see Equation (4.6) in Chapter 4).

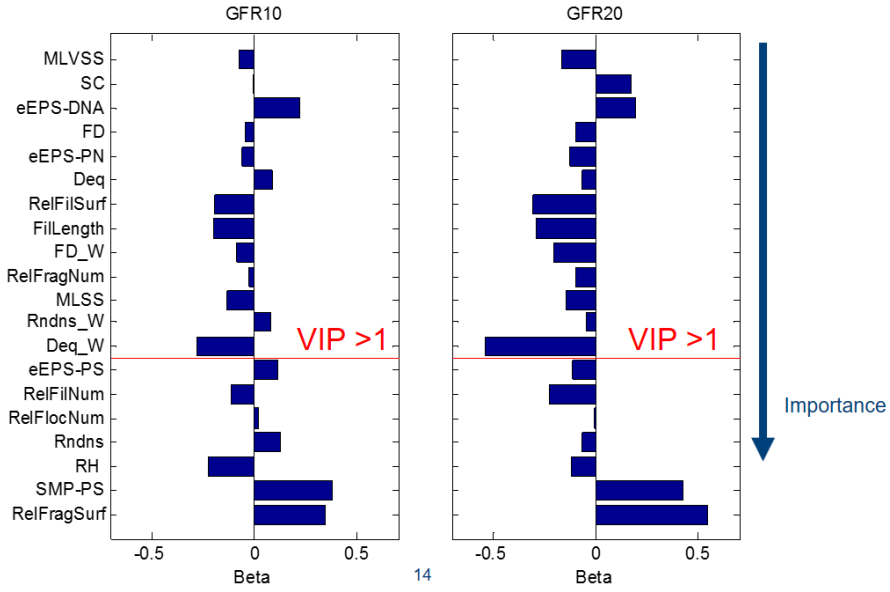

Figure 7.7: Regression coefficients β between normalised sludge characteristics and normalised global fouling rates @10 L/m^{2}h (left) and 20 L/m^{2}h (right).

Figure 7.8 (right) validates these findings, although the relative hydrophobicity does have a VIP slightly smaller than one. The importance of a good balance between filaments and flocs for adequate settling is confirmed.

The model performances for predicting both fouling rates and the settleablity are shown in Table 7.2. Eriksson et al. [2013] suggest that sufficient PLS components are included when the goodness of fit (R^2Y) is larger than 0.9 and the goodness of prediction (Q^2Y) is higher than 0.5. The data from Table 7.2 depict that all three performance indicators can be fitted onto a PLS model of 6 components, retaining more than 95 % of variance within the dataset. Moreover, although the dataset is limited, the average fouling rate can be predicted through crossvalidation with an accuracy of 78 %. This predictive power, however, is lower for the other two performance indicators (GFR and SVI), but still about as much as suggested by Eriksson et al. [2013].

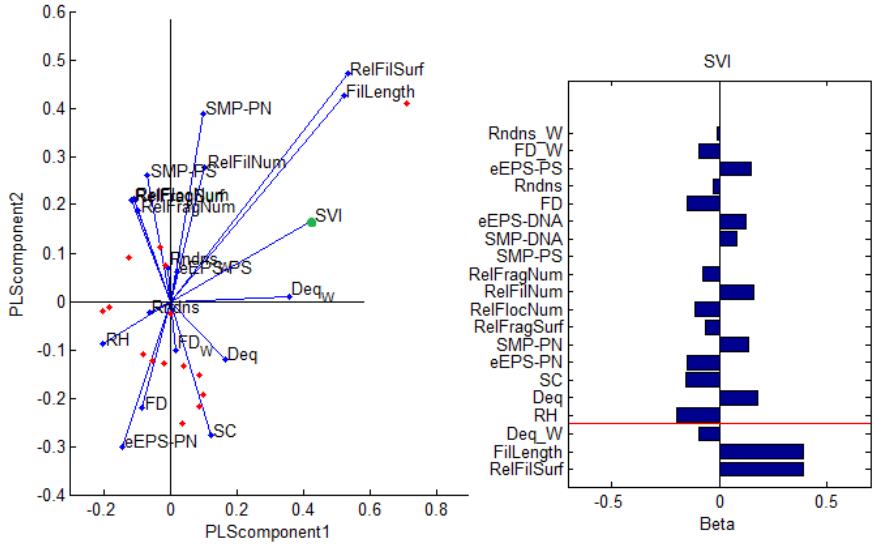

Figure 7.8: Left: biplot of SVI PLS regression. Weights are denoted by the blue lines, scores are denoted by the small (red) dots. The position of the SVI is indicated by the (big) green dot. Right: regression coefficients β between normalised sludge characteristics and sludge volume index.

Table 7.2: PLS regression performance.

	AFR_{10}	AFR_{20}	GFR_{10}	GFR_{20}	SVI
Goodness of fit (R^2Y)	0.9965		0.9914		0.9564
Goodness of prediction Q^2Y)	0.7808		0.5722		0.4837
PRESS	7.90	5.58	5.24	8.50	4.88
Components	6	6	6	6	6

7.3 Conclusion

Partial least squares regression has been demonstrated to be a valuable tool in unravelling the relationship between bioflocculation and activated sludge separation. Two filtration parameters: the average fouling rate, as a measure of reversible fouling and the global fouling rate, as a measure of irreversible

fouling have been linked to sludge characteristics, as well as the settleability, measured through the sludge volume index.

It is clear that although a large number of variables are measured during measurement, only a few of these variables appear to have a significant impact on the PLS model. In the biplot, those are the variables with high absolute weight values, situated close to, or on opposite sides of the origin, of the performance indicator of interest. These variables should be monitored more closely in the process, and by tuning process conditions, like aeration or feeding regime, steered in the direction that increases performance, as depicted in the β-plots.

Although the number of samples was rather limited, a few conclusions regarding the relationships between bioflocculation and separation performance could be drawn.

- The occurrence of small sludge fragments, colloidal matter and polysaccharide content in the soluble microbial products were the most detrimental for filtration among the samples tested.
- Filtration improved when flocs were large, hydrophobic and roundly shaped.
- While the occurrence of some filaments was favourable for filtration, since it led to the creation of a dynamic secondary membrane layer, that could capture incoming small particulate matter, their abundance was confirmed to be the most prevalent cause for sedimentation problems. It must be noted that this hypothesis, although providing a reasonable explanation for the beneficial effect of the filaments, could not be experimentally visualised or verified.
- In general, image analysis related information regarding morphology and size distribution of flocs, together with hydrophobicity were shown to be the most relevant for detecting changes in bioflocculation states, which can affect both filtration and settling performance.

Due to the limited number of samples, no real validation of the proposed models could be performed yet. Crossvalidation provided a reasonable alternative. With a larger number of samples, part of the measured data set can be used for training, while the other part can be used for validation.

It was pointed out in Section 7.2.1 that PLS models are very sensitive towards outliers. In this section, two high outliers had a strong influence on the model, reducing its effectiveness and had to be removed from the dataset. Therefore,

having a good data spread, both in training as validation set, together with adequate data preparation is of high importance. To this end, a comprehensive tutorial that handles data spread and model validation has recently been published by Westad and Marini [2015]. Moreover, since PLS is a data driven technique, adequate physico-chemical background knowledge on the process, remains of key importance, e.g., in selecting the variables included in the model and removal of outliers.

Chapter 8

A study on the longterm interactions between cations and activated sludge separation

8.1 Introduction

In this chapter, the longterm interactions between cations and activated sludge separation techniques are studied. In Section 3.1.3, the divalent cation bridging (DCB) theory was highlighted to be the most influential for bioflocculation. This theory, as explained by [Sobeck and Higgins, 2002], states that multivalent cations can provide a bridge-like binding site between two or more negatively charged functional groups present in the activated sludge/EPS-matrix. Monovalent cations, however, do not possess enough charge to fulfil such role. Therefore, it was postulated that a high ratio of monovalent-over-polyvalent (M/P-ratio) cations would lead to a destabilization of the activated sludge matrix, resulting in deflocculation.

The results of this section have been published in Van De Staey, G., Smits, K., & Smets, I. (2015). An experimental study on the impact of bioflocculation on activated sludge separation techniques. Separation and Purification Technology, 141, 94–104.

Two experiments were performed to assess the validity of the divalent cation bridging theory. In the first experiment (Section 8.2), two conventional lab-scale activated sludge systems were fed with synthetic influent. The first reactor was given a feed that held a low M/P-ratio, while the second reactor's feed contained a high M/P ratio. In both cases glucose was used as a carbon source and both reactors received an equal amount of nutrients and minerals. Deflocculation occured in Reactor 2, whereas in Reactor 1, the activated sludge flocculated further to obtain flocs of over 1 mm diameter.

In the second experiment (Section 8.3), the effect of the reactor configuration was studied. A conventional lab-scale activated sludge system and a lab-scale membrane bioreactor were started up using the low M/P-influent from Experiment I. After a few weeks, both reactors were switched to the high M/P-influent, which was maintained for a prolonged period of time. Deflocculation occurred in both systems. Several months later, the initial feed was given again, to assess whether the sludge could recover from deflocculation after a prolonged period of multivalent cation-deficiency.

8.2 Experiment I: simultaneous M/P differentiation in conventional activated sludge systems

8.2.1 Materials and methods

Lab-scale activated sludge systems

Two 20 L lab-scale activated sludge systems, each connected to a 5 L conical settling tank (see Figure 8.1), were seeded with activated sludge from a full-scale municipal wastewater treatment plant. The reactors were continuously stirred and aerated, resulting in an average dissolved oxygen concentration of over 4 mg/L. On average, $1/25^{th}$ of the total reactor volume, was wasted on a daily basis, resulting in an SRT of 25 days. The pH was monitored on a daily basis and adjusted using 2M NaOH or HCl when it deviated from 6-8.

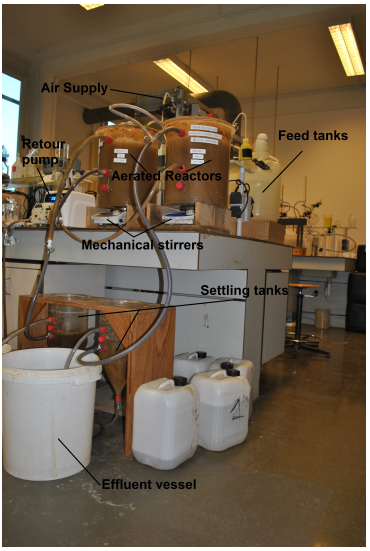

Figure 8.1: Lab-scale conventional activated sludge system.

Synthetic influent

Two synthetic wastewater feeds were designed, based on the work of Van den Broeck et al. [2010]. Table 8.1 depicts the feed compositions. Glucose[1] was chosen as carbon source.

Until day 38 of the experiment, both reactors were given Feed 1, which is characterized by a low monovalent over polyvalent (M/P) cation ratio [2], thus bioflocculation-promoting. From then on, Reactor 2 was given Feed 2, which consisted of a high M/P ratio, aiming at inducing deflocculation.

The overall yield that was assumed is 0.2 g MLSS per g COD. This overall yield takes into account the yield of biomass per gram of COD (0.7 g MLSS/g COD), the decay rate of the sludge (0.1 day^{-1}) and the sludge retention time, the latter set at 25 days. In combination with a targeted steady state MLSS concentration of 5 g MLSS, 25 g COD/day had to be administered which was divided over 5 L of feed solution, corresponding with a steady state sludge loading of 0.2 g COD/

[1] Although acetate is sometimes regarded as a more representative carbon source for wastewaters, it was opted to stick to glucose, to enable comparison with previously published work.

[2] The cation ratio is expressed in terms of equivalents, with an equivalent being equal to the number of moles of the ion multiplied by its valence.

g MLSS.day. The daily 5 L synthetic wastewater was administered during 10 feeding periods of 20 minutes each, rather than continuously to suppress growth of filamentous organisms as much as possible. This resulted in an average HRT of four days, which should enable the activated sludge to successfully break down the feed.

Table 8.1: Synthetic wastewater feeds.

Feed 1 Low M/P		Feed 2 High M/P	
Component	mg/L	Component	mg/L
$C_6H_{12}O_6$	4080	$C_6H_{12}O_6$	4080
Yeast extract	240	Yeast extract	240
$(NH_4)_2HPO_4$	347	$(NH_4)_2HPO_4$	901
$FeCl_3$	139	$FeCl_3$	14
$CaCl_2$	132	$CaCl_2$	91
NH_4NO_3	955	K_2HPO_4	3000
KCl	138	NaCl	120
Na_2SO_4	212	$MgSO_4 \cdot 7\,H_2O$	120
$MgCl_2 \cdot 6\,H_2O$	602		
M/P	2.02	M/P	17.4
Ionic strength	23 mM	Ionic strength	28 mM

Sludge characterisation

Most characterisation methods have been discussed in Section 4.1. The following variables have been measured in this study.

- Mixed liquor (volatile) suspended solids (ML(V)SS) - Section 4.1.1.
- Relative hydrophobicity (RH) - Section 4.1.3.
- SMP extraction: proteins and polysaccharides - Section 4.1.5.
- eEPS heat extraction: proteins and polysaccharides - Section 4.1.5.

- Phase contrast microscopy[3] and image analysis (ASIAP) - Section 4.1.6 and Chapter 5.

Performance indicators

To assess the activated sludge separation efficiency, three types of performance indicators were used. **Settleability** was measured using the sludge volume index (Section 4.2.1).

The dead-end filterability as a measure of the sludge **dewaterability**, was measured by means of the time to filter (TTF_{25}) and the weight of filtrate (WOF_{250}), as explained in Section 4.2.2.

To assess **cross-flow filterability**, the small-scale filtration test set-up was used (Section 4.2.3). The smallest version of the set-up was used, with a working volume of 1.6 L. Figure 8.2 (left) illustrates the flux-step experiment that was carried out on activated sludge from each reactor on a weekly basis. The flux ranges from 3 L/m^{2}h up to 33 L/m^{2}h, going up with 3 L/m^{2}h intervals.

A stepwise increase with downstepping, based on the work of Espinasse et al. [2002], was chosen over the classical up-down profile. The reasoning behind this choice is twofold: firstly, the time interval between two fluxes of the same magnitude is always equal, enabling a fair calculation of the irreversible fouling for each flux. Secondly, the fluxes increase throughout the experiment. Should, due to intense fouling, the pressure sensor reach its maximum measurable value, then the filtration stops. Since this is more likely to happen for higher fluxes, they are measured lastly. From the flux-step experiment, the *sustainable flux* ($SF_{0.5}$) is determined.

The definition of the sustainable flux used in this research is based on the work of van der Marel et al. [2009]. For each flux-step, the fouling rate (FR) is defined as the average rate at which the transmembrane pressure increases during filtration, hence the slope of the first order fit through the time-TMP profile. The sustainable flux ($SF_{0.5}$), as graphically illustrated in Figure 8.2 (right), is then defined as the flux for which this fouling rate is consistently higher than an arbitrary threshold value. As a threshold value, 0.5 mbar/min was prefered over the suggested 0.1 mbar/min, since by doing so, differences in filterability for both sludge types emerge more clearly.

[3]Part of the images analysed during this study were taken using the old Olympus BX51 microscope. For these images, variables are expressed per image. For the images taken using the new Olympus IX83 microscope (with stitching), variables are expressed per megapixel.

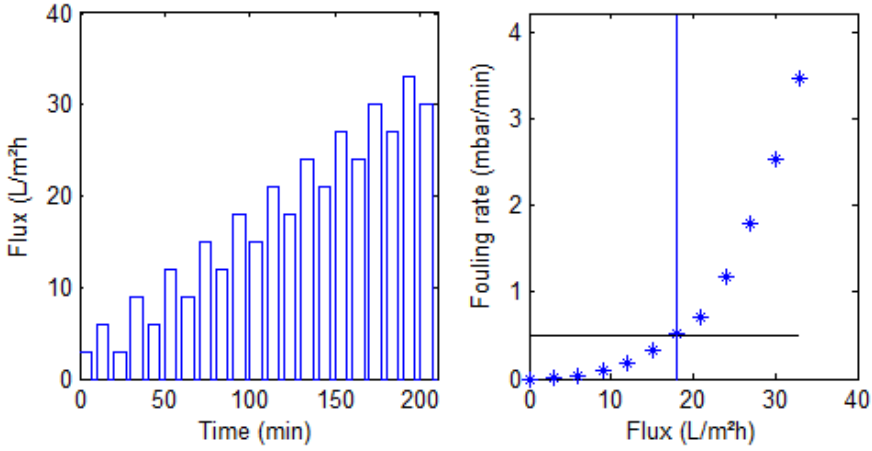

Figure 8.2: **Left**: flux-step profile. **Right**: determination of sustainable flux from flux-fouling rate profile. The sustainable flux is shown as the vertical line.

8.2.2 Results

The MLSS in both reactors fluctuated around 5 g/L, as intended, and were 4.79 ± 0.78 and 5.00 ± 0.15 g/L for Reactors 1 and 2, respectively. Biological performance was measured by the filtered effluent COD, which indicated at least 97% of carbon removal throughout the experiment. Moreover, the effluent suspended solids (ESS), remained well below 4% of the sludge's MLSS, except on a few instances where settleability was hampered, or when tube-plugging issues caused subsequent sludge overflow in the effluent vessel. The mean ESS values for Reactors 1 and 2 were, respectively, 0.094 ± 0.086 g/L and 0.104 ± 0.088 g/L.

Figure 8.3 depicts the sustainable flux throughout the experiment. The dead-end filtration characteristics are shown in Figure 8.4. The duration of the experiment is divided into five consecutive periods, which will be discussed in more detail.

A first glance at the overall filterability of Reactor 2 (Figures 8.3 and 8.4), shows that the high M/P influent led to a general deterioration of filtration properties in comparison with Reactor 1, which received the bioflocculation-promoting, low M/P influent.

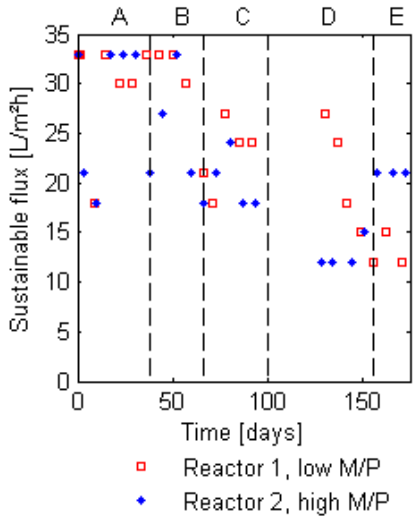

Figure 8.3: Evolution of the sustainable flux ($SF_{0.5}$) throughout the experiment.

Period A (days 1-38) - Adaptation

During the first 38 days of operation, both reactors were given the low M/P feed. Waste sludge was removed starting from day 15. During Period A, the communal activated sludge adapted to the laboratory conditions, favouring growth of those organisms that are best suited to break down the synthetic glucose-based feed. As both reactors were given the same feed, the activated sludge was expected to evolve similarly.

During the first period, the organic fraction of both reactors, as calculated by the MLVSS/MLSS ratio, increased from 68 % to 84%, after which it remained constant throughout the experiment. By day 22, the dead-end filtration characteristics of Reactor 2 reach a maximum steady state value. Reactor 1, on the other hand, did not show stable filtration characteristics after 22 days, which can be explained by measured pH fluctuations (data not shown).

Nevertheless, on day 38, when the pH in Reactor 1 had been stable for several days, the contents of both reactors were mixed and redistributed over both vessels. Subsequently, the influent of Reactor 2 was changed to the high M/P feed, while Reactor 1 continued to receive the low M/P feed.

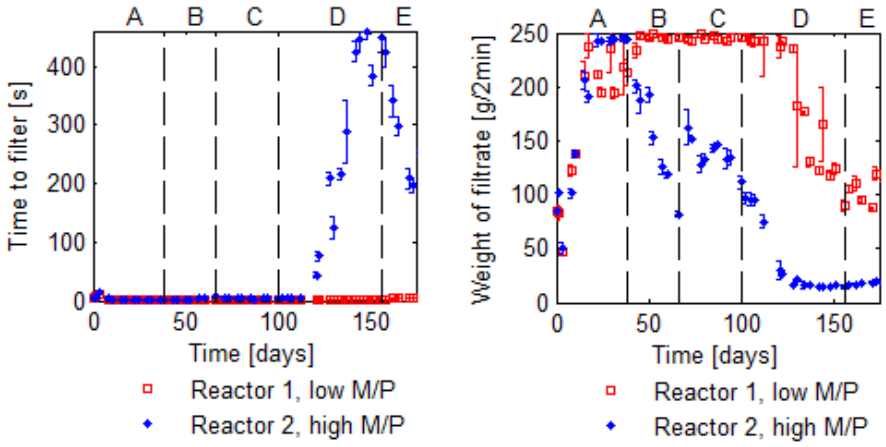

Figure 8.4: Evolution of the dead-end filtration characteristics throughout the experiment. **Left:** time to filter (TTF_{25})., **Right:** weight of filtrate (WOF_{250}).

Period B (days 38-66) - Filaments in Reactor 1. Deflocculation in Reactor 2

From day 38 on, the sludge in Reactor 2 was subjected to Feed 2, containing a relatively higher amount of monovalent cations. This change induced significant deterioration of the filtration properties of the sludge in Reactor 2, which could be attributed to deflocculation. Evidence of this deflocculation is illustrated by the decrease in the area-weighted average equivalent floc diameter Deq_W and the increase in the number of flocs per image, both depicted in Figure 8.5.

The equivalent floc diameters Deq_W diverge significantly ($p = 0.0256$) as Reactor 1 successfully recovers from the pH disturbances, and improves in flocculation. This is shown in Figure 8.5 (left), that depicts an increase in average floc diameter, and in Figure 8.5 (right), that shows an increase in the number of flocs, meaning more organic material flocculates, resulting in less small particulate matter in the reactor. Moreover, Reactor 1 reaches optimal dead-end filterability, confirming the positive effect of well flocculated sludge on filtration.

The evolution of the relative hydrophobicity is shown in Figure 8.6. The measurements indicate a significant divergence between Reactor 1 and 2 that initiates around day 40 and continues until the end of the experiment.

During the last weeks of Period B, the number of filamentous bacteria increased tremendously in Reactor 1. This increase was noticed by the rise in total

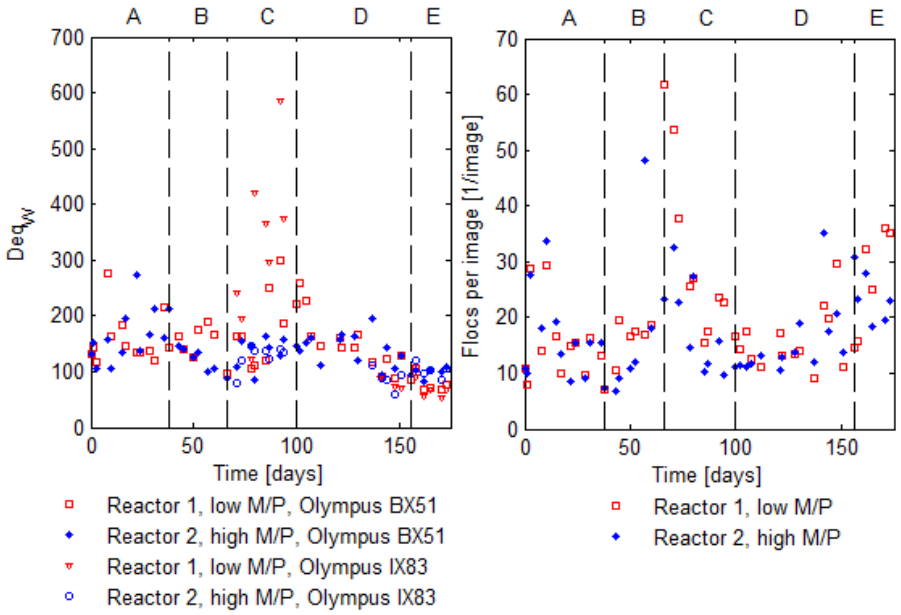

Figure 8.5: **Left**: evolution of the area-weighted average equivalent floc diameter Deq_W throughout the experiment. Filled symbols are taken using the Olympus BX51 microscope, open symbols are taken using the more advanced Olympus IX83 microscope, enabling stitching of images and analysis of large flocs that span multiple fields of view. Data differ significantly during Period B, p= 0.0256, during Period C, p=0.00266 and Period E, p=0.006225. **Right**: evolution of the number of flocs per image throughout the experiment. Data differ significantly during Period C, p=0.0.004 and during Period E, p=0.045.

filament length per image, as depicted in Figure 8.7 (left) and resulted in a significant increase in SVI, which corresponds to bad settleability (Figure 8.7 (right)) and in bad cross-flow filterability (Figure 8.3). Dead-end filterability, however, remained high (Figure 8.4).

The exact cause of this sudden increase in filamentous bacteria is unknown, since the feast-faminefeeding pattern is known to be floc-formation promoting [Chiesa et al., 1985]. Possibly, the proposed feast-famine regime was still too continuous, or some filamentous organisms were seeded from contaminations in the feeding tubes, where oxygen concentrations were low and thus growth of

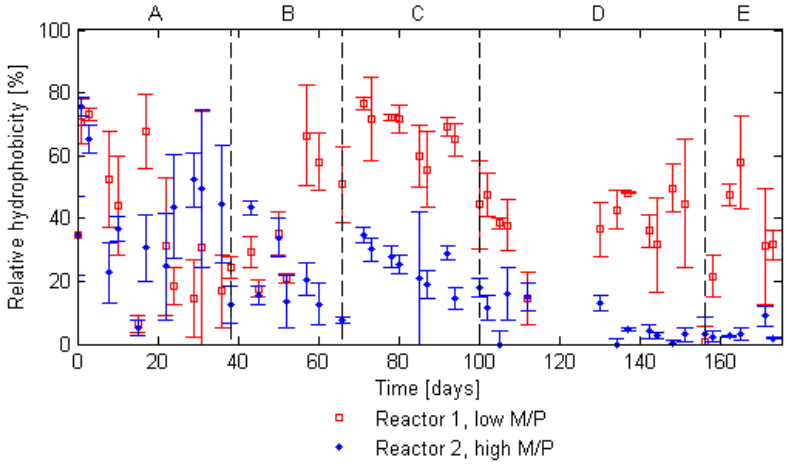

Figure 8.6: Evolution of the relative hydrophobicity throughout the experiment.

filamentous bacteria was favoured.

A plausible reason why the occurrence only took place in Reactor 1, is that due to the higher number of polyvalent cations in this reactor, successful integration of the filaments into the floc structure was enabled, whereas in the second reactor, they could have been washed out if they were not successfully integrated into the well settling sludge.

Throughout the whole experiment, Reactor 2 showed a very low amount of filaments, resulting in an imbalance between flocs and filaments. The absence of filaments coincided with the high abundance of monovalent cations, resulting in strong deflocculation throughout the experiment.

Period C (days 66-100) - Megaflocs in Reactor 1. Partial reflocculation in Reactor 2

Period C starts at day 66 and is initiated by a small deflocculation event in Reactor 1, as shown in Figures 8.5 (left) and 8.5 (right), which has probably been caused by a decrease in pH[4].

[4]From time to time acidification of the glucose feed solution (probably due to contamination of the feed) caused pH disturbances in the reactor. As the pH was measured on a daily basis, and adjusted using NaOH when it deviated below 6, the pH was neutral for the major duration of the experiment. The fluctuations took place in both reactors, but seemed more

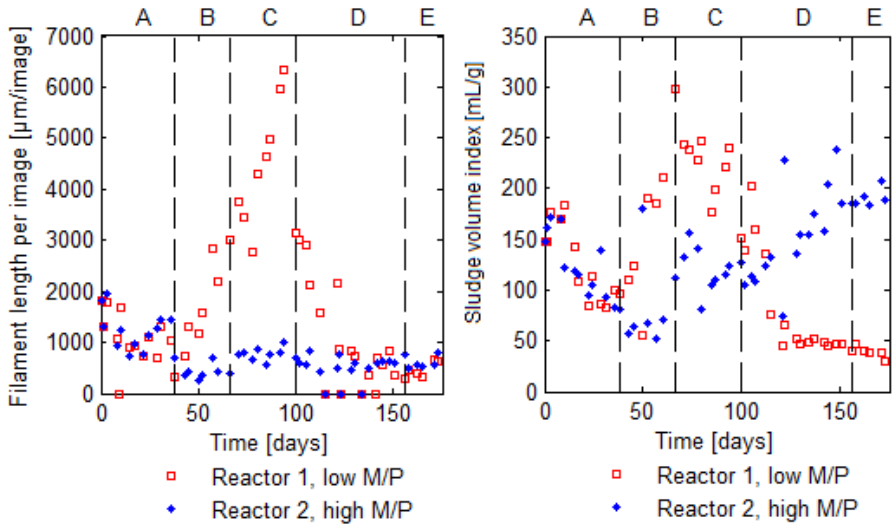

Figure 8.7: **Left**: evolution of the total filament length per image throughout the experiment. **Right**: evolution of the sludge volume index throughout the experiment.

The consequences of this deflocculation event, which are a large increase in floc numbers and a noticeable decrease in Deq_W, resulted in a significant decrease of the cross-flow filterability (Figure 8.3). The dead-end filtration characteristics, however, remained unchanged.

Only a few days after the deflocculation, very significant reflocculation took place. Due to the reshaping and re-attachment of the sludge flocs onto the filamentous backbone structure, very voluminous activated sludge flocs (megaflocs, see Figure 8.8) were formed in Reactor 1, as clearly shown by the change in the area-weighted average floc diameter in Figure 8.5 (left). As the sludge flocs completely covered the field of view of the Olympus BX51 microscope, stiched images were obtained using the more advanced Olympus IX83, which explains the difference in measurements with both microscopes in Figure 8.5 (left) for Reactor 1 during Period C.

The formed sludge flocs did not settle well due to the presence of numerous

pronounced in Reactor 1. Note, furthermore, that, around day 66, pH measurements were not possible for a few days. Given that the corresponding neutralization by NaOH could not be implemented, the occurrence of a pH disturbance, probably led to a short period of a few hours where the pH was below 5.

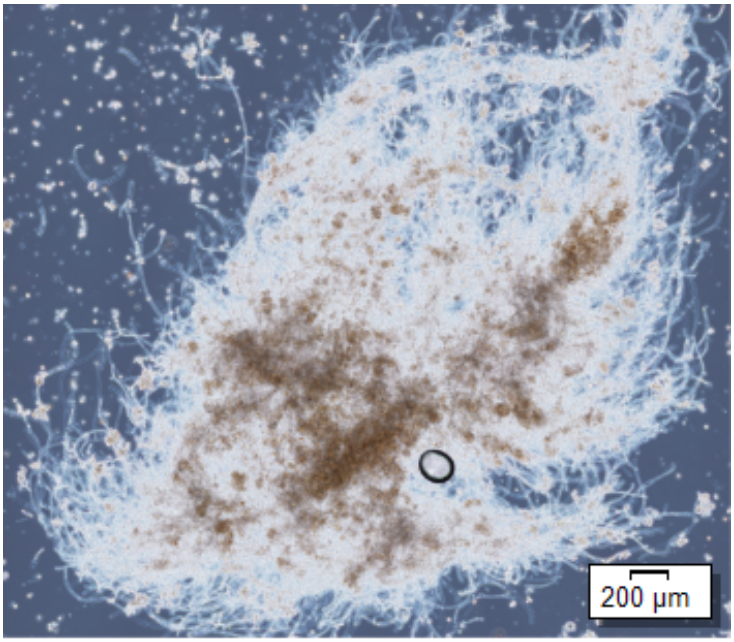

Figure 8.8: Proliferation of very voluminous activated sludge flocs (megaflocs) in Reactor 1 during Period C.

filaments as shown by Figure 8.7. These filaments probably also contributed to the further rise in relative hydrophobicity, that was measured in Reactor 1 during this period. Possibly, the earlier pH disturbances allowed for proliferation of yeast, which could also explain the presence of these hydrophobic *filaments*.

Moreover, the flocs were so large in size, that the air-scouring induced turbulence prevented them from contributing to cake layer formation during MBR-filtration, leaving the membrane vulnerable to the smaller, more fouling, activated sludge constituents. Therefore, although bioflocculation was very strong in Reactor 1, cross-flow filtration performance was not significantly altered.

The dead-end filtration characteristics, on the other hand, where influenced by the bioflocculation, which resulted in very good filtration performance due to the formation of a well structured, porous cake layer.

During Period C, a partial reflocculation took place in Reactor 2, resulting in an increase in floc diameter (Figure 8.5 (left)). This reflocculation resulted in an improvement of both filtration characteristics.

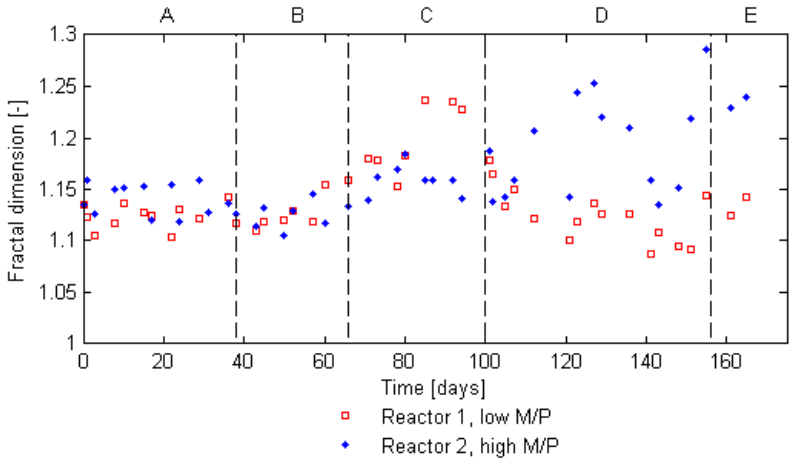

Figure 8.9: Evolution of the fractal dimension throughout the experiment.

Figure 8.9 depicts the course of the fractal dimension throughout the experiment. The fractal dimension is a measure for the roughness/irregularity of the floc's edges and is measured using the Box-counting algorithm as a value between 1 and 2, with a higher values corresponding to more irregular perimeters. As can be seen in the figure, the fractal dimension increases for Reactor 1 during Period C as the filaments manifest, while it remained rather constant for Reactor 2 until day 100.

Period D (days 100-156)- Loss of filaments in Reactor 1. Continued deflocculation in Reactor 2

From day 100 on, the situations in both reactors started to change. In Reactor 1, a steady decrease of filaments manifested, as can be seen by the decrease in total filament length (Figure 8.7 (left)). This decrease resulted in a reduction in average floc diameter and fractal dimension, but also improved settlability, which is shown in the SVI profile (right). Moreover, the loss of filaments in Reactor 1, occured in parallel with a decrease in relative hydrophobicity (Figure 8.6), corroborating the possible connection between both parameters, through the proliferation of an hydrophobic filamentous bacteria or yeast.

The smaller floc sizes in Reactor 1 did not show much change in the WOF_{250} and TTF_{25} profiles during the first weeks of Period D. During this period,

the small-scale filtration set-up was not available. However, from day 125, a significant deterioration of the dead-end and cross-flow filtration parameters was observed. At this time, the number of filaments had dropped even below its initial value, significantly impacting bioflocculation due to the loss of a filamentous backbone to which flocs could deposit. As the activated sludge was present in smaller flocs, more biomass was able to contribute to the fouling layer during the flux-step test, resulting in a steep drop in sustainable flux.

In Period D, Reactor 2 continued to deflocculate, which was evidenced by an, although fluctuating, increase in number of flocs. Moreover, the flocs became more irregularly shaped and seemed more and more stripped of all dense filling material. This observation is illustrated by Figure 8.10, that shows typical sludge morphologies at the end of Period D. Moreover, the fractal dimension of Reactor 2 increases significantly during Period D and although some fluctuations are observed, it reaches its maximum around day 156.

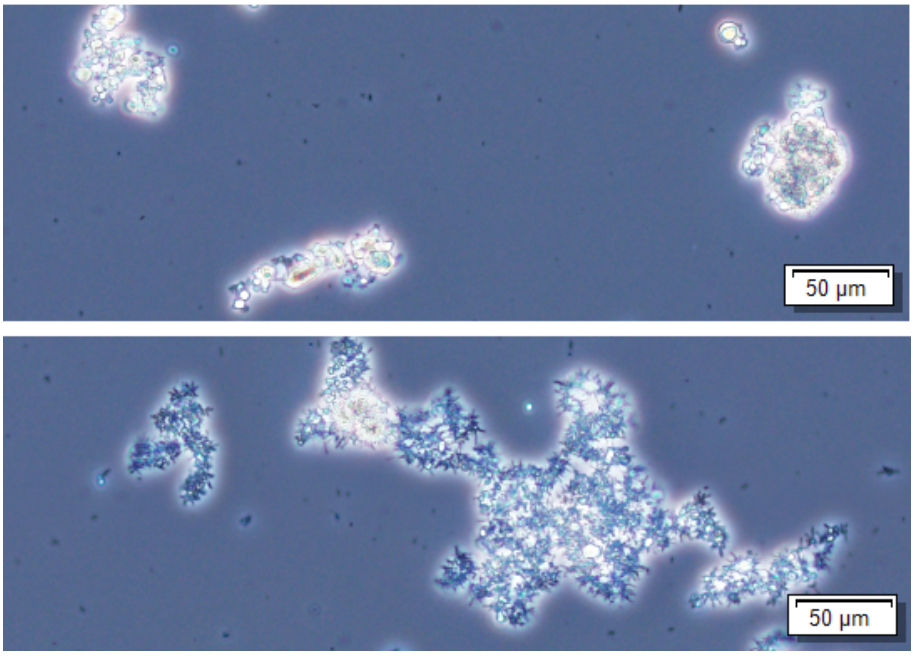

Figure 8.10: Morphology in Reactor 1 (top) and Reactor 2 (bottom) at the end of Period D.

During the further deflocculation of Reactor 2, the relative hydrophobicity dropped to an absolute minimum level, indicating that the loss of hydrophobicity

worsened bioflocculation. The filterability of Reactor 2 was poor, indicated by the high TTF_{25} and the low sustainable flux.

Period E (days 156-178)- Decreased filterability in Reactor 1. *Empty* flocs in Reactor 2

Period E is defined by a decrease of cross-flow filterability in Reactor 1 and an increase in Reactor 2.

In Reactor 2, most of the dense filling material that had been released into the bulk suspension during Period D, had been washed out by then. This gradual decrease of small constituents, caused a slow improvement in time to filter and weight of filtrate, and resulted in a significant increase in sustainable flux. The difference in filtration improvement for both modes can be explained by the floc size. Since the small constituents have been washed out, only medium sized flocs remain, which, due to the high aeration rate, do not contribute as much to the fouling layer during the submerged filtration. During the dead-end filtration, however, they still remain able to foul the membrane. SVI and relative hydrophobicity remained unchanged in comparison with the end of Period D. Flocs remain *empty*, which corresponds to a very irregular shape and a high fractal dimension (Figure 8.9).

In Reactor 1, filament numbers had been drastically reduced, which led to a low average floc diameter and a high number of smaller flocs and fragments, resulting in an increase in time to filter and sustainable flux by the end of Period E.

Relative hydrophobicity in Reactor 1 remained significantly higher than in Reactor 2, although not as high as during Period C, which confirms that the abundance of filaments during Period C was (at least) partly responsible for the high hydrophobicity.

Role of extracellular polymeric substances

EPS were measured as the protein and polysaccharides present in the soluble and thermally extractable extracellular polymeric substances (see Section 4.1.5). Data is shown in Figure 8.11. In general, the polysaccharide content was higher than the protein content in both reactors.

Noticable is the higher eEPS protein content in Reactor 2, which corresponds to a lower relative hydrophobicity. This suggests that in this research the

eEPS proteins could not directly be linked to the overall hydrophobicity of the activated sludge.

The higher concentration of EPS proteins in Reactor 2 could possibly be attributed to the reduced resistance of the bound EPS to the heat treatment, as the number of binding cations was lower, or might be attributed to differences in microbial communities in both reactors.

The soluble protein fraction showed no significant trend after the start-up phase and remained rather low for both reactors. However, short-term increases are noted in Reactor 2 which affirms indications of deflocculation periods during which filling activated sludge constituents were released in the bulk mixture, which according to Figure 8.11, probably consisted of SMP-proteins.

During Period C, the eEPS polysaccharides were of much higher concentration in Reactor 1, coinciding with the occurrence of filaments. Presumably, the bacteria present produced a higher amount of polysaccharides in their EPS layer.

The difference in polysaccharide content was also noted in the soluble EPS and was much higher in Reactor 1. This could be attributed to microbial differences or residuals of the glucose-based feed, as glucose was also used as a standard for polysaccharide measurements.

8.2.3 Discussion

In the first reactor, that received the low M/P feed, the abundance of polyvalent cations led to the incorporation of numerous filaments in the floc structure and yielded very large flocs, through the formation of cation bridges.

During the abundance of filaments, the activated sludge could be characterized as bulking sludge and showed very bad settleability.

On the other hand, dead-end filterability was improved, since a well structured, porous cake layer could be formed.

However, the flocs were too large to contribute to the fouling layer in the cross-flow set-up, which led to a small decrease in performance, since, according to the force-balance theory only the smaller constituents are able to foul the membrane [Broeckmann et al., 2006], which was verified by Meng et al. [2008], who noted a significant increase in relative content of colloidal particles and solutes on the membrane as compared to the sludge suspension. As the aeration rate ($5.75\ Nm^3/m^2h$) was relatively high as compared to other studies, the provided shear probably caused most of the larger flocs to stay in the bulk

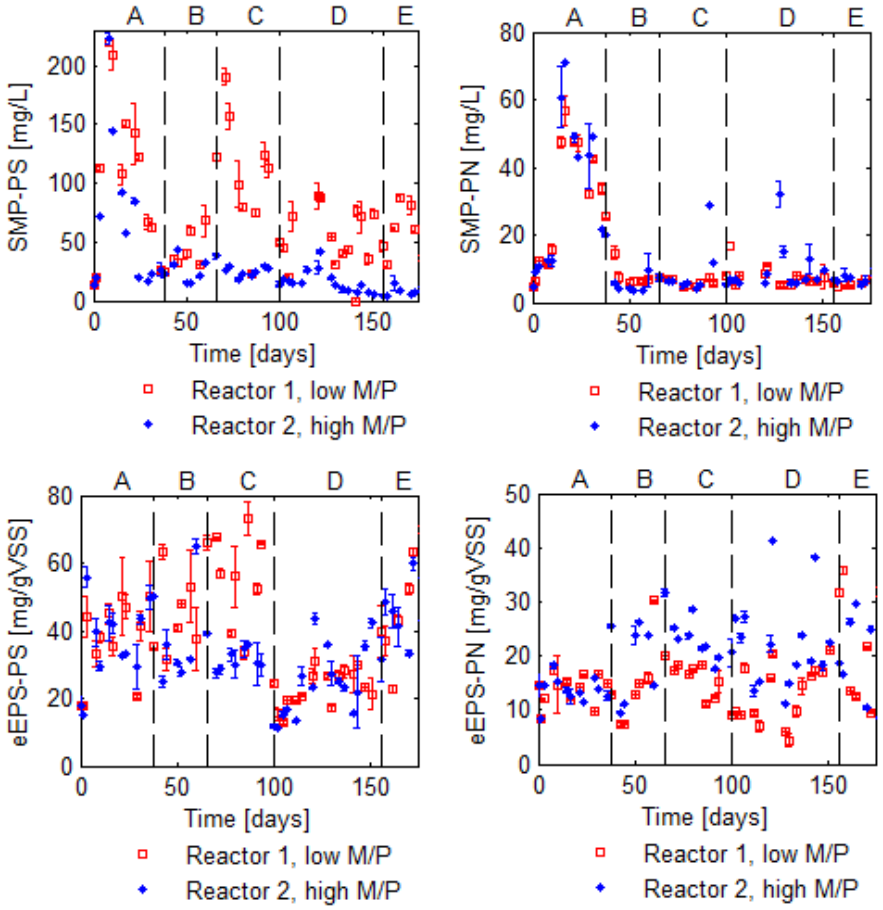

Figure 8.11: Evolution of extracellular polymeric substances throught the course of the experiment. **Top:** Soluble microbial products. **Bottom:** Thermally extractable EPS. **Left:** Polysaccharides. **Right:** Proteins.

liquid phase [Braak et al., 2011; Prieske et al., 2010; Van den Brink et al., 2011; Wu et al., 2012].

Moreover, it can be observed that dead-end filtration tests are not always able to make a good prediction regarding MBR-filtration of activated sludge, affirming the importance of using small-scale cross-flow filtration tests.

In Reactor 1, the relative hydrophobicity was high, which could be partly attributed to the filaments, since several species are known to be of hydrophobic nature, often involved in foaming problems (e.g., filamentous *Alphaproteobacteria*) [Seviour and Nielsen, 1998].

The reason for the sudden occurrence of the filaments is unknown as the floc forming bacteria were promoted by the feast-famine feeding regime, but after two sludge retention times, the number of filaments decreased again to their initial levels. This decrease resulted in smaller floc sizes in Reactor 1, which led to a better settleability, but a worsened dead-end and cross-flow filterability, as more small constituents were able to cause fouling due to the floc detachment.

In the second reactor, the number of filaments was low throughout the whole experiment, which led to a rather ill-defined filamentous backbone throughout the whole experiment. Moreover, Reactor 2 received numerous monovalent cations, which, according to the divalent cation bridging theory, are not suited for bridging between negatively charged functional groups within the activated sludge [Sobeck and Higgins, 2002]. Hence, the sludge in this reactor, slowly deflocculated over time, resulting in a decrease in filtration performance.

Furthermore, results show the release of particles into the bulk suspension, which worsened filterability, similarly to the detrimental effect of submicron particles as highlighted by the works of Mikkelsen and Keiding [2002a], Ivanovic et al. [2008], Gao et al. [2013], De Temmerman et al. [2014] and Faust et al. [2014].

During the last period of the experiment, filterability in Reactor 2 improved since most of the released biomass particles had been washed out or removed through waste sludge.

The release of filling material caused the sludge flocs' edges to appear irregular and *empty*, which led to a bad settleability near the end of the experiment. The released material consisted probably of SMP-proteins.

Bound polysaccharide EPS contents were higher than protein contents, which is in agreement with Meng and Yang [2007] and Van Dierdonck et al. [2013b]. Nevertheless, the protein content was the highest in Reactor 2, where sludge was of hydrophilic nature, thus the hydrophobic character of bound EPS protein, as observed by Jorand et al. [1998], and Van Dierdonck et al. [2013b] could not be confirmed and the results are more in agreement with Wilén et al. [2003], who measured a negative correlation between total EPS content and relative hydrophobicity.

EPS production and composition was found to be varying along with sludge morphology and microbial community during all periods in both reactors. This

observation affirms the work of Lin et al. [2011], which states that small and large flocs have different microbial communities and that certain species appear to be responsible for producing more EPS. This idea is illustrated in Period C, where EPS-polysaccharide content peaks in Reactor 1 during the abundance of filaments and the manifestation of bulking sludge, but diminishes along with the reduction of filaments during Period D. A similar observation was made by Meng and Yang [2007], who noted an increased bound EPS content in bulking sludge as compared to deflocculated sludge.

An important final remark is that, in Experiment I, both reactors were conventional aerated systems. As will be shown in the next experiment, these systems are less vulnerable for disturbances that induce flocculation, since they naturally select for well settling, dense bioflocs [Christensen et al., 2015]. Small particulate and colloidal matter does not have a well-settling tendency and can easily escape the conventional system via the effluent. In Experiment II, the extent of this configuration-influence on separation performance will be studied.

8.3 Experiment II: temporal M/P differentiation in a conventional activated sludge system and a membrane bioreactor

8.3.1 Materials and methods

Lab-scale wastewater treatment systems

To study the activated sludge bioflocculation in the different treatment schemes, lab-scale set-ups were designed for both the membrane bioreactor configuration and the conventional aerated system. Both set-ups had a total volume of 25 L and were subjected to the same synthetic influent. On average, $1/25^{th}$ of the total reactor volume was wasted on a daily basis from each reactor, resulting in an SRT of 25 days. The different set-ups and the influent will be discussed in the next paragraphs.

Membrane bioreactor (MBR). A 25 L submerged lab-scale membrane bioreactor (Figure 8.12) was equiped with a flat sheet membrane of 0.11 m^2 (Kubota, Type 203 cartridge) with nominal pore size of 0.4 µm. Air sparging provided a constant membrane cross-flow velocity of 1.5 m/s. During the major part of the experiment, the flux was set at 15 L/m^2h, but during days 158-168, when severe filterability issues occurred, the flux was lowered to 10 L/m^2h. In

order to treat the desired 6 L of daily influent, the filtration/relaxation regime was set to 8 min/45 min and 8 min/28 min for the fluxes of 15 and 10 L/m^{2}h, respectively. The reactor level, transmembrane pressure (TMP), permeate flow, pH and dissolved oxygen level were monitored and controlled using an online data acquisition system (NI PCI-6229, National Instruments) and software (LabVIEW 8.0, National Instruments). From the TMP data, the MBR-fouling rate, expressed as the TMP-increase per minute of filtration during the filtration steps, was calculated.

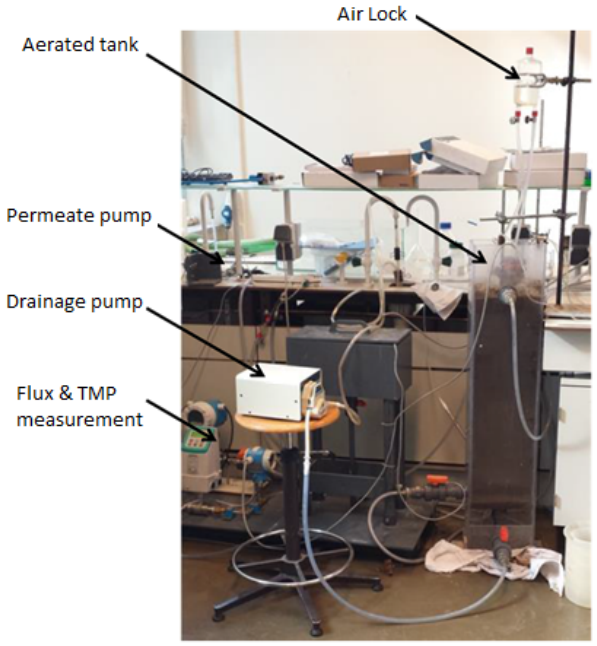

Figure 8.12: Lab-scale membrane bioreactor.

Conventional activated sludge system (CAS). A 20 L aerated stirred tank reactor, connected to a 5 L conical settling tank (see Section 8.2.1 and Figure 8.1), was used as a lab-scale conventional aerated system. The reactor was continuously stirred and aerated, resulting in an average dissolved oxygen concentration of over 4 mg/L. The pH was monitored on a daily basis and adjusted using 2M NaOH or HCl when it deviated from the 6 to 8 pH value range.

Synthetic influent. The synthetic influents were made with the same composition as in Experiment I (see Table 8.1). Treating 6 L influent/day, the resulting HRT of around 4 days should provide a long enough contact time for the biomass to break down the influent COD and nutrients. Dilution of the feed was done in the reactor rather than in advance. The synthetic wastewater consisted of 3 highly concentrated stock solutions, containing, respectively, the carbon source (glucose), the chlorides and the other salts, to avoid precipitation. From each of these solutions, 100 mL was administered on a daily basis, split into four feeding moments, and diluted with a continuous flow of demineralised water, adding up to a total of 6 L per day. The feeding regime was different than in Experiment I and was adapted to uncouple the strict dosing of the feast-famine regime with a continuous supply of water to maintain a constant reactor level and to avoid growth of microorganisms and precipitation in the feeding tanks and tubing.

Sludge characterisation

Most characterisation methods have been discussed in Section 4.1. The following variables have been measured in this experiment.

- Mixed liquor (volatile) suspended solids (ML(V)SS) - Section 4.1.1.
- Relative hydrophobicity (RH) - Section 4.1.3.
- Surface charge (SC) - Section 4.1.4.
- SMP extraction: proteins and polysaccharides - Section 4.1.5.
- eEPS heat extraction: proteins and polysaccharides - Section 4.1.5.
- Phase contrast microscopy (ASIAP) - Section 4.1.6 and Chapter 5. The microscopy parameters used in this experiment are depicted in Table 8.2.

Performance indicators

The following performance indicators are used in Experiment II.

Settleability. Sludge volume index (SVI) - Section 4.2.1.

Dead-end filterability/dewaterability. Time to filter (TTF_{25}) and weight of filtration (WOF_{250}) - Section 4.2.2.

Table 8.2: Image analysis parameters used in Experiment II.

Abbreviation	Description	Units
RelFlocNum	Number of sludge flocs per megapixel of image	Megapixel^{-1}
RelFilNum	Number of sludge filaments per megapixel of image	Megapixel^{-1}
RelFragNum	Number of sludge fragments (diameter < 5 μm) per megapixel of image	Megapixel^{-1}
RelFilSurf	Pixel area of filaments per megapixel of image	(-)
RelFragSurf	Pixel area of sludge fragments per megapixel of image	(-)
$A_{<13\mu m}$	Area fraction of objects with diameter < 13 μm	%
Deq_W	Mean equivalent floc diameter, weighted with floc size	μm
FilLength	Mean filament length	μm
FD	Mean fractal dimension of flocs (box counting algorithm)	(-)

Cross-flow filterability. Average fouling rate (AFR) and global fouling rate (GFR) measured at fluxes of 10 and 20 L/m^{2}h using the 2 L filtration setup, equipped with a standard A4 Kubota membrane (type 203 cartridge) - Sections 4.2.3 and 7.1.3.

8.3.2 MBR filtration - trends explained

Figure 8.13 depicts the MBR flux and TMP profile, as well as the average fouling rate at 10 L/m^{2}h (AFR_{10}) for the MBR sludge. This filtration profile is divided into seven periods, which will be discussed in the next paragraphs. The AFR_{10} profile, which is plotted on the same chart (different vertical axis), illustrates how the 2 L lab-scale filtration setup can successfully monitor trends of TMP and fouling rates. Above the chart, the feeding regime is depicted.

Both reactors start off with the low M/P influent. It is shown that after Period 1 (day 31), the influent is altered to contain a higher M/P ratio and is maintained until Period 6 (day 170), when it is changed back to the initial feed.

Table 8.3 summarizes the average values of the performance indicators ($AFR_{10,20}$, GFR_{10}, SVI, TTF_{25}, WOF_{250}) and selected sludge characteristics for each period.

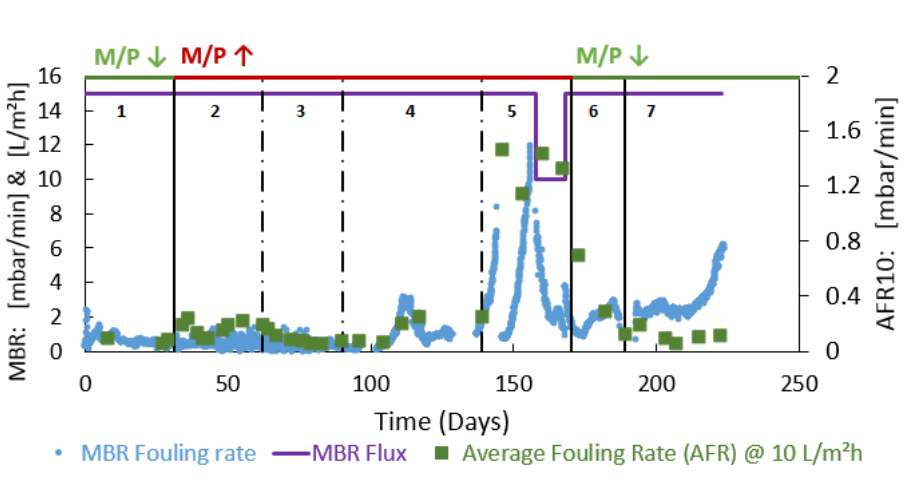

Figure 8.13: MBR filtration profile. Some modifications to the existing infrastructure had to be made, in which the MBR monitoring program was temporarily unavailable during days 96-102 and 126-137.

The selected sludge characteristics are a subset of the whole measurement range, selected based on their relevance and ability to describe the observed trends in the performance indicators. The values of the bound extracellular polymeric substances (eEPS) composition are omitted, since no trend or significant correlation was observed with neither performance indicator or other sludge characteristics. were the main SMP constituent, which is in line with the results from Experiment I (Section 8.2).

Table 8.3: Average activated sludge separation performance indicators and selected sludge characteristics for the MBR during each period.

Period	**1**	**2**	**3**	**4**	**5**	**6**	**7**
Days	13-31	31-62	62-90	90-139	139-170	170-189	189-222
M/P	2.02	17.86	17.86	17.86	17.86	2.02	2.02
Performance indicators							
AFR$_{10}$ [mbar/min]	0.07	0.17	0.11	0.15	1.35	0.37	0.11
AFR$_{20}$ [mbar/min]	0.62	1.62	0.98	2.95	30.50	3.89	0.58
GFR$_{10}$ [mbar/min]	0.022	0.049	0.028	0.038	0.514	0.061	0.037
TTF$_{25}$ [s]	2	2	35	506	352	31	2
WOF$_{250}$ [g]	174	188	148	14	23	129	242
SVI [mL/g]	181	90	45	36	87	98	72
Sludge characteristics							
Soluble COD [mg/L]	80.7	31.2	13.6	32.5	53.2	19.7	21.6
Surface charge [meq/gMLSS]	-0.17	-0.22	-0.18	-0.47	-0.38	-0.27	-0.19
Relative hydrophobicity [%]	34	22	12	12	11	13	34
Deq$_W$ [μm]	178	113	92	86	71	58	60
RelFlocNum [Megapixel^{-1}]	10.7	4.0	11.2	99.3	22.2	18.5	8.6
Fractal Dimension [-]	1.23	1.19	1.18	1.19	1.17	1.16	1.12
RelFragNum [Megapixel^{-1}]	404	312	244	392	296	192	54
RelFragSurf [-]	3720	2392	1819	12451	4266	2706	525
A$_{<13\mu m}$ [%]	14	9	12	50	22	14	5
FilLength [μm]	30.8	16.7	9.1	7.4	9.5	13.0	11.5
RelFilNum [Megapixel^{-1}]	15.6	6.3	12.2	70.9	18.3	19.4	13.6
RelFilSurf [-]	6661	1173	823	2947	1242	2201	1714

Period 1 (days 1-31) - Startup

During the first period, the sludge, which originates from a local municipal wastewater treatment plant, adapts to the synthetic influent and the laboratory conditions. During these first days, dead-end and cross-flow filterability are poor, probably due to the release of extracellular polymeric substances (Figure 8.17 (left)), caused by the stress of changing the microbial environment, as was also observed in Experiment I. Noticable is the change in SMP from a balanced mixture between predominantly polysaccharides (PS) but also proteins (PN)(PN/PS ratio of 0.29 on day 1), to a situation where very few proteins remain, and in which the SMP nearly completely consists of polysaccharides (PN/PS = 0.03 on day 29). In Experiment I, the amount of polysaccharides was also consistently more than twice the protein content.

Because the sludge adapts to the new feed during the first days of the experiment, the data in Table 8.3 for Period 1 only takes into account measurements starting from day 13, when stable and good filtration regimes have been established, as is shown on the MBR filterability profile (Figure 8.13) and the time to filter graph, shown in Figure 8.14 (left).

Due to the feast and famine feeding regime, the growth of filaments is suppressed, as opposed to Reactor 1 from the previous experiment. The result is a reduction of the, initially high, amount and length of filaments, that in turn improves settleability of the MBR sludge. This effect is shown in Figure 8.15.

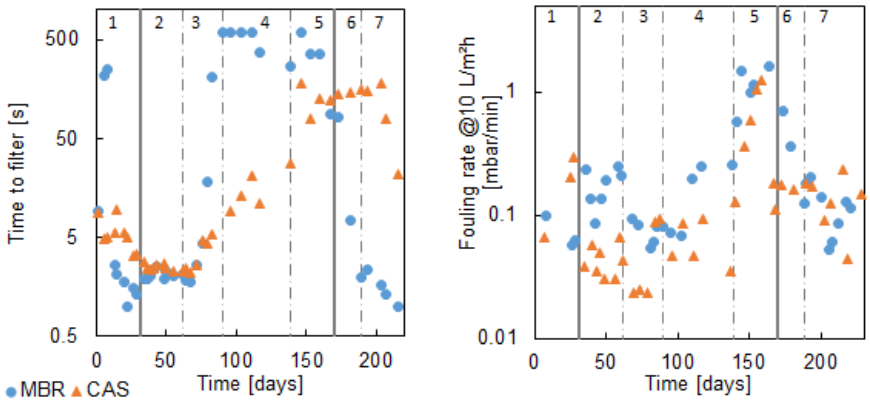

Figure 8.14: Time to filter (TTF_{25}, **left**) and average fouling rate at 10 L/m^{2}h (AFR_{10}, **right** of both reactors throughout Experiment II.

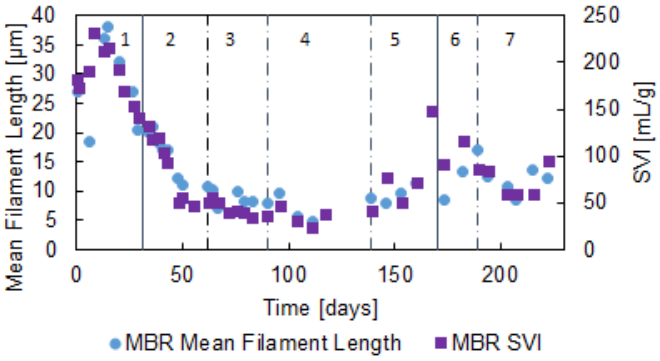

Figure 8.15: Mean filament length and sludge volume index (SVI) of the MBR throughout Experiment II.

Period 2 (days 31-62) - M/P change, adaptation.

On day 31, the influent in both reactors is changed from Feed 1 (low M/P) to Feed 2 (high M/P). The desired effect of this change is to promote deflocculation through ionic exchange with the negatively charged functional groups in the sludge from polyvalent to monovalent cations, which causes floc break-up.

Minor effects of this exchange and breakup mechanism are already noticed after a few days, since around day 36, a minor peak in the average fouling rate (AFR_{10}, Figure 8.13) can be seen. The cause of this disturbance might be a small temporary increase in the number of small objects (Figure 8.16 (left)), but is most likely linked to the sudden and strong increase in the soluble microbial products (Figure 8.17 left), which could be, similarly to Period 1, a reaction of the activated sludge to the changing environment.

At the end of Period 2, around day 55, a second disturbance caused a slight temporal increase in the average fouling rate. Again, this slight increase coincided with an increase in SMP. However, this time, the amount of small objects ($A_{<13\mu m}$) showed no change.

On average, both the AFR and GFR were higher during Period 2, than during Period 1, both increased by 100%. Contrary to this fouling rate-increase, the dead-end filterability improved slightly, as evidenced in Table 8.3 by the increase of the average WOF_{250} from 174 to 188 from Period 1 onto the next.

By analysing previously shown data, it is hypothesized that, during the first weeks after changing the cationic balance towards more monovalent cations,

the activated sludge releases weakly bound components since the outer loosely bound cationic bridges are lost. This shell-shedding behaviour would continue to go on in waves of particles and SMP release until the stable floc cores are exposed to the surrounding mixed liquor. Confirmation to this theory is found in the steady decrease of the mean equivalent flocdiameter (Deq_W). Since the number and size of flocs was still relatively high, a porous and well structured cake could still be formed during dead-end conditions, explaining why those respective performance indicators were hardly affected, similarly to Reactor 1 in Experiment I.

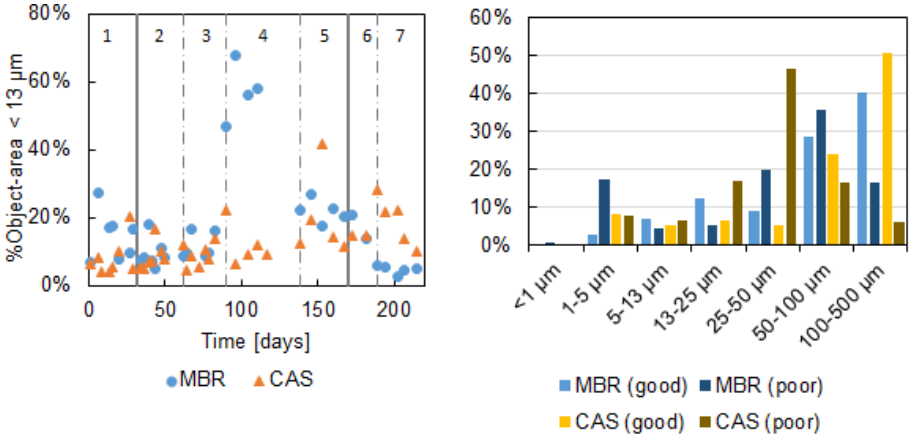

Figure 8.16: **Left:** surface fraction of objects with a Deq < 13 µm in both reactors during Experiment II. **Right:** particle size surface-distributions of both reactors at times of good and poor filterability.

Period 3 (days 62-90) - Stable cross-flow.

About 35 days after the M/P change, a stable cross-flow filtration regime is reached. During this period, flocs are still broken up, as evidenced by the decreasing average floc-diameter and the fluctuations in the number of objects smaller than 13 μm. This process, however, does not seem to affect the cross-flow filterability, which remains high (low AFR & GFR) throughout Period 3. Parallel to the fouling rate, is the stable and low value of the SMP concentration.

The dead-end filtration characteristics are, in contrast with the cross-flow indicators, strongly affected by the release of small particles and decrease in floc size. From day 67 to day 90, a tenfold increase in time to filter is observed, which indicates that the formation of a porous cake layer is no longer possible.

Period 4 (days 90-139) - Deflocculation.

During Period 4, the activated sludge further deflocculates, which is evidenced by an almost tenfold increase in the relative floc and fragment number (respectively RelFlocNum and RelFragNum in Table 8.3) and the strong increase in $A_{<13\mu m}$ (Figure 8.16 (left)).

The dead-end filtration properties are the most affected by the deflocculation. The average time to filter increases to 506 s in Period 4, coming from an average of 35 s in the previous period. From 250 mL of diluted activated sludge, only a mere average of 14 g filtrate can be collected, down from 148 g (WOF_{250}).

The cross-flow fouling propensity increases as well, but this effect is far less pronounced. The average fouling rate for the lowest flux (10 L/m^{2}h) increases only marginally, but the fouling rate for the higher flux of 20 L/m^{2}h nearly triples. In comparison with previous periods, only a weak SMP-increase can be observed.

These observations can be explained according to the critical cut-off diameter theory. The higher the flux, the larger the resulting force for particles to migrate towards and adhere onto the membrane. For each set of permeate flux and cross-flow back-transport conditions, there exists a maximum particle diameter, above which particles have no resulting force driving them towards the membrane and hence, contribute to fouling [Broeckmann et al., 2006]. The higher the flux, or the lower the cross-flow shear-force, the higher this cut-off diameter. Accordingly, fouling rates will depend more on particles of larger sizes, when the exerted flux is higher. In this case, the AFR_{20} will be stronger affected by the deflocculation event than the AFR_{10} since a larger portion of the lower-end particle size distribution has a resulting force towards the membrane.

As dead-end filtration can, within this context, be interpreted as a limiting case, where the back-transport shear force is negligible in comparison to the driving force towards the membrane, so can this phenomenon explain why the dead-end filtration properties depend so strongly on the particle size distribution.

Figure 8.16 (right) illustrates the effect of the deflocculation on the particle size distribution. The figure clearly illustrates the increase of particles from 1-5 μm and the decrease of particles between 5-25 μm. Particles larger than 100 μm are broken up into smaller pieces. Since Figure 8.16 (right) is an area-fraction distribution, inherently, large particles amount for a higher fraction, which means the relatively high peak at 1-5 μm actually corresponds to a huge increase in particle numbers of small size (see also Section 5.3.6).

Surface charge reaches its absolute maximum in Period 4. The reason for this is presumably the deflocculation of the activated sludge, by which a higher

surface per unit of biomass is exposed to the medium. An explanation is given by Mikkelsen and Keiding [2002b], who point out that this effect is inherent to the surface adsorption of cationic polymers, which is the basis of the surface charge measurement.

Period 5 (days 139-170) - SMP release, filtration problems.

From day 139, the MBR fouling rate increases significantly (Figure 8.13) and only a few days later, the TMP in the MBR reaches the maximum attainable pressure of 200 mbar. The MBR was shut down overnight and chemical membrane cleaning was performed using sodium hypochloride and citric acid solutions to remove organic and inorganic foulants, respectively. Filtration was restarted, however, only a few days later, the maximum was reached again. The procedure was repeated but the flux was lowered from 15 to 10 L/m^2h.

The same trend is observed in the average fouling rate, which increases by 5-fold and 20-fold for AFR_{10} and AFR_{20} over the course of a few days. This sudden fouling phenomenon is probably mainly caused by a sharp and sudden increase of the SMP concentrations (Figure 8.17 (left)). Polysaccharides, remaining the most prevalent SMP component, increase with 89% from days 139 to 143, while proteins increase by 3254%. Soluble COD reaches a maximum of 73.1 mg/L on day 143, probably due to the high amount of SMP released. These macromolecules are deemed to be caused by the prolonged effect of the polyvalent cation-deficiency and result from the combined effects of cell decay and catabolysm and EPS production as a stress response to the deflocculation.

Although the amount of fragments and flocs decreases in comparison to the flocculation from only Period 4, their numbers remain high. These rather constant numbers result in only a minor improvement of the dead-end performance indicators (WOF_{250} & TTF_{25}) in comparison to the previous period.

During Period 5, the settleability decreases, which is in contrast with the other periods. The reason for this decrease, as evidenced by the increase in SVI, is probably related to the mean filament length (Figure 8.15), which increases as well.

Period 6 (days 170-189) - M/P change, filtration improves.

On day 170, the synthetic influent was changed back to Feed 1, with a lower M/P ratio, and thus a higher amount of polyvalent cations. This change resulted in an almost immediate significant reduction of both the cross-flow and dead-end

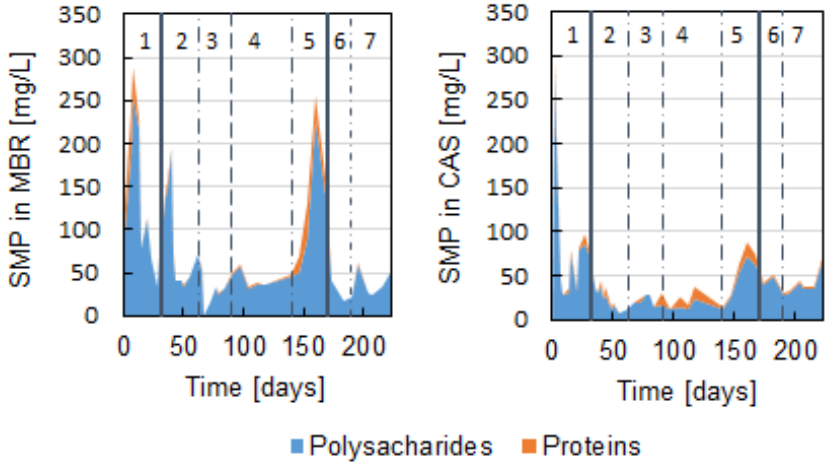

Figure 8.17: Soluble microbial product concentration in MBR (**left**) and CAS (**right**) throughout Experiment II.

fouling. The polyvalent cations succesfully aided flocculation in reducing the number of fragments by 50% and the SMP by almost 74% over a few days.

During Period 6, the $SMP_{PN/PS}$ ratio decreased again to an average of 0.014, down from an average of 0.15 in Period 5. Extracellular DNA in SMP was reduced by 86%, which indicates a more stable and viable bioflocculation state. In short, the sludge recovered from the prolonged deflocculative effect of monovalent cation-overdose in a number of days, after which the MBR flux could be reset to its original value of 15 L/m^{2}h.

In Experiment I, it has already been assumed that the presence of polyvalent cations aided in filament-integration in the floc structures. During Period 6 of this experiment, when the amount of polyvalent cations was increased, so did the average filament length, which resulted in a parallel increase of SVI, affirming the previously stated assumption.

Period 7 (days 189-222) - Stable filtration, irreversible fouling.

During the final period, no major disturbances occurred. However, MBR-filtration was briefly interrupted from day 187 to day 193 due to a power failure and a minor fluctuation in the SMP content around day 194 coincided with a

temporary minor increase in MBR fouling rate. In general, during Period 7, the floc and fragment number decreased, while the equivalent floc diameter increased, which indicates improvement in bioflocculation as a result of the higher polyvalent cation-content.

From day 215, the MBR fouling rate started to deviate from the average fouling rate, which could be attributed to accumulating internal fouling of the MBR-membrane. On day 222 both reactors were shut down and the experiment was concluded.

8.3.3 Comparison MBR and CAS

In Experiment I, the effect of cation-induced bio(de)flocculation was studied using two identical lab-scale conventional set-ups, which rose the question what the situation would have been if membrane bioreactors had been used. In the next paragraphs will be shown that the reactor configuration indeed strongly affects the performance of the tested separation techniques.

Figure 8.14 (right) depicts the evolution of the AFR_{10} in both reactors throughout the study. A few things can be noticed. Firstly, the cross-flow filterability in the conventional system is always better than in the MBR, since the AFR_{10} is nearly always higher in the latter. Secondly, the general trend towards deflocculation near day 150 is also observed for the CAS, but the intermediate turbulent periods (Period 2 and 4) do not show significant deterioration of filterability in the conventional system. It is only at the beginning of the fifth period that significant fouling emerges.

Similarly, when looking at the dead-end filterability (Figure 8.14 (left)), one can clearly observe that, while the TTF_{25}-increase in MBR is very sudden in Period 3, the conventional reactor shows a far more steady increase up from Periods 3 to 5.

The reason for this discrepancy is a direct consequence of the reactor set-up. As can be seen in Figures 8.16 (left) and 8.17, which respectively depict the objects smaller than 13 µm and the SMP, the amount of those fouling constituents is much lower in the conventional reactor than in the MBR. Hence, it comes as no surprise that the filterability in the conventional system remains higher.

Moreover, it is known that a conventional system has a natural tendency to optimise for well settling biomass. Therefore, it is postulated that the small sludge fragments and objects, together with the abundance of SMP are washed out during the first periods of deflocculation, when the shell-shedding behaviour took place in waves. Only in Period 5, when complete sludge-breakup was

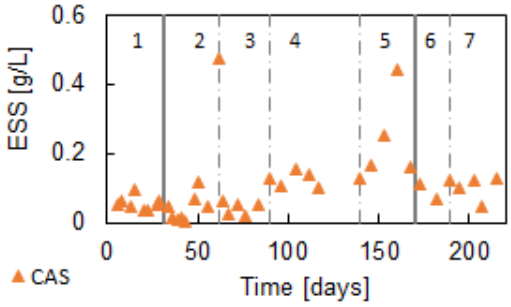

Figure 8.18: Effluent suspended solids (ESS) in CAS throughout Experiment II.

followed by strong SMP-release, the mixed liquor in the conventional system did change significantly enough such that the filterability was compromised.

This postulation can be confirmed when looking at the effluent suspended solids, as an indicator of the biomass that was lost to wash-out, which is depicted in Figure 8.18.

A discussion that relates the results from Experiments I and II and from Chapter 7 to observations by other researchers will be given in the next chapter.

8.4 Conclusion

From the results of Experiments I and II, the following conclusions can be drawn.

- The divalent cation bridging theory, as explained in Section 3.1.3 is affirmed. A high monovalent-over-polyvalent (M/P) cation-ratio induced deflocculation in three reactors, while a low M/P-ratio led to the formation of large flocs, and successfully aided in recovering from deflocculation caused by monovalent cation abundancies.
- In Experiment I, filamentous bulking occured in the reactor fed with many polyvalent cations. Most likely, the filaments proliferated due to insufficient feast-famine feeding and were incorporated into the floc structures with the aid of the polyvalent cations. Whereas in Reactor 2, the absence of these polyvalent cations led to the washout of the non-

settling filaments. In Experiment II, feast-famine feeding was better and the proliferation of filamentous bulking was successfully suppressed.

- The particle size distribution and fraction of small particulate and colloidal matter was most detrimental for moderate and high flux cross-flow and dead-end filtration modes. Low-flux cross-flow filtration was more affected by the surface properties (hyrophobicity, surface charge, fractal dimension). These effects are in line with the critical cut-off diameter theory by Broeckmann et al. [2006], explained in Section 2.3.3.

- In this regard, dead-end filtration systems can be regarded as a limiting case, where the backtransport and shear-stress is overruled by permeation drag. These dead-end systems should not be used as an indicator for low/moderate flux cross-flow filterability.

- Relative hydrophobicity has shown to be related with filtration and settling. As flocs become hydrophobic, flocculation improves, which relates to better filtration and settling. However, (part of) the hydrophobicity in Reactor 1 from Experiment I could be attributed to the proliferation of many filaments, which in turn hampered settling.

- The continued deflocculation of Reactor 2 in Experiment I led to the formation of poor-settling *open* flocs. These flocs had very irregular perimeters, which was denoted by a distinct increase in fractal dimension. This relationship was affirmed in Experiment II, where the poorest settling (in Period 1) corresponded with the highest fractal dimension.

- In Experiment II, deflocculation was initiated by a step-wise shell-shedding behavior in which the outer parts of sludge flocs in the CAS and MBR were released under the form of small particles and SMP. During this shell-shedding behaviour, filterability worsened. This effect is an exact copy of the deflocculation-regime from Reactor 2 in Experiment I.

- 100 days after changing the M/P ratio, total deflocculation occurred in both reactors from Experiment II, coinciding with a large SMP-production, which caused a severe increase in the average fouling rate. Therefore, SMP are deemed the most contributing factor to membrane fouling in this experiment.

- Changing the M/P back to its original value restored flocculation completely within approximately three weeks in Experiment II, while some immediate amelioration of filtration was observed as well.

- Experiment II revealed a strong dependency of the reactor set-up on the extent, duration and consequences of deflocculation events. Conventional

(settling) systems have a natural tendency to select for well-settling biomass, while dispersed bacteria are washed out through the effluent [Christensen et al., 2015]. As a consequence, the effect of deflocculation events will be tempered to some extent, by washing out the non-settling eroded particles and colloidal matter. Although this leads to a short period of poor effluent quality, the duration of such disturbance is usually shorter than in MBR systems, where such foulants can only be removed via the waste sludge.

- In both experiments, the transition of the municipal sludge to the laboratory conditions entailed a period of poor filterability in which a lot of SMP were produced as a stress response.
- Both experiments revealed a higher fraction of polysaccharides than proteins in the soluble and extractable EPS. This might be a typical effect from the glucose carbon source, as it is also used as the reference standard for the polysaccharide measurement.
- The role of eEPS in bioflocculation and separation performance remains unclear.

Chapter 9

Bioflocculation versus activated sludge separation: what have we learned?

In the following sections, the results from Chapters 7 and 8 are summarized and compared to data from literature in order to refine the uncovered insights in the relationship between bioflocculation and activated sludge separation.

To this end, firstly, from the MBR-data obtained in Experiment II (Chapter 8), Pearson correlation coefficients are calculated to link the different performance indicators with the sludge characteristics. Secondly, these correlations, as depicted in Table 9.1 will be compared to the data from Experiment I, the multivariate study from Chapter 7 and literature. For each performance indicator, a dedicated section will provide the relevant information.

In the final section, the longterm effect of cations on bioflocculation and, as a consequence, on filterability and settleability, will be discussed. To this end, the data from Experiments I and II will be compared to previous experiments by other researchers and a unified theory concerning the cation-affected flocculation principles will be proposed.

Table 9.1: Pearson correlation coefficients between performance indicators and selected sludge characteristics in the MBR of Experiment II (Chapter 8).

	AFR_{10}	GFR_{10}	TTF_{25}	SVI
Soluble COD	0.55	0.33	0.15	0.77
Relative hydrophobicity	-0.27	-0.21	-0.31	0.56
| Surface charge |	0.42	0.29	0.70	-0.40
SMP_{PN}	0.84	0.85	0.30	0.34
SMP_{PS}	0.48	0.52	0.02	0.64
$SMP_{PN/PS}$	0.49	0.48	0.21	0.07
Deq_W	-0.17	-0.11	-0.16	0.57
RelFlocNum	-0.06	-0.06	0.79	-0.31
Fractal Dimension	-0.12	-0.07	0.10	0.43
RelFragNum	0.09	0.10	0.30	0.32
RelFragSurf	0.03	0.09	0.65	-0.10
Frag/Floc-Surf	0.22	0.20	0.62	0.00
$A_{<13\mu m}$	0.18	0.12	0.88	-0.26
FilLength	-0.21	-0.15	-0.45	0.92
RelFilNum	-0.07	-0.08	0.77	-0.25
RelFilSurf	-0.15	-0.14	0.03	0.72
Fil/Floc-Surf	-0.19	-0.16	-0.19	0.87

9.1 Cross-flow filterability

9.1.1 Extracellular polymeric substances

Soluble microbial products. As can be seen from Table 9.1, the cross-flow filtration indicators (AFR & GFR) are mostly related to the amount of SMP and soluble COD. This observation comes as no surprise since each increase in SMP during the filtration experiment has led to a subsequent increase in cross-flow fouling rate. These findings were noticed as well by Van den Broeck et al. [2010]. Since SMP are soluble organic macromolecules, they are also detected during the COD measurement when they permeate through the membrane, an observation affirmed by Arabi and Nakhla [2008]. The same authors found in their study on the effect of cation concentrations, that SMP concentrations for both protein and carbohydrates were higher when the M/P ratio increased, which is in line with the results from Experiment II [Arabi and Nakhla, 2009]. However, in Experiment I, a higher polysaccharide content was observed in Reactor 1, which was fed with the low M/P ratio, which could be related to

the different established microbial community, containing more filamentous bacteria.

Li and Yang [2007] explain the detrimental effect of SMP on effluent clarification by stating that an increase in loosely bound EPS content, would worsen the attachment between cells and weaken the structure of sludge flocs, leading to erosion. Although loosely bound EPS should be able to bridge neighbouring cells for floc formation, the turbulent regime would render them more detrimental than beneficial for flocculation. A strong correlation between SMP and membrane fouling has been reported as well by Cho and Fane [2002]; Wang et al. [2014] and [Lin et al., 2009]. In the measuring campaign described in Chapter 7, the polysaccharide fraction of the SMP was also found to be the most influential and detrimental for cross-flow filtration amongst samples from different origins (see also Figure 7.5), which was an affirmation of the work by [Van den Broeck et al., 2011], who noticed a clear correlation between fouling and the polysaccharide content of SMP as well.

Noticable in Table 9.1, is the also high correlation of the average fouling rate with the protein fraction of the SMP. Indeed, during each SMP-peak, not only did the total number of SMP rise significantly, but so did the $\text{SMP}_{PN/PS}$ ratio. This correlation is affirmed by the work of Zhang et al. [2014], who found that their modified fouling index (MFI) strongly correlated with the proteins in the supernatant, but only moderately with the polysacharides. Moreover, in their work, no significant correlation could be found between the modified fouling index (MFI) and the tightly bound EPS. The correlation between the $\text{SMP}_{PN/PS}$ ratio and fouling rate is consistent with the findings of Arabi and Nakhla [2008], Van den Broeck et al. [2010] and Gao et al. [2013]. In the latter's work, investigating different cake layer structures, it is stated that a higher portion of proteins in the supernatant would favor the formation of a more sticky cake layer. In Experiment I, the soluble protein content remained low in both reactors. However, as the polysaccharide content increased in Reactor 1, the PN/PS ratio decreased, while it remained higher for Reactor 2, for which the filtration performance was the lowest during the course of Experiment I.

It should be noted that, although the number of polysaccharides was correlated most with fouling, that the proteins may play a very important role as well. The data from Experiment II show that, at times were significant deflocculation occurs, the number of SMP proteins proportionaly increases a lot more than those of the polysaccharides. This SMP-PN outburst, however, only occurred once. As all sludge samples from the measuring campaign were taken during normal reactor regime, disturbance-related protein interactions may not have been detected.

Bound extracellular polymeric substances. In none of the performed experiments, the bound EPS were found to be of direct impact on any separation performance indicator. However, it is assumed that, at least to some extent, floc surface characteristics, such as charge or hydrophobicity, are a consequence of specific EPS production by certain bacteria. E.g., Jorand et al. [1998] found that at least 12% of proteins are involved in activated sludge hydrophobicity. Moreover, bound EPS are involved in the process of bioflocculation not only through their functional groups, but also via entanglement and hydrophobic interactions [Liao et al., 2001].

Possibly one of the reasons for the contradictory findings regarding the role of EPS in sludge separation processes is due to the classification and extraction methods used. EPS are generally classified into proteins and polysaccharides, occasionally extended with DNA, humic acids or lipids. These categories, however, are still very broad. E.g., proteins can be of hydrophilic or hydrophobic nature, depending on their respective amino acids and can possess a multitude of functional roles. Moreover, it was already observed in Chapter 6, where the cation exchange resin and heat extraction methods were compared, that both methods yield different results. This observation was confirmed by the work of Zhu et al. [2015] and makes comparison of results obtained by different researches difficult. As a response, Sun et al. [2015] proposes a sequential extraction combining several methods. However, the application of such sequential extraction is rather cumbersome.

9.1.2 Hydrophobicity and surface charge

Although some correlations are weak, the expected trends regarding relative hydrophobicity and surface charge are observed. Surface charge and relative hydrophobicity are inversely related ($r^2 = 0.44$), which was also observed by other authors [Liao et al., 2001]. Thus, an increase in surface charge will lead to a reduction in hydrophobicity, although hydrophobicity can also be related to filament growth ($r^2 = 0.60$) as was already observed in Experiment I.

Hydrophobicity has been shown to correlate well with adhesion to sludge flocs [Zita and Hermansson, 2015] and as hydrophobicity increases, generally flocculation improves [Liu and Fang, 2003]. The idea that activated sludge hydrophobicity mostly relates to activated sludge separation through flocculation has been pointed out by Liao et al. [2001] and Urbain et al. [1993] as well.

With respect to fouling, increasing the hydrophobicity and decreasing the surface charge of the sludge leads to a reduction of the fouling rates, which was affirmed in the measuring campaign of Chapter 7 and is in line with Experiment I where Reactor 2, that showed a lower relative hydrophobicity, also exhibited a

Table 9.2: Pearson correlation coefficients between average fouling rates and selected sludge image analysis parameters in the MBR from Experiment II, excluding Period 5.

	$\mathbf{AFR}_{10}$	$\mathbf{AFR}_{20}$
Deq_W	-0.04	-0.15
RelFragNum	-0.05	0.28
RelFragSurf	-0.10	0.45
Frag/Floc-Surf	0.02	0.57

reduction in filterability. In their study relating activated sludge characteristics to sludge filterability, Van den Broeck et al. [2011] proposed a classification tool for filterability. In this tool, hydrophobicity was used as one of the key characteristics that improve filtration of watery sludge suspensions.

9.1.3 Particle sizes and distribution

Surprisingly, during Experiment II, the sludge particle size distribution and morphology showed only a minor influence on the AFR_{10}, which is partly explained by the fact that the strongest increase in fouling rate happened during Period 5 and was driven by the release of SMP.

However, removing the data from Period 5 and repeating the correlation calculation for both AFR_{10} and AFR_{20} yields the results from Table 9.2.

It is clear that for the low flux of 10 $\mathrm{L/m^2h}$, the fouling rate is not deemed dependent on the floc size or the amount of small sludge fragments in the mixture, while for a higher flux, having a smaller floc size and a larger number of fragments proves to be detrimental for filtration. Thus, one can assume, in accordance with the critical cut-off diameter theory (see Section 2.3.3), that the cut-off diameter for the lowest flux, is below the fragment diameter (5 µm), while for the higher flux, fragments can successfully migrate towards the membrane and contribute to the fouling layer. This theory is in agreement with the general consensus about the high fouling propensity of small particles and colloidal matter [Gao et al., 2013; Ivanovic et al., 2008; Van den Broeck et al., 2011], which was also pointed out in Section 8.3.2. The same results regarding the detrimental nature of particulate fines were obtained in the measuring campaign of Chapter 7, in which besides SMP-PS, the number and surface of fragments were deemed to be most influential for membrane fouling (see Figure 7.5). In the same section, it was also observed that the fouling by SMP and particles worsened when the flux was increased from 10 to 20 $\mathrm{L/m^2h}$. Since

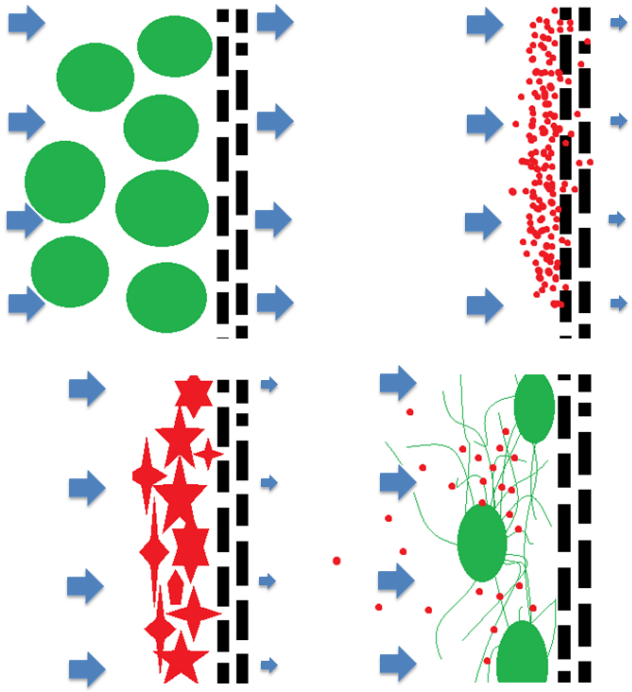

Figure 9.1: Schematic overview of effects of particle size, sludge morphology and filaments on crossflow filtration. **Top:** large flocs create a well structured permeable cake layer while small fragments and colloidal matter are detrimental. **Bottom-left:** irregular floc shapes create non-permeable cake layers. **Bottom-right:** filaments can create a secondary *net*, that captures incoming small foulants.

the hydrophobicity's role diminished as well, it is clear that as the permeation suction force increases, particle sizes distribution related characteristics become more dominant over surface characteristics. The same observation was made by [Hwang et al., 2012]. An increased flux results in a higher TMP, which also results in higher cake layer compression [Jørgensen et al., 2014; Poorasgari et al., 2015].

9.1.4 Floc morphology

In Chapter 7, the influence of the roundness and fractal dimension on filtration was studied for several sludge samples. In general, it can be concluded that

round flocs with smooth edges (high roundness, low fractal dimension) have a positive effect on filterability. The same observation was made in Experiment I, where near the end of Period E the flocs from Reactor 2 had much more irregular edges than those of Reactor 1. The irregular flocs, having a much higher fractal dimension, showed poor filtration properties. A possible explanation for this behaviour comes from the fact that irregular shapes do not easily form a well structured cake layer, which leads to a higher cake resistance, see also Figure 9.1 (bottom-left).

9.1.5 Filaments

In Section 7.2.1, a slightly positive effect of filaments on cross-flow filtration was observed. A possible reasoning behind this phenomenon may be the creation of a filamentous network that may capture flocs or debris being attracted towards the membrane, much alike the dynamic secondary membrane theory as depicted in Section 2.3.6 (see also Figure 9.1 (bottom-right)). Similarly, filaments provide binding sites and entanglement, leading to large floc structures as in Experiment I, which sizes are above the critical diameter for particle deposition (see also Sections 2.3.3 and 9.1.3).

9.2 Dead-end filterability

9.2.1 Particle sizes and distribution

In previous sections, it has already been clarified that the dead-end filterability more strongly depends on sludge morphology than its cross-flow counterpart, while depending less on SMP. These observations are confirmed in Table 9.1, that clearly shows the strong correlations between the TTF_{25} and the amounts of flocs, fragments and small sludge objects (RelFlocNum, RelFragSurf and $A_{<13\mu m}$, respectively). The reasoning behind this is that back-transport in the dead-end case is very limited and that as such, the critical diameter as described by Broeckmann et al. [2006] (see Equation (2.13) in Section 2.3.3), is high, such that nearly all flocs can deposit onto the membrane.

9.2.2 Relative hydrophobicity and surface charge

The results from Table 9.2 only show a weak negative correlation between the floc's relative hydrophobicity and the time to filter. However, during

Experiment I, the time to filter of Reactor 2 was always lower than Reactor 1, while the inverse observation was made for the relative hydrophobicity. Therefore, one may state that hydrophobic flocs have a lower dead-end filtration resistance than flocs of hydrophillic nature.

A possible explanation for this effect comes from the hydraulic force balance. In dead-end filtration mode, the suction force is very high in comparison with the backtransport, resulting in the build-up of a larger cake layer than in cross-flow filtrations set-ups. As such a cake layer has an increased local charge concentration, plenty more counter-ions will be present, increasing the local ionic strength. This effect, in turn, provides an osmotic pressure difference between feed and permeate side, which contributes to the filtration resistance, since filtration can be seen as the mobilisation of solvent (water) from a high to a low ion concentration [Chen et al., 2012] (see also Section 2.3.7).

9.2.3 Filaments

An interesting note is the positive influence of the filament length on the dead-end filterability (negative correlation with the TTF_{25}), while the number of filaments (RelFilNum) negatively affects the filtration. This effect can be explained by the formation of a well structured and porous cake layer in the presence of longer filaments, creating a loose and easily permeable structure, as already explained in Section 8.2 of this chapter and Section 7.2.1. Since the correlation with the total surface of filaments (RelFilSurf) is negligible, having a higher number of filaments in this sence translates to them being very short, thus more easily blocking the cake layer's pores.

9.3 Settleability

The sludge volume index, as a measure of the sludge volume after settling, increases when settling is hindered. The correlations of this parameter with the sludge characteristics from Experiment II, are shown in the last column of Table 9.1.

9.3.1 Extracellular polymeric substances

The SVI is positively correlated with the soluble COD and the SMP. Turbid matter of submicron size is known to have poor settling properties. Moreover, this correlation was already noted by Li and Yang [2007], who state that loosely

bound EPS would contain a high water content, thus reducing the density difference between flocs and their surroundings, leading to a loss in settleability. In the multivariate study of Chapter 7, no impactful effect of eEPS or SMP on settleability could be detected.

9.3.2 Particle sizes and distribution

As opposed to the other performance indicators from Experiment II, the sludge volume index does rely somewhat on the floc size. Large flocs tend to have a more open and loose structure, being held together by filaments, resulting in a lower average floc density and thus, a slower settling with a larger sludge volume index [Andreadakis, 1993]. A parameter that plays a role in this process is the fractal dimension. The more edgy the flocs border, the higher the total drag-force from settling, and thus, the higher the sludge volume index [Jin et al., 2003; Liao et al., 2006]. The interaction between the fractal dimension and the settleability has also been demonstrated in Experiment I and was observed as well in previous research [Van Dierdonck et al., 2013a]. Note that sludge with rough edges also takes up more space in the settling sludge blanket itself.

In contrast, in the measuring campaign of Chapter 7, the relationship between the average particle size and the SVI is found to be more ambiguous. On one hand, having large flocs, as depicted by the normal average (D_{eq}) was found to be positively correlated with the SVI, while the surface weighted average was negatively correlated. Possibly, this was the result of a mathematical fitting, so the relationship is not clear from these results. However, it is known that very small and colloidal particles have hampered settling as well [Biggs and Lant, 2000; Van Dierdonck et al., 2013a]. Nevertheless, it is much more the average floc density than the average floc size itself that determines the floc's settling behaviour, which could also explain the difference between both obtained results.

9.3.3 Filaments

The strongest correlation with the SVI is found with the average length of filaments. A good balance between filaments and flocs is key to obtaining good settling conditions. This relationship is very clearly shown in the positive correlation between SVI and the Fil/Floc-Surface ratio and in Figure 8.15, where both SVI and FilLength graphs are displayed during the course of the experiment. Having a high number of filaments is not always related to poor settling, as can be observed in the negative correlation between the filament number and the SVI in Table 9.1. The same observations were made in Experiment I and in

Section 7.2.3. Therefore, it can be concluded that the length of filaments is of more importance than their numbers.

9.3.4 Relative hydrophobicity and surface charge

In contrast to the filterability measurements, the SVI of Experiment II is positively correlated with the relative hydrophobicity, meaning that settling worsens when the relative hydrophobicity of the sludge increases. However, since the number of filaments is strongly reduced by Period 5, the effect of hydrophobicity is probably masked by the reduction of filaments, which is in line with findings of Jin et al. [2003], who state that highly hydrophobic or negatively charged floc surfaces were associated with relatively poor settleability. In Experiment I, a similar effect was noticed. An abundance of filaments was parallelled by a strong increase in hydrophobicity.

In contrast to Experiments I and II, Section 7.2.3 depicted a negative correlation between SVI and relative hydrophobicity. In neither of the samples tested during this study, filaments hampered the relationship between both parameters. Therefore, it is assumed that, when no filaments are present, hydrophobicity can be a positive influence on settleability. These assumptions coincide with the idea behind the model by Urbain et al. [1993]. In their work, a model is proposed that describes the hydrophobic and hydrophilic intractions inside the biological floc, assuming that a hydrated structure, like an activated sludge floc, contains internal hydrophobic bondings. Again, like mentioned in Section 9.1.2, hydrophobicity is deemed to be related to settling more indirectly through flocculation.

In Section 7.2.3, it was also found that the SVI was negatively correlated with the surface charge. The same observation was made during Experiment II. These results are somewhat contradictive to earlier findings, that would suggest a surface charge increase would lead to higher repulsion, and a larger retained water content from the sludge flocs, reducing their settleability. Therefore, the role of surface charge on settling is not clear.

9.4 A unified theory on the longterm effects of cations on flocculation

In this section, a unified theory on the long term effects of cations on flocculation is proposed. As was described in Section 3.1.3, the monovalent over polyvalent cation ratio is, according to the divalent cation bridging theory, crucial for

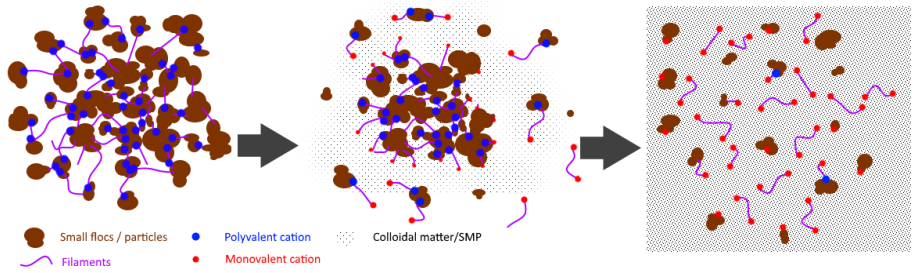

Figure 9.2: Proposed cation-induced deflocculation mechanism by increasing the M/P ratio of the influent. In the first days/weeks, shell-shedding behaviour occurs, increasing the numbers of primary particles and SMP at peak moments. After several weeks, the floc matrix collapses.

activated sludge bioflocculation. Multivalent cations are involved in bridging between negatively charged functional groups in the activated sludge matrix, while monovalent cations do not possess sufficient charge for this. A critical M/P ratio of 2 was proposed by Novak et al. [1998]. The deflocculative effect of a M/P ratio above this critical value has been shown by several authors [Van den Broeck et al., 2010; Van Dierdonck et al., 2013a]. Deriving from these works and with the inclusion of Experiments I and II, the following deflocculation/reflocculation mechanism can be proposed.

High M/P ratio - deflocculation.

1. **The first days: minor effects.** During the first days, the multivalent cations that form bridges in the outer layers of the activated sludge are being replaced by the monovalent cations from the influent. This results in a small release of primary particles and some EPS in the bulk mixture (see also Figure 9.2). This pertinent observation was made twice in this work as well as in the study of Van Dierdonck et al. [2013b].

2. **Shell-shedding.** In the following days, more and more parts of the sludge flocs are being released in the bulk mixture (erosion). This effect, described as *shell-shedding* in Section 8.3.2, leads to peaks in fragment numbers and SMP and results in a gradual decrease of floc-diameters and fits well within the hypothesis by Keiding and Nielsen [1997] who assume that the outer layers of activated sludge flocs consist of loosely bound macromolecules and primary particles that can be easily detached from

the floc core when colloidal stability changes. Moreover, the authors relate this layer to a protective barrier and attribute a faster ion exchange to it than in the inner floc layers.

Incorporated filaments are released as well in the shell-shedding period, leading to weaker and small flocs. The whole process of shell-shedding takes several weeks and results in periods of slightly worsened separation performance alternated by periods of reasonable operation, as was also described in works by Van den Broeck et al. [2010] and [Peeters and Herman, 2007].

3. **2-3 weeks: collapse.** After several weeks, nearly all multivalent cations in the sludge matrix have been replaced by monovalents. The floc-structure has been weakened to a point where the resulting flocs break up (fragmentation), which is paralleled by a substantial release of EPS in the bulk mixture. In Experiment II and in the work of Van den Broeck et al. [2010], the polysaccharide content of the SMP were deemed the most foulant EPS constituents.

Low M/P ratio - reflocculation.

1. **Immediately: sweep flocculation.** Immediately after increasing the amount of polyvalent cations, already a small improvement can be noticed, which is most likely caused by the flocculative effect of the trivalent ions, such as Fe^{3+}, although divalent ions can also exhibit this behaviour. The same immediate effects were observed by [Peeters and Herman, 2007] and [Ding et al., 2015].

2. **2-3 weeks: reintegration of multivalent cations.** Gradually, over time, the polyvalent cations are being reintegrated into the floc matrix, which restores the floc structures. The same effect was noticed in earlier studies [Van den Broeck et al., 2010; Van Dierdonck et al., 2013b].

Part III

Shortterm effects of cations on filtration

Chapter 10

What is the impact of osmotic pressure on membrane fouling?

In this chapter, the validity of the osmotic pressure effect as described in Section 2.3.7, is evaluated.

10.1 Introduction and rationale

In Chapter 8, the longterm effects of cations on filterability have already been discussed. A prolonged exposure to a high monovalent-over-polyvalent cation ratio resulted in severe deflocculation and fouling. However, the shortterm effects of altering the ion concentration of the activated sludge mixed liquor are still a point of discussion.

In their study on the effects of ionic strength on membrane fouling in a membrane bioreactor, Wang et al. [2014] pointed out that the osmotic pressure effect may provide an explanation for fouling phenomena that cannot be explained by the conventional particle sizes/cake filtration theories as discussed in Section 2.3.3. In their study, amongst others from the same research group, the osmotic pressure effect is brought forward as a potential explanation.

The osmotic pressure effect has already been explained in Section 2.3.7. In short, during cake layer formation, functional groups present in the sludge accumulate

at the retentate side of the membrane. Since macroscopic electroneutrality has to be maintained, counterions present in the supernatant will counteract these functional groups, which leads to an ionic strength difference across the membrane. This difference, in turn, results in an osmotic pressure resistance, as filtration across such concentration gradient can be regarded as the mobilisation of water from low to high chemical potential. Since SMP have a high charge density, the retention and accumulation of SMP at the membrane side increases the potency of the osmotic pressure effect. This effect was demonstrated by [Shen et al., 2015], who used a stirred batch filtration cell to attribute 87% of the total cake resistance to the SMP's osmotic pressure effect contribution.

10.2 Preliminary experiments

10.2.1 Materials and methods

Three preliminary experiments were performed according to the method described by [Shen et al., 2015]. In this method, the supernatant of sludge samples is replaced by a NaCl solution of known ionic strength (50 mM) using centrifugation at a low speed (500g, 5 min, 4°C, Eppendorf 5810R using rotor F34-6-38) to avoid disrupting the sludge morphology.

Both the original samples as the new samples were subjected to a filtration test. In the original experiments by Shen et al. [2015], a stirred batch filtration set-up is used. The experiments from this study were performed in the labscale filtration set-up as described in Section 4.2.3 equipped with a standard A4 Kubota membrane in a 2 L filtration vessel. The sludge samples were subjected to a flux-step experiment with three different fluxes: 15, 20 and 25 L/m^{2}h. Each flux was imposed three times for 10 minutes with a relaxation period of 5 minutes in between. From these flux steps, the average fouling rate for each flux was calculated.

To detect possible changes in morphology, both samples were subjected to a microscopic analysis using ASIAP (Chapter 5).

Activated sludge samples from the CAS and MBR reactors of Section 8.3 were used. Later, the same procedure was repeated for sludge of the local municipal wastewater treatment plant.

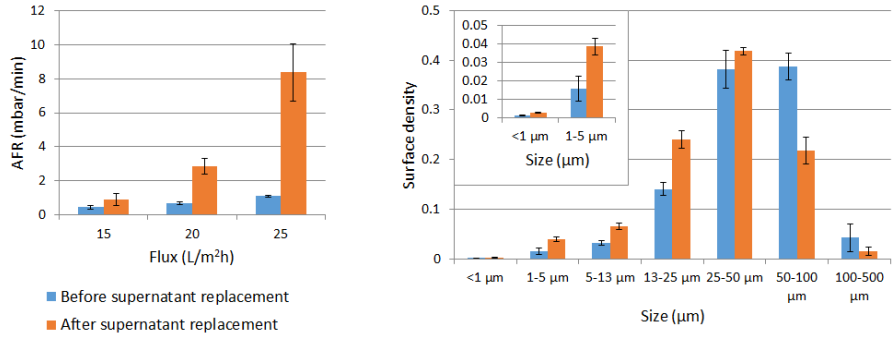

Figure 10.1: Preliminary experiment with sludge from a labscale membrane bioreactor. The supernatant is replaced by a 50 mM NaCl solution. **Left:** filtration characteristics. **Right:** surface weighted particle size distribution.

10.2.2 Results - MBR sludge

The results of replacing the supernatant of the MBR-sludge with the 50 mM solution are shown in Figure 10.1. As can be seen on the figure, the filterability worsens for all three fluxes when the supernatant is replaced by the monovalent salt solution. Moreover, it can be seen from the particle size distriution on the right hand side of the figure, that this replacement was paralleled by a deflocculation of the sludge. Therefore, the findings of Shen et al. [2015] could not be proven and the, if there is any, detrimental effect of the supernatant's composition was overshadowed by the fouling caused by the small matter.

10.2.3 Results - CAS sludge

Figure 10.2 depicts the results of the preliminary tests on sludge from the laboratory CAS reactor. The effects are practically the same as in Section 10.2.2. Interestingly, the effect seems to be increasing with the flux, which could be explained by Broeckmann et al. [2006]'s theory. A higher flux attracts a larger fraction of the smaller particles (see also Section 9.1.3).

10.2.4 Results - municipal

Finally, the same experiment was performed on municipal sludge. However, during this test, after supernatant replacement, the maximum attainable TMP

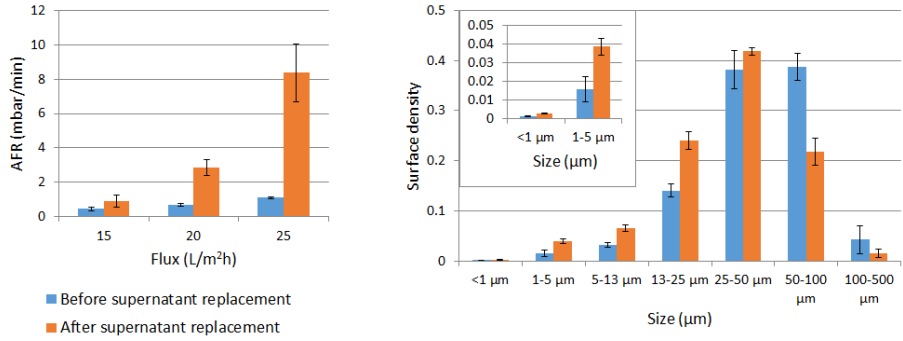

Figure 10.2: Preliminary experiment for labscale conventional activated sludge system. Supernatant is replaced by 50 mM NaCl solution. **Left:** filtration characteristics. **Right:** Surface weighted particle size distribution.

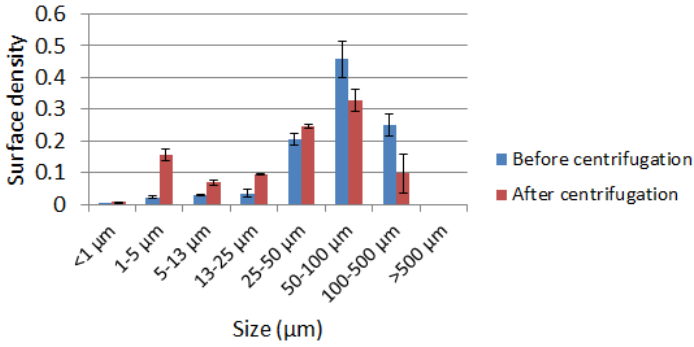

Figure 10.3: Surface weighted particle size distribution for preliminary experiment on sludge from municipal wastewater treatment plant. Supernatant is replaced by 50 mM NaCl solution.

of 150 mbar was reached very quickly. The membrane was cleaned and the experiment was repeated, but the same effect occurred. Microscopic analysis showed a strong deflocculation, as can be seen in Figure 10.3, which affirms the previously noted observations.

10.2.5 Conclusion

In conclusion, the preliminary experiments have shown the detrimental effect of deflocculation on filtration but were all in contradiction with the findings of Shen et al. [2015]. Moreover, the deflocculation appears to be the result of shortterm cationic influences on the floc matrix. Therefore, it was decided to continue the experiments by studying the exact nature of the activated sludge's supernatant in terms of ion concentrations (Section 10.3) and by repeating the experiments while varying the ionic strength and M/P-ratio (Section 10.4).

10.3 Supernatant composition

From the work of Shen et al. [2015], it is clear that the contribution of the supernatant to fouling is far from negligible. To unravel the impact of the supernatant on filtration and the interaction between the dosed salt solutions, the sludge and the supernatant, a study on the actual supernatant's ionic strength and composition is performed first (Section 10.3.1). Next, a theoretical estimate is performed on the required ion concentration difference to yield a significant osmotic pressure effect (Section 10.3.2).

10.3.1 Ionic strength and composition of supernatant

In this section, the supernatant of activated sludge is studied in terms of its ionic strength and composition. First, conductivity measurements are explained as a method of estimating the solution's total ionic strength. Next, inductively coupled plasma mass spectrometry (ICP-MS) and testkits are described to measure the composition of the supernatant.

Conductivity measurements

To assess the ionic strength of the supernatant, the conductivity is measured (HACH HQ 40d) and calibration curves are used to relate these conductivity measurements to ionic strengths. For the calibration curves, three standard salt solutions with known ionic strengths are made, namely NaCl, $CaCl_2$ and $FeCl_3$. As the range for the ionic strengths used in this study goes from 0.05 mM up to 500 mM, a log-log calibration is made between the salt solutions' ionic strength (I, with units of M) and the conductivity (S, with units of µS/cm). The results

of these calibrations are shown in Equations (10.1) - (10.3):

$$\text{NaCl:}\quad \log(\text{I}) = 1.1799 \cdot \log(\text{S}) - 5.7481 \qquad R^2 = 0.9989 \tag{10.1}$$

$$\text{CaCl}_2:\quad \log(\text{I}) = 1.1953 \cdot \log(\text{S}) - 5.6432 \qquad R^2 = 0.9952 \tag{10.2}$$

$$\text{FeCl}_3:\quad \log(\text{I}) = 1.3221 \cdot \log(\text{S}) - 5.9771 \qquad R^2 = 0.9981 \tag{10.3}$$

Next, the supernatant is measured and the ionic strength is calculated using the equations above. This calculation results in an ionic strength of 10 mM, 15 mM and 17 mM for NaCl, $CaCl_2$ and $FeCl_3$, respectively, assuming the dissociation of those salts would provide the only charged species present in the activated sludge supernatant.

Supernatant composition

To assess the supernatant's ionic composition, testkits (HACH LANGE LCK series) and ICP-MS (Aligent Technologies, 7700 series) are used. The metal ions in the supernatant are quantified by the ICP-MS measurement. First, the supernatant is filtered using a syringe filter with 0.45 µm pore size. Next, the samples are diluted using MilliQ water so that the elements are within the detectable concentration range. Subsequently, 100 µL pure HNO_3 is added to 10 mL diluted sample to avoid precipitation, whereafter the ICP-MS measurement is performed.

Testkits are used to detect the nitrate, nitrite and ammonium concentrations. After mixing the supernatant with the reactive components (dependent on the ion of interest), the samples are allowed to react during half an hour after which a value for the desired component's concentration is obtained spectophotometrically (HACH DR 5000). Table 10.1 depicts the results of supernatant analysis.

The components that are summarised in Table 10.1 yield an ionic strength of 3.00 mM, which results in a difference with the conductivity measurements of 7-12 mM. While part of this difference may be attributed to unmeasured ions, such as phosphates, carbonates or trace elements, the majority of charges are probably provided by functional groups present on the SMP. Therefore, it is affirmed that SMP is indeed responsible for a major portion of the charges present in the activated supernatant.

Table 10.1: Composition of activated sludge supernatant

Component	Measured value	Literature value
Sodium (Na^+)	47.10 ± 0.84 mg/L	20.90 mg/L[1]
		34.20 mg/L[2]
Magnesium (Mg^{2+})	3.30 ± 0.09 mg/L	3.80 mg/L[1]
		3.03 mg/L[2]
		14.60 mg/L[3]
		8.80 mg/L[4]
Aluminium (Al^{3+})	9.00 ± 0.70 µg/L	250 µg/L[1]
Phosphor (P)	0.36 ± 17.49 mg/L	2.30 mg/L[1]
		8.40 mg/L[2]
Potassium (K^+)	8.26 ± 0.15 mg/L	2.10 mg/L[1]
		8.40 mg/L[2]
Calcium (Ca^{2+})	30.18 ± 1.04 mg/L	48.6 mg/L[3]
		58.00 mg/L[4]
		30 - 60 mg/L[5]
Iron (Fe^{3+})	13.00 ± 0.30 mg/L	2.40 mg/L[1]
		350 µg/L[3]
Nitrate (NO_3-N)	7.88 mg/L	15.90 mg/L[1]
		24.5 mg/L[2]
Nitrite (NO_2-N)	13.00 µg/L	600 µg/L[2]
Ammonium (NH_4-N)	81.00 µg/L	500 µg/L[1]
Total ionic strength	3.00 mM	
M/P ratio	1.26	

[1][Nguyen et al., 2008], [2][Yang et al., 2013], [3][Lyko et al., 2007], [4][Loulergue et al., 2014], [5][Ye et al., 2016]

The table also depicts several values found in literature, which are depicted as a reference. Differences between the measurements in this study and the literature values can be attributed to the fact that the exact composition of sludge and supernatant strongly depend on the kind of wastewater and the used treatment methodology.

10.3.2 Theoretical calculation of osmotic pressure effect

In this section, the theoretical possibility of the osmotic pressure effect will be briefly calculated. Assuming a permeate temperature of 20°C, Equation (2.17)

Table 10.2: Different ionic strengths and monovalent-over-polyvalent cation ratios tested.

	I = 0.05 mM	I = 5 mM	I = 500 mM
M/P = 0.2			
M/P = 20			

can be used to calculate the osmotic pressure effect as a function of the difference in ion concentration across the membrane, i.e., between the cake layer and the permeate. Rewriting this formula as a function of the osmotic pressure effect yields Equation (10.4), which expresses the concentration difference (ΔC) between permeate and cake layer as a function of the osmotic pressure effect.

$$\Delta C = \frac{\Delta\pi}{\mathrm{RT}} = \frac{100 \text{ mbar} \cdot 100 \text{ Pa/mbar}}{8.3145 \text{ J/mol K} \cdot 293.15 \text{ K}} = 4.10 \text{ mM} \tag{10.4}$$

As can be seen by the expression, in order to achieve a 100 mbar TMP-increase, a concentration difference of 4.10 mM must be achieved between the cake layer and the permeate. Therefore, it is reasonable to assume that the osmotic pressure effect might indeed be responsible for some increase in filtration resistance.

10.4 Impact of salt solution composition

In this section, the supernatant of activated sludge samples will be replaced by different salt solutions, as was performed in the preliminary experiments (Section 10.2). These salt solutions will be made up from NaCl and $CaCl_2$ and will differ in ionic strength (I) ranging from 0.05 to 500 mM and in monovalent over polyvalent cation ratio, being low (0.2) or high (20). Table 10.2 summarizes the different solutions tested. All solutions were made using MilliQ water.

Supernatant was replaced by centrifugation (500g, 5 min, 4°C, Eppendorf 5810R using rotor F34-6-38). Filtration and microscopy/image analysis were performed in the same manner as in the preliminary experiments (Section 10.2.1).

10.4.1 Effect of ionic strength

Low M/P ratio of 0.2

Figure 10.4 depicts the effect of replacing the supernatant with salt solutions of different ionic strenghts, but with a fixed M/P ratio of 0.2.

Low I: 0.05 mM. As SMP were shown to be major foulants (see Chapter 9), it is reasonable to assume that the replacement of supernatant containing SMP by a lowly concentrated salt solution would result in a filtration improvement.

However, for the low ionic strength, a flocculation can be observed (orange bars in Figure 10.4), which results in a decrease in the particle size distribution of the smaller floc classes and an increase in the larger classes. Statistically, this flocculation is shown by the difference in average surface weighted floc size ($p = 0.026$).

The filterability increases for all three fluxes for the low ionic strength, which is most likely due to the observed flocculation. One may argue that this flocculation is the result of divalent cation bridging, but as the same effect is observed at a high M/P ratio, which will be shown in Section 10.4.1, this is unlikely.

The improvement in filtration is the highest for the lowest fluxes, which is in line with what was already discussed in Chapter 9, that lower fluxes are less dependent on particle sizes but more on surface (i.e., charge related) characteristics.

Intermediate I: 5 mM. At intermediate ionic strength, the results are in similarity with the above paragraph. The improvements in filterability are, however, not as pronounced, while the flocculation seems to be of the same magnitude. As more charged species are present due to a 100-fold increase in cation concentrations, probably the charge related effects such as cake double layer compression (Section 2.3.2) impacted filtration more strongly.

High I: 500 mM. When the supernatant is replaced by the salt solution with the highest ionic strength, an inverse effect is observed. As can be seen on Figure 10.4, the filterability deteriorates for all three fluxes in comparison with the supernatant case. The effect is the most pronounced for the highest flux. As can be seen at the bottom part of the figure, the change of supernatant causes an increase in particles between 1-25 µm. The increase in small fragments is

Table 10.3: Calculation of critical $C^{sat}_{CO_3^{2-}}$ concentration for precipitation using the $CaCO_3$ solubility product.

I	M/P	$C_{Ca^{2+}}$	$C_{Ca^{2+}}$	$C^{sat}_{CO_3^{2-}}$
mM	[-]	g/L	M	M
0.05	0.2	6.0 x10^{-4}	1.5 x10^{-5}	2.2 x10^{-4}
5	0.2	6.0 x10^{-2}	1.5 x10^{-3}	2.2 x10^{-6}
500	0.2	6.0	1.5 x10^{-1}	2.2 x10^{-8}
0.05	20	0.46 x10^{-4}	1.2 x10^{-6}	2.9 x10^{-3}
5	20	0.46 x10^{-2}	1.2 x10^{-4}	2.9 x10^{-5}
500	20	0.46	1.2 x10^{-2}	2.9 x10^{-7}

statistically relevant as well (p = 0.0381). This apparent deflocculation could in fact be a flocculation of small dissolved and colloidal matter, that cannot be detected microscopically and could be caused by the sweep flocculation effect after dosing such high amounts of calcium ions [Biggs et al., 2001; Ding et al., 2015; Peeters and Herman, 2007].

Alternatively, the increase of small matter could be the formation of a carbonate precipitate. Therefore, the solubility of calcium carbonate ($CaCO_3$) was evaluated. The solubility product K_{sp} of $CaCO_3$ is 3.3 x10^{-9} [Benjamin, 2002]. Using this information and the definition of solubility product (Equation (10.5)), the carbonate saturation concentration ($C^{sat}_{CO_3^{2-}}$) was calculated for each used salt mixture. If the carbonate ion concentration increases above this value, oversaturation occurs and the formation of precipitate is possible. The same observation was made by Peeters and Herman [2007], who, aside the sweep flocculation effect, noticed that during flocculation large fractions of calcium ions were incorporated in the floc structure as inorganic precipitates rather than as bridges between organic functional groups.

$$K_{sp} = [Ca^{2+}] \cdot [CO_3^{2-}] = 3.3 \text{ x}10^{-9} \tag{10.5}$$

As can be seen from the table, the critical carbonate concentration is rather low in both high ionic strength cases. However, as MilliQ has been used to formulate the salt solutions, chances of precipitation formation have been minimised. Still, some carbonate ions may have been retained in the activated sludge matrix or, in the cases where salt was dosed to solutions containing supernatant (see Section 10.5), may have been present in the supernatant.

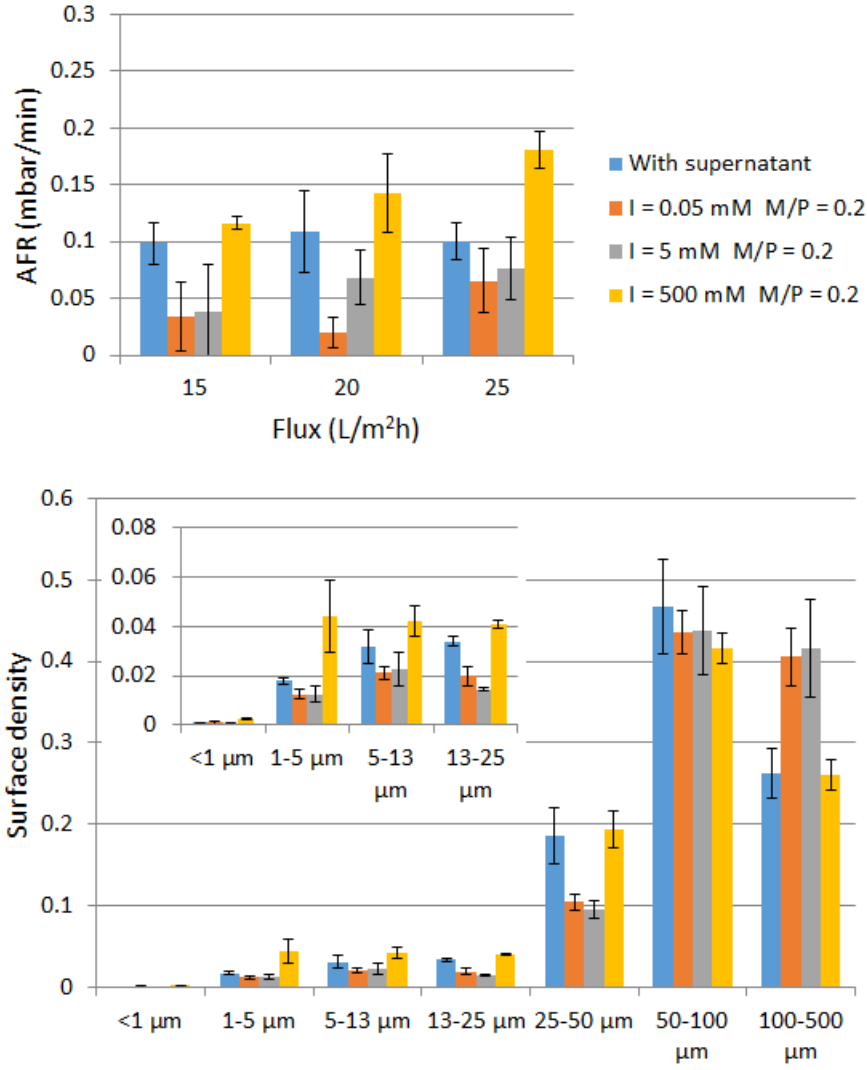

Figure 10.4: Effect of replacing supernatant with salt solutions of different ionic strengths, but the same low M/P ratio of 0.2. **Top:** average fouling rates as a function of flux and salt solution. **Bottom:** surface weighted particle size distributions.

High M/P ratio of 20

The same procedure was performed using a salt mixture with a monovalent-over-polyvalent cation ratio of 20. The results from these experiments are shown in Figure 10.5.

Low I: 0.05 mM and intermediate I: 5 mM. For the low and intermediate ionic strengths, the same effects were observed for the high M/P ratio of 20 as for the low ratio from Section 10.4.1. Flocculation leads to a reduction of the smallest floc sizes and an increase in the higher floc sizes. The extent of this flocculation is, however, less pronounced than for the previous case, probably due to the lesser amount of polyvalent cations.

For the low and intermediate ionic strengths, the observed fouling rates are again lower than those of the native sludge solution, which is in accordance with the observations made by [Shen et al., 2015] and could point towards the osmotic pressure effect by the SMP which were absent after supernatant replacement.

High I: 500 mM. Dosing a high number of monovalent cations resulted in deflocculation, as can be seen at the bottom of Figure 10.5. Especially the number of objects between 13-25 µm increases ($p = 0.033$), but also the number of small fragments was statistically proven to augment ($p_{RelFragNum} = 0.044$).

The effect on filtration of the shift in the particle size distribution is shown by the average fouling rates. For the moderate fluxes, the fouling rates are lower than the initial case, but for the higher flux of 25 L/m^{2}h, the fouling rate increases substantially. This phenomenon can be explained by the critical particle diameter including the range of particles of which the numbers increase due to deflocculation [Broeckmann et al., 2006].

10.4.2 Effect of M/P ratio

Figure 10.6 summarizes the effect of the monovalent-over-polyvalent cation ratio on filterability for the different ionic strengths tested in the previous sections.

Low I: 0.05 mM. At low ionic strength, not much difference is noted between both M/P ratio's. In both cases, filterability improves over the case including supernatant, as was explained in Section 10.4.1.

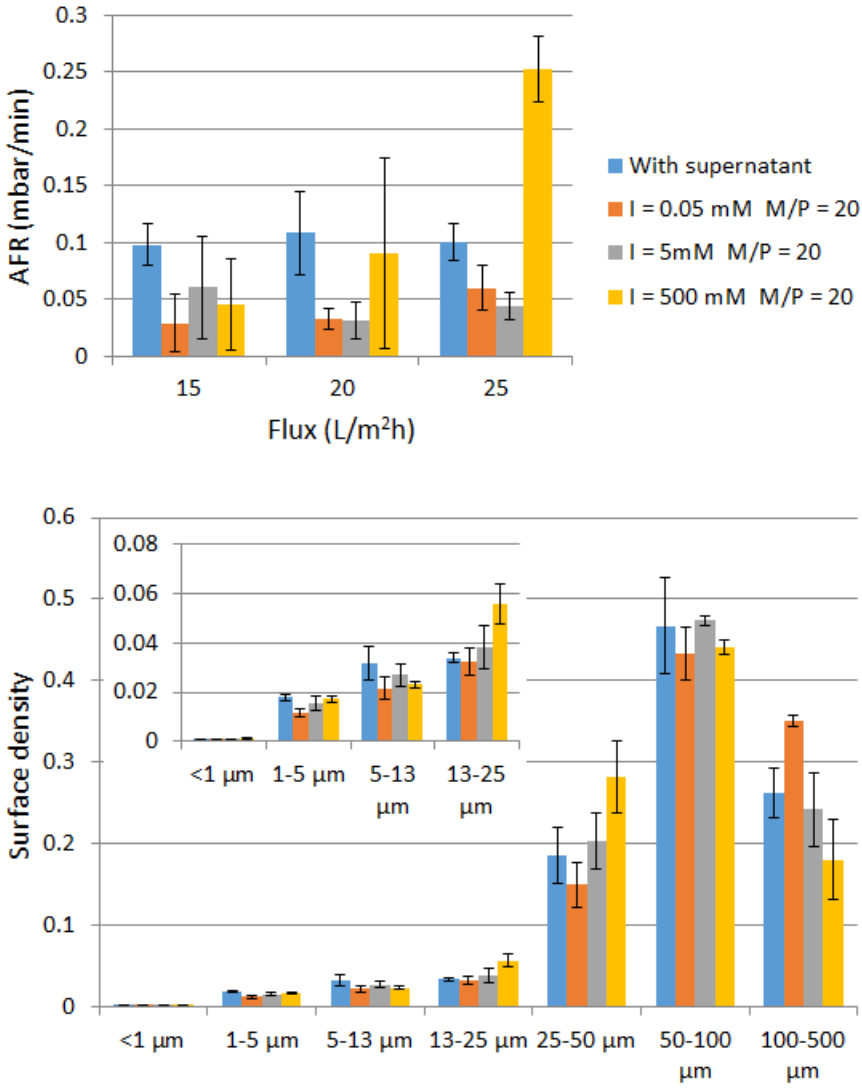

Figure 10.5: Effect of replacing supernatant with salt solutions of different ionic strengths, but the same high M/P ratio of 20. **Top:** average fouling rates as a function of flux and salt solution. **Bottom:** surface weighted particle size distributions.

Intermediate I: 5 mM. At intermediate ionic strength, the situation at the lowest flux appears inverse in regard to the situation at the two higher fluxes. However, the error margins of the first flux are high. The differences beween both M/P ratios cannot be explained by the DCB theory, because according to this theory, the inverse effect would be expected. For the low M/P ratio, the trends can be explained by flocculation (see Section 10.4.1), due to the formation of a denser cake layer. The results for the high M/P however, cannot be explained through the morphology of the sludge, since no substantial changes in morphology were detected. A possible explanation is that EPS, which was not measured during this study, has had a detrimental influence on filtration.

High I: 500 mM. In both cases, at high ionic strength, the number of small particles increases. At the M/P ratio of 20, this increase could be an accelerated effect from the divalent cationic bridging theory, since the amount of monovalent ions that were added to the mixture is quite high, hence rapid diffusion into the floc matrix would have been possible.

However, for the low M/P ratio, the amount of small particles increased as well, which could not be explained by the DCB theory, as in this theory, a low M/P actually induces flocculation. Therefore, two other explanations are proposed. Firstly, it might have been the case that the solubility of $CaCO_3$ was exceeded and that the extra small matter was in fact of inorganic nature. Alternatively, the increased amounts of fragments may have been the result from sweep flocculation of the Ca^{2+} addition [Biggs et al., 2001; Ding et al., 2015; Peeters and Herman, 2007].

10.4.3 Conclusion

From the above experiments can be concluded that no single theory was able to explain all different phenomena. Moreover, a large discrepancy was observed between the results of adding 5 mM and 500 mM salt solutions. In the next experiments, this range of concentrations will be studied further. What concerns the M/P, the results were quite similar between both solutions, although the mechanisms behind some effects may have been different. Future research is needed to clarify these observations.

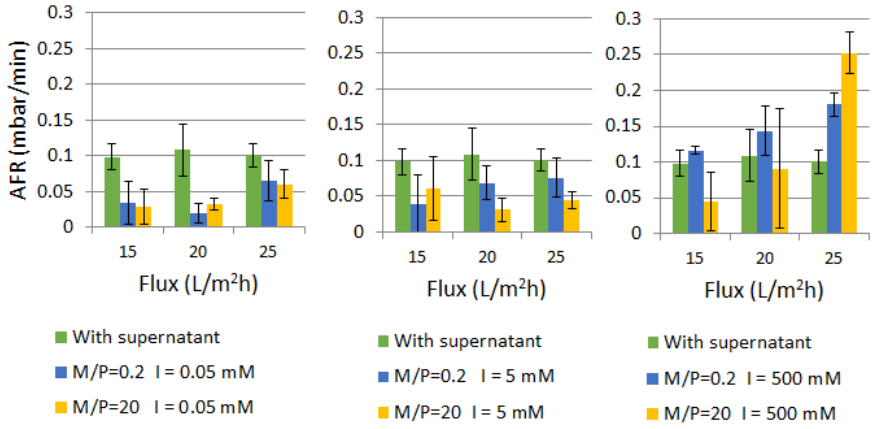

Figure 10.6: Effect of replacing supernatant with salt solutions of M/P-ratios for each ionic strength tested on average fouling rates. **Left:** 0.05 mM. **Middle:** 5 mM. **Right:** 500 mM.

10.5 Gradual salt addition

In the following series of experiments, a concentrated salt solution was used to increase the ionic strength of the mixed liquor in the filtration tank during filtration. By the time these experiments were performed, the filtration set-up was upgraded to allow two separate mixtures to be tested simultaneously.

10.5.1 Experiment 1 - addition of NaCl

In the first experiment, two filtration tests are performed on activated sludge from the local wastewater treatment plant. For one of the sludges, the supernatant was replaced by MilliQ using centrifugation (500g, 5 min, 4°C, Eppendorf 5810R using rotor F34-6-38). Filtration is started up at a flux of 20 L/m^{2}h and a continuous regime of 10 minutes filtration and 5 minutes of relaxation is maintained throughout the whole experiment. The pH was monitored throughout the experiment and adjusted when the value deviated from 6-8.

Figure 10.7 depicts the evolution of the average fouling rate for both set-ups while Figure 10.8 shows the particle size distribution for the reactor in which the supernatant was replaced by MilliQ water.

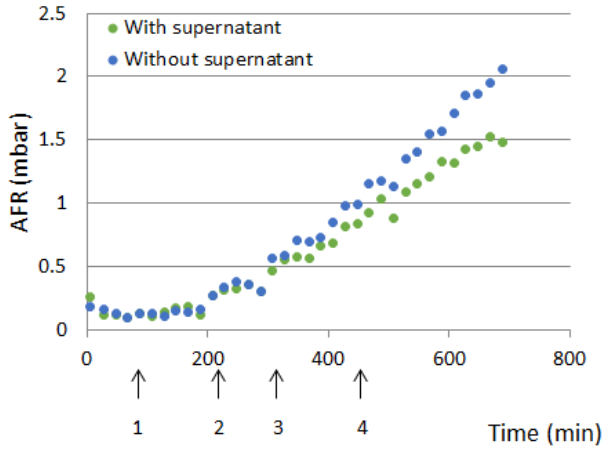

Figure 10.7: Average fouling rate of sludge mixtures for Experiment 1. Supernatant is replaced by MilliQ water for one reactor. NaCl is added at moments indicated by the arrows with resulting ionic strengths of 5 mM (1), 170 mM (2), 335 mM (3) and 500 mM (4).

As can be seen from Figure 10.7, in both cases the average fouling rate increases over time with the addition of more salt and in both cases, a significant increase in fouling rate occurs from an elevated ionic strength ($I > 350$ mM). However, for the reactor in which the supernatant was kept, this increase is slightly lower than for the reactor where it was replaced.

For both reactors, a deflocculation occurs, yielding increased numbers of small flocs and particles over time. Figure 10.8 depicts the particle size distributions for the reactor in which the supernatant was replaced by MilliQ.

Two observations can be drawn from these results. First, the data is not in accordance with the results from [Shen et al., 2015], as in their case removing the supernatant resulted in a strong increase of filterability. Secondly, adding NaCl leads to deflocculation, which results in an increase in fouling rates through the formation of a dense cake layer.

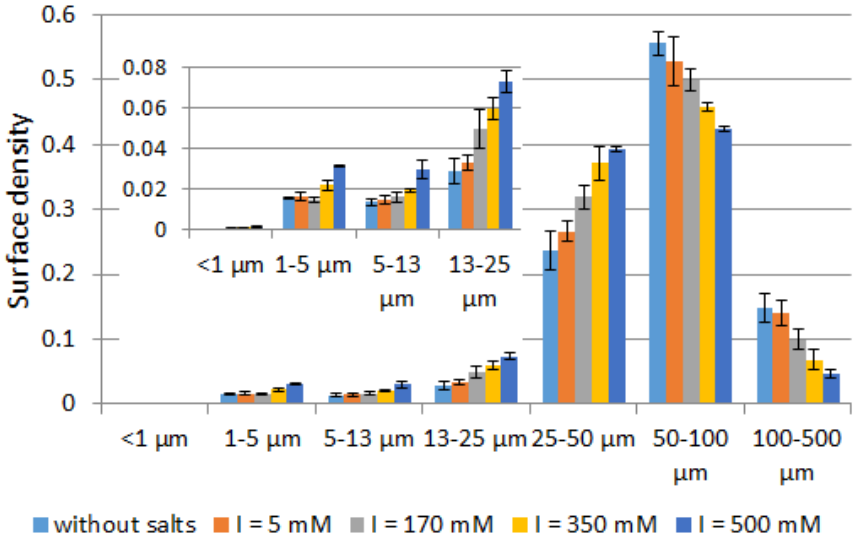

Figure 10.8: Particle size distributions for Experiment 1 during the NaCl addition for the sludge mixture in which supernatant was replaced by MilliQ water.

10.5.2 Experiment 2 - addition of salt solution with M/P = 0.2

The same experiment as in the previous section was repeated, but a different concentrated salt solution was used this time. Instead of NaCl, a concentrated salt solution with a monovalent-over-polyvalent cation ratio of 0.2 was used. The average fouling rates that result from gradually adding this solution to both filtration set-ups are shown in Figure 10.9.

As can be seen from Figure 10.9, the fouling rates increase for both reactors when the salt concentration is increased. However, as opposed to Experiment 1 (Section 10.5.1), no differences in the particle size distribution or the activated sludge's morphology could be observed for either reactor throughout the experiment.

The same observation regarding the difference with or without supernatant can be made. Again, removing the supernatant from the mixture did not result in an improvement of filterability, but rather the opposite effect was observed.

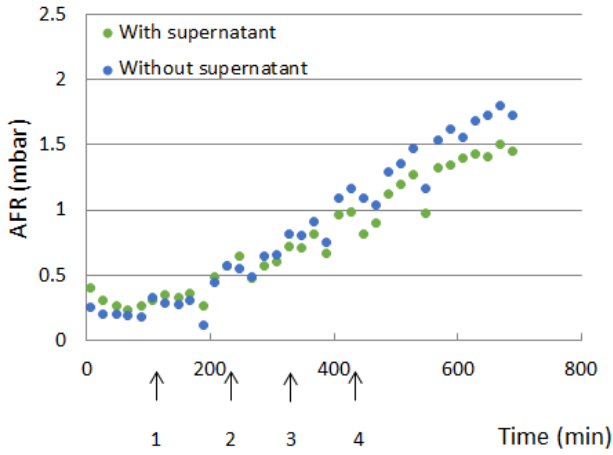

Figure 10.9: Average fouling rate of sludge mixtures throughout Experiment 2. Supernatant is replaced by MilliQ water for one reactor. A concentrated salt solution with a M/P ratio of 0.2 is added at moments indicated by the arrows with resulting ionic strengths of 5 mM (1), 170 mM (2), 335 mM (3) and 500 mM (4).

10.5.3 Experiment 3 - addition of salt solution with M/P = 0.2 versus reference (inc. supernatant)

In Experiments 1 and 2, both reactors were subjected to an increase in the mixed liquor ion concentration, leading to fouling of the membrane. However, the initial mixture may have an intrinsic irreversible fouling potential of its own, which would cause a gradual TMP-increase over time as well. To uncouple both effects, both filtration tests from Experiment 2 are repeated in the next two sections. This section (Experiment 3) will tackle the situation where the original supernatant remains included in the starting mixture, whereas the next section (Experiment 4) will handle the situation in which the supernatant is replaced by MilliQ. In both experiments, one of the reactors will be subjected to the increase in cation concentration, whereas the ionic strength of the other reactor, named the *reference*, will be unchanged after starting up.

Figure 10.10 depicts the average fouling rates from Experiment 3. As can be seen on the figure, the fouling increases for both the reference and the mixture in which the salt concentration is increased.

For the reference reactor, no significant change in the sludge's morphology and

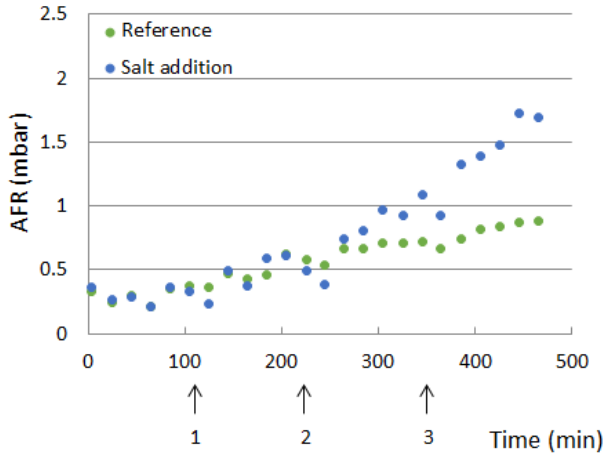

Figure 10.10: Average fouling rates during Experiment 3. Supernatant is kept throughout this experiment. A concentrated salt solution (M/P = 0.2) is added gradually to one reactor, resulting in ionic strengths of 5 mM (1), 225 mM (2) and 500 mM (3). The other reactor (reference) is not subjected to any change throughout the filtration test.

particle size distribution are observed, so the fact that the reference's fouling rate increases slowly over time indicates that the relaxation periods were not sufficient to completely remove the fouling from the filtration periods.

For the salt-addition reactor, the number of small particles increases over time, as shown in Figure 10.11, which could be related to the formation of precipitate as described in Section 10.4.1. Alternatively, the increase of small particles could be the result of the sweep flocculation effect from the dosed calcium cations.

10.5.4 Experiment 4 - addition of salt solution with M/P = 0.2 versus reference (excl. supernatant)

Figure 10.12 depicts the average fouling rates for both samples (left) and the particle size distribution of particles smaller than 25 µm for the sample in which the salt solution (M/P = 0.2) was added. In this experiment, the supernatant was replaced by centrifugation for both samples, prior to analysis.

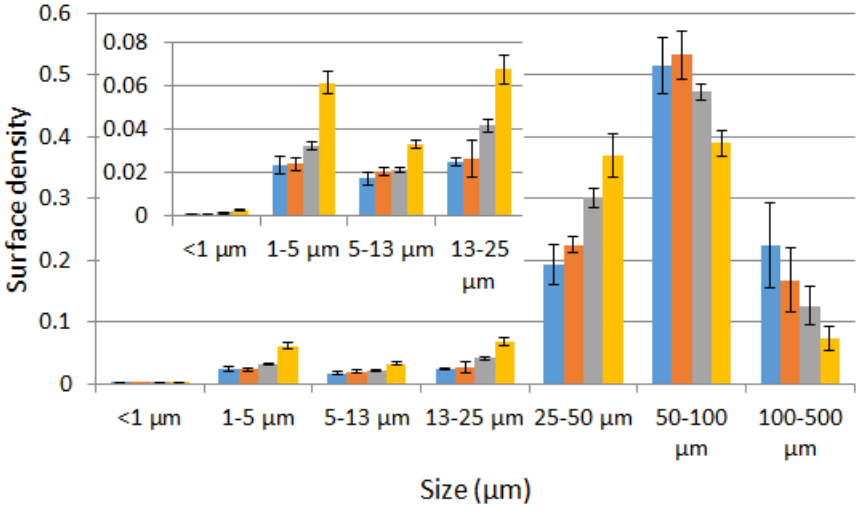

Figure 10.11: Particle size distributions during Experiment 3 for the reactor in which a salt solution with M/P = 0.2 is added to the sludge mixture. Supernatant was kept during this experiment.

The results show a similar trend in filterability as the one during Experiment 3. Both the reference and the salt-addition sample increase in average fouling rate over time, but the increase for the salted sample is higher.

In the reference sample, no change in morphology was detected throughout the experiment, whereas for the salted case, the particle size distribution (Figure 10.12 (right)) depicts an increase in smaller particles, which could be explained by reasons above.

In Figure 10.13, the filtration profiles of the salted samples from Experiments 3 and 4 are compared. As can be seen in the figure, in this case, adding the supernatant to the sample leads to an increase in fouling rates, which is in accordance with the results from [Shen et al., 2015]. However, the increase is not as impactful as the phenomenon observed by these authors and the results do not coincide with prior obtained results (e.g., Sections 10.2 and 10.5.2).

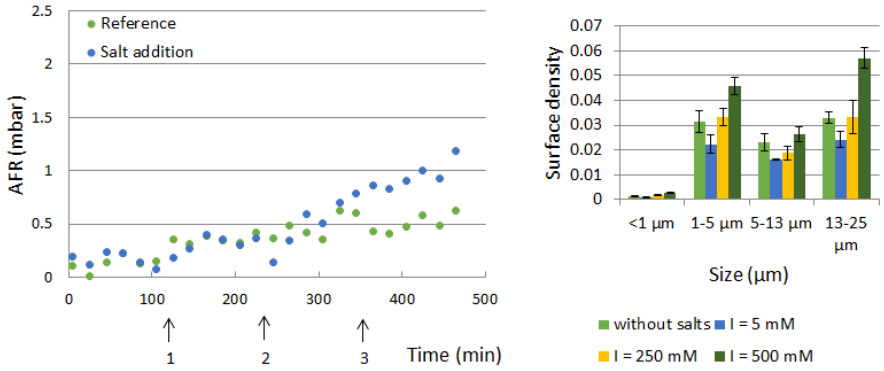

Figure 10.12: **Left:** average fouling rates during Experiment 3. The supernatant is replaced by MilliQ. A concentrated salt solution (M/P = 0.2) is added gradually to one reactor, resulting in ionic strengths of 5 mM (1), 225 mM (2) and 500 mM (3). The other reactor (reference) is not subjected to any change throughout the filtration test. **Right:** small particle size distributions for the salt-addition reactor.

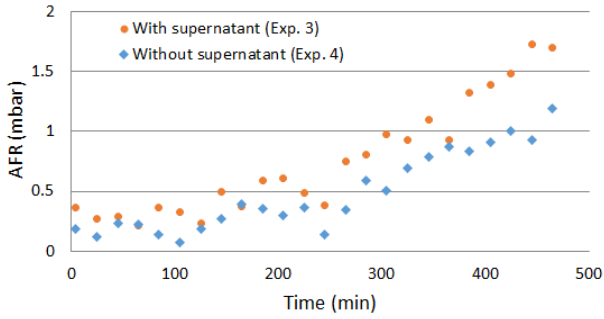

Figure 10.13: Comparison of average fouling rates for the sludge mixtures with and without supernatant from Experiments 3 and 4.

10.6 Discussion

In this section, the results from the previously described experiments will be discussed and compared with literature.

10.6.1 No single theory

The first observation that can be made is that there is no single theory that can explain all phenomena. The results from the gradual experiments (Section 10.5) show that in some cases when the supernatant was removed, the filterability improved, whereas in others the filterability worsened, not even considering any change in ionic strength. This observation, together with the results from the preliminary experiments (Section 10.2) proof that the osmotic pressure effect alone is not capable of explaining the obtained results.

Moreover, in cases where deflocculation occurred (Sections 10.2, 10.4.1 and 10.5.1), the results are in contradiction with the findings of [Shen et al., 2015] and are more in line with the general consensus that the creation of small particulate matter is detrimental for filtration through the formation of a dense cake layer.

10.6.2 Low / intermediate ionic strength

The supernatant of the activated sludge is assumed to have an ionic strength of the order of 1-20 mM, as was measured in Section 10.3. When the supernatant was replaced with a salt solution that had a much lower (0.05 mM) ionic strength, filterability generally improved.

Aside from the removal of SMP as foulant, part of this improvement can possibly be attributed to the reduction of the amounts of small sludge particles, as observed in Section 10.4.1 although the exact reason behind this flocculation phenomenon cannot be explained through any of the charge-related theories.

Potentially, hydrophobic interactions may have provided alternative binding possibilities, which was shown by Kara et al. [2008], since in their study, an inverse relationship between the sodium content in the reactor and the relative hydrophobicity of the sludge particles was observed.

Alternatively, reducing the ion content in the supernatant has led to the increase of the double layer's radius, as described in Section 2.3.2. With the increase of the double layers, the sludge particles that form the cake layer have increased repulsion for each other, leading to a more porous and permeable layer.

10.6.3 High ionic strength

In all experiments, the increase of the ionic strength led to a reduction in filterability. In many cases, the fouling could be attributed to the increase of small particles, through deflocculation, potential formation of precipitate or through sweep flocculation by the calcium ions [Biggs et al., 2001; Ding et al., 2015; Peeters and Herman, 2007].

However, during Experiment 2 (Section 10.5.2), no change in the mixed liquor's particle size distribution could be detected, while the fouling rates still increased proportional to the increase in ionic strength. A potential explanation could be given by the reduction of the charged particles' double layers, leading to a more dense cake layer and by the easier particle attachment after the electrostatic energy barrier has diminished (Figure 2.12).

In retrospect, increasing the salt content may have provided the necessary conditions at the cake layer for the creation of the osmotic pressure resistance, as in Section 10.3.2 it was calculated that only a few mM of difference in ion concentration across the membrane may provide already a substantial osmotic pressure effect. This theory is supported by the empirical relationship between ionic strength and osmotic pressure (see Equations (2.20) and (2.23)), as proposed by Zhang et al. [2013]. Although this relationship is somewhat arbitrary, as discussed in Section 2.3.7, the same authors did observe an increase in specific filtration resistance with increasing ionic strength (ranging from 0 - 200 mM), which is in accordance with this study.

In their study, Zhang et al. [2013] also measured the difference between influent and effluent conductivity, which is shown in Figure 2.18. In the figure, a gap of approximately 100 µS/cm clearly separates both profiles, whereas the trends are similar. This effect indicates that a part of the influent's ions may be retained in the cake layer. Using Equations (10.1) and (2.17), an estimation is made for the extent of the osmotic pressure effect under these conditions. The calibration curve of the NaCl solution is used as it is in line with the authors' assumptions. The results for the estimation are shown in Equations (10.6) and (10.7).

$$\mathrm{I} = 10^{1.1799 \cdot \log(100\ \mu\mathrm{S/cm}) - 5.7481} = 4.07\ \mathrm{x10^{-4}\ M} \tag{10.6}$$

$$\Delta\pi = \Delta\mathrm{CRT} = 4.07\ \mathrm{x10^{-4}\ M} \cdot 8.3145\ \mathrm{J/mol\ K} \cdot 293.15\ \mathrm{K} = 9.90\ \mathrm{mbar} \tag{10.7}$$

As can be seen from the outcome of Equation (10.7), the 100 µS/cm difference in conductivity yields an osmotic pressure which is just short of 10 mbar, which

is the case if no elevated ion concentrations occur in the cake layer. In order for the osmotic pressure effect to become significant, it would require a 5 to 10 fold increase of this difference. Moreover, the difference in conductivity between the influent and effluent may also have been caused by microbial activity (e.g., the consumption or production of acetate).

10.7 Conclusion

From the above experiments, the following conclusions are drawn.

- The effect of flocculation/deflocculation dynamics is more important than the osmotic pressure effect. Changes in particle size distributions have shown to exhibit a stronger influence on filtration and even counteract OPE-related effects.
- In theory, the osmotic pressure effect is possible. To provide a significant (100 mbar) osmotic pressure, the ionic strength difference between cake layer and permeate needs to be 4.10 mM, which was the same order of magnitude as the measured supernatant ionic strength.
- Calculations inferred from the results of Zhang et al. [2013] have shown that the difference in ionic strength between the influent and effluent resulted in a slight osmotic pressure effect (10 mbar), but large upconcentration factors in the cake would be required for this effect to become the main source of filtration resistance. Unfortunately, with the performed experiments, the occurance of such significant upconcentration factors could not be experimentally verified.
- At low ionic strengths, filtration was good. However, increasing the ionic strength always led to deterioration of filterability, which could in nearly all cases be related to an increase in small particulate matter. Alternatively, high ionic strength can lead to a cake compaction through charge neutralization effects.
- In all cases, increasing the ionic strength above 350 mM led to worsened filtration performance. For the case of a high M/P ratio, deflocculation was assumed to be responsible for the increased average fouling rates at high ionic strengths, which is in line with the divalent cation bridging (DCB) theory . However, at low M/P ratio, the amounts of small particles increased as well, which could be explained through precipitation or sweep flocculation. The DCB theory's bioflocculation improving effect of a low M/P ratio is affirmed to be a more longterm process, as in Section 9.4.

Alternatively, the deflocculation of the sludge may have been the result from a biological stress response to increased salt contents.

Chapter 11

General conclusion and outlook

In this chapter, a conclusion (Section 11.1) will be presented to this dissertation. Next, an outlook towards future research opportunities will be provided (Section 11.2).

11.1 General conclusion

In Section 1.3 and Figure 1.2, the primary aim of this work was defined to give an answer to *what sludge characteristics cause separation problems, what is the underlying cause and can it be avoided?* To this end, three goals were defined: (*i*) the creation of a framework for bioflocculation and filterability monitoring, (*ii*) to experimentally define the relationship between bioflocculation and activated sludge separation and (*iii*) to study more in-depth the influence of cations on bioflocculation and filterability in order to validate the different theories regarding this matter.

11.1.1 Framework for bioflocculation and filterability monitoring

In Part I, monitoring tools for bioflocculation and filterability assessment of activated sludge were further developed.

Dead-end filtration tests were standardised. The dead-end filtration tests: time to filter (TTF_{25}) and weight of filtrate (WOF_{250}) were standardised (see Section 4.2.2). For samples with poor filterability, the weight of filtrate is preferable over the time to filter since its duration is fixed, and the results show less variance.

Development of a small cross-flow filtration set-up. The cross-flow filtration set-up was developed to allow small sample volumes (2 L) to be tested in hydraulic conditions that more closely resemble MBR operation (see Section 4.2.3). The flux-driven set-up is operated through a flexible LABVIEW program, which allows easy-to-use flux setting. Two vessels that can hold tailor made or standardized A4 Kubota membranes allow for testing of two sludge samples simultaneously.

Improved phase contrast image analysis. Chapter 5 describes several adjustments that were made to the existing activated sludge image analysis program, which was given a new name: *ASIAP*. Changes included better thresholding (segmentation), improved recognition of filaments and fragments and the ability to handle pictures of variable sizes. The color image requirement was overcome as well. Statistical analysis showed that 20 grids of 3x3 images were sufficient to obtain statistically significant results.

Quantitative epifluorescence microscopy. An explorative study on the use of epifluorescence microscopy for bioflocculation monitoring was performed in Chapter 6. Dyes were selected for several activated sludge characteristics for which concentrations and staining routines were optimised.

Two quantitative MATLAB routines were created to accommodate the fluorescence images. ASIAP-Fluo serves as an add-on for the existing phase contrast routine, while FLASIAP is a standalone version that only uses the fluorescence information for image analysis.

Proteins, polysaccharides and hydrophobicity were quantified using the new fluorescent imaging method and statistically compared with their chemocolometric counterparts. From these results, the following conclusions could be drawn.

- Alexa 405-NHS ester was used to label proteins in activated sludge samples. The results showed good correlation with the heat-treatment method for EPS extraction and the modified Lowry method for protein content determination.

- Fluorescein isothiocyanate (FITC) did not yield good results when labelling proteins, due to a too high background signal and a fast bleaching rate.
- α-polysaccharides were labeled using a fluorescently labelled Concanavalin A conjugate (ConA-Alexa488). Images showed distinct locations in the flocs where the concentration of those sugars were very high, while the rest of the image showed nearly no fluorescence. These results did not match with either of the EPS extraction methods. It was concluded that the specificity of both methods was different.
- Nile Red labeling could successfully differentiate between hydrophobic organic regions and hydrophilic inorganic regions in flocs. However, differentiation in hydrophobicity within organic regions was not possible with the concentrations tested. Possibly the amount of used dye was too high for this purpose.

A semi-quantitative comparison between a proposed fluorescent method for Gram staining and the conventional staining method yielded good similarities. Using the new method, in conjunction with FLASIAP, quantitative Gram staining will become feasible.

Heat treatment versus cation exchange resin for eEPS extraction. eEPS were extracted using both extraction methods and analysed for polysaccharides and proteins using the Dubois and modified Lowry method (see Section 4.1.5).

For the polysaccharides, both extraction methods yielded similar results, with good correlation between both datasets.

The results from the protein measurements, however, indicate very different extract compositions. As described above, the results from the heat treatment method could be correlated to quantitative fluorescent staining with A405-NHS. Therefore, the heat treatment method is brought forward as the most universal EPS extraction method.

11.1.2 Impact of bioflocculation on activated sludge separation

The impact of bioflocculation on activated sludge separation was assessed in Chapters 7 and 8. In Chapter 7, several activated sludge samples of different origin were characterised and assessed for their separation performance. In Chapter 8, the balance between monovalent and polyvalent cations was

manipulated to result in different bioflocculation states, which in turn led to significant alterations of filtration and settling performance. The conclusions from both chapters were summarized and discussed in Chapter 9.

MBR filtration

Size matters. Large and dense activated sludge flocs were confirmed to provide feasible filtration conditions, while large numbers of colloidal and particulate matter significantly reduced permeate productivity.

The particle selection theory, as described by Broeckmann et al. [2006] was used to explain this relationship. Shear forces hinder large sludge particles from reaching the membrane, whereas they do not exert enough influence on small matter to avoid deposition.

Moreover, colloidal matter are notorious for their blinding effect, in which they fill up interparticle gaps in the cake layer, reducing its porosity.

Shape matters as well. Round flocs were shown to improve filterability, while the occurrence of edgy flocs, with higher fractal dimensions, correlated with increased fouling rates.

SMP cause fouling. SMP affect filterability through pore and cake blocking effects, also reducing porosity, but are known to create a highly compressible gel layer as well, which provides a sticky basis for subsequent activated sludge flocs to deposit. Especially the polysaccharide fraction the SMP has been shown to cause significant fouling. However, in Experiment II, during the total floc collapse that resulted in severe filtration problems, the amounts of SMP proteins increased proportionally more than the polysaccharides.

Surface characteristics are important at low flux, PSD at high flux. Surface characteristics (relative hydrophobicity, surface charge) were found to be of higher impact for low fluxes, while particle size related characteristics and cake structuring was of higher importance during high fluxes. Hydrophobic forces have shown to promote aggregation, resulting in improved filterability, while a high surface charge was generally detrimental. At high flux, cake layer compression probably becomes more important as well, but this was outside this work's boundaries.

Role of bound EPS unclear. In general, it was observed that the bound EPS content had little direct influence on either separation technique. Therefore, it can be concluded that, although bound EPS are important since they determine activated sludge surface characteristics, they cannot be used as a fouling indicator.

Filaments create a secondary net. It was hypothesised that some filaments can prevent fouling through the creation of a dynamic net, onto which particles can deposit to form a structure that is more susceptible to shear. As such, the blinding effect of small matter is alleviated.

Dead-end filtration

Dead-end filtration tests for filterability monitoring are a dead end. During the experiments, it was observed that in several cases, dead-end filtration tests were unable to predict cross-flow filterability, and therefore care must be taken when comparing both filtration methods.

More cake, more impact. Dead-end filtration can be assumed as a limiting case of cross-flow filtration for which the backtransport forces are negligible in comparison with the suction force. In dead-end filtration, therefore, most of the activated sludge flocs are subjected to a positive resulting force towards the membrane, which leads to a large cake build-up. Because the amount of cake is much higher, charge related effects, blinding effects and probably cake compression effects are of much more impact than during cross-flow conditions.

Settleability

Long filaments in large numbers are bad. Settling was found to be mostly impacted by filament growth. In this regard, the length of the filaments showed a higher correlation with the sludge volume index than the number of filaments. In the labscale experiments, a feast/famine feeding regime and a careful monitoring of the dissolved oxygen concentration and pH resulted in a suppression of filamentous bulking.

Size matters, density matters more. In general, large flocs settle well. However, Experiment I has shown two cases where density was more important than size. In Reactor I, megaflocs were formed consisting of large floc structures

embedded in a filamentous matrix, while in Reactor II, although the floc size remained high, the floc structures became *empty*. Neither floc types settled well due to their too-low density.

CAS systems recover faster from disturbances than MBRs. Membrane bioreactors were found to be more vulnerable for deflocculation events and disturbances than conventional activated sludge systems that use settlers. The reason for this is twofold. Firstly, CAS systems tend to naturally select for well settling microbial community structures. Secondly, in CAS systems, released SMP and colloidal material tends to wash out in the effluent, whereas in MBR systems they are usually retained by the membrane. Therefore, it takes much longer for MBR systems to recover from such disturbances.

11.1.3 The influence of salts on MBR performance and bioflocculation

The **longterm** influence of the influent salt composition on MBR performance was assessed in Chapter 8 and a unified theory was proposed in Section 9.4. A high monovalent-over-polyvalent (M/P) cation ratio gave rise to significant deflocculation. During the first days and weeks, shell-shedding behaviour causes the release of particles and some amounts of colloids and SMP. After several weeks, total floc collapse happens, coincinding with the release of high numbers of SMP and colloidal material, which caused significant filtration problems. When dosing a low monovalent-over-polyvalent cation ratio, the situation alleviates immediately through sweep flocculation of colloids and dissolved SMP. After several weeks, the floc structure is completely restored as multivalent cations are taken up in the floc matrix.

In Chapter 10, the **shortterm** effects of salts on MBR performance were assessed. In all cases, a high ionic strength led to increased fouling rates, whereas at low ionic strength (< 5 mM), good filterability was measured. The osmotic pressure effect was not able to explain all observed phenomena, but was, nevertheless, deemed significant for filterability. The increase in ionic strength may have caused the formation of precipitates, but this is unlikely since the use of MilliQ limited the availability of precipitating anions. Potentially cake double layer compression resulted in an increased resistance at elevated ion levels. At high M/P ratios and high ionic strengths, the activated sludge showed a shortterm deflocculation, but an increase in smaller particles was also observed at the low M/P ratios, which could be related to sweep flocculation by calcium ions. Therefore, no definite statements could be given regarding the shortterm validity of the divalent cation bridging theory.

11.2 Outlook

In this section, an outlook will be given towards future research opportunities.

11.2.1 Understanding fouling

Fouling is, by nature, a complex phenomenon. In this section, a few propositions are made for future research that concerns understanding fouling.

In situ determination of fouling

Many theories and models attempt at describing fouling. It was already concluded that no single theory suffices to explain all relevant phenomena. In these theories, information regarding the cake layer thickness, porosity and composition is often estimated or approximated. To verify these models *in situ*[1] measurements of fouling is crucial. Several studies have already been dedicated to this purpose.

A detailed review regarding earlier non-invasive observation techniques was given by Chen et al. [2004]. Over the past years, several new technologies have surfaced. Fluid dynamic gauging measures the cake layer thickness through carefully withdrawing mixed liquor at the retentate side of the membrane surface [Jones et al., 2010, 2012; Mattson et al., 2015]. An alternative technique, based on infrared thermography, was recently developed by Ndukaife et al. [2015] and uses infrared wavelengths to measure surface temperature and emissivity of foulants on the membrane surface. Using this technique, differentiation between metallic and non-metallic model foulants was possible. The direct observation method, adopted from [Marselina et al., 2009] using a transparent membrane, has recently been used in conjunction with particles that differ in surface charge and hydrophobicity to unravel their effects on fouling [Lorenzen et al., 2016]. Another feasible approach during the filtration phase is currently being developed by the group of Ingmar Nopens (BIOMATH, Ugent) in collaboration with our own research group. In this work, a Wyko NT3300 profilometer will be used to scan the membrane surface.

Although previous research provided much information, in many cases model foulants have been used instead of real activated sludge. However, it was described before that fouling is not a process based on one single theory. Thus, to capture all relevant phenomena, subsequent research should attempt to focus

[1] *In situ* means during filtration, without disturbing the filtration hydrodynamics.

more on the characterization and application of activated sludge flocs themselves in hydrodynamic conditions that resemble real MBRs.

Detailed extracellular polymeric substances and microbial community analysis

A major part of the confusion regarding the role of EPS in membrane fouling comes from the confusing terminology and the absence of a generally agreed upon extraction protocol [Wang et al., 2013]. However, the definitions of EPS are inherently coupled to the used protocol. Moreover, it is not certain that the extracted molecules are effectively the ones that relate to fouling, as the EPS-groups are still very broad. This, together with the lack of detailed EPS information has most likely led to the conflicting results found in literature. Current EPS measurements are still a measure of *who knows what?*

In several recent works, microbial community analysis has been used to relate specific species of bacteria to fouling. Using quantitative fluorescence microscopy, bacterial species that form strong microcolonies such as *Nitrospira* and *Accumulibacter* were identified as bioflocculation and filtration promotors [Bugge et al., 2013]. It is in this regard that future research should focus on identifying the specific properties that such bacteria possess or create through the secretion of EPS. Using staining procedures, FISH and co-localization routines, bacteria that are involved in, e.g., the production of highly hydrophobic surfaces may be identified. Detailed studies on the EPS properties may provide key information regarding their origin and functionality. It is when such knowledge is obtained and when the particular macromolecules of interest and their producing microbial species have been identified, that a general extraction protocol, tailored towards these molecules, can be proposed to link EPS to fouling.

11.2.2 Efficient fouling control and mitigation

Online determination of optimal process conditions

In previous chapters, it was concluded that several fouling mechanisms are dependent on process conditions such as shear and flux and that bioflocculation is a complex phenomenon which cannot be easily modelled. Therefore, due to the complexity of the fouling phenomenon, moderate fluxes, long relaxation times and high aeration intensities are often employed to minimise fouling as much as possible. However, these may not be the most cost effective strategies. E.g., aside flux stepping experiments, optimal relaxation time variation has shown to vary between 0.2 and 4 minutes, depending strongly on the type of

activated sludge [Christensen et al., 2016]. Alternatively, shear and aeration may be varied in stepping experiments to yield optimal filtration conditions [Fox and Stuckey, 2015; Jørgensen et al., 2014; Monclus et al., 2010].

Online[2] tools that measure the effect of shear/aeration, flux and relaxation on net permeate yield may provide an alternative. As such, the optimal settings may be obtained without requiring in depth knowledge about the exact bioflocculation phenomena, but using a blackbox and empirical approach based on the filtration data itself. As obtaining information concerning the bioflocculation state is an exhaustive process, it cannot always be performed in time or at the location. Alternatively, these small, reliable and easy-to-use blackbox tools can be used in the wastewater treatment plant itself, hence on the sludge in question. Of course, those tools can and should be used in conjunction with measuring campaigns and chemometric analysis to provide in-depth mechanistic information about the fouling phenomenon.

Foulant concentration based flocculator dosage

To date, many fouling reducers, such as powdered activated carbon or cation-based polymers are dosed based on the MLSS concentration as recommended by their manufacturers. However, in previous chapters it was concluded that not the MLSS, but the concentration of SMP or colloids are mostly responsible for fouling. Therefore, it may be advisable to review current dosing strategies and have them relate to the concentration of these fouling species.

In the same sense, cake structure may be controlled. It has been shown in recent works that activated sludge cakes are highly compressible. Although adding melamine particles into the biofluid did not result directly in a change in compressibility, it did make the cake layer more porous and permeable and aided in the adsorption of organic matter (SMP) [Loulergue et al., 2014]. These changes resulted in a filterability improvement. Such methodologies, denoted by the authors as *cake engineering*, may provide another means of controlling fouling .

Cations

A high concentration of monovalent cations impairs filtration. *Avoid it!* While for municipal treatment facilities, the wastewater composition is rather constant, in winter, the salts that are used for defrosting the roads should be considered if the resulting water is not separately collected. E.g., one might think of using

[2] *Online* means at the site, simultaneously with the filtration process.

$CaCl_2$ instead of NaCl. Industrial applications should treat process streams with a high M/P content separately instead of allowing them to the usually collective treatment.

11.2.3 A paradigm shift towards biorefining

For a long time, wastewater treatment has been considered as an *end of pipe* technique with a negative image. Pollutants were to be broken down in a somewhat effective manner to allow water discharge in the ecosystem. The process entailed a necessary cost which had to be minimised as much as possible.

In current times, however, wastewater is more and more regarded as an assembly of resources including energy, nutrients and, of course, water itself. Aerobic MBRs, as presented in this study, provide water with already high reuse potential, as compared to their conventional counterparts. MBR-effluent should, therefore, be reused as much as possible.

Nevertheless, the water loop is not the only cycle that is to be closed. Water treatment with MBRs entails a high energy cost. While part of this cost can be abated through improved fouling control and efficient operation, the majority is inherent to aerobic systems themselves. Useful energy is degraded through the breakdown of organic molecules into carbon dioxide. In this regard, a paradigm shift from wastewater treatment facilities to *biorefineries* is needed. Future research should focus technologies that refine and extract valuable components from the used water rather than considering it a to-be-treated wastestream. Wastewater, in essence, should be considered a *resource* [Verstraete, 2014].

The closest brother for aerobic MBRs which already provides a next step towards sustainability is the *anaerobic MBR* (AnMBR). Through the production of biogas, AnMBRs have the potential of being energy producers rather than consumers. Moreover, the benefits of membrane filtration, such as complete biomass retention and disinfection, are retained. However, the challenges of abating membrane fouling are even more prominent in this technology, as anaerobic sludge has an even higher fouling propensity [Lin et al., 2013].

Another alternative method for water recovery through membrane bioreactors is the forward osmosis MBR, which can be used in conjunction with AnMBRs. In this technology, a salted drawing solution is used at the permeate side to withdraw purified water through the membrane from the mixed liquor. As such, the pressure-driven drawing force is replaced by an osmotic gradient, which results in much lower fouling on the retentate side. Subsequently, the purified water needs to be extracted from the draw solution. To this end, external

pressure remains required but, as the composition of this solution is well known, fouling propensity and sudden disturbances are limited [Huang and Lee, 2015].

Bibliography

H. Abdi. Partial least squares regression and projection on latent structure regression (PLS regression). *Wiley Interdisciplinary Reviews: Computational Statistics*, 2(4): 387–515, 2010.

M. Abramowitz. Microscope, basics and beyond. Technical report, Olympus America Inc, Scientific Equipment Division, 2003.

A. Amaral and E. Ferreira. Activated sludge monitoring of a wastewater treatment plant using image analysis and partial least squares regression. *Analytica Chimica Acta*, 544(1-2):246–253, 2005.

A. L. Amaral, D. P. Mesquita, and E. C. Ferreira. Automatic identification of activated sludge disturbances and assessment of operational parameters. *Chemosphere*, 91(5): 705–10, 2013.

U. A. Amarasinghe and V. Smakhtin. Global water demand projections: Past, present and future. Technical report, International Water Management Institute, 2014.

A. Andreadakis. Physical and chemical properties of activated sludge floc. *Water Research*, 27(12):1707 – 1714, 1993.

S. Arabi and G. Nakhla. Impact of protein/carbohydrate ratio in the feed wastewater on the membrane fouling in membrane bioreactors. *Journal of Membrane Science*, 324(1-2):142–150, 2008.

S. Arabi and G. Nakhla. Impact of cation concentrations on fouling in membrane bioreactors. *Journal of Membrane Science*, 343(1-2):110–118, 2009.

P. Bacchin, P. Aimar, and R. Field. Critical and sustainable fluxes: Theory, experiments and applications. *Journal of Membrane Science*, 281:42–69, 2006.

M. M. Benjamin. *Water Chemistry*. Waveland Press, Incorporated, 2002.

C. Biggs and P. Lant. Activated sludge flocculation: on-line determination of floc size and the effect of shear. *Water Research*, 34(9):2542–2550, 2000.

C. Biggs, A. Ford, and P. Lant. Activated sludge flocculation: direct determination of the effect of calcium ions. *Water Science and Technology*, 43(11):75–80, 2001.

E. Braak, M. Alliet, S. Schetrite, and C. Albasi. Aeration and hydrodynamics in submerged membrane bioreactors. *Journal of Membrane Science*, 379:1–18, 2011.

J. Brink, A. Jönsson, and J. Lindau. Influence of pH on the adsorptive fouling of ultrafiltration membranes by fatty acid. *Journal of Membrane Science*, 164:187–194, 2000.

A. Broeckmann, J. Busch, T. Wintgens, and W. Marquardt. Modeling of pore blocking and cake layer formation in membrane filtration for wastewater treatment. *Desalination*, 189(1-3):97–109, 2006.

A. Brookes, B. Jefferson, P. Le-Clech, and S. Judd. Fouling of membrane bioreactors during treatment of produced water. In *Proceedings of the IMSTEC*, Sydney, Australia, 2003.

A. Brookes, B. Jefferson, G. Guglielmi, and S. Judd. Sustainable flux fouling in a membrane bioreactor: impact of flux and MLSS. *Separation Science and Technology*, 41:1279–1291, 2006.

T. V. Bugge, P. Larsen, A. M. Saunders, C. Kragelund, L. Wybrandt, K. Keiding, M. L. Christensen, and P. H. Nielsen. Filtration properties of activated sludge in municipal MBR wastewater treatment plants are related to microbial community structure. *Water research*, 47(17):6719–6730, 2013.

J. Busch, A. Cruse, and W. Marquardt. Modeling submerged hollow-fiber membrane filtration for wastewater treatment. *Journal of Membrane Science*, 288(1-2):94–111, feb 2007.

H.-J. Butt, K. Graf, and M. Kappl. *Physics and Chemistry of Interfaces*. Wiley-VCH, 2008.

G. Bylund. *Dairy processing handbook*. Tetra Pak Processing Systems, 1995.

T. A. Cao. *Integrating activated sludge floc size information in membrane bioreactor (MBR) fouling modeling*. PhD thesis, KU Leuven, 2016.

C. Cenens, K. Van Beurden, R. Jenné, and J. Van Impe. On the development of a novel image analysis technique to distinguish between flocs and filaments in activated sludge images. *Water Science and Technology*, 46(1-2):381–387, 2002.

L. Cerqueira, N. Azevedo, C. Almeida, T. Jardim, C. Keevil, and M. Veira. DNA mimics for the rapid identification of microorganisms by fluorescence *in situ* hybridization (FISH). *International Journal of Molecular Sciences*, 9:1944–1960, 2008.

M. Chalfie and S. R. Kain, editors. *Green Fluorescent Protein: Properties, Applications and Protocols*. John Wiley & Sons Inc., 2006.

I. Chang and S. Kim. Wastewater treatment using membrane filtration - effect of biosolids concentration on cake resistance. *Process Biochemistry*, 40:1307–1314, 2005.

I. Chang and C. Lee. Membrane filtration characteristics in membrane coupled activated sludge system - the effect of physiological states of activated sludge on membrane fouling. *Desalination*, 120:221–233, 1998.

I. Chang, M. Gander, B. Jefferson, and S. Judd. Low-cost membranes for use in a submerged MBR. *Process Safety and Environmental Protection*, 79:183–188, 2001.

P. Cheeseman, A. Toms-wood, and R. Wolfe. Isolation and properties of fluorescent compound *factor420* from *methanobacterium* strain. *Journal of Bacteriology*, 112 (1):527–531, 1972.

J. Chen, M. Zhang, A. Wang, H. Lin, H. Hong, and X. Lu. Osmotic pressure effect on membrane fouling in a submerged anaerobic membrane bioreactor and its experimental verification. *Bioresource Technology*, 125:97–101, 2012.

M.-Y. Chen, D.-J. Lee, Z. Yang, X. F. Peng, and J. Y. Lai. Fluorescent staining for study of extracellular polymeric substances in membrane biofouling layers. *Environmental science & technology*, 40:6642–6646, 2006.

V. Chen, H. Li, and A. G. Fane. Non-invasive observation of synthetic membrane processes - A review of methods. *Journal of Membrane Science*, 241(1):23–44, 2004.

S. Chiesa, R. Irvine, and J. Manning. Feast/famine growth environments and activated sludge population selection. *Biotechology and Bioengineering*, 27:562–569, 1985.

B. Cho and A. Fane. Fouling transients in nominally sub-critical flux operation of a membrane bioreactor. *Journal of Membrane Science*, 209(2):391–403, 2002.

M. L. Christensen, K. Keiding, P. H. Nielsen, and M. K. Jorgensen. Dewatering in biological wastewater treatment: a review. *Water Research*, 82:14–24, 2015.

M. L. Christensen, T. V. Bugge, B. H. Hede, M. Nierychlo, P. Larsen, and M. K. Jørgensen. Effects of relaxation time on fouling propensity in membrane bioreactors. *Journal of Membrane Science*, 504:176–184, 2016.

J. Chuboda, P. Grau, and V. Ottova. Control of activated sludge filamentous bulking - II. selection of microorganisms by means of a selector. *Water Research*, 7:1389–1398, 1973.

N. Cicek, J. Franco, M. Suidan, V. Urbain, and J. Manem. Characterization and comparison of a membrane bioreactor and a conventional activated sludge system in the treatment of wastewater containing high-molecular-weight compounds. *Separation Science and Technology*, 71:64–70, 1999.

E. M. Contreras, L. Giannuzzi, and N. E. Zaritzky. Use of image analysis in the study of competition between filamentous and non-filamentous bacteria. *Water Research*, 38(11):2621–30, 2004.

M. Davidson and M. Abramowitz. Optical microscopy review article. Technical report, Olympus America Inc, Scientific Equipment Division, 1999.

L. De Temmerman, T. Maere, H. Temmink, A. Zwijnenburg, and I. Nopens. Salt stress in a membrane bioreactor: Dynamics of sludge properties, membrane fouling and remediation through powdered activated carbon dosing. *Water research*, 63C: 112–124, 2014.

L. De Temmerman, T. Maere, H. Temmink, A. Zwijnenburg, and I. Nopens. The effect of fine bubble aeration intensity on membrane bioreactor sludge characteristics and fouling. *Water research*, 76:99–109, 2015.

A. De Wael. Development of a microencapsulation technique for microbial aggregates. Master's thesis, KU Leuven, 2016.

L. Defrance and M. Jaffrin. Reversibility of fouling formed in activated sludge filtration. *Journal of Membrane Science*, 157:73–84, 1999.

V. Diez, D. Ezquerra, J. L. Cabezas, A. García, and C. Ramos. A modified method for evaluation of critical flux, fouling rate and in situ determination of resistance and compressibility in MBR under different fouling conditions. *Journal of Membrane Science*, 453:1–11, 2014.

A. Ding, W. Pronk, F. Qu, J. Ma, G. Li, K. Li, and H. Liang. Effect of calcium addition on sludge properties and membrane fouling potential of the membrane-coupled granular sludge bed process. *Journal of Membrane Science*, 489:55–63, 2015.

A. Drews. Membrane fouling in membrane bioreactors—Characterisation, contradictions, cause and cures. *Journal of Membrane Science*, 363(1-2):1–28, nov 2010.

A. Drews and M. Kraume. Process improvement by application of membrane bioreactors. *Chemical Engineering Research and Design*, 83(3):276–284, 2005.

A. Drews, M. Vocks, V. Iversen, and M. Kraume. Process improvement by application of membrane bioreactors. In *Proceedings of the International Congress on Membranes and Membrane Processes (ICOM)*, Seoul, Korea, 2005.

I. G. Droppo, D. T. Flannigan, G. G. Leppard, C. Jaskot, and S. N. Liss. Floc stabilization for multiple microscopic techniques. *Applied and Environmental Microbiology*, 62(9):3508–3515, 1996.

J. F. Drouin, L. Louvel, B. Vanhoutte, H. Vivier, M. N. Pons, and P. Germain. Quantitative characterization of cellular differentiation of *Streptomyces ambofaciensin* submerged culture by image analysis. *Biotechnology Techniques*, 11 (11):819–824, 1997.

M. Dubois, K. Gilles, J. Hamilton, P. Rebers, and F. Smith. Colorimetric method for determination of sugars and related substances. *Analytical Chemistry*, 28:350–356, 1956.

L. Eriksson, T. Byrne, E. Johansson, J. Trygg, and C. Vikström. *Multi- and Megavariate Data Analysis - Basic Principles and Applications*. Umetrics Academy, 2013.

D. Errampalli, K. Leung, M. Cassidy, M. Kostrzynska, M. Blears, H. Lee, and J. Trevors. Applications of the green fluorescent protein as a molecular marker in environmental microorganisms. *Journal of Microbial Methods*, 35:187–199, 1999.

B. Espinasse, P. Bacchin, and P. Aimar. On an experimental method to measure critical flux in ultrafiltration. *Desalination*, 146:91–96, 2002.

H. Evenblij and J. van der Graaf. Occurence of EPS in activated sludge from a membrane bioreactor treating municipal wastewater. *Water Science and Technology*, 50:293–300, 2004.

R. S. Faibish, M. Elimelech, and Y. Cohen. Effect of interparticle electrostatic double layer interactions on permeate flux decline in crossflow membrane filtration of colloidal solutions: an experimental investigation. *Journal of Colloid and Interface Science*, 204:77–86, 1998.

F. Fan, H. Zhou, and H. Husain. Identification of wastewater sludge characteristics to predict critical flux for membrane bioreactor processes. *Water Research*, 40(2): 205–212, 2006.

A. Fane and C. Fell. A review of fouling and fouling control in ultrafiltration. *Desalination*, 91:117–136, 1987.

L. Faust, H. Temmink, A. Zwijnenburg, A. Kemperman, and H. Rijnaarts. High loaded MBRs for organic matter recovery from sewage: Effect of solids retention time on bioflocculation and on the role of extracellular polymers. *Water Research*, 56:258–266, 2014.

F. Fawehinmi, P. Lens, T. Stephenson, F. Rogalla, and B. Jefferson. The influence of operating conditions on EPS, SMP and bio-fouling in anaerobic MBR. In *Proceedings of the Water Environment-Membrane Technology Conference*, Seoul, Korea, 2004.

R. Field and G. Pearce. Critical, sustainable and threshold fluxes for membrane filtration with water industry applications. *Advances in colloid and interface science*, 164:38–44, 2011.

R. Field, D. Wu, J. Howell, and B. Gupta. Critifal flux concept for microfiltration fouling. *Journal of Membrane Science*, 100:259–272, 1995.

H. Flemming. The forces that keep biofilms together. *Biofilms in Aquatic Systems*, pages 1–12, 1999.

R. A. Fox and D. C. Stuckey. The effect of sparging rate on transmembrane pressure and critical flux in an AnMBR. *Journal of Environmental Management*, 151:280–285, 2015.

B. Frølund, T. Griebe, and P. H. Nielsen. Enzymatic activity in the activated-sludge floc matrix. *Applied Microbial Technology*, 43:755–761, 1995.

B. Frølund, R. Palgrem, K. Keiding, and P. H. Nielsen. Extraction of extracellular polymers from activated sludge using a cation exchange resin. *Water Research*, 5 (8):1749–1758, 1996.

W. Gao, M. Han, X. Qu, and B. Liao. Characteristics of wastewater and mixed liquor and their role in membrane fouling. *Bioresource Technology*, 128:207–214, 2013.

S. Geilvoet. *The Delft Filtration Characterisation method - Assessing membrane bioreactor activated filterability.* PhD thesis, TU Delft, 2010.

E. Giraldo and M. Le Chavellier. Let them wear cake. *Journal of Water and Environment Technology*, 19(3):47–51, 2007.

C. Glasbey and G. Horgan. *Image analysis for the biological sciences.* J. Wiley, 1995.

R. Govoreanu, H. Saveyn, P. Van der Meeren, and P. A. Vanrolleghem. Simultaneous determination of activated sludge floc size distribution by different techniques. *Water Science and Technology*, 50(12):39–46, 2004.

K. Grijspeerdt and W. Verstraete. Image analysis to estimate the settleability and concentration of activated sludge. *Water Research*, 31(5):1126 – 1134, 1997.

J. Guan, R. Amal, and T. Waite. Effect of aggregate size and structure on specific resistance of biosolids filter cakes. *Water Science and Technology*, 44:215–229, 2001.

G. Guglielmi, D. Chiarani, D. Saroj, and G. Andreottola. Impact of chemical cleaning and air-sparging on the critical and sustainable flux in a flat sheet membrane bioreactor for municipal wastewater treatment. *Water Science & Technology*, 57: 1873–1879, 2008.

B. Gunder and K. Krauth. Replacement of secondary clarification by membrane separation - results with plate and hollow fibre modules. *Water Science and Technology*, 38:383–393, 1998.

M. Hamoda and I. Al-Attar. Effects of high sodium chloride concentrations on activated sludge treatment. *Water Science and Technology*, 31(9):61–72, 1995.

M. Hermansson. The DLVO theory in microbial adhesion. *Colloids and Surfaces*, 14: 105–119, 1999.

R. Holdich and J. Boston. Microfiltration using a dynamically formed membrane. *Filtration and Separation*, 27(3):184–187, 1990.

S. Hong, T. Bae, T. Tak, S. Hong, and A. Randall. Fouling control in activated sludge submerged hollow fiber membrane bioreactors. *Desalination*, 143:219–228, 2002.

I. Horiba Instruments. *A guidebook to particle size analysis.* Irivine, USA, 2014.

L. Huang and D.-J. Lee. Membrane bioreactor: A mini review on recent R&D works. *Bioresource Technology*, 194:383–388, 2015.

B. K. Hwang, C. H. Lee, I. S. Chang, A. Drews, and R. Field. Membrane bioreactor: TMP rise and characterization of bio-cake structure using CLSM-image analysis. *Journal of Membrane Science*, 419-420:33–41, 2012.

T. Itonaga, K. Kimura, and Y. Watanabe. Influence of suspension viscosity and colloidal particles on permeability of membrane used in membrane bioreactor (MBR). *Water Science and Technology*, 50:301–309, 2004.

I. Ivanovic, T. Leiknes, and H. Ødegaard. Fouling Control by Reduction of Submicron Particles in a BF-MBR with an Integrated Flocculation Zone in the Membrane Reactor. *Separation Science and Technology*, 43(7):1871–1883, 2008.

N. Jang, Y. Yeo, M. Hwang, S. Vigneswaran, J. Cho, and I. Kim. The effect of dissolved air on the filtration resistance in hollow fiber MBR. In *Proceedings of the Water Environment-Membrane Technology Conference*, Seoul, Korea, 2004.

N. Jang, X. Ren, K. Choi, and I. Kim. Comparison of membrane biofouling in nitrification and denitrification for the membrane bio-reactor (MBR). In *Proceedings of the IWA on Aspire*, Singapore, 2005.

D. Jeison, I. Diaz, and J. van Lier. Anaerobic membrane bioreactors: Are membranes really necessary? *Electronic Journal of Biotechnology*, 11(4), 2008.

R. Jenné, C. Cenens, A. H. Geeraerd, and J. Van Impe. Towards on-line quantification of flocs and filaments by image analysis. *Biotechnology Letters*, 24:931–935, 2002.

R. Jenné, E. Banadda, I. Smets, J. Deurinck, and J. Van Impe. Detection of filamentous bulking problems: developing an image analysis system for sludge composition monitoring. *Microscopy and Microanalysis*, 13(1):36–41, 2007.

L. Ji and J. Zhou. Influence of aeration on microbial polymers and membrane fouling in submerged membrane bioreactors. *Journal of Membrane Science*, 276:168–177, 2006.

T. Jiang, M. Kennedy, B. Guinzbourg, P. Vanrolleghem, and J. Schippers. Optimising the operation of a MBR pilot plant by quantitative analysis of the membrane fouling mechanism. *Water Science and Technology*, 51:19–25, 2005.

B. Jin, B.-M. Wilén, and P. Lant. A comprehensive insight into floc characteristics and their impact on compressibility and settleability of activated sludge. *Chemical Engineering Journal*, 95(1-3):221–234, 2003.

I. Johnson and M. T. Spence, editors. *The Molecular Probes Handbook ®*. Invitrogen, 2010.

S. A. Jones, Y. M. J. Chew, M. R. Bird, and D. I. Wilson. The application of fluid dynamic gauging in the investigation of synthetic membrane fouling phenomena. *Food and Bioproducts Processing*, 88(4):409–418, 2010.

S. A. Jones, Y. M. J. Chew, D. I. Wilson, and M. R. Bird. Fluid dynamic gauging of microfiltration membranes fouled with sugar beet molasses. *Journal of Food Engineering*, 108(1):22–29, 2012.

F. Jorand, P. Guicherd, V. Urbain, J. Manem, and J. Block. Hydrophobicity of activated sludge flocs and laboratory-grown bacteria. *Water Science and Technology*, 30:211–218, 1994.

F. Jorand, F. Zatarian, F. Thomas, J. Block, J. Bottero, G. Villemin, V. Urbain, and J. Manem. Chemical and Structural (2D) linkage between bacteria within activated sludge flocs. *Water Research*, 29(7):1639–1647, 1995.

V. Jorand, F. Boué-Bigne, J. Block, and V. Urbain. Hydrophobic/hydrophilic properties of activated sludge exopolymeric substances. *Water Science and Technology*, 37:307–315, 1998.

M. K. Jørgensen, K. Keiding, and M. L. Christensen. On the reversibility of cake buildup and compression in a membrane bioreactor. *Journal of Membrane Science*, 455:152–161, 2014.

S. Judd. Submerged membrane bioreactors: flat plate or hollow fibre? *Filtration and Separation*, 39:30–31, 2002.

S. Judd. *The MBR book*. Butterworth-Heinemann, Elsevier, second edition, 2011.

S. Judd. The status of industrial and municipal effluent treatment with membrane bioreactor technology. *Chemical Engineering Journal*, 2015.

F. Kara, G. Gurakan, and F. Sanin. Monovalent cations and their influence on activated sludge floc chemistry, structure and physical characteristics. *Biotechnology and Bioengineering*, 100(2), 2008.

K. Keiding and P. Nielsen. Desorption of organic macromolecules from activated sludge: effect of ionic composition. *Water Research*, 31(7):1665–1672, 1997.

H. Kim, K. Yeon, C. Lee, S. Lee, and T. Swaminathan. Biofilm structure and extracellular polymeric substances in low and high dissolved oxygen membrane bioreactors. *Separation Science and Technology*, 41:1213–1230, 2006.

C. Laspidou and B. Rittmann. A unified theory for extracellular polymeric substances, soluble microbial products, and active and inert biomass. *Water Research*, 36(11): 2711–2720, 2001.

P. Le-Clech, B. Jefferson, I. Chang, and S. Judd. Critical flux determination by the flux-step method in a submerged membrane bioreactor. *Journal of Membrane Science*, 227:81–93, 2003a.

P. Le-Clech, B. Jefferson, and S. Judd. Impact of aeration, solids concentration and membrane characteristics on the hydraulic performance of a membrane bioreactor. *Journal of Membrane Science*, 218:117–129, 2003b.

P. Le-Clech, B. Jefferson, and S. Judd. A comparison of submerged and sidestream tubular membrane bioreactor configurations. *Desalination*, 173:113–122, 2005.

P. Le-Clech, V. Chen, and T. Fane. Fouling in membrane bioreactors used in wastewater treatment. *Journal of Membrane Science*, 284:17–53, 2006.

D. S. Lee, M. W. Lee, S. H. Woo, Y.-J. Kim, and J. M. Park. Nonlinear dynamic partial least squares modeling of a full-scale biological wastewater treatment plant. *Process Biochemistry*, 41(9):2050–2057, 2006.

N. Lee, G. Amy, J. Croué, and H. uisson. Identification and understanding of fouling in low-presure membrane (MF/UF) filtration by natural organic matter (NOM). *Water Research*, 38(20):4511–4523, 2004.

S. Lee, A. Fane, and T. Waite. Impact of natural organic matter on floc size and structure effects in membrane filtration. *Environmental Science and Technology*, 39: 6477–6486, 2005.

B. Lesjean, S. Rosenberger, C. Laabs, M. Jekel, R. Gnirss, and G. Amy. Correlation between membrane fouling and soluble/colloidal organic substances in membrane bioreactors for municipal wastewater treatment. *Water Science and Technology*, 51: 1–8, 2005.

D.-H. Li and J. J. Ganczarcyk. Stroboscopic determination of settling velocity, size and porosity of activated sludge flocs. *Water Research*, 21(3):257–262, 1987.

D.-H. Li and J. J. Ganczarcyk. Size distribution of activated sludge flocs. *Research Journal of the Water Pollution Control Federation*, 63(5):806–814, 1991.

X. Li and B. Logan. Permeability of fractal aggregates. *Water Research*, 35:3373–3380, 2001.

X.-y. Li and X.-m. Wang. Modelling of membrane fouling in a submerged membrane bioreactor. *Journal of Membrane Science*, 278(1-2):151–161, 2006.

X. Y. Li and S. F. Yang. Influence of loosely bound extracellular polymeric substances (EPS) on the flocculation, sedimentation and dewaterability of activated sludge. *Water research*, 41(5):1022–30, 2007.

B. Q. Liao, D. G. Allen, I. G. Droppo, G. G. Leppard, and S. N. Liss. Surface properties of sludge and their role in bioflocculation and settleability. *Water Research*, 35(2): 339–350, 2001.

B. Q. Liao, I. G. Droppo, G. G. Leppard, and S. N. Liss. Effect of solids retention time on structure and characteristics of sludge flocs in sequencing batch reactors. *Water Research*, 40:2583–2591, 2006.

H. Lin, W. Gao, F. Meng, B.-Q. Liao, K.-T. Leung, L. Zhao, J. Chen, and H. Hong. Membrane bioreactors for industrial wastewater Treatment: a critical review. *Critical Reviews in Environmental Science and Technology*, 42:677–740, 2012.

H. Lin, W. Peng, M. Zhang, J. Chen, H. Hong, and Y. Zhang. A review on anaerobic membrane bioreactors: applications, membrane fouling and future perspectives. *Desalination*, 314:169–188, 2013.

H. J. Lin, K. Xie, B. Mahendran, D. M. Bagley, K. T. Leung, S. N. Liss, and B. Q. Liao. Sludge properties and their effects on membrane fouling in submerged anaerobic membrane bioreactors (SAnMBRs). *Water Research*, 43:3827–3837, 2009.

H. J. Lin, W. J. Gao, K. T. Leung, and B. Q. Liao. Characteristics of different fractions of microbial flocs and their role in membrane fouling. *Water Science and Technology*, 63(2):262–9, 2011.

Z. Lin and H. Yu. The pupil location based on the OTSU method and Hough transform. In *2011 International Conference on Environment Science and Biotechnology*, volume 8, pages 352–356, 2011.

Y. Liu and H. H. P. Fang. Influences of extracellular polymeric substances (EPS) on flocculation, settling, and dewatering of activated sludge. *Critical Reviews in Environmental Science and Technology*, 33(3):237–273, 2003.

S. Lorenzen, Y. Ye, V. Chen, and M. L. Christensen. Direct observation of fouling phenomena during cross-flow filtration: influence of particle surface charge. *Journal of Membrane Science*, 510:546–558, 2016.

P. Loulergue, M. Weckert, B. Reboul, C. Cabassud, W. Uhl, and C. Guigui. Mechanisms of action of particles used for fouling mitigation in membrane bioreactors. *Water Research*, 66:40–52, 2014.

O. Lowry, N. Rosebrough, A. Lewis Farr, and R. Randall. Protein measurement with folin phenol reagent. *Journal of Biological Chemistry*, 1:265–275, 1951.

S. Lyko, D. Al-Halbouni, T. Wintgens, A. Janot, J. Hollender, W. Dott, and T. Melin. Polymeric compounds in activated sludge supernatant - characterisation and retention mechanisms at a full-scale membrane bioreactor. *Water Research*, 41: 3894–3902, 2007.

A. Marschall, P. Munro, and G. Tragardh. The effect of protein fouling in microfiltration and ultrafiltration on permeate flux, protein retention and selectivity: a literature review. *Desalination*, 91:65–108, 1993.

Y. Marselina, P. Le-Clech, R. Stuetz, and V. Chen. Characterisation of membrane fouling deposition and removal by direct observation technique. *Journal of Membrane Science*, 341:163–171, 2009.

E. Matthiasson. The role of macromolecular adsorption in fouling of ultrafiltration membranes. *Journal of Membrane Science*, 16:23–36, 1983.

T. Mattson, W. J. T. Lewis, Y. M. J. Chew, and M. R. Bird. In situ investigation of soft cake fouling layers using fluid dynamic gauging. *Food and bioproducts processing*, 93:205–210, 2015.

T. Melin and R. Rauntenback. Membranverfahren. Springer, 2004.

F. Meng and F. Yang. Fouling mechanisms of deflocculated sludge, normal sludge, and bulking sludge in membrane bioreactor. *Journal of Membrane Science*, 305: 48–56, 2007.

F. Meng, H. Zhang, Y. Li, X. Zhang, and F. Yang. Application of fractal permeation model to investigate membrane fouling in membrane bioreactor. *Journal of Membrane Science*, 262(1-2):107–116, 2005.

F. Meng, H. Zhang, F. Yang, Y. Li, J. Xiao, and X. Zhang. Effect of filamentous bacteria on membrane fouling in submerged membrane bioreactor. *Journal of Membrane Science*, 272(1-2):161–168, 2006.

F. Meng, F. Yang, B. Shi, and H. Zhang. A comprehensive study on membrane fouling in submerged membrane bioreactors operated under different aeration intensities. *Separation and Purification Technology*, 59(1):91–100, 2008.

A. Menniti, S. Kang, M. Elimelech, and E. Morgenroth. Influence of shear on the production of extracellular polymeric substances in membrane bioreactors. *Water Research*, 43(17):4305–4315, 2009.

D. P. Mesquita, O. Dias, A. L. Amaral, and E. C. Ferreira. A comparison between bright field and phase-contrast image analysis techniques in activated sludge morphological characterization. *Microscopy and microanalysis*, 16:166–174, 2010.

D. P. Mesquita, A. L. Amaral, and E. C. Ferreira. Identifying different types of bulking in an activated sludge system through quantitative image analysis. *Chemosphere*, 85:643–652, 2011a.

D. P. Mesquita, A. L. Amaral, and E. C. Ferreira. Characterization of activated sludge abnormalities by image analysis and chemometric techniques. *Analytica chimica acta*, 705(1-2):235–42, 2011b.

D. P. Mesquita, A. L. Amaral, and E. C. Ferreira. Activated sludge characterization through microscopy: a review on quantitative image analysis and chemometric techniques. *Analytica chimica acta*, 802:14–28, 2013a.

D. P. Mesquita, C. Leal, J. R. Cunha, A. Oehmen, A. L. Amaral, M. A. M. Reis, and E. C. Ferreira. Prediction of intracellular storage polymers using quantitative image analysis in enhanced biological phosphorus removal systems. *Analytica Chimica Acta*, 770:36–44, 2013b.

D. P. Mesquita, A. L. Amaral, C. Leal, A. Oehmen, M. A.M. Reis, and E. C. Ferreira. Polyhydroxyalkanoate granules quantification in mixed microbial cultures using image analysis: Sudan Black B versus Nile Blue A staining. *Analytica Chimica Acta*, 865:8–15, 2015.

A. T. Mielczarek, C. Kragelund, P. S. Eriksen, and P. H. Nielsen. Population dynamics of filamentous bacteria in Danish wastewater treatment plants with nutrient removal. *Water research*, 46(12):3781–3795, 2012.

A. T. Mielczarek, H. T. T. Nguyen, J. L. Nielsen, and P. H. Nielsen. Population dynamics of bacteria involved in enhanced biological phosphorus removal in Danish wastewater treatment plants. *Water research*, 47(4):1529–1544, 2013.

L. H. Mikkelsen and K. Keiding. Equilibrium aspects of the effects of shear and solids content on aggregate deflocculation. *Advances in colloid and interface science*, 80: 151–182, 1999.

L. H. Mikkelsen and K. Keiding. The shear sensitivity of activated sludge: an evaluation of the possibility for a standardised floc strength test. *Water Research*, 36:2931–2940, 2002a.

L. H. Mikkelsen and K. Keiding. Physico-chemical characteristics of full scale sewage sludges with implications to dewatering. *Water Research*, 36(10):2451–2462, 2002b.

D. J. Miller, S. Kasemset, D. R. Paul, and B. D. Freeman. Comparison of membrane fouling at constant flux and constant transmembrane pressure conditions. *Journal of Membrane Science*, 454:505–515, 2014.

F. Mohlman. The sludge index. *Sewage Work*, 6:119–122, 1934.

H. Monclus, S. Zacharias, A. Santos, M. Pidou, and S. Judd. Criticality of Flux and Aeration for a Hollow Fiber Membrane Bioreactor. *Separation Science and Technology*, 45(7):956–961, 2010.

J. Morgan, C. Forster, and L. Evison. A comparative study on the nature of biopolymers extracted from anaerobic and activated sludges. *Water Research*, 1990.

F. Morgan-Sagastume, P. Larsen, J. L. Nielsen, and P. H. Nielsen. Characterization of the loosely attached fraction of activated sludge bacteria. *Water Research*, 42 (4-5):843–854, 2008.

M. Mulder. *Basic Principles of Membrane Technology*. Kluwer Academic Publishers, Dordrecht, 2000.

H. Nagaoka, S. Yamanishi, and A. Miya. Modeling of biofouling by extracellular polymers in a membrane separation activated sludge system. *Water Science and Technology*, 38(4/5):497–504, 1998.

K. Ndukaife, J. Ndukaife, and A. A. Nnanna. Membrane fouling characterization by infrared thermography. *Infrared Physics & Technology*, 68:186–192, 2015.

T. Neu, G. D. Swerhone, and J. R. Lawrence. Assessment of lectin-binding analysis for in situ detection of glycoconjugates in biofilm systems. *Microbiology (Reading, England)*, 147:299–313, 2001.

C. Ng, D. Sun, J. Zhang, H. Chua, W. Bing, S. Tay, and A. Fane. Strategies to improve the sustainable operation of membrane bioreactors. In *Proceedings on the International Desalination Association Conference*, Singapore, 2005.

T. Nguyen, N. Hilal, H. N., and J. Novak. Determination of the effect of cations and anionic polyelectrolytes on the characteristics and final properties of synthetic and activated sludge. *Desalination*, 222:307–317, 2008.

P. H. Nielsen, C. Kragelund, R. J. Seviour, and J. L. Nielsen. Identity and ecophysiology of filamentous bacteria in activated sludge. *FEMS microbiology reviews*, 33(6):969–998, 2009.

J. Nilsson. Protein fouling of UF membranes: causes and consequences. *Journal of Membrane Science*, 52:121–142, 1990.

J. Novak, N. Love, M. Smith, and E. Wheeler. The effect of cationic salt addition on the settling and dewatering properties of an industrial activated sludge. *Water Environment Research*, 70(5):984–996, 1998.

S. Ognier, C. Wisniewski, and A. Grasmick. Influence of macromolecule adsorption during filtration of a membrane bioreactor mixed liquor suspension. *Journal of Membrane Science*, 209:27–37, 2002.

J. R. Pan, Y.-C. Su, C. Huang, and H.-C. Lee. Effect of sludge characteristics on membrane fouling in membrane bioreactors. *Journal of Membrane Science*, 349 (1-2):287–294, mar 2010.

P. Park and S. Lee. Permeability of Collapsed Cakes Formed by Deposition of Fractal Filtration. *Environmental Science & Technology*, 40(8):2699–2705, 2006.

D. Parker, W. Kaufman, and D. Jenkins. *Characteristics of biological flocs in turbulent regimes.* Sanitary Engineering Research Laboratory, University of California, Berkeley, SERL Report No. 70-5, 1970.

B. Peeters and S. Herman. Monitor cations in CPI wastewater for better performance. *Chemical Engineering*, 114, 2007.

Y. G. Perez, S. G. F. Leite, and M. A. Z. Coelho. Activated sludge morphology characterization through an image analysis procedure. *Brazilian Journal of Chemical Engineering*, 23(3):319–330, 2006.

E. Poorasgari, T. V. Bugge, M. L. Christensen, and M. K. Jorgensen. Compressibility of fouling layers in membrane bioreactors. *Journal of Membrane Science*, 475:65–70, 2015.

H. Prieske, L. Böhm, A. Drews, and M. Kraume. Optimised hydrodynamics for membrane bioreactors with immersed flat sheet membrane modules. *Desalination and Water Treatment*, 18:270–276, 2010.

P. Principi, F. Villa, M. Bernasconi, and E. Zanardini. Metal toxicity in municipal wastewater activated sludge investigated by multivariate analysis and in situ hybridization. *Water Research*, 40(1):99–106, 2006.

A. Raszka, M. Chorvatova, and J. Wanner. The role and significance of extracellular polymers in activated sludge. Part I: Literature review. *Acta Hydrochimica et Hydrobiologica*, 34(5):411–424, 2006.

P. Reynolds and E. Colleran. Evaluation and improvement of methods for coenzyme F420 analysis in anaerobic sludges. *Journal of Microbiological Methods*, 7(2-3): 115–130, 1987.

R. Rocha, R. S. Santos, P. Madueira, C. Almeida, and N. F. Azevedo. Optimization of peptide nucleic acid fluorescence *in situ* hybridization (PNA-FISH) for the detection of bacteria: The effect of pH, dextran sulfate and probe concentration. *Journal of Biotechnology*, 226:1–7, 2016.

C. Romero and R. Davis. Experimental verification of the shear-induced hydrodynamic diffusion model of crossflow microfiltration. *Journal of Membrane Science*, 62:249–273, 1991.

M. Rosenberg, D. Gutnick, and E. Rosenberg. Adherence of bacteria to hydrocarbons: A simple method for measuring cell-surface hydrophobicity. *FEMS Microbiology Letters*, 9(1):29–33, 1980.

S. Rosenberger and M. Kraume. Filterability of activated sludge in membrane bioreactors. *Desalination*, 146:373–379, 2002.

S. Rosenberger, H. Evenblij, S. te Poele, T. Wintgens, and C. Laabs. The importance of liquid phase analysis to understand fouling in membrane assisted activated sludge processes: six case studies of different European research groups. *Journal of Membrane Science*, 263:113–126, 2005.

M. C. Sarraguça, A. Paulo, M. M. Alves, A. M. A. Dias, J. A. Lopes, and E. C. Ferreira. Quantitative monitoring of an activated sludge reactor using on-line UV-visible and near-infrared spectroscopy. *Analytical and Bioanalytical Chemistry*, 395(4): 1159–1166, 2009.

A. M. Saunders, P. Larsen, and P. H. Nielsen. Comparison of nutrient-removing microbial communities in activated sludge from full-scale MBRs and conventional plants. *Water Science and Technology*, 68(2):366–71, 2013.

M. Schmid, A. Thill, U. Purkhold, M. Walcher, J. Y. Bottero, P. Ginestet, P. H. Nielsen, S. Wuertz, and M. Wagner. Characterization of activated sludge flocs by confocal laser scanning microscopy and image analysis. *Water research*, 37(9): 2043–2052, 2003.

M. A. Seka and W. Verstraete. Test for assessing shear sensitivity of activated sludge flocs: a feasibility study. *Water Research*, 37(14):3327–3334, 2003.

R. Seviour and P. Nielsen. *Microbial ecology of activated sludge*. IWA publishing, London, 1st edition, 1998.

L.-G. Shen, Q. Lei, J.-R. Chen, H.-C. Hong, Y.-M. He, and H.-J. Lin. Membrane fouling in a submerged membrane bioreactor: impacts of floc size. *Chemical Engineering Journal*, 269:328–334, 2015.

S. Shirazi, C.-J. Lin, and D. Chen. Inorganic fouling of pressure-driven membrane processes - a critical review. *Desalination*, 250:236–248, 2010.

I. Y. Smets, E. N. Banadda, J. Deurinck, N. Renders, R. Jenné, and J. F. Van Impe. Dynamic modeling of filamentous bulking in lab-scale activated sludge processes. *Journal of Process Control*, 16(3):313–319, 2006.

D. Snidaro, F. Zartarian, F. Jorand, J. Y. Bottero, J. Block, and J. Manem. Characterization of activated sludge flocs structure. *Water Science and Technology*, 36(4):313–320, 1997.

D. C. Sobeck and M. J. Higgins. Examination of three theories for mechanism of cation-induced bioflocculation. *Water Research*, 36:527–538, 2002.

L. Sun, L. Chen, W. Guo, T. Ye, and Y. Yang. Extraction of extracellular polymeric substances in activated sludge using sequential extraction. *Chemical Technology and Biotechnology*, 90:1448–1454, 2015.

S. G. Sveegaard, K. Keiding, and M. L. Christensen. Compression and swelling of activated sludge cakes during dewatering. *Water Research*, 46(16):4999–5008, 2012.

A. Sweity, W. Ying, S. Befer, G. Oron, and M. Herzberg. pH effects on the adherence and fouling propensity of extracellular polymeric substances in a membrane bioreactor. *Journal of Membrane Science*, 378, 2011.

S. Szilveszter, B. Ráduly, B. Ábrahám, and S. Lányi. In situ imaging of biopolymers and extracellular enzymes in activated sludge flocs of a municipal wastewater treatment plant. *Journal of Chemical Technology & Biotechnology*, 2012.

K. H. Tan. *Humic matter in soil and the environment: principles and controversies*. CRC Press, second edition, 2014.

P. Teppola, S.-P. Mujunen, and P. Minkkinen. Partial least squares modeling of an activated sludge plant: a case study. *Chemometrics and Intelligent Laboratory Systems*, 38:197–208, 1997.

B. Teychene, C. Guigui, C. Cabassud, and G. Amy. Toward a better identification of foulant species in MBR processes. *Desalination*, 231(1-3):27–34, 2008.

A. Thill, S. Veerapaneni, B. Simon, M. Wiesner, J. Bottero, and D. Snidaro. Determination of structure of aggregates by confocal scanning laser microscopy. *Journal of Colloid and Interface Science*, 204(2):357–362, 1998.

R. K. Tomita, S. W. Park, and O. A. Sotomayor. Analysis of activated sludge process using multivariate statistical tools—a PCA approach. *Chemical Engineering Journal*, 90(3):283–290, 2002.

United Nations. The united nations world water development report 2016 - water and jobs, 2016.

V. Urbain, J. Block, and J. Manem. Bioflocculation in activated sludge: an analytic approach. *Water Research*, 27(5):829–838, 1993.

G. Van De Staey, K. Smits, and I. Smets. An experimental study on the impact of bioflocculation on activated sludge separation techniques. *Separation and Purification Technology*, 141:94–104, 2015.

G. Van De Staey, G. Gins, and I. Smets. Biofocculation and activated sludge separation: a PLS case study. In *11th IFAC Symposium on Dynamics and Control of Process Systems, including Biosystems*, volume 11, pages 1151–1156, Norway, 2016. NTNU Trondheim.

P. Van den Brink, O. Satpradit, A. van Bentem, A. Zwijnenburg, H. Temmink, and M. van Loosdrecht. Effect of temperature shocks on membrane fouling in membrane bioreactors. *Water Research*, 45:4491–4500, 2011.

R. Van den Broeck. *Activated sludge mixed liquor characteristics versus membrane fouling in MBRs*. PhD thesis, KU Leuven, 2011.

R. Van den Broeck, J. Van Dierdonck, B. Caerts, I. Bisson, B. Kregersman, P. Nijskens, C. Dotremont, J. Van Impe, and I. Smets. The impact of deflocculation–reflocculation on fouling in membrane bioreactors. *Separation and Purification Technology*, 71(3):279–284, 2010.

R. Van den Broeck, P. Krzeminski, J. Van Dierdonck, G. Gins, M. Lousada-Ferreira, J. Van Impe, J. van der Graaf, I. Smets, and J. van Lier. Activated sludge characteristics affecting sludge filterability in municipal and industrial MBRs: unraveling correlations using multi-component regression analysis. *Journal of Membrane Science*, 378(1-2):330–338, 2011.

R. Van den Broeck, J. Van Dierdonck, P. Nijskens, C. Dotremont, P. Krzeminski, J. van der Graaf, J. van Lier, J. Van Impe, and I. Smets. The influence of solids retention time on activated sludge bioflocculation and membrane fouling in a membrane bioreactor (MBR). *Journal of Membrane Science*, 401-402:48–55, 2012.

R. M. R. Van den Broeck, J. F. M. Van Impe, and I. Y. M. Smets. Assessment of activated sludge stability in lab-scale experiments. *Journal of biotechnology*, 141 (3-4):147–54, 2009.

P. Van Den Kerkhof, G. Gins, R. Van den Broeck, and J. F. M. Van Impe. Multivariate assessment of activated sludge stability in lab-scale experiments. *Process Biochemistry*, 48(11):1789–1793, 2013.

P. van der Marel, A. Zwijnenburg, A. Kemperman, M. Wessling, H. Temmink, and W. van der Meer. An improved flux-step method to determine the critical flux and the critical flux for irreversibility in a membrane bioreactor. *Journal of Membrane Science*, 332:24–29, 2009.

A. van der Schoot. Dual-Channel Particle Size and Shape Analyzer. *China Particuology*, 2(1):44–45, 2004.

J. Van Dierdonck. *Impact of influent characteristics on activated sludge bioflocculation in lab-scale systems*. PhD thesis, KU Leuven, 2013.

J. Van Dierdonck, R. Van den Broeck, E. Vervoort, P. D'haeninck, D. Springael, J. Van Impe, and I. Smets. Does a change in reactor loading rate affect activated sludge bioflocculation? *Process Biochemistry*, 47(12):2227–2233, 2012a.

J. Van Dierdonck, J. Van Impe, and I. Smets. Toward a reliable and generic applicable soluble microbial polymer extraction protocol. *Environmental Engineering Science*, 29(3):174–179, 2012b.

J. Van Dierdonck, R. Van den Broeck, A. Vansant, J. Van Impe, and I. Smets. Microscopic image analysis versus sludge volume index to monitor activated sludge bioflocculation: a case study. *Separation Science and Technology*, 48:1433–1441, 2013a.

J. Van Dierdonck, R. Van den Broeck, E. Vervoort, J. Van Impe, and I. Smets. The effect of alternating influent carbon source composition on activated sludge bioflocculation. *Journal of biotechnology*, 167(3):225–34, 2013b.

S. Veerapaneni and M. Wiesner. Hydrodynamics of fractal aggregates with radially varying permeability. *Journal of Colloid and Interface Science*, 177:45–57, 1996.

W. Verstraete. The manufacturing microbe. *Microbial Biotechnology*, 8(1):36–37, 2014.

E. V. Volpi and J. M. Bridge. FISH glossary: an overview of the fluorescence in situ hybridization technique. *Biotechniques*, 45:385–409, 2008.

F. Wang, M. Zhang, W. Peng, Y. He, H. Lin, J. Chen, H. Hong, A. Wang, and H. Yu. Effects of ionic strength on membrane fouling in a membrane bioreactor. *Bioresource Technology*, 156:35–41, 2014.

Z. Wang and Z. Wu. A review of membrane fouling in MBRs: characteristics and role of sludge cake formed on membrane surfaces. *Separation Science and Technology*, 44(15):3571–3596, 2009.

Z. Wang, X. Mei, J. Ma, A. Grasmick, and Z. Wu. Potential foulants and fouling indicators in MBRs: a critical review. *Separation Science and Technology*, 48 (October 2014):22–50, 2013.

F. Westad and F. Marini. Validation of chemometric models – a tutorial. *Analytica Chimica Acta*, 893:14–24, 2015.

B. Wilén, B. Jin, and P. Lant. Relationship between flocculation of activated sludge and composition of extracellular polymeric substances. *Water Science and Technology*, 47:95–103, 2003.

B. Wilén, M. Onuki, M. Hermansson, D. Lumley, and T. Mino. Microbial community structure in activated sludge floc analysed by fluorescence in situ hybridization and its relation to floc stability. *Water Research*, 42(8-9):2300–2308, 2008.

J. Wingender, M. Strathmann, A. Rode, A. Leis, and H. Flemming. Isolation and biochemical characterization of extracellular polymeric substances from *Pseudomonas aeruginosa*. *Methods in Enzymology*, 336:302–314, 2001.

S. Wold, E. Johansson, and M. Cocchi. *3D QSAR in Drug Design: Theory, Methods and Applications*, chapter PLS-partial least-squares projections to latent structures, pages 523–550. ESCOM, 1993.

B. Wu, T. Kitade, T. Chong, T. Uemura, and A. Fane. Role of initially formed cake layers on limiting membrane fouling in membrane bioreactors. *Bioresource Technology*, 118:589–593, 2012.

J. Wu, P. Le-Clech, R. M. Stuetz, A. G. Fane, and V. Chen. Novel filtration mode for fouling limitation in membrane bioreactors. *Water research*, 42(14):3677–84, 2008.

N. Yamato, K. Kimura, T. Miyoshi, and Y. Watanabe. Difference in membrane fouling in membrane bioreactors (MBRs) caused by membrane polymer materials. *Journal of Membrane Science*, 280:911–919, 2006.

Y. Yang, N. Nakada, R. Nakajima, M. Yasojima, C. Wang, and H. Tanaka. pH, ionic strength and dissolved organic matter alter aggregation of fullerene c60 nanoparticles suspensions in wastewater. *Journal of Hazardous Materials*, 244:582–587, 2013.

C. Ye, X. Yang, F. Zhao, and L. Ren. The shift of the microbial community in activated sludge with calcium treatment and its implication to sludge settleability. *Bioresource Technology*, 207:11–18, 2016.

A. Yeo and A. Fane. Performance of individual fibers in a submerged hollow fiber bundle. *Water Science and Technology*, 51:165–172, 2005.

S.-H. Yoon. *Membrane Bioreactor Processes: principles and applications*. CRC Press, 2016.

F. Zernike. Phase contrast, a new method for the microscopic observation of transparent objects - Part II. *Physica*, 9:974–980, 1942.

H. Zhang, Z. Wang, L. Zhang, and L. Song. Impact of sludge cation distribution pattern on its filterability in membrane bioreactor. *Bioresource technology*, 171: 16–21, 2014.

J. Zhang, H. Chua, J. Zhou, and A. Fane. Factors affecting the membrane performance in submerged membrane bioreactors. *Journal of Membrane Science*, 284:54–66, 2006.

M. Zhang, W. Peng, J. Chen, Y. He, L. Ding, A. Wang, H. Lin, H. Hong, Y. Zhang, and H. Yu. A new insight into membrane fouling mechanism in submerged membrane bioreactor: osmotic pressure during cake layer filtration. *Water Research*, 47(8): 2777–2786, 2013.

X.-H. Zhou, H.-C. Shi, Q. Cai, M. He, and Y.-X. Wu. Function of self-forming dynamic membrane and biokinetic parameters' determination by microelectrode. *Water Research*, 42(10-11):2369–76, 2008.

L. Zhu, H. Yu, Y. Liu, H. Qi, and X. Xu. Optimization for extracellular polymeric substances extraction of microbial aggregates. *Water Science and Technology*, 71 (7):1106–1112, 2015.

A. Zita and M. Hermansson. Effects of bacterial cell surface structures and hydrophobicity on attachment to activated sludge flocs. *Applied and Environmental Microbiology*, 71(3):1168–1170, 2015.

FACULTY OF ENGINEERING SCIENCE
DEPARTMENT OF CHEMICAL ENGINEERING
BIO- & CHEMICAL REACTOR ENGINEERING AND SAFETY SECTION
Celestijnenlaan 200F box 2424
B-3001 Leuven
http://cit.kuleuven.be/creas